



Pedro Alexandre Glória Cardoso

Mestre em Engenharia Física

**X-ray fluorescence spectroscopic technique for
quality control in pharmaceutical, agronomy and
automobile industry from a biomedical
perspective**

Dissertação para obtenção do Grau de Doutor em
Engenharia Biomédica

Orientador: José Paulo Moreira dos Santos, Professor
Catedrático, FCT-NOVA

Co-orientador: Mauro António Moreira Guerra, Professor
Auxiliar, FCT-NOVA

Júri

Presidente: Maria Adelaide de Almeida Pedro de Jesus,
Professora Catedrática, FCT-NOVA

Arguentes: Ignasi Queralt Mitjans, Research Scientist,
Institute of Environmental Assessment and
Water Research (Spain)

Ana Luísa Monteiro da Silva, Professora
Auxiliar, Universidade de Aveiro

Vogais: João Manuel Rendeiro Cardoso, Professor
Auxiliar, Universidade de Coimbra

José Paulo Moreira dos Santos, Professor
Catedrático, FCT-NOVA

Maria Adelaide de Almeida Pedro de Jesus,
Professora Catedrática, FCT-NOVA



FACULDADE DE
CIÊNCIAS E TECNOLOGIA
UNIVERSIDADE NOVA DE LISBOA

September, 2021



Pedro Alexandre Glória Cardoso

Mestre em Engenharia Física

**X-ray fluorescence spectroscopic technique for
quality control in pharmaceutical, agronomy and
automobile industry from a biomedical
perspective**

Dissertação para obtenção do Grau de Doutor em
Engenharia Biomédica

Orientador: José Paulo Moreira dos Santos, Professor
Catedrático, FCT-NOVA

Co-orientador: Mauro António Moreira Guerra, Professor
Auxiliar, FCT-NOVA

Júri

Presidente: Maria Adelaide de Almeida Pedro de Jesus,
Professora Catedrática, FCT-NOVA

Arguentes: Ignasi Queralt Mitjans, Research Scientist,
Institute of Environmental Assessment and
Water Research (Spain)

Ana Luísa Monteiro da Silva, Professora
Auxiliar, Universidade de Aveiro

Vogais: João Manuel Rendeiro Cardoso, Professor
Auxiliar, Universidade de Coimbra

José Paulo Moreira dos Santos, Professor
Catedrático, FCT-NOVA

Maria Adelaide de Almeida Pedro de Jesus,
Professora Catedrática, FCT-NOVA



FACULDADE DE
CIÊNCIAS E TECNOLOGIA
UNIVERSIDADE NOVA DE LISBOA

September, 2021

X-ray fluorescence spectroscopic technique for quality control in pharmaceutical, agronomy and automobile industry from a biomedical perspective

Copyright © Pedro Alexandre Glória Cardoso, NOVA School of Science and Technology, NOVA University Lisbon.

The NOVA School of Science and Technology and the NOVA University Lisbon have the right, perpetual and without geographical boundaries, to file and publish this dissertation through printed copies reproduced on paper or on digital form, or by any other means known or that may be invented, and to disseminate through scientific repositories and admit its copying and distribution for non-commercial, educational or research purposes, as long as credit is given to the author and editor.

ACKNOWLEDGEMENTS

This research was funded in part by FCT (Portugal) under research center grant UID/FIS/04559/2020 (LIBPhys). I want to acknowledge the support from FCT and Volkswagen Autoeuropa, Lda for the PhD research grant, under Contract PDE/BDE/114483/2016

I want to thank my two advisors for the duration of this project, Professors José Paulo Santos and Mauro Guerra, for their supervision and insight in both theoretical and practical subjects necessary for the development of both this thesis but also the prototypes. Their scientific guidance and deep expertise was one of the main driving forces of this work and was absolutely invaluable. I would also like to acknowledge the great working conditions and infrastructures provided by them and their scientific group that made this work possible.

On the company side, I would like to thank Carlos Fujão from the Volkswagen Autoeuropa, lda. ergonomics department, that went above and beyond as my main connection to the company. His availability throughout this work was of unrelenting helpfulness. His positive attitude was the primordial reason that working with such an heavy company structure never felt too overwhelming.

I want also to take paragraph to acknowledge the help of some other people and groups that shaped this work. First of all the people in the workshops, both mechanical and electronic, from both the Department of Physics of our university and the Autoeuropa plant. They were very helpful and provided great contributions to developed prototypes. On this subject, I want to give a special thanks to Fabio Evangelista who provided not only the technical help needed for the completion of many electronics tasks but also worked as brainstorming partner for many concepts of the actual prototypes. His help cannot be understated and I am very thankful to the way he selflessly dedicated so many hours of his own time to help with this project. Another special thanks goes to Professors João Goes and João Pedro Oliveira from the Department of Electronical and Computer Engineering, for all the in depth technical feedback on the code and electronics developed in this work to establish a GPRS/GSM client via arduino. Moreover, I want to thank our secretary staff specifically Luiza Oliveira and Filipa Reis for their availability and help with both the bureaucratic nuances of my PhD but also processing the orders of materials and components used. And finally, to all my colleagues from the department in particular Luis Martins, Patricia Carvalho and David Fernandes.

Last but not least, to my family, my parents Miguel Cardoso and Sónia Cardoso and

my sister Inês Cardoso, I want to thank for all the unwavering support they provided, up until and during, the course of this long PhD work. And above all, I want to thank my wife Inês Leitão who was the emotional and psychological support that lead me to complete this work even when obstacles were stacking up and seem too big to overcome. She was not only the emotional support, but often, also the moral and decision making compass for this work and for that she knows I will be forever thankful. Finishing this work would have been impossible after all the setbacks without her presence in my life. Lastly, I would also like to thank her for proof reading most of my work and giving me great and constructive feedback.

ABSTRACT

In this work, we investigate the versatility of X-ray fluorescence spectroscopic technique specifically in biomedical applications. To prove the robustness of the method we developed three case studies from three very distinct industries with different backgrounds. In the first example, we study the application to the pharmaceutical industry by analyzing a group of samples of commercially available iron supplement pills. This analysis shows that even though iron concentrations are measured to meet the advertised values, there are important elemental contaminants, specifically, manganese and nickel. In the second example, we have analyzed food samples, more specifically, biofortified wheat grains. This analysis focus on assessing the ability of different genotypes for retaining the biofortified element - zinc. Even though most sample show enhanced zinc content, zinc distribution inside the grain is not homogeneous and this element tends to be found in higher concentrations in the embryo and vascular bundle. In the third example, we have developed a study in collaboration with the biggest automotive plant in Portugal – Volkswagen Autoeuropa. The main goal is to install, at least, one low-cost air quality control device in one of the workstations of the factory. For this purpose, we designed two prototypes that used the *wind tunnel* principle to deposit suspended particles in these workstations onto quartz fiber filters. These filters were then analyzed not only by XRF but also via microscopic camera analysis, SEM with EDX. Results for both size and composition concentrations show a linear behavior with deposition time, for a range of four identified trace elements: Iron, Zinc, Manganese and Copper. From these samples we conclude that the number of suspended metallic particles is not negligible and a repeated and accumulated long time exposure might have health consequences.

Keywords: EDXRF, composition analysis, industry, iron supplements, biofortification, aerosol, quartz fiber filter, SEM

RESUMO

Neste trabalho foi estudada a versatilidade da técnica de espectroscopia de fluorescência de Raios-X especificamente em aplicações biomédicas. Para demonstrar a robustez do método foram investigados três cenários provenientes de indústrias de origens e naturezas muito distintas. No primeiro exemplo discutido, estudou-se a aplicação à indústria farmacêutica, aplicando a técnica a um conjunto de amostras de suplementos de ferro comercialmente disponíveis. Esta análise demonstrou que apesar das concentrações de ferro estarem de acordo com as tabeladas no rótulo, existem contaminantes importantes, nomeadamente níquel e manganês. No segundo exemplo, foram analisadas amostras de comida, especificamente, trigo biofortificado. Esta análise focou-se num conjunto grande de amostras onde se averiguou a habilidade de reter o elemento biofortificado - zinco - em cada um dos genótipos de trigo analisados. Apesar dos grãos biofortificados mostrarem um claro aumento de zinco, a distribuição de zinco no grão não é no entanto uniforme, sendo que, na grande maioria dos casos, este elemento está concentrado no embrião e sistema vascular. O terceiro exemplo, foi desenvolvido em ambiente industrial na maior fábrica automóvel de Portugal - Volkswagen Autoeuropa. O foco principal deste trabalho é o desenvolvimento e instalação de uma solução *low-cost* de controlo de qualidade do ar num dos postos de trabalho na linha de montagem da fábrica. Para tal, desenvolvemos dois protótipos baseados num conceito clássico de *túnel de vento* para possibilitar a deposição das partículas suspensas no ar num filtro de fibra de quartzo. Para além da análise por XRF estes filtros foram também sujeitos a inspeção óptica por micro-câmara binocular e análise SEM com EDX. Os resultados mostram que existe uma relação linear entre o tempo de deposição e a concentração de partículas nos filtros e revelam que os elementos de traço desta análise são o ferro, o zinco, o manganês e o cobre. Esta análise revela que temos quantidades de todos estes elementos acima dos nossos limites de detecção e como tal o impacto na saúde dos funcionários devido a uma exposição de longa duração deve ser apurado.

Palavras-chave: EDXRF, análise elemental, indústria, suplementos de ferro, biofortificação, aerossóis, filtros de fibra de quartzo, SEM

CONTENTS

List of Figures	xvii
List of Tables	xxi
Listings	xxiii
1 Introduction	1
1.1 XRF technique	2
1.1.1 X-ray production	3
1.1.2 X-ray interaction with matter	6
1.1.3 Designs, geometries and beam optics	7
1.1.4 X-ray detection and spectra	11
1.1.5 Quantification	13
1.1.6 Applications	17
2 XRF technique applied to the pharmaceutical industry	21
2.1 Scope and objectives	21
2.2 Methods and materials	24
2.2.1 Sample description and preparation	24
2.2.2 Experimental setup	24
2.2.3 Calibration of the analytical method	25
2.3 Results and Discussion	27
3 XRF technique applied to the agronomy/food industry	31
3.1 Scope and objectives	31
3.2 Materials and methods	35
3.2.1 Plants	35
3.2.2 Field trials	35
3.2.3 Analytical methods	36
3.3 Results and discussion	37
3.3.1 Whole grain	37
3.3.2 Grain structures	40
3.3.3 Statistical analysis	42

CONTENTS

3.3.4	Whole grain analysis	43
3.3.5	Grain structures analysis	45
4	XRF technique applied to the automobile industry	49
4.1	Scope and objectives	49
4.2	Aerosols	52
4.2.1	Aerosol properties	55
4.2.2	Aerosol health impact	58
4.2.3	Aerosol measurement techniques	62
5	Prototype design and development	73
5.1	Development of the first prototype	74
5.2	Development of the second prototype	77
5.3	Electronics	82
6	Prototype installation and measurements	87
6.1	Experimental setups	88
6.1.1	Size distribution analysis	88
6.1.2	Composition analysis	90
6.2	Results	92
6.2.1	Size distribution results	92
6.2.2	Composition results	97
7	Conclusions	103
	Bibliography	107
	Appendices	125
A	Appendix 1	125
B	Appendix 2	127
B.1	Power source and management	127
B.2	DC fan	128
B.3	Step motor control	129
B.4	DC motor control	130
B.5	I ² C communication	131
B.6	Server communication via GSM/GPRS	133
C	Appendix 2	147
C.1	Arduino Code	147
C.1.1	Arduino Master	147
C.1.2	Arduino Slave	151
C.2	Server Code	154

C.2.1	Views	154
C.2.2	Models	158
C.2.3	Admin	160
C.2.4	App Urls	161
C.2.5	Site Urls	161
C.2.6	Settings	161
C.2.7	History html	163
C.2.8	Home html	165
C.3	Image processing script	168

LIST OF FIGURES

1.1	Schematic representation of an EDXRF instrument[7].	4
1.2	Schematic comparison of processes 1 and 2. Light yellow represents the primary particle, blue is the nucleus, yellow the electrons, black is the photon and orange is the atomic relaxation.	5
1.3	Typical X-ray tube spectrum[8].	5
1.4	XRF instrument schematic using the triaxial geometry[11].	9
1.5	μ -EDXRF analysis of a biofortified wheat grain [5].	10
1.6	Example of X-ray fluorescence spectrum [8].	13
2.1	Picture of the EDXRF spectrometer with triaxial geometry used in this work, obtained from [8].	25
2.2	Two measured EDXRF spectra corresponding to an Anemifer sample (black solid line) and a Neutrofer Fóllico sample (red dotted line). The counts are plotted versus the detector energy in keV.	27
3.1	Structure of a wheat grain as reproduced in [91]. a is a representation of the whole grain and b is a cross section view of the grain.	33
3.2	Elemental map of two grains corresponding to different samples, highlighting the anatomical structure selection procedure. In a) it can be seen that the vascular bundle was severed upon sample preparation, while in b) one can see that the vascular bundle has remained solely on one side of the cut grain. . .	37
3.3	Concentrations of iron (Fe) and zinc (Zn) as measured by methods M1 and M2.	39
3.4	Average Zn concentration, in $\mu\text{g/g}$, of all of the studied samples, divided by anatomical structure. The error bars represent the quadrature sum of the instrumental uncertainties with one standard deviation.	40
3.5	Zn concentration, in $\mu\text{g/g}$, of all of the studied samples, divided by anatomical structure. The average values of the samples grown in the Zn-rich soil as well as in normal soil are shown as blue and red solid lines, respectively. The dashed lines represent one standard deviation.	41
3.6	Zn and Fe concentrations by kernel anatomic structure in $\mu\text{g/g}$: EM - embryo; EN - endosperm; V - vascular bundle. G1 values are the mean values from both normal and enriched soils.	42

LIST OF FIGURES

3.7	Plot of Zn vs Fe concentrations together with fitted classical (red) and robust (dashed blue) regression lines, plus the 95% confidence region (gray) computed from the classical fit.	47
4.1	John Aitken’s first dust particle counter.[118]	53
4.2	Schematic representation of an aerosol chemical interactions.[114]	54
4.3	Atmospheric aerosol number and volume distributions.[114]	57
4.4	Human respiratory tract deposition fractions profiles[133].	59
5.1	Schematic representation of the design approach.	74
5.2	CAD drawings of the sample holder parts.	75
5.3	Acrylic platform for connections and power management.	76
5.4	77
5.5	78
5.6	DVD optics slide mechanism example.	79
5.7	CAD drawing of the sliding sample holder part.	80
5.8	Sliding mechanism assemble.	80
5.9	CAD drawing of the acrylic boxes to store the filters.	81
5.10	CAD drawing of the parts to be 3d printed to couple the motor with the filter roll.	82
5.11	83
5.12	Circuit schematic for the first prototype.	83
5.13	Circuit schematic for the second prototype.	84
6.1	Installation of the first prototype on a case study welding station (top right).	87
6.2	88
6.3	89
6.4	Our design of a triboluminescence X-ray source to be encapsulated in an acrylic box in order to conserve the vacuum intended inside.	91
6.5	92
6.6	Particle concentration per mm^2 normalized by the logarithm of the corresponding bin particle diameter. X error bars are estimated by bin size and Y error bars are estimated using the standard deviation of our datasets.	94
6.7	SEM image with overlapping spectra obtained with EDX for the highlighted small area.	95
6.8	SEM image with overlapping spectra obtained with EDX for the highlighted small area.	95
6.9	96
6.10	Typical EDXRF spectrum obtained by mapping our deposited quartz fiber filters. The two filters shown are the same as figures 6.2a and 6.2h.	98

6.11 Concentrations comparison across all the filters of the most prevalent trace elements of the EDXRF analysis: Fe, Zn, Mn and Cu. All these plots show both the results for the total deposited particles and the central area of deposition. Error bars are estimated from the difference between the concentrations in the two different areas. This is representative of the particle deposition variability that is the biggest source of uncertainty in this type of measurements.	99
B.1 Server homepage developed for this thesis.	140
B.2 Server admin page screenshots.	144
B.3	145

LIST OF TABLES

2.1	Information on the iron supplements used in this work.	24
2.2	Elemental concentration ($\mu\text{g/g}$) present in certified standard samples. Values are listed either with one standard deviation (value \pm standard deviation) or with an asterisk (*), meaning that the value was obtained by non-certified methods. <i>LOD</i> stands for limit of detection. Three standard reference materials with light organic matrices and several concentration levels were considered, namely, dogfish muscle (NRRC-DORM-2), lobster hepatopancreas (NRCC-TORT-2) and orchard leaves (NIST-SRM1571).	26
2.3	Elemental concentrations of manganese, iron and nickel in <i>Anemifer</i> measured by ICP-AES and those obtained with our analytical method.	27
2.4	Reference and measured concentrations of the iron supplements analyzed.	28
2.5	Comparison between measured amounts of nickel and manganese and PDE(permitted daily exposure).	28
3.1	Concentration group means and standard errors of Zn and Fe for genotypes, methods and soils in the case of the whole grain data.	38
3.2	Concentration group means and standard errors of Zn and Fe for genotypes, anatomical structures and soils in the case of the structural grain data.	43
3.3	Results from the classical and robust fits of model (3.1). σ_s^2 , σ_m^2 and σ_e^2 are the variance associated with soil, method and residuals distributions respectively.	44
3.4	Genotype estimates and ranking after the classical and robust fits of model (3.1). Concentration values are in $\mu\text{g/g}$	45
3.5	Results from the classical and robust fits of model (3.2).	46
3.6	Genotype estimates and ranking after the classical and robust fits of model (3.2). Concentration values are in $\mu\text{g/g}$	46
4.1	Aerosol measuring instruments classification. *Examples of measuring techniques. Full size on the appendix A.1.	65
6.1	Particles per mm^2 binned by size for each of the deposited filters shown in Figure 6.2. Values averaged across 21 images per filter.	93

LIST OF TABLES

6.2	Mass comparison between the XRF analysis and microcamera observations. The last column corresponds to the amount of particles needed with 0,4 μm of diameter to account for the missing mass.	100
A.1	Aerosol measuring instruments classification. *Examples of measuring techniques.	126

LISTINGS

ACRONYMS

AC	Alternate current
ADC	Analog to digital converter
AL	Alveolar region
AMS	Aerosol mass spectrometer
APN	Access point name
APS	Aerodynamic particle analyzers
AT	ATtention commands
CAD	Computer aided design
CNC	Condensation nucleus counters
CNT	Classic nucleation theory
CPC	Condensation particle counters
CPU	Central processing unit
DAC	Digital to analog converter
DC	Direct current
DF	Deposition fraction
DFT	Discrete fourier transform
DMA	Differential mobility analyzers
EDS	Energy dispersive spectroscopy
EDX	Energy dispersive X-ray spectroscopy
EDXRF	Energy dispersive X-ray fluorescence
ET	Extrathoracic compartment
FFT	Fast fourier transform
GDE	General dynamic equation
GPRS	General packet radio service
GSM	Global system for mobile communications

ACRONYMS

HRT	Human respiratory tract
HTTP	Hypertext transfer protocol
I ² C	Inter-integrated circuit
I/O	Input/Output
ICP	Inductively coupled plasma
IP	Internet protocol (address)
LMM	Linear mixed model
LOD	Limit of detection
MCA	Multi-channel analyzed
MOSFET	Metal oxide semiconductor field effect transistor
OPC	Optical particle counters
PDE	Permitted daily exposure
PDF	Probability density function
PIXE	Proton induced X-ray emission
PM ₁₀	Particle matter under 10 μm
PM _{2.5}	Particle matter under 2.5 μm
PWM	Pulse width modulation
QCM	Quartz-crystal microbalance
SDA	Serial data line
SDD	Silicon drift detector
SDK	Serial clock line
SEM	Scanning electron microscopy or Scanning electron microscope
Si(Li)	Lithium drift Silicon detectors
SIM	Subscriber identification module
SOAs	Secondary organic aerosols
SSD	Solid state detector
TB	Tracheobronchial region
TCP	Transmission control protocol
TEM	Transmission electron microscopy or Transmission electron microscope
TEOM	Tapered-element oscillating microbalance
TXRF	Total reflection X-ray fluorescence

UFP	Ultra-fine particles
VM	Virtual Machine
WDXRF	Wavelength dispersive X-ray fluorescence

SYMBOLS

B	ventilation rate
c_i	elemental concentration
d_{50}	cut-off diameter
δ_{ij}	enhancement factor
D_v	diffusivity
D_p	particle diameter
ϵ_{ij}	enhancement effects coefficient
h	Planck constant
I	beam intensity
I_i	characteristic elemental fluorescence emission intensity
k_B	Boltzmann constant
λ	mean free path or electromagnetic wavelength depending on context
m	mass
μ	statistical mean or effective mass absorption coefficients depending on context
N	aerosol particle number concentration
n_0	inhalability ratio
N_a	Avogadro number
v	molecular volume or particle velocity depending on context
p	momentum
p_i	pressure of a gas specie

SYMBOLS

π	the numerical value of pi
r	particle or cluster radius
R	gas constant
r^*	critical radius of a cluster
R^2	coefficient of determination
$\rho\nu$	number density of a gas specie
σ	surface tension or standard deviation depending on context
σ^2	variance
T	temperature

INTRODUCTION

In this work, a review of biomedical applications of the X-Ray Fluorescence (XRF) technique is presented. For this purpose, we have developed three case studies in which this technique is applied in order to obtain a biomedical analysis of samples from different industries. The chosen industries for this work were: the pharmaceutical industry, the agricultural/food industry and the automobile industry. The reasoning behind the choice of these three industries will become clearer throughout this thesis. However, as the objective of this thesis is to show the versatility and sensitivity of the XRF technique, it was important to choose a diverse set of industries. This is also visible in the variety of samples obtained, which will have very different typologies across all three cases to show the robustness of the methods used. Most importantly, all the examples studied and presented have an intrinsic safety and health motivation that urge a biomedical analysis.

This document is structured to provide a complete overview of the work, from the technique to the results. We will begin to describe the theoretical background and applications of the XRF technique in section 1.1. Then we will proceed to describe the three case studies that were analyzed. Even though we provide three separate industry examples, our focus and effort is not evenly distributed across all three, due to the complexity of the associated problems. Specifically, the first two case studies, the pharmaceutical (chapter 2) and the agronomy/food (chapter 3) industry studies were developed in the first year of this work, while the automobile industry example was the main focus of the remaining PhD years. Therefore, it is only fitting that we dedicate a bigger portion of this thesis, to the work developed associated with that case study. The automobile industry biomedical application of the XRF technique starts in chapter 4, where an introduction of the problem is provided. In this introduction, we approach the scope and objectives that

were aligned with the factory and provide a theoretical overview of the measuring object - aerosols. In chapter 5, we provide an in-depth description of the development and construction process of two different prototype instruments to accomplish the tasks needed for this problem. Finally, we present and discuss the results of the analysis performed on samples obtained with our devices in chapter 6. This leaves us with a segmented analysis of this last case study into three chapters, while the first two examples (chapters 2 and 3) follow the same kind of approach - introduction, methods and results, but condensed in a single chapter.

1.1 XRF technique

The first big milestone for X-ray research dates back to the year 1901, when Wildhel Röntgen received the Nobel prize for the discovery of this band of the electromagnetic spectrum. Soon after this discovery, many groups took an interest and started developing techniques based on X-ray spectroscopy. Several Nobel prizes were awarded in the scope of this technique and its applications, from the late 10s to early 20s decades. Commercially, X-ray based apparatus traces back to the 50s decade.

Nowadays, X-ray spectrometry counts with several different kinds of instruments. Generally speaking, these instruments usually differ on the excitation source and process. In this work, we have chosen to work with X-Ray Fluorescence (XRF) where there is an electromagnetic radiation source, either an X-ray tube, a synchrotron beam or a radioactive source. Some other examples of X-ray spectrometry also deserve to be mentioned. Notoriously the Proton Induced X-ray Emission (PIXE)[1], which uses a beam of charged particles, i.e. ions (usually protons), as an excitation source, or the SEM-EDS where the excitation source is an electron beam.

XRF is a widely used technique, which traditionally uses a polychromatic beam to excite a sample which induces the production of photons via fluorescence that are counted by a detector in order to produce an X-ray spectrum. There are two types of XRF techniques: wavelength dispersive (WDXRF) and energy dispersive (EDXRF). The former spectrometers use crystals to disperse the radiation emitted from the sample and select a narrow wavelength band. This technique limits the analysis to an element by element assessment. On the other hand, EDXRF uses a high resolution solid state detector connected to multichannel analyzers in order to assess a wide range of elements' concentrations within a sample.

EDXRF is one the most popular spectrometric techniques nowadays[2, 3, 4, 5]. There are several appeals to this technique. One of the most important is the fact that it is a non-destructive technique bar very few exceptions. This is only possible because the energy and intensity of primary X-rays is not enough to cause structural changes in the sample. This allows for cross instrument calibration since one sample can be analyzed by many different spectrometers. This is specially useful for quantifying standard samples. Another advantage of this technique is the lack of or minimal sample preparation[6]. Any

state of matter can be easily analyzed with the only concern of being able to be placed in the specific sample holder of the instrument. Moreover, EDXRF is also a very fast and cheap technique when compared with other "competing" techniques. It is possible to obtain element quantification within a few minutes in many cases. Often, for the sole purpose of extending the amount of spectral data, it is advised to go up to one hour or more. This technique ends up being quite inexpensive given that there is no sample preparation and the costs of operating the spectrometers are also quite low.

Many configurations are possible for acquiring an x-ray spectrum with EDXRF. From benchtops to hand-held to experimental designs, these instruments can be tailored to the user needs. With an ease for very fast quantification of wide range of elements, EDXRF spectrometers find many applications in various scientific fields from geology and biology, to art analysis and forensic sciences.

This technique is not however suitable to be blindly applied to every sample analysis. For example, if you want to measure very detailed and small components, the usual beam size of around the mm scale will deter you from good results. The typical output of this technique aims towards a whole sample type of analysis. It is also not suitable for determining structures and chemical bonds, since it has no sensibility for matter arrangements. Furthermore, some elements provide very low fluorescence yields, traditionally very light elements, hence becoming unsuitable for their quantification.

A generic representation of an X-ray spectrometer can be found in Figure 1.1. From this figure we can see the major components of a basic EDXRF instrument with an x-ray tube directed towards a sample holder at an angle with a detector. This detector is then connected to a multichannel analyzer and through an ADC which allows the spectral information to be available on a computer. Designs can then vary based on geometry and optical components (such as collimators or X-ray lenses) used.

1.1.1 X-ray production

This is the first step that occurs within an EDXRF spectrometer, and more specifically, on the X-ray tube for most current instruments. X-rays, as it has been stated, are a band of the electromagnetic radiation spectrum. This band corresponds to wavelengths from 0.01 nm to 10 nm which translates into 120 keV to 0.12 keV energy wise. Physically, X-rays can be produced by three different processes:

1. deceleration of highly energetic particles (electrons, alpha particles, ions);
2. electronic transitions in the inner orbitals promoted by the interaction with high-energy particles or photons;
3. radioactive decay;

The third process will not be elaborated in this thesis due to its lack of relevance for our instruments. The first process on the other hand is very predominant since it

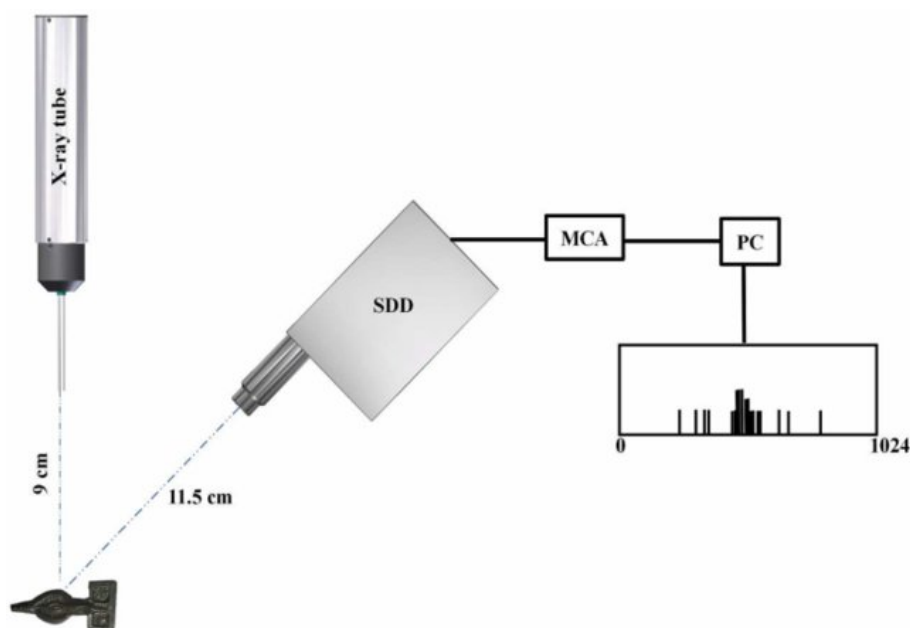
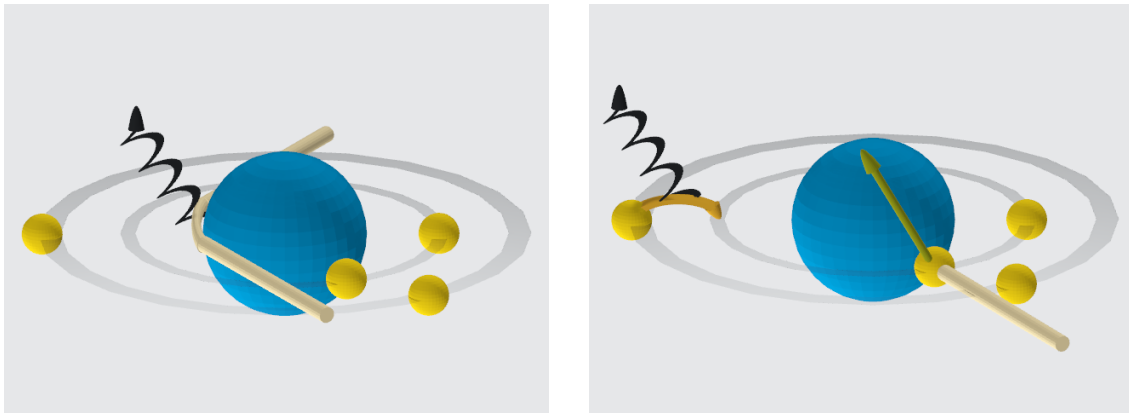


Figure 1.1: Schematic representation of an EDXRF instrument[7].

results in the production of Bremsstrahlung radiation. In this process, when a high energy charged particle transversing a medium gets in contact with an atom, it suffers an inelastic scattering by its nucleus, which changes the direction of propagation and causes a loss of energy, culminating with the emission of a photon. As this process is dependent on the angle and on the energy of the colliding particle, the energy of the photon can assume any value within a range, creating a continuous spectrum of radiation.

Regarding the second mechanism, similarly a highly energetic particle comes into contact with an atom. However, in this interaction the energy is absorbed by a bound electron. This results in the ionization of the atom and in the creation of a vacancy on one of the full inner shells. As the atom becomes unstable due to this vacancy, one of its electrons from the outer shells can lower its energy in order to fill that vacancy, by emitting a photon or another electron (Auger electron). Therefore, these transitions have very well defined energies that correspond to the energy difference between the two levels. These transitions are categorized in the Siegbahn nomenclature, according to the vacant inner shell's denomination, being K transitions (transitions to the K shell, the innermost shell) the most important for low to medium atomic number spectrometry, followed by L transitions that are usually employed for heavy elements. Furthermore, underline indexes are added in the form of α or β , for example, to account for the outer shell orbital provenience of the electron. The Auger emission is a competing channel to the X-ray photon and is specifically important for lighter elements (atomic numbers under 40). In Figure 1.2 we can see a schematic comparison of processes 1 and 2, side by side.

There are many configurations for an X-ray tube, however, the more standard X-ray tube is composed of three major parts: a filament to be heated and produce electrons, an electric field to accelerate them and an anode where these electrons initiate the processes



(a) Schematic representation of the Bremsstrahlung photon emission.

(b) Schematic representation of the inner shell electronic ionization proceeded by atomic relaxation.

Figure 1.2: Schematic comparison of processes 1 and 2. Light yellow represents the primary particle, blue is the nucleus, yellow the electrons, black is the photon and orange is the atomic relaxation.

1 and 2. This creates a flux of electrons within a solid angle from the anode that is directed towards a window (typically beryllium), which lets them out of the tube. As it has been stated above, in process 1, the photons generated form a continuous spectrum, while in process 2, the photons have very specific discrete energies for the allowed electronic transitions within the atoms of the anode. This means that the possible energies are intrinsically related to the anode's material. This specific energies are referred to, in X-ray spectrometry, as the characteristic lines of an element.

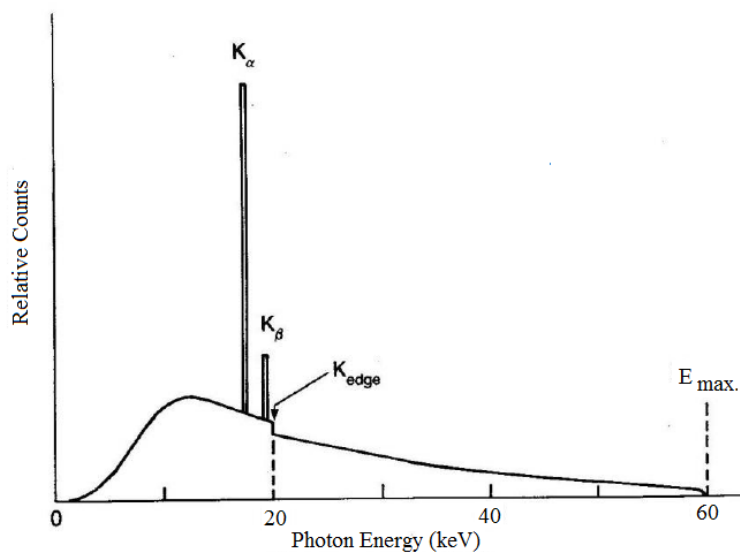


Figure 1.3: Typical X-ray tube spectrum[8].

In Figure 1.3 we can see a typical X-ray tube spectrum which is an histogram representation of the amount of photons per energy bin. As it can be observed in this graph there is a smooth line of background that rises from 0 keV to ~ 12 keV, and then it smoothly decreases until E_{\max} is reached. This background curve is associated with the Bremsstrahlung radiation, being E_{\max} the highest possible energy for photons, which can be related to the primary electrons energy and the electric field across the tube. This spectrum is not however 100% smooth, as there is a discontinuity at K_{edge} , which is the binding energy of the K-shell. What happens at this point is that the photons generated have enough energy to induce a secondary photoelectric ionization, "consuming" themselves in the process and never exiting the tube. This photoelectric effect will also cause a vacancy in the inner shell that will be filled with an atomic relaxation process and the emission of a characteristic X-ray photon or the corresponding Auger electron ejection. K_{α} and K_{β} are the two most important characteristic lines of this anode's element and are represented as prominent peaks. This means that photons with these energies will be the primordial source of ionization of our sample.

X-ray tubes can vary greatly from anode and window materials, to cooling systems and geometries, etc. The option between two X-ray tubes should be application oriented. For example, heavier anodes provide more intensity of Bremsstrahlung radiation. However, it is desirable that this material is also a good heat conductor, since the majority of primary electrons will transfer heat to the anode. The window of choice is also a compromise. On one hand we want it to be as thin and permeable to photon transmission as possible, but on the other hand, it needs to be thick and durable enough to withstand the vacuum and heat inside the tube without breaking.

1.1.2 X-ray interaction with matter

There are several ways a beam of photons can interact with matter, however, depending on what the beam energy range is, the number of channels can be narrowed to a few main processes. When we are referring to a beam of X-rays provided by an X-ray tube, we usually have energy ranges from the order of magnitude of a few keV up to tens of keV well below the 1MeV range. For these ranges, the main processes can be narrowed to photoelectric absorption and scattering.

The photoelectric effect has already been mentioned in the last section and is similar to the first part of process 2 that happens in the tube's anode. However, in these cases, instead of a beam of electrons the excitation source is a beam of photons. Similarly, when this beam comes in contact with the atoms of the sample, there is a probability of a bound electron absorbing its energy. This probability is maximum when the photon energy matches the exact value of the binding energy of that electron, since in this case an ionization occurs. If the energy of the photon is smaller than the binding energy, then this electron is not ejected and rather just excited into a higher level orbital. This channel's cross section is also correlated with the atomic number of atoms in the sample being

proportional to $\sim Z^4$ for low energies and $\sim Z^5$ for high energies [9].

When the beam comes in contact with the sample's atoms there can also occur scattering of its photons either by the nucleus or bound electrons. Scattering assumes two different forms: elastic coherent scattering and inelastic incoherent scattering, which are also referred to as Rayleigh and Compton scattering, respectively.

As it can be assumed, in Rayleigh scattering there is no loss of energy for the photon (apart from energy loss due to nucleus recoil, which is very small). The photons in this kind of scattering change direction due to the sample bound electrons leaving with approximately the same energy that they initially had. The cross section of this process is proportional to $\sim Z^2$, meaning it is more probable at higher values of Z . This process is also more probable for lower energy photon interactions, compared to its counterpart.

In Compton scattering, the photons lose energy when scattered by the sample's lowly-bound electrons. The lost energy is transferred to these electrons. This process is more probable for higher energies and lower values of Z , compared to its counterpart, because the dependence of the atomic number is only $\sim Z$. This phenomenon is also very dependent on the angle of scattering[4]. Both Compton and Rayleigh peaks do not carry a lot of information about the sample composition and are usually interpreted as background, hence not very useful for samples identification.

All of these processes, photoelectric effects and scattering, contribute to the attenuation of the X-ray photon beam. Even though some photoelectric effects might result in the ionization of the atom and lead to atomic relaxation, which emits a characteristic X-ray photon for that element, most of the energy absorbed will just promote atomic electrons excitation. Therefore, the beam is attenuated in the sample in a layer by layer fashion. When this effect is not properly accounted in thick samples, it might result in an incomplete analysis, since the excitation beam doesn't reach the bottom layers. For this purpose, mass attenuation coefficients (cm^2/g) exist to gauge how much a sample will absorb photons of a given energy. Even though in lower Z elements, Compton scattering is very relevant for attenuation. In the typical X-ray range, photoelectric effects are the predominant source of attenuation.

1.1.3 Designs, geometries and beam optics

Between the X-ray source and the detector there are usually several optical devices, from filters to collimators, the design options can be varied. Filters are used to improve the signal-to-noise ratio and are measurement driven. This means that option between one or another might be different from sample to sample. As it is the case for other types of filters, they are used to select a range of photon energies. They are usually implemented as high-pass filters when we want to exclude some lower energies in order to reduce noise around what is expected to be measured. Filters can be chosen accordingly by composition alone but also by thickness. As it is common in the instrumentation field, there must be a compromise, in this case between the ability to filter some energies and

not reducing tremendously the intensity of the X-ray beam.

The other optic device that appears in most designs is the collimator. When the X-ray beam exits the tube it usually does so with an angular distribution of $\sim 100^\circ - 150^\circ$. This wide angular range is not very adequate for most X-ray experiments, hence there is a need to use collimators. These devices absorb most of the photons of the beam that are not within a very narrow hole. This allows for the beam to be focused onto the sample with a reduced angular spread and at the expense of beam intensity. Most setups use several collimators in series, such that they can guarantee a very specific diameter for the beam. In order to minimize the excitation caused by the primary X-ray beam photon, the material of these optical devices must be chosen accordingly.

Regardless of the optics used, the objective of each experiment is to improve the signal-to-noise ratio. One of the main sources of noise, in an XRF instrument is usually associated with Bremsstrahlung radiation which has a continuum spectrum of energies as discussed above. Furthermore, the primary beam from the X-ray source is usually polychromatic and unpolarized. However, for XRF spectrometry it would be ideal that the opposite was true, since a very monochromatic and polarized beam would leave less uncertainty in the fluorescence composition quantification. With the purpose of reducing the Bremsstrahlung background some designs have been implemented using a secondary target.

This method was first described in 1973 by Porter [10]. In this work, it was studied the possibility of exciting a secondary target with the primary beam. What was observed was that with the help of a thick secondary target, it was possible to create a secondary beam that was quasi-monochromatic. In this beam, the characteristic X-ray lines of that target will represent the vast majority of photons outgoing from the target reducing Bremsstrahlung radiation. For this kind of setups, it is obviously needed higher power X-ray tubes, since there is a significant drop of intensity not only on the optical devices used but specially on the secondary target excitation. These setups also offer a different kind of versatility by the means of choosing the secondary target. Since the primary beam is polychromatic, it is possible to excite a wide range of different secondary targets, which in turn produces characteristic quasi-monochromatic secondary beams with specific energies, that might be more or less adequate for each measurement. It is however important to design the combination of anode-secondary target in order to maximize the amount of photons in the primary beam with energies equal or close to the ionization energy of the K shell of the atoms of the secondary target. This will allow to maximize the intensity of the characteristic lines of the secondary target since the cross-section of the photoelectric effect has an abrupt rise at these energies.

The mentality behind using a secondary target can be extended with the use of the triaxial geometry. As opposed to the traditional dual axis geometry, where the beam is refracted at angles all contained within the same plane, the triaxial geometry takes an advantage of the full three dimensions. In Figure 1.4 we have the schematic of this kind of implementation. In these instruments the primary beam excites the secondary target,

which has an inclination. A secondary beam is then produced due to the excitation of this target and with the help of one or more collimators the angular distribution is narrowed to photons reflected at a 90° angle with the original beam. These photons proceed to excite the sample, which in turn will produce a third beam due to fluorescence. This last beam is also selected with collimators in a way that it does a 90° angle with the secondary beam, but also with the primary beam.

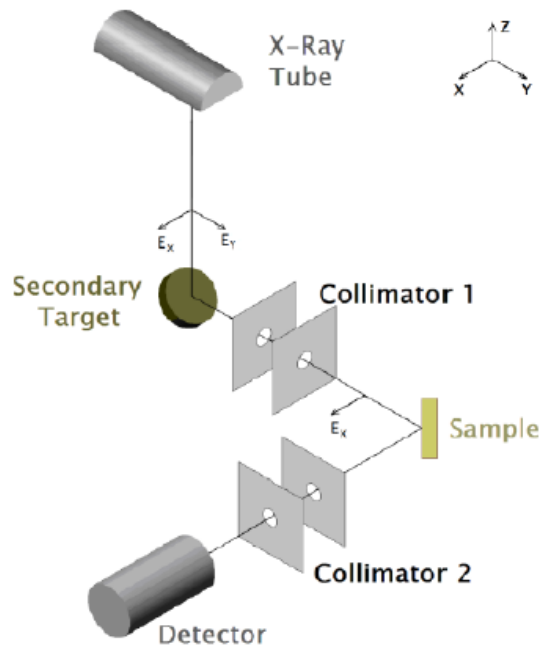


Figure 1.4: XRF instrument schematic using the triaxial geometry[11].

This kind of geometry allows for a major improvement on the signal-to-noise ratio since it can reduce immensely the Bremsstrahlung radiation. One of the reasons being the Klein-Nishina differential scattering cross-section[12] specifically for the angle of 90° . This expression is used for the description of photon inelastic scattering probability as function of the angle. The cross-section of this process, at these energies, has a global minimum for a 90° scattering angle, meaning that we can minimize the number of photons from the Compton scattering on the target by selecting this angle. Similarly, elastic scattering has a minimum for the same scattering angle which will further reduce scattered photons from the Bremsstrahlung radiation of the source.

Moreover, when the Bremsstrahlung radiation of the beam is scattered by a target it becomes polarized almost entirely in the direction perpendicular to the scattering plane[13]. The cross-section for linearly polarized photons becomes 0 when the scattering angle is 90° . Hence, when there is a second scattering on the sample, theoretically, polarized photons will be forbidden to scatter at a 90° angle. This would be only possible with an infinite level of collimation for each beam and zero divergence. In reality Bremsstrahlung radiation can only be highly reduced with good collimation. However,

the more we collimate a beam, the more intensity we lose, and so a compromise must be reached.

Unlike the scattering photons, the fluorescence ones have isotropic polarization, which means that characteristic X-ray lines both from the target and sample will be unaffected by angle selection. Fluorescence photons from the secondary target are able to scatter on the sample and hence both coherent and incoherent features will still appear on the X-ray spectrum.

Other notable designs for EDXRF spectrometers include μ -EDXRF and TXRF (Total Reflection X-ray Fluorescence). The former is not really different from standard EDXRF techniques, the only difference being on the focus of controlling the beam size to the micrometer range. As discussed before, reducing the beam size is usually associated with loss of beam intensity (this effect is significantly reduced if we are referring to polycapilar optics instead of collimators) and thus these instruments must be well optimized in this sense and have higher power tubes. These kind of techniques allow for many applications, since size resolution is often very important to analyze heterogeneous and complex samples. In Figure 1.5 we can see a μ -EDXRF analysis of a biologic sample where you can see the advantage of having a better size resolution on the beam. Some of the biologic structures can then be accurately mapped.

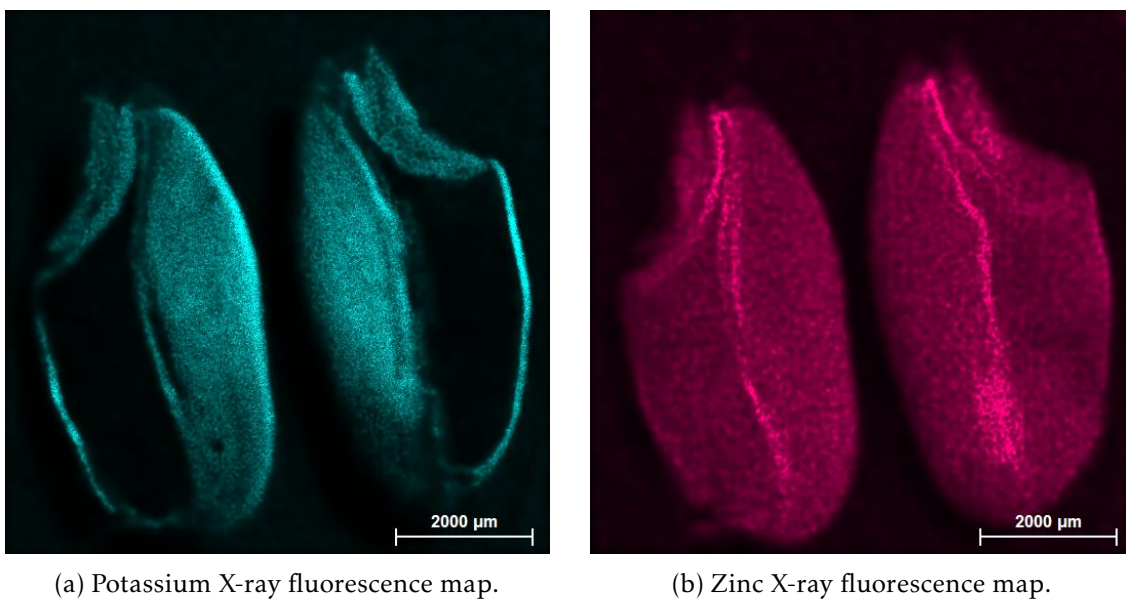


Figure 1.5: μ -EDXRF analysis of a biofortified wheat grain [5].

Regarding TXRF, the focus is in reducing the background of the Bremsstrahlung radiation, just like in the triaxial geometry. In this technique, it is used a physical process known as total reflection. From optic theory, it is known that a beam of light that comes into contact with a surface of another medium at an angle inferior or equal to the critical angle is totally reflected. This means that no radiation is theoretically transmitted or absorbed. It is then possible to calibrate an EDXRF apparatus, in order to make a well

colimated X-ray beam come into contact with the sample at a very narrow angle, inferior to the system critical angle. This way, it is possible to get rid of most background since the major scattering contribution for the X-ray spectrum will be totally reflected away from the detector. The detector will be positioned perpendicular to the sample and receiving mostly the photons from the characteristic lines of the sample.

1.1.4 X-ray detection and spectra

Detectors are the part of spectrometer system that is able to obtain information from the incident radiation. Detectors come in all shapes and forms and must meet the necessities of the instrument in question. Detectors can vary in the most observable characteristics like size, area, thickness, but also in more technical parameters such as principle of detection, energy and time resolutions, efficiency...

In EDXRF spectrometers, the most commonly used are the Si(Li) detectors (Lithium drifted Silicon detectors), followed by the germanium based ones. More recently, Peltier cooled Silicon Drift detectors (SDDs) have also become mainstream. The energy ranges measured by both Si(Li) and SSD detectors are comparable in the order of $\sim 1\text{keV}$ to 50keV . Even though the latter has a better resolution and higher counting rates, the former is still the most used due to its availability and price.

Si(Li) detectors are based on the semiconductor capabilities of silicon and are constituted at their core level by a lithium doped single crystal p-type silicon sensing tube. These crystals work like an electronic diode, which means that when current as a forward bias it is allowed to flow across the diode, but when it is reversely biased the diode enter in shutdown mode and blocks electronic flux across its junction. For proper operation, it is necessary however that both the crystal and the preamplifier to be cooled down (typically with liquid nitrogen) in order to reduce electronic noise and restrict the mobility of the lithium ions.

When X-ray photons come into contact with the detector they induce the photoionization of the crystal's atoms. This generates extra charge in the conduction band of the semiconductor, which will be proportional (most of the time) to the energy of the incoming photon. This charge will flow through the diode, due to the voltage applied to its terminals, generating a current pulse directly into the preamplifier stage. In this stage, and with the help of a capacitor, it is then possible to obtain a voltage pulse with big enough amplitude for it to go through a pulse processor. After that, we end up with a measurement, based on the amplitude and shape of this pulse, of the incoming X-ray photon energy. This measurement, will then be digitized, by the means of a multichannel analyzer with an ADC. At this stage, the measured energy will determine in which channel the event will be added, summing one count to that channel. After a period of time, we get multiple channels with a count number, which can then be processed by a computer to plot an histogram representation of the number of photons in each energy bin. This is what we call the accumulated X-ray energy spectrum of the sample.

As it has been implied in the previous paragraph, the charge induced on the detector might not always be proportional to the incoming photon energy, as there are some artifacts in the detecting process. Some detector interactions that may induce a bad energy measurement in this kind of detectors include: sum peaks, escape peaks and incomplete charge collection. The first one, as the name implies, corresponds to a detection where instead of measuring only one photon, two photons come into the detector in a small time frame. In this case, the time difference between two photons is so small that the detector time resolution is not enough to determine that two separate photons are inducing charge in the same event. As a result, this event's energy will be measured as a sum of the energies of the contributing photons.

Relatively to the escape peaks, an interesting phenomenon occurs. As the detected photons are mostly X-ray characteristic fluorescence lines of the samples, they are like the exciting primary beam, very energetic photons. This means that when they come in contact with the silicon crystal, they may also photoionize electrons from the inner shells that induce a posterior atomic relaxation process with a characteristic X-ray emission. Hence, the detector's Si atoms will sometimes emit their own characteristic X-ray line, mostly the K_α line, which has the energy of 1.74 keV. This means that in this event some of the energy absorbed by the detector will be sent out again in the form X-ray photon. For this reason, it is possible to detect in some X-ray spectra a smaller peak next to big a peak with 1.74 keV less energy, which corresponds to this kind of events.

Moreover, sometimes there is an incomplete charge collection. This can mean that either the photons didn't deposit all of their energy into the detector or that the electronics were not able to collect every single electron generated. The latter leads to low energy tails in the resulting X-ray spectra peaks creating an asymmetry on an otherwise symmetric peak. The former occurs by inelastic scattering, which means that instead of photons being absorbed they only lose energy and escape out of detector. As this is a much more indeterminate effect, due to photons being able to lose any amount of energy due to Compton, it results in a continuum background noise on the final X-ray spectrum.

An example of a triaxial EDXRF spectrum can be found in Figure 1.6 where some of the peaks and artifacts discussed can be found. As it can be observed the spectrum starts with a wide peak due to scattering in the detector for very low energies. It is also possible to observe the characteristic background of this kind of measurement if we abstract from the characteristic lines. Keep in mind that this spectrometer is designed with a triaxial geometry, hence the very low background. From the characteristic lines we can see which elements are present in our sample, and with proper quantification, it is possible to convert these counts into concentrations. Most of the present elements have their K_α and K_β very visible above the background. Also, there is a heavy element present in the sample (Lead) that has its L_α and L_β in this energy range. For higher energies we can see the peaks due to the scatter in the sample. As it is the case for secondary target EDXRF spectrometer, the X-ray beam that excites the sample is quasi-monochromatic. For this reason, Compton and Rayleigh scattering will occur in the sample and will have

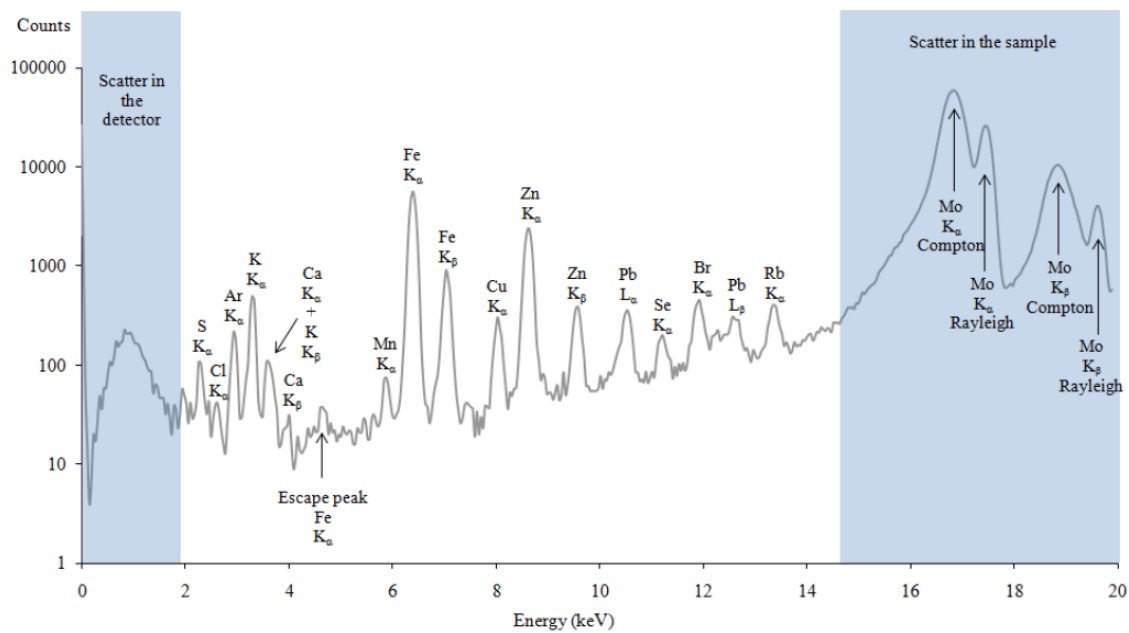


Figure 1.6: Example of X-ray fluorescence spectrum [8].

their peaks on the spectrum dependent on the K_α and K_β of the secondary target, in this case Molybdenum.

1.1.5 Quantification

The next logical step after obtaining the spectral information, in counts per energy channel, is to try to convert these quantities into elemental concentrations on the sample. This elemental concentration information will give us a more in depth physical description of the analyzed samples. However, this is far from a straightforward process where we can easily translate one into the other. As we have explored in the last section a XRF spectrum is a graphical representation of a superposition of many photons originated from very diverse physical phenomena. The amount of variables and processes that determines what we observe in each energy bin is very high, because of all the interactions in the tube, on the sample and inside the detector. Even the electronics have an impact due to their time and energy resolution limitations, signal to noise ratios and so on. All these reasons make it very complex to associate spectral data to an exact composition quantification.

In order to determine what is the concentration of each element on the sample, we need to start by understanding its characteristic peak. On a basic conceptual level, every element i in our samples when excited by the X-ray beam will generate a number of photons distributed along what we call its characteristic peak. However, in reality these characteristic peaks will have their shapes and intensities I_i affected by peaks relative to other elements j . Primary fluorescence photons of a specific element i will also have a probability of exciting other elements j and thus changing what we would expect from both characteristic peaks. Moreover, this process can repeat itself resulting in third-order,

forth-order and so on, fluorescence photons, even though each new fluorescence interaction is increasingly more unlikely. These secondary fluorescence emissions can occur both ways with element i exciting element j and the other way around impacting both I_i and I_j accordingly. However, an element's X-ray emission and absorption properties are also directly proportional with its concentration c_i . What this entails is that the relationship between I_i and c_i is not linear and the so called matrix effects (X-ray photons secondary absorption within the sample) have a big impact on what the observed I_i is. Hence, it is very challenging to model the elemental characteristic peaks of a sample and this has been the focus of many scientific studies [14, 15] from around 1950 onward. It was in 1955 that was first proposed an equation to calculate the characteristic X-ray intensity. It became known as the Sherman equation, in honor of physicist who proposed it, and it allowed for the I_i to be calculated for the characteristic line with an energy E_i of an element i with concentration c_i when excited by polychromatic X-ray beam[16]. The importance of this equation for modern calculations is that was the first to account for all the matrix effects and therefore all the modern calculations of matrix effects are based on it. The original formulation of the Sherman equation was the following:

$$I_i(E_i) = g_i c_i \int_{E_{edge,i}}^{E_0} \frac{I_0(E) \mu_i(E)}{\mu'_s(E) + \mu''_s(E_i)} \left[1 + \sum_j c_j \delta_{ij}(E) \right] dE \quad (1.1)$$

where g_i is an instrumental factor, μ refers to effective mass absorption coefficients and $\delta_{ij}(E_i)$ is an enhancement factor. More specifically, $\mu_i(E)$ refers to a specific element absorption of the beam energy E , while $\mu'_s(E)$ refers to the sample absorption of the beam energy E and $\mu''_s(E_i)$ refers to the sample absorption of characteristic line of energy E_i . The enhancement factor refers to the emission of characteristic X-ray of element i , with energy E_i , due to excitation from the characteristic lines of other elements j . The unknown quantities in this equation need to be calculated based on fundamental parameters, such as sub-shell fluorescence yields or jump-ratios.

The Sherman equation served as starting point for researchers to try to model characteristic lines intensity. Building upon the calculations of Sherman, in the 80s, Rousseau reformulated this equation in terms of concentration c_i with only algebraic manipulation and no approximations[17, 18]. In 1986, with the collaboration of Bouchard, the reformulation was presented as the Fundamental Algorithm[19] with the following expression:

$$c_i = R_i \frac{1 + \sum_j \alpha_{ij} c_j}{1 + \sum_j \epsilon_{ij} c_j}, \quad \text{where} \quad R_i = \frac{I_i(E)}{I_{(i)}(E)}. \quad (1.2)$$

R_i refers to the ratio between the intensity of the characteristic peak of element i in the sample $I_i(E)$ and the intensity of the characteristic peak in standardized sample made only of element i represented as $I_{(i)}(E)$. The coefficients α_{ij} and ϵ_{ij} are correction coefficients for absorption and enhancement effects, respectively. Summarily, what the Fundamental Algorithm shows is that the concentration of an element c_i is proportional to the relative measured intensity R_i and all absorption effects represented by coefficients α_{ij} . On the

other hand, the correction coefficient ϵ_{ij} related to enhancement effects on the sample are inversely proportional to the concentration. Therefore, this represents an arguably clearer formulation to correlate to physical parameters than the original equation presented by Sherman.

The two expressions 1.1 and 1.2 are perhaps the most known formulations of the relationship between the intensity $I(E)$ and the concentration of each element in the sample c_i , but there are other expressions used as functions of different parameters. However, in the end, all these formulations, have several parameters that do not have straightforward calculation. At this point, in order to obtain the elemental concentrations from spectral data, we need to chose whether to do more empirical approach and do a calibration with standards, or use advanced models to try to estimate all the necessary values.

Comparison with standards is a very commonly used solution for the calibration of X-ray fluorescence spectral data. This approach relies on the use of known standardized samples with known elemental concentrations and compare them to the values obtained in the sample with unknown values. The standardized samples must be chosen accordingly, in the sense that, the matrix materials must be as comparable to the measuring sample as possible. Then, using the peak intensities of each element in each of the set of standardized samples I_i , it is possible to obtain linear calibration of such values as function of the concentrations c_i . Using the calibration values obtained it is then possible to do a direct conversion from the measured sample peak intensities into elemental concentrations. The precision of comparison with standards method will be inherently correlated to how well the standard samples replicate the same matrix effects that will occur on the measuring sample. This ends up representing one of the biggest limitations of this approach given that is hard to find standardized samples that fully replicate the matrix effects of our samples. This drawback obviously scales with the complexity of the samples. Also, the accuracy of this method is also limited by the accuracy of the instrument in the sense that both the standards and samples will be analyzed separately both subject to instrumental errors. In the end, this approach is typically an easier quantification solution that can produce good results for common matrices but it is not very versatile.

As it was suggested above, instead of a linear calibration of the spectral data using standards, we can try to employ mathematical models to solve the equations related to peak intensity and elemental concentrations. Perhaps the most popular approaches for these purposes are the Fundamental Parameter method and the Influence Coefficient methods. The starting point for these two methods is identical as they both start by using the mathematical expressions that describe the relationship between peak intensity and elemental concentrations such as equations 1.1 and 1.2. However, when trying to solve these equations we will need to determine various unknown parameters that vary from sample to sample resulting in different systems of equations. The two methods will then differ on the approach to solve these systems of equations.

The first difference to be highlighted between the two methods approaches is related

to how they treat the contributions from all photonic energies of the beam to the elemental characteristic peak intensity. The more accurate way is to do integral calculation for all these energy contributions like the Fundamental Parameter method does. The alternative used in the Influence Coefficient method is to approximate the polychromatic beam with a monochromatic beam with a single wavelength designated as the *effective wavelength*. This simplifies the non-linear equations into linear equations that are easier to solve. The name of this method comes from the influence coefficients that we obtain in these linear equations α_{ij} that translate the effect of the fluorescence of all the elements j in the fluorescence of element i . These coefficients were firstly calculated in the original Sherman work. Nevertheless, the choice between which of these coefficients to use in an experiment and the accurate determination of the effective wavelength is still a modern science research topic. This method represents the first approach to this calculation in a time where computer access and power in science was very limited. One of the major drawbacks is that to do a calibration of the instrument with this method we must know *a priori* what are the elements present in the sample. Also, this method also implies that the calibration is still done with standards in order to obtain the values for the influence coefficients.

The Fundamental Parameters method focus on solving the intensity related equations with no approximations. Instead of using coefficients to estimate the effect of the fluorescence of all the elements in the sample between each other, these inter-element effects are represented in the solved equations in the form of absolute fundamental parameters of the physical interactions involved. For this reason, this method has the potential to be more accurate than the Influence Coefficient, whereas losing in simplicity and computational power requirements. The method itself relies on a iterative approach of comparing theoretical calculated intensities with measured intensities from standard samples. This algorithm has a starting guess of the sample composition and thickness and iterates upon it meanwhile trying to minimizing a χ^2 function dependent on the instrumental standard deviation and measured intensities. An instrument specific calibration, with instrumental calibration factor g , is then reached when the χ^2 function converges into its minimum, with the resulting solved equations being able to calculate the elemental concentrations. This does not happen without uncertainty though, as the so called fundamental parameters used in these equation, such as, absorption coefficients, or emission energies, or fluorescence yields, have yet to be all calculated with a very high accuracy. The uncertainty in each fundamental parameter can be very significative up to and around 10%. Regardless of the impact of these uncertainties, as the method is still calibrated with standard samples, the instrumental calibration factor g will diminish the impact on the final results massively and the uncertainties on the various parameters sometimes end up canceling each other out.

Nowadays, a big portion of the research done in the more conceptual side of the XRF technique is related to improving on the quantification methods. As we have seen above, regardless of the method used we are introducing uncertainties that should be

mitigated in order to make this technique even more prevalent in elemental composition analysis studies. The improvements can come from developing standardless algorithms or improving the uncertainty on the fundamental parameters for example. This coupled with instrumental technological advancements that allow us to dilute the background and enhance the detection limits of our spectrometers will allow this technique to be even more competitive.

1.1.6 Applications

XRF spectrometry is a widely used and versatile technique, and thus it is very much prevalent in many and diverse fields of scientific research. Because of its simplicity to set up, its cost-effective and non-destructive (sample wise) approach, it becomes a very useful tool to quickly access the composition of samples in any state of matter. Perhaps the most interesting applications are the biomedical ones given the worldwide interest of the impacts on human health of our surrounding substances. From food quality and nutrient assessment to global health problems like airborne pollution, many scientific studies make use of XRF spectrometers to measure elemental concentrations and determine trace elements within those kinds of samples.

One of the biggest topics that is transversal to multiple research subjects are cancer related studies. XRF spectroscopy has also provided its contributes to this field. Various works that try to study cancerous tissues chose to analyze them via this technique. For example, in [20] the authors use a micro-XRF spectrometer coupled with a synchrotron to assess the phosphorus quantity in mammary tumorous tissues. As it was expected from other studies [21, 22] all trace elements of these kind of tissues are usually elevated above normal levels regardless if they are benign or malign. Not only that, but they were also able to address the heterogeneous spatial distribution of phosphorus specifically which might provide information on localized tumor cell growth. Another study [23] also using XRF and synchrotron radiation XRF was able to identify elemental concentration deviations in scalp hair between healthy women and women suffering from breast cancer. The results show a decrease in selenium and zinc in cancer patients with a parallel increase in chromium. These findings are corroborated in [24] via XRF and X-ray diffraction techniques where it was identified a significant trace element concentration decrease on scalp hair of women affected by breast cancer. Both studies seem to suggest that analysis of the patient hair could be enough to detect cancer and possibly its stage. Even though, there are many studies focusing specifically on breast cancer there are similarly many other studies regarding different types of cancer using XRF based techniques.

Water control is another essential research topic that sparks a lot of interest across multiple scientific groups due to their importance to our quotidian life. Being this essentially a composition analysis problem, XRF is one of the techniques that provides good results for both solid and liquid state samples of this nature. As an example, in [25], the authors demonstrate the capabilities of a portable XRF spectrometer to measure the salinity of

water and consequently its electrical conductance. In this work, the technique proves itself capable of obtaining similar results to inductively coupled plasma atomic emission spectroscopy (ICP-AES), which is one of the most sensitive and accurate spectroscopic techniques. The ability to detect chloride as well other vestigial elements demonstrates the viability of controlling water samples via XRF for both trace elements and contaminants. Some studies like [26] reiterate this viability of measuring trace elements in drinking water and conclude that the samples analyzed are within normal parameters. Others like [27] however, measure contaminant levels above acceptable levels in samples collected in Taiwan.

Food is also an equally interesting scientific challenge for spectroscopic techniques due to its natural heterogeneous diversity among different samples. In [28], for example, an extensive statistical analysis of XRF measurements is presented, highlighting the trace elements in a multitude of different commercially available food samples: paprika powder, cinnamon, coffee, tea, chocolate, rice, wheat flour, cane sugar, coconut water, honey and bovine milk. This study aims to encourage the construction of a database for elemental concentrations across these diverse types of foods, in order to try and establish a baseline for each of these products and across each origin/source. This would also eventually allow to set standards for products to meet. Another interesting topic regarding food, is nutrient enhancement and biofortification but we will explore this in chapter 3. As we will delve in that chapter, XRF spectrometry allows for great elemental mapping of these kind of samples and thus provide great feedback for agronomy techniques used.

Heavy metals are also one of the focus of many studies using XRF spectroscopy due to their toxicity to the human body. Soil analysis and control are among the most common samples on which to search for heavy metals. The importance of these types of samples is that they provide insight on the pollution in the ecosystem surrounding the sample extraction zone. Also, if this soil is fertilized to be used as source of food, or is home to local bodies of water it is important to control the presence above the recommended values of heavy metals. For example, in [29], the authors provide a XRF analysis of soils from Ghana in terms of both regular metallic elements and heavy metals, specifically: Zn, Pb, Cr, Cu, Co, Ni, Cd, Hg, and As. While there are some of these elements that stay within standardized maximum references, some are detected to be up to 900% of their maximum. Several other studies show the adequacy of XRF techniques for fast quantification of heavy metal samples[30, 31]. Food[32] and water samples[33] are also subject to numerous studies in order to assert that heavy metals are within normal values.

Pharmaceutical application of XRF analysis is also a widely spread solution both in academic and corporate environment. XRF provides a lot of tools to assess and control the quality of drugs, vaccines and all kinds of medic substances. As an example of research in [34], the authors use EDXRF spectrometry for routine screening of oral solid dosage drug products (OSD) and to detect the presence of elemental impurities. One of the objectives of this study is to prove the viability of XRF spectrometry for pharmaceutical control, and the methods used are compliant with the European Pharmacopeia, which is regarded as

the official european standards for drug quality control. Pharmaceutical drug quality is the focus of many XRF based analysis and is further explored in this thesis in chapter 2.

Environmental studies are also a big challenge for XRF spectrometry due to the difficulty of analyzing suspended matter. These kind of research is also of major importance since it gives some insight into pollution whether it is for outdoor spaces or for indoor environments such as workplaces and homes. Some studies like [35] chose to do an indirect analysis to this phenomenon by studying in this case mostly soil samples via XRF spectrometry to address both metal content but also heavy metal contamination. Another example, [36], provides a very large scale spatial and chemical profiles of of a multitude of road dust samples obtained all across the mega-city of Buenos Aires. The analysis in this paper is focused on the antimony contamination of these samples using XRF and ICP-MS, and provides very interesting insight on the correlation of traffic and dust pollution. There are also more direct measurements of suspended matter like in [37], where they also focus automobile related emissions but do an aerosol study of the elemental contents with particle matter partitioning and XRF spectral profiling. In chapter 4 we will discuss further examples of aerosol applications of XRF analysis.

Not all the XRF spectroscopy applications are based on samples with biomedical and health implications though, there are also several other applications that are based on drastically different fields like in art studies, patrimonial restoration, forensic sciences and many more. As an example, in [38] the authors do a multi-analytical spectroscopic analysis using several different techniques (including XRF) to study a colored Dutch map from the eighteenth century. Spectroscopic techniques in these kind of applications provide a very big insight to what type of inks/pigments are used for coloring and thus help reconstruct the history of that specific art piece, providing clues for more exact dating and source location. They can also go further and help restore degraded art by, for example, using elemental mapping to determine where in a painting the author used each color even if it vanished with the years. In [39], for example, a method to restore paintings using spectroscopic techniques is described and tested on Vincent van Gogh painting. XRF can help restore art but on the other end of the spectrum of applications it can also give insight on crime scenes. Forensic sciences provide yet another challenge for the application of this technique. For example, in [40] the authors demonstrate that by doing a large scale mapping of a room they are able to determine the lead trace of a bullet and thus reconstruct the path of a gunshot. The examples provided in this section are just small sample of XRF based studies, but there are plenty more scientific fields that take advantage of the versatility of this technique.

XRF TECHNIQUE APPLIED TO THE PHARMACEUTICAL INDUSTRY

2.1 Scope and objectives

The pharmaceutical industry has a major role in global health via the development of medication, vaccines and treatments to enhance quality of life or prevent and cure diseases and medical conditions. The main contributions from this industry come in the form of research and development of drugs to meet the ever-changing healthcare demand. This is a trillion dollar industry comprised of many subfields from discovery to marketing. With technology and scientific advancements, the goal to produce newer or better medication with reduced side effects results in a very competitive and dynamic industry. As our standards must evolve hand in hand with technological progression there is a need for better testing of developed drugs. Usually every new substance meant to be used on humans as a medical treatment, must undergo a series of pre-clinical tests, clinical trials and safety/compliance assessments to scrupulously meet every standard and regulation norm, before being launched into the market.

It is straightforward that the pharmaceutical industry is a very complex and diverse industry focused on tackling multiple global health problems. In this case study, we will be focusing on a specific global problem, nutrient deficiency, or, more specifically, iron deficiency. Iron is a very important nutrient for humans and animals alike because it is one of the few elements present in every cell on our bodies. Moreover, iron is present in many proteins that regulate most human body functions [41]. Some of the most notorious are: hemoglobin - responsible for transporting oxygen to the tissues, cytochromes - enablers of electron transportation within cells, myoglobin - facilitators of oxygen storage in muscles, enzymes - regulation of internal cell reactions. These are just some examples, and there are several other body functions to which iron is directly connected such as

neuronal and immune systems [42, 43].

Iron deficiency is the most common form of nutritional anemia across the world, affecting more than two billion people according to WHO[44]. Moreover, it is also estimated that about 50% of all anemia is due to iron deficiency. The symptoms of this kind of anemia are usually increased fatigue[45] and hindering of cognitive and motor functions which are even more impactful in development stages of the human body[46]. Therefore, this problem is increasingly problematic for pregnant women and may result in underweight babies or in more extreme cases in perinatal death[47]. The incidence of this problem is more impactful in developing countries due to the lack of means to diagnose and treat iron deficiency anemia. Global perinatal, neonatal and maternal deaths numbers as reported by WHO have been systematically above several millions per year. While it is hard to identify exact numbers of how many of these are related with nutritional anemia, it is known that it represents a big slice of the numbers. This could be completely preventable since the main form of treatment to this disease are iron supplements. WHO estimates that if iron supplements were easily accessible to everyone they would be enough to amend 42% of children's anemia and 50% of women's anemia[44].

In developed countries pharmaceutical iron supplements are a widespread response with multiple companies working on their development and distribution. The most common compounds used in this kind of supplements are based in ferrous salts like iron(II) or (III) sulfates and iron glycinate. Compounds based on iron sulfates are very easily accessible and therefore become very cheap and profitable to mass produce as a pharmaceutical drug. However, the ingestion of these kind of compounds has been connected with increased gastrointestinal tract and liver toxicity[48] as well as some other side effects.

The fact that some of the compounds might have hidden side effects would be enough to warrant further scientific analysis of these kind of samples. However, this research topic is further motivated by the fact that this type of drug is often just regarded as alimentary supplement and thus not as properly regulated or controlled as medical prescription drug. In fact, in many countries its acquisition and distribution is not really supervised whether the commercial transaction occurs on a pharmacy, drug store or even a general store. As a specific example, the supplements analyzed in this study are commercially distributed in Brazil where they are not regulated by their pharmaceutical regulatory body - ANVISA[49].

Furthermore, lower quality control can easily result in more contaminant substances in these supplements, usually of metal elements. These contaminants are unwanted elements that can add unforeseen side effects to these drugs. Moreover, there has been some scientific evidence that in some cases, they might even degrade the active ingredient[50]. Two of the most common metallic contaminants found in these kind of supplements are manganese and nickel.

Manganese is both an essential and a toxic element, meaning that it can have its purpose in the human body nutrition but the body's tolerance to it is not very high

and, thus, can easily become toxic. On the nutrition side, the deficiency of this element can also lead to health problem because it functions as an activator and a constituent of several enzymes[51]. On the toxic side, manganese poisoning significantly impacts the respiratory tract and the brain, and may cause memory loss and nerve damage[52, 53]. The Scientific Committee on Occupational Exposure Limits suggest a limit based on lowest-observed-adverse-effect-level on animal studies for ingested manganese daily intake of 10-40 μg per kg of body weight[54].

Nickel is slightly different from manganese in the sense that it is not documented to have beneficial effects to human health, it is only regarded as a toxic element. Keep in mind, that neither of these elements are as toxic as other substances like arsenic, mercury or lead for example. However, even though our tolerance to these elements is greater their toxicity still warrants caution. Nickel toxicity is correlated with lung cancer incidence, high blood pressure, neurological deficits, slower development in children[55]. Nickel has also been shown to have big correlation with the incidence of breast cancer[56, 57]. Regardless of the known hazards of exceeding the dose of nickel intake there are apparently no set official daily maximum levels in food for consumption. The closest regulation, comes in the form of maximum concentration of nickel in water for human consumption, from the Council Directive 98/83/EC and the commission Directive 2003/40/EC, set to 20 $\mu\text{g}/\text{L}$ [58]. There is however, a relatively recent recommendation from the European Food Safety Authority of a maximum daily-ingested intake of nickel of about 2.8 μg per kg of body weight[58].

Metal impurities are a very prominent problem associated with these kind of supplements that require a closer examination. Regarding pharmaceutical pills, in the USA, which agglomerate the biggest pharmaceutical industries, regulation of metal contaminants has been historically done according the standard USP <231>[59]. This was done via chemical color test with a sulfide ion under a specific protocol and preparation conditions. This norm was substituted with the modern standards USP <232> (elemental impurities limits)[60] and USP <233> (elemental impurities procedures)[61], which are based on modern quantification techniques, which are much more accurate, such as inductively coupled plasma–mass spectrometry (ICP-MS)[62, 63, 64] or inductively coupled plasma–atomic (optical) emission spectroscopy (ICP-AES or ICP-OES)[65, 66]. Although ICP based techniques provide excellent limits of detection in the order of parts per billion, the sample preparation procedures often contains chemical treatment that negates the possibility of further analysis. Another issue with ICP-MS for the specific case of iron (^{54}Fe and ^{57}Fe) is that for this technique there is a spectral interference with $^{14}\text{N}^{40}\text{Ar}^{16}\text{O}^{38}\text{Ar}$ and $^{40}\text{Ar}^{16}\text{O}^1\text{H}$ [62], which often warrants the use of pressured cell collision techniques. Thus, there has been increased research in providing alternatives to these standardized that provide other types of advantages. XRF is one of the most prominent *competing* techniques whether under the form of WDXRF[67], standard EDXRF[68, 69, 70] or even high-energy polarized-beam EDXRF[71]. As we have mentioned in chapter 1 XRF techniques provide a less expensive, portable, easier to use and non-destructive

analysis, alternative do ICP.

In this study, we will be using EDXRF with triaxial geometry for fast and accurate multi-elemental analysis of iron supplements. The objectives are to determine with precision how the measured iron content compares to the labeled one and to identify possible contaminants. In the end, this case study aims to prove adequacy of XRF technique as an alternative method to the standard ICP.

2.2 Methods and materials

2.2.1 Sample description and preparation

In this study, we examined five different popular iron supplements that were acquired in Brazil, namely: Neutrofer Fólico, Anemifer, Noripurum, Sulferbel and Combiron Fólico. Table 2.1 contains a description of these iron supplements with the mass of the active iron compound, the mass of elemental iron and of the pill, and the concentration of elemental iron.

Table 2.1: Information on the iron supplements used in this work.

Iron supplement	Compound	Compound mass (mg)	Elemental iron (mg)	Pill mass ± 10 (mg)	Iron concentration (%)
Neutrofer Fólico	Iron glycinate ($Fe(C_2H_4NO_2)_3$) + folic acid	150	30	540	5.6
Anemifer	Iron(II) sulfate monohydrate ($Fe(SO_4) + H_2O$)	190	60	340	17.6
Noripurum	Iron(III)-hydroxide polymaltose[72]	330	100	720	13.9
Sulferbel	Iron(II) sulfate monohydrate	152	50	310	16.1
Combiron Fólico	Carbonyl iron	126	120	670	17.9

All of the pills tested were crushed, and the protective capsule was removed. The powder was then compressed with 10 tons of pressure into pellets 2.0 cm in diameter and 1 mm in thickness, without any chemical treatment. For each brand of iron supplement, two pellets were produced for further analysis. The pellets were glued to a mylar film on a sample holder and exposed directly to X-rays for elemental determination. Two replicates were made for each sample.

2.2.2 Experimental setup

As it has been stated above in this study we will be using EDXRF spectrometer with triaxial geometry installed at the Laboratório de Física Atômica e Molecular, LIBPhys-UNL, Departamento de Física, FCT-NOVA. This spectrometer was assembled by our research group and consists mainly of an X-ray source, an Ag filter, a secondary target, a sample arrangement and an detector system as it can be seen Figure 2.1.

The excitation source consists of a commercial X-ray tube (Philips, PW 1140; 100 kV, 80 mA) paired with a secondary target made of molybdenum. This EDXRF setup employs a Si(Li) detector with a 30 cm² active area and an 8 μ m beryllium window to

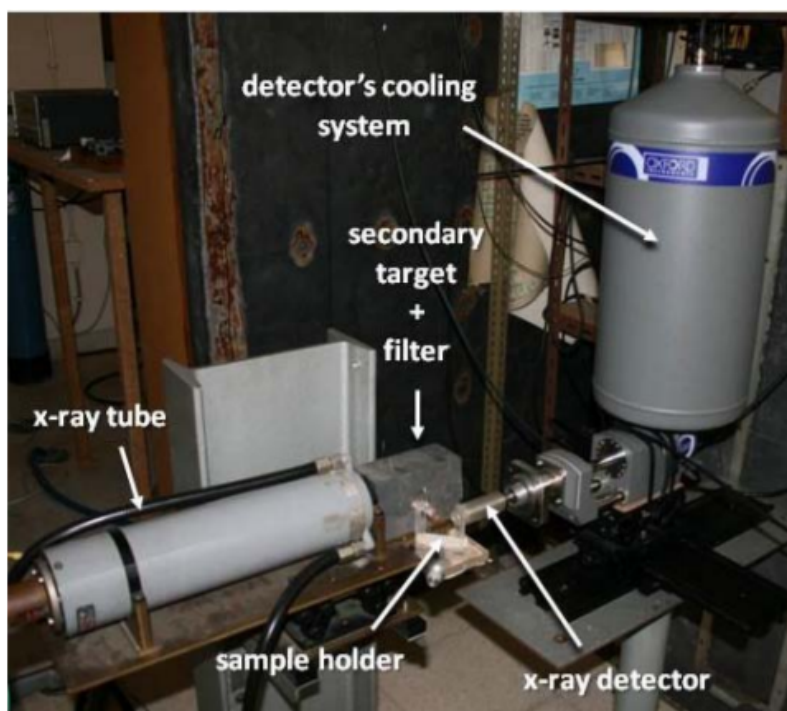


Figure 2.1: Picture of the EDXRF spectrometer with triaxial geometry used in this work, obtained from [8].

measure the characteristic radiation emitted by the elements in the samples. With the acquisition system of a Nucleus PCA card, paired with a commercial pulse processor (Oxford) that automatically adjusted the pulse and applied dead time corrections, we observed an energy resolution of 135 eV at 5.9 keV. The X-ray source was operated at 50 kV and 20 mA. The energy spectrum of each pellet was measured for 15 minutes to acquire the necessary statistics of the concentrations detected.

A triaxial geometry, or indirect excitation, was employed in the experimental apparatus of the X-ray tube, secondary target and the detector[73]. This setup induces a strong suppression of background of the scattered radiation (Rayleigh and Compton radiation) coming from the Bremsstrahlung radiation of the X-ray tube. With this setup, the background consists of a nearly monochromatic source of radiation, addressed to the K_{α} and K_{β} fluorescence lines of molybdenum of 17.4 keV and 19.6 keV energies, respectively. The limits of detection in this geometry are thus much lower compared with common planar geometries, which allow for not only the precise determination of dominant elements but also for the identification of and even quantification of the trace elements present in the material's matrix.

2.2.3 Calibration of the analytical method

Absolute quantification of the various elements was performed with the fundamental parameters method. This method retrieves the relative concentration of each element present in the sample with the help of atomic quantities, e.g., fluorescence yields or

Table 2.2: Elemental concentration ($\mu\text{g/g}$) present in certified standard samples. Values are listed either with one standard deviation (value \pm standard deviation) or with an asterisk (*), meaning that the value was obtained by non-certified methods. *LOD* stands for limit of detection. Three standard reference materials with light organic matrices and several concentration levels were considered, namely, dogfish muscle (NRRC-DORM-2), lobster hepatopancreas (NRCC-TORT-2) and orchard leaves (NIST-SRM1571).

Element	LOD	Certified biological material					
		Dogfish muscle NRRC-DORM-2		Lobster hepatopancreas NRCC-TORT-2		Orchard leaves NIST-SRM1571	
		Certified value	Present work	Certified value	Present work	Certified value	Present work
S	100					2300*	
K	10					14700 \pm 300	15300 \pm 900
Ca	20					20900 \pm 300	21000 \pm 900
Mn	3	3.66 \pm 0.34	4 \pm 1	13.6 \pm 1.2	13 \pm 1	91 \pm 4	95 \pm 5
Fe	3	142 \pm 10	143 \pm 10	105 \pm 13	102 \pm 13	300 \pm 20	308 \pm 20
Ni	1	19.4 \pm 3.1	17 \pm 2	2.50 \pm 0.19	2.9 \pm 1.2	1.1 \pm 0.6	2 \pm 1
Cu	1	2.34 \pm 0.16	3 \pm 1	106 \pm 10	101 \pm 10	12 \pm 1	13 \pm 2
Zn	1	25.6 \pm 2.3	24 \pm 3	180 \pm 6	180 \pm 10	25 \pm 3	26 \pm 3
As	1	18.0 \pm 1.1	19 \pm 1	21.6 \pm 1.8	22 \pm 2	14 \pm 2	14 \pm 2
Se	0.8	1.40 \pm 0.09	1.0 \pm 0.7	5.63 \pm 0.67	5 \pm 1		
Br	0.8					10*	10*
Rb	0.8						
Sr	0.8			45.2 \pm 1.9		37*	36*
Pb	0.8	0.1	<LOD			45 \pm 3	44 \pm 4

absorption cross-sections[74, 75]. We validate the present method via two procedures; in the first, we compare the obtained concentrations with known concentrations present in standard reference materials of organic-type matrixes (as in the pill excipients). Three reference materials, namely, dogfish muscle (NRRC-DORM-2), lobster hepatopancreas (NRCC-TORT-2) and orchard leaves (NIST-SRM1571), were considered in the present study. These materials contain various light organic matrices with several concentrations of the elements of interest, ranging from K to Pb, which allows for the assessment of the present method for different concentration regimes. Pellet preparation of the standard reference materials followed the same procedure as the other samples tested. Table 2.2 lists the values obtained with the fundamental parameters method as well as the certified values. Overall, the fundamental parameters method is able to retrieve the same concentrations of elements as the certified values, within the uncertainty level. In both cases, the uncertainty corresponds to 95% confidence limits (i.e., to three standard deviations) of the fitting procedure. The limits of detection (*LOD*) presented in Table 2.2 were evaluated according to:

$$LOD = 3\sqrt{N_b} \frac{C_i}{N_p} \quad (2.1)$$

where C_i is the concentration of the element i , N_p represents the total counts for the corresponding peak and N_b represents the counts of the background under the peak.

For the second procedure, we employed the ICP-AES technique for measuring the elemental content in one sample of Anemifer. The sample preparation followed a standard chemical digestion procedure with 2.5 ml of hydrochloric acid (HCl 35%) and 2.5 ml of nitric acid (HNO₃ 69%) for 100 mg of sample. As described in the next section,

Table 2.3: Elemental concentrations of manganese, iron and nickel in Anemifer measured by ICP-AES and those obtained with our analytical method.

Element	ICP-AES	Present method
Mn	537 ± 2	530 ± 5
Fe	$18.4 \pm 0.1\%$	$18.3 \pm 0.8\%$
Ni	43.8 ± 0.2	45 ± 5

Values for iron are given as percentages and for the other elements in $\mu\text{g/g}$.

the samples only contained contaminants of nickel and manganese within the *LOD*, so we restricted our measurement to those elements. Table 2.3 shows the concentrations obtained by ICP-AES and by our method.

2.3 Results and Discussion

The elemental concentration was analyzed for each of the ten individual pellets. Two of the x-ray spectra obtained (Anemifer and Neutrofer Fólico) are shown in Figure 2.2. An important characteristic of these spectra is that, due to the triaxial geometry, they manifest a very low background from the scattered radiation. This setup allows for a clearer interpretation of the fluorescent lines as it lowers the detection limit.

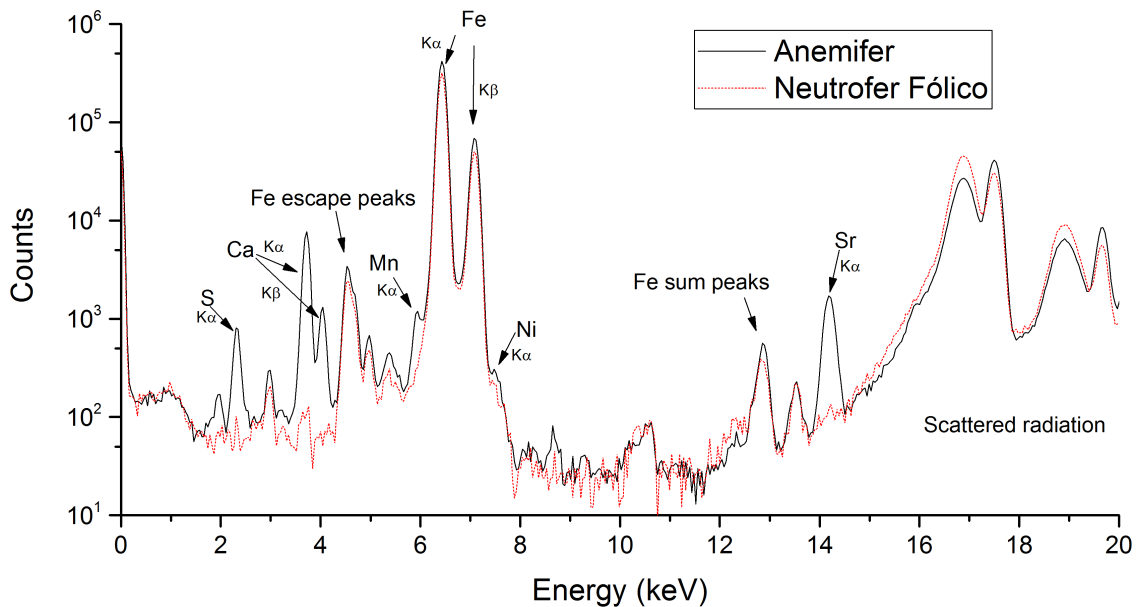


Figure 2.2: Two measured EDXRF spectra corresponding to an Anemifer sample (black solid line) and a Neutrofer Fólico sample (red dotted line). The counts are plotted versus the detector energy in keV.

As expected, both spectra reveal high peaks for the K_{α} and K_{β} fluorescent lines of iron and the corresponding escape peaks and sum peaks. Few elements, such as calcium

CHAPTER 2. XRF TECHNIQUE APPLIED TO THE PHARMACEUTICAL INDUSTRY

Table 2.4: Reference and measured concentrations of the iron supplements analyzed.

Element	Sulferbel		Noripurum		Combiron Fólico		Anemifer		Neutrofer Fólico	
	Reference	Measured	Reference	Measured	Reference	Measured	Reference	Measured	Reference	Measured
S	-	80000±3000	-	BDL	-	12000±5000	-	73000±8000	-	<LOD
Ca	-	120±20	-	110±8	-	400±50	-	30000±2500	-	<LOD
Mn	-	352±30	-	240±20	-	50±5	-	530±5	-	<LOD
Fe	16.1%	15.4±0.6%	13.9%	14.9±0.7%	18.3%	17.9±0.8%	17.9%	18.3±0.8%	5.6%	6.0±0.6%
Ni	-	41±4	-	50±5	-	51±20	-	45±5	-	45±6
Sr	-	<LOD	-	<LOD	-	<LOD	-	65±3	-	<LOD

Values for iron are given as percentages and for the other elements in $\mu\text{g/g}$.

Table 2.5: Comparison between measured amounts of nickel and manganese and PDE(permitted daily exposure).

Iron supplement	Ni measured (μg)	Ni ratio from PDE (%)	Mn measured (μg)	Mn ratio from PDE (%)
Sulferbel	12±4	5	109±11	4.3
Noripurum	36±5	14.4	172±14	6.9
Combiron Fólico	34±2	13.7	33±3	1.3
Anemifer	15±2	6.1	180±20	7.2
Neutrofer Fólico	24±1	9.7	<LOD	-

and sulfur, have noticeable differences in the respective fluorescent lines between Anemifer and Neutrofer Fólico, which can be attributed to the lack of these elements in the excipients of the latter iron supplement. Both calcium and strontium are alkaline earth metal elements that justify the contamination of strontium in samples containing calcium. Furthermore, there is a lack of manganese in Neutrofer Fólico. Manganese can be considered an important contaminant for Anemifer but not for Neutrofer Fólico (below the detection limit), and nickel is present in both. It is apparent that the corresponding peaks of nickel and manganese fluorescent lines overlap the iron peaks. This will not result in any discrepancy because the software discriminates each contribution in the fitting process.

In Table 2.4, the reference and measured iron concentrations for all of the pills are shown. In addition, we added the measured concentrations of other elements to this discussion: calcium, sulfur, nickel, strontium and manganese. Overall, we note the agreement for the iron content between the values obtained and those indicated in the pill prescription information. While calcium, sulfur and strontium are expected in the excipients of some pills (exact quantities not mentioned), no pharmaceutical prescription mentions levels of nickel and manganese, yet our measurements reveal them to be within the detection range. The question arises if pharmacies and doctors are aware of these contaminants.

Using data on the acceptable concentrations of metal contamination in medicinal products for human consumption from the EMEA (European Medicines Agency)[76], we have established that the PDE (permitted daily exposure) for manganese and nickel is 2.5 mg/day and 0.25 mg/day, respectively. This information is compiled in Table 2.5. For nickel, we measured values as high as 14.4% of the PDE in Noripurum. This value might

be especially concerning for patients, who depend on multiple daily iron supplement pills, as it is possible to reach toxic levels if we add to the daily average dietary intakes. Sulferbel shows the lowest percentage of nickel, which was 5% of the PDE.

Even though manganese is also a contaminant in these pills, its ratio of the PDE is considerably lower in comparison with nickel. Moreover, manganese is an important nutrient for humans and, for that reason, its role as a contaminant is not as impactful. The highest ratio of the PDE was observed for Anemifer at 7.2%. Neutrofer Fólico shows the best results, with a level of manganese below the detection limit.

As a takeaway from this case study, we can state that manganese and nickel were identified as important contaminants of the tested iron supplements, even though the prescriptions do not warn of their presence. Neutrofer Fólico is the only supplement with no detectable amount of manganese and the lowest amount of nickel. The presented results highlight the need for better control of metal impurities in iron supplements.

This work bases its approach on a multi-element analysis of the samples. Although we are able to measure the concentrations of iron and other contaminants in these supplements with good precision, further studies on these compounds using other techniques might reveal additional interesting findings. For example, using Raman spectroscopy, we would be able to analyze the molecular forms of the inorganic compounds with nickel and manganese and further assess its potential toxicities to humans.

We conclude that the method is appropriate for pharmaceutical purposes as it circumvents the destruction of the sample associated with traditional methods and has *LODs* for contaminant metals. This technique allows a rapid *in-loco* analysis of a wide range of elements simultaneously and thus can be an alternative analytical technique to plasma-induced coupling-based techniques.

This method would give pharmaceutical control institutes the opportunity to improve their own quality control and thus provide another tool to the industry to assure that the advertised elemental concentrations in prescribed medication are scrupulously met.

XRF TECHNIQUE APPLIED TO THE AGRONOMY/FOOD INDUSTRY

3.1 Scope and objectives

The safety and quality control of food products are of the utmost importance to insure global well-being of the population. Therefore, it is mandatory that the chain of events from field to table is certified to provide safe and nutritious food. Given its historical and socioeconomical framework, this industry is less regulated than the pharmaceutical industry. Hence, there is usually something to optimize or improve upon the methods used on the diverse stages of the process of supplying food to the consumer. The rise of contaminants and fraudulent food is one of the concerns that worry specialists and governing bodies alike. These concerns urge for better science based food quality control processes that are simple, sensitive and transparent to all the concerning parts.

Atomic and molecular spectroscopy provide some useful analytical tools to study this kind of samples. Scientifically, biological systems provide a big challenge, due to their complex and heterogeneous nature. Therefore, there is a symbiosis relationship between techniques and biological samples. XRF spectroscopy is one of the analytical tools that is among this set of techniques. As we have mentioned in this text, XRF is a very widespread academic and commercial solution for fast and cheap elemental analysis[77, 78]. Even though competing techniques such as Synchrotron Radiation micro-XRF (SR-XRF)[79], Inductive Coupled Plasma Mass Spectrometry (ICP-MS)[80], nano Secondary Ion Mass Spectrometry (nanoSIMS)[81] and Scanning Electron Microscope coupled to Energy Dispersive Spectrometry (SEM-EDS)[82], tend to have lower limits of detection and better lateral resolution, they are not as fast and require more layers of sample preparation and operational costs.

The scientific interest of biological tissue samples extends specifically to the ones

meant to be consumed as food[83, 84, 85, 86]. As the dietary impact of certain nutrients becomes clearer, via the progresses of health focused research, the need for a better understanding of the presence and localization of such elements in food products is warranted. Using some of the analytical tools described, it is then possible to pursue such endeavors.

More specifically, in this case study we will be directing our attention to cereal based products. Cereal based tissues are a very interesting research topic to the spectrometry scientific community due to their heterogeneous nature. These types of samples are very suited to being mapped and imaged with techniques such as μ -XRF due to their interesting elemental localization[87]. Moreover, they tend to be at the base of the food pyramid of most countries, and thus, make up a big portion of global population's diet. Perhaps the most researched cereals are rice grains due to their prevalence in most Asian countries' diet.

The research on this topic is itself very heterogeneous combining different analytical techniques and diverse science subjects. For example, in [80], an *in vivo* mineral distribution analysis of rice grains was performed in order to determine mineral distribution patterns that correlate with the progressive stages of germination via SR-XRF. This paper also features ICP-MS measurements of mineral concentrations (i.e., Ca, Mn, Fe, Zn, and K) in whole rice grains, hulls, brown rice, bran and polished rice. On another paper [88], they use both inductively coupled plasma optical emission spectrometry (ICP-OES) and μ -XRF mapping to evaluate the dynamic changes in some nutritionally important nutrient like P, Ca, K, Fe, Zn, Cu, due to accumulation of phytic acid during the rice seed development stage. Elemental analysis of this kind of samples can sometimes also be focused in detecting and measuring toxic elements. Some examples of this kind of research can be seen in [89, 90], where the authors provide an ICP-MS with laser ablation analysis of brown rice collected in Korea to detect the presence of both arsenic and mercury.

In this case study we will focus on wheat grains samples. Wheat is a monocot plant species, which is traditionally referred in academic context as *triticum aestivum*. The cereal grains of this specie are comprised of a number of highly specialized structures, as it is schematically represented in Figure 3.1. Like other cereal species, wheat possess *caryopses* (cereal grains) as propagation units, which are single-seeded fruits where the *testa* (seed coat) is fused with the thin *pericarp* (fruit coat). Wheat grains possess a *triploid endosperm* (meaning three chromosome sets per nucleus) which is subdivided into *aleurone layer* (living cells) and the *starchy endosperm* (dead storage tissue). They also possess highly developed *embryos* which involve the following organs: *coleoptile* (shoot sheath), the *scutellum*, the *radicula* and the *coleorrhiza* (root sheath). All these organs will be involved in germination of new grains by using the nutrients stored in *endosperm* the wheat ear will continuously grow.

When wheat grains go through a traditional milling process the *bran* is removed in order to expose to *endosperm* which is very rich in proteins and the major ingredient in traditional flour. This will result of the test, *pericarp* and *aleurone layer*. Even tough

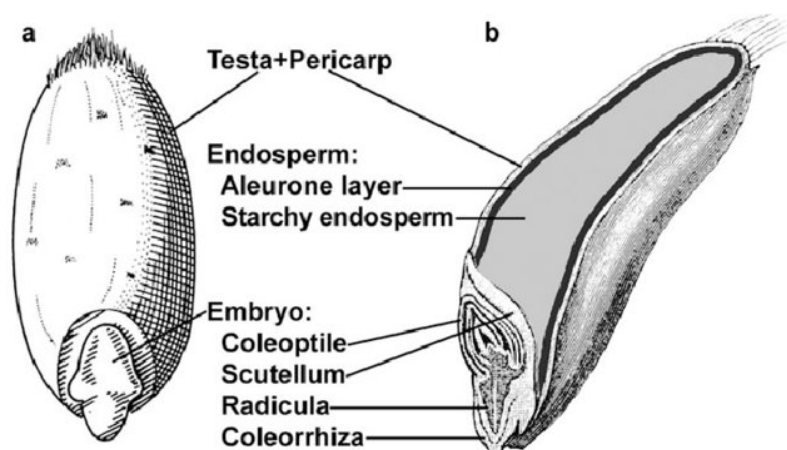


Figure 3.1: Structure of a wheat grain as reproduced in [91]. **a** is a representation of the whole grain and **b** is a cross section view of the grain.

aleurone layer botanically is not part of the capsule of the seed, in reality it is strongly attached to it and the removal of the *bran* will usually imply the removal of this layer. Nowadays, and due to this kind of research, we know that the *bran* is actually composed of a lot of beneficial nutrients, with the majority being stored the *aleurone layer*. The awareness of this fact has pushed the food industry to start producing whole-wheat flour which is made using the complete wheat seed.

The two most notable micronutrients that whole-wheat flour is enriched with in comparison to white flour are iron and zinc[91]. Since nutrient dietary deficiency is nowadays considered as a worldwide epidemic that affects more than two billion people according to the World Health Organization (WHO)[92] it is important to understand how important these two micronutrients are for the world's dietary needs. In chapter 2, we have already provided an overview of how iron deficiency affects global population. Zinc deficiency is also a worldwide nutritional problem which is particularly impactful in infants, children, adolescents, pregnant and lactating women, for whom the requirements of this substance is higher. Zinc is intrinsically connected to the development and growth stages of the human body, and thus, its importance to these segments of the population. Moreover, zinc deficiency during these stages has been connected with problems affecting the following human body systems: epidermal, central nervous, immune, skeletal, gastrointestinal and reproductive system[93]. These physiological stages increase the normal need for zinc, but there are other segments of the population which do not meet the daily dietary recommended intakes. For example, rural diets in developing countries which consist mostly of plant-based food, or, diseases that induce excessive losses or impair utilization of zinc, also lead to zinc deficiency[94]. Furthermore, clinical diagnosis of zinc deficiency is not trivial specially in developing countries. The best known indicators are blood plasma/serum zinc concentration, dietary intake, and stunting prevalence [93].

If it is hard for developing countries to diagnosis zinc deficiency due to the lack overwhelming symptoms and the low assess to clinical staff and equipment, it is possibly

harder to administer a proper medical response. The reason being that the main treatment for zinc deficiency are nutrient supplements and, as it might be straightforward, their availability and assess in developing countries is scarce at best. Moreover, similarly to what we have seen in the last chapter with the iron supplements they might introduce unwanted elements into the consumer's diet, specially if the quality control on pharmaceutical doesn't enforce high standards.

An alternative natural solution to zinc deficiency is to take the already nutritious cereal based food and apply a series of techniques in order to biofortify the plants. This is specifically impactful due to the fact that multiple forms of cereals are considered staple food and already constitute the largest part of the diet in some of these countries[84]. Biofortification is the agronomic practice of manipulating plant species in order to enhance their nutritional value. This technique comes in different forms and through diverse methods like selective breeding, nutrient rich fertilizers or genetic manipulation. Studies find that through these kind of manipulations there is a big increase in selected micronutrients concentrations on the crop samples[95, 96, 97, 98]. Furthermore, there are also studies that suggest that zinc biofortified wheat based food has a direct connection to serum zinc[99]. However, in this same study the authors claim to not have observed any increase in the population's serum zinc when the wheat was simultaneously biofortified with other micronutrients other than zinc.

It seems clear from scientific research that biofortification can combat to a degree the zinc deficiency global nutritional problem. However, there are some issues and challenges when crops are treated with different techniques and try to enhance multiple nutrients of the crops. For example, it is important when biofortifying cereal grains or fruits that we not surpass certain elements thresholds (for elements like Zn or Fe) in order to not disturb ionic balance of the plants and producing lower crop yields. There is a fine balance between biofortifying these plant species and not reach a level of toxicity detrimental to the whole crop. Another challenge is for example the widely used phosphorus fertilization methods that have been proven to decrease zinc concentrations in wheat grains[100]. Phosphorus is stored in the plants in a compound that known as phytic acid that strongly binds with metallic anions. This means that not only it replaces the zinc content on the grain it actually decreases its bioavailability. Bioavailability refers to the ability of absorption of the human body of a compound in a specific form. This means phytic acid is known strongly bind with micronutrients which prevents them from being absorbed by intestinal mucosa.

As it has been stated before, plant based samples provide a very interesting challenge for spectroscopy and imaging techniques. Specifically, biofortified wheat grains seem to be part of a research topic of major importance to the global population's diet. Therefore, the application of micro-XRF and triaxial EDXRF analysis to this kind of samples can provide very important insight into element localization and element biofortification efficiency. For this purpose, in this case study, we will provide a thorough analysis of

eleven different genotypes of biofortified wheat grains and their comparison with non-biofortified control wheat species. It will then be possible to rank genotypes based on zinc content rating. As our spectroscopy techniques are also sensible to most other nutrients we will also be able to assess how the element balance is shifted or if any unwanted impurities arise. Another important focus will be iron concentrations because of its relevance to human well being, which was highlighted in the last chapter. Iron/zinc association will also be assessed and genotype ranking for this will be provided.

3.2 Materials and methods

3.2.1 Plants

A set of eleven biofortified and non-biofortified wheat varieties developed at the International Maize and Wheat Improvement Center (CIMMYT), Mexico were used for this study. Wheat varieties included in the study are: first semi-dwarf green revolution varieties (Sonalika and Siete Cerros T66), a synthetic-hexaploid derived drought-tolerant soft wheat variety 'Vorobey', and Baj, a early-maturing variety which in this work will be used as control as it is a non-biofortified but high-yielding genotype. As another control sample, we will also use the 'Borlaug 100' which is a recently released high-yielding wheat variety with no previous fortification. In this work, 5 biofortified high Zn wheat lines from the biofortification breeding program will be studied as well, namely Zinc Shakti (Sample #1 and #8) which is a high Zn and Fe density genotype with +14 ppm Zn over local varieties and is being grown by more than 250,000 farmers in India, and Zincol2016 (sample #7) is a recently released high Zn wheat variety in Pakistan that is being adopted in more than 25,000 ha in Pakistan.

3.2.2 Field trials

Field trials were conducted at the Norman E. Borlaug Experimental Station in Ciudad Obregon, Mexico during 2013-14 crop seasons. The experimental materials (samples 7-11) were produced from the Zn-enriched area where basal application of $25 \text{ kg ha}^{-1} \text{ ZnSO}_4 \cdot 7\text{H}_2\text{O}$ was applied to minimize soil Zn heterogeneity in the experimental fields. The rest of the samples (1-6) was produced under optimum growing conditions with recommended rates of NPK fertilizers which were applied as basal and top-dressings during the crop growing season. Optimal water was supplied through five irrigation systems during the crop period to favor good plant stand. The trial was laid out in alpha-lattice design with two checks with two replicates. Each entry, with approximately 60–70 seeds, was grown in 1 m long paired rows, spaced 20 cm apart on top of 80 cm wide raised beds, with a 0.5 m pathway. Pesticides were applied as needed to keep experimental plots free from diseases and aphids.

3.2.3 Analytical methods

3.2.3.1 EDXRF with triaxial geometry

The triaxial EDXRF setup used in this case study is the same as the one described in the last chapter (chapter 2). The operating conditions of this system for all analyzed spectra were 50 kV and 20 mA. Quantification of the spectra was performed with an in-house developed code based on the fundamental parameters method and checked against several standard reference materials, such as orchard leaves (NBS-1571), Poplar Leaves (GBW 07604) and Bush Branches (GBW 07603) which share a biological matrix with the wheat grains composed essentially of hydrocarbons. The wheat samples were prepared by grinding 6 grains in a mortar and the resulting powder was pressed under 10 tons force for two minutes. The obtained pellet was then glued with a hydrocarbon glue onto a mylar sheet and placed on an acrylic frame which was then positioned at a 90° angle between the incoming X-ray beam and the detector. Three measurements were performed for each sample in order to minimize statistical errors.

3.2.3.2 μ -EDXRF

All elemental maps of the wheat grains were obtained using the micro-Energy Dispersive X-Ray Fluorescence (μ -EDXRF) system (M4 TornadoTM, Bruker, Germany). This commercial spectrometer consists of an air-cooled micro-focus side window a Rh-anode X-ray tube, powered by a low-power HV generator. The system features poly-capillary X-ray optics, which allow a beam spot size of 25 μm . In all of the measurements, the X-ray generator was operated at 50 kV and 100 μA without the use of filters, in order to enhance the ionization of low-Z elements without compromising the peak-to-background ratio for medium-Z elements such as Zn.

Detection of the fluorescence radiation is performed by an energy-dispersive silicon drift detector, XFlashTM, with a 30 mm² sensitive area and an energy resolution of 142 eV for Mn K α . As in previous studies, the wheat grains were cut in half longitudinally, along the crease tissue, with a stainless steel razor blade. The two halves of the longitudinally cut grains were then glued onto a mylar foil with the inner sides upward, and placed on the M4 Tornado x, y, z translation stage for analysis.

Measurements were taken under 20 mbar vacuum conditions and performed directly on the two sides of the grains. The maps were performed with a pixel spacing of 15 μm , in order to completely cover the grain, with a measuring time of 6 ms per pixel, and the final images were created with the built-in software from the M4 TornadoTM, ESPRIT. The obtained mass fractions were not corrected to the total grain's biomass, and hence the values for the individual structures within the grain naturally present much higher concentration than values for the whole grain. This is due to the fact that the endosperm, which accounts for more than 80% of the grain biomass, is mainly composed by low atomic weight elements that cannot be measured by this technique.

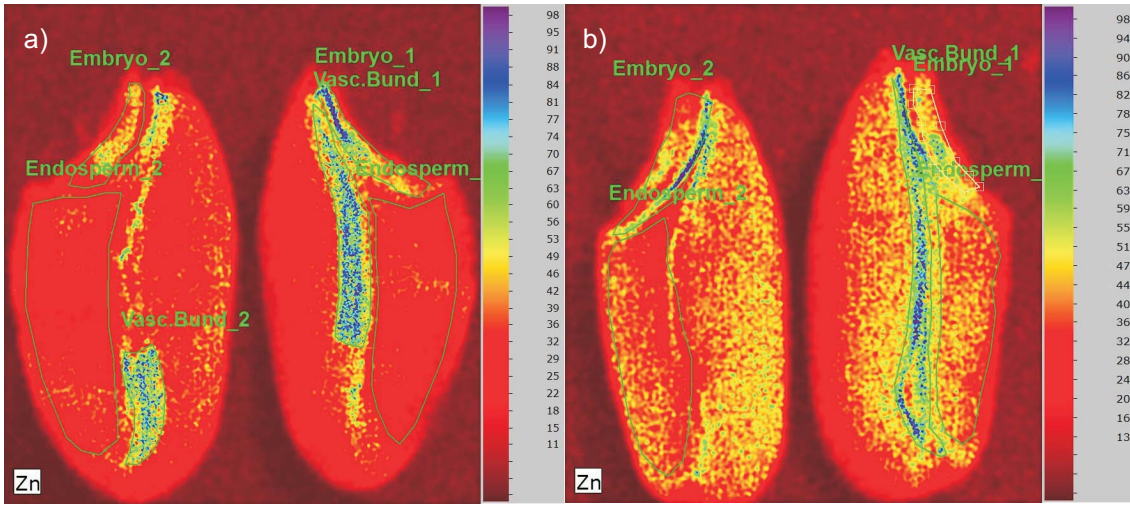


Figure 3.2: Elemental map of two grains corresponding to different samples, highlighting the anatomical structure selection procedure. In a) it can be seen that the vascular bundle was severed upon sample preparation, while in b) one can see that the vascular bundle has remained solely on one side of the cut grain.

The geometrical constraints of the spectrometer do not allow the X-ray beam to hit the sample perpendicularly, instead the sample is irradiated from the side at a 50° angle, making a 100° angle with the detector. Most of the times, this results in shadows in the elemental maps, which have to be analyzed bearing this in mind. With the object area selection tool of the software we were able to select subsets of the whole elemental map, corresponding to different structures within the grain, namely the embryo, endosperm, vascular bundle as well as the whole grain as can be seen in Figure 3.2. In the cases where either the vascular bundle or the embryo was severed upon slicing of the grain, the structures, easily identified in the elemental maps, were properly delimited within the maps in order to obtain a more reliable quantification. In Figure 3.2 a) it is easily seen that the vascular bundle was sliced during sample preparation, and the chosen areas for quantification, on both halves of the grain, were chosen so that only the signal from that structure was processed. Quantification of the pixel sum spectra of these selected regions was performed with the fundamental parameters method of the ESPRIT software.

3.3 Results and discussion

3.3.1 Whole grain

For the whole grain quantification, we employed both the μ -EDXRF method and the high-sensitivity analytical method EDXRF with a triaxial geometry as described in section 3.2.3. Both methods will be labeled M1 and M2, respectively, from now on for simplicity. The final mass fractions for the whole grain were then obtained through an weighted average of the M1 and M2 results to take into account the sample size for each technique.

The results produced by method M1 show, in general, slightly higher readings of both

Zn and Fe concentrations than the ones obtained via method M2 (Table 3.1; Figure 3.3). This disparity may be related, not only to the grain to grain variation within a spike [101] for Zn and Fe, but also to the fact that the sample preparation for the elemental mapping in M1 exposes the vascular part and embryo of the grain to the excitation beam, effectively increasing the Zn, and especially Fe concentration readings. Poor calibration within the quantification procedures has been ruled out by comparing quantification results of the 3 standard reference materials referred in Section "EDXRF with triaxial geometry" with the two methods. The discrepancy between both readings is bigger in the quantification of Fe concentrations where there is no overlap (Figure 3.3 left). Here, the greatest differences are observed in the cases of genotypes G6-G10, which are the ones coming from the zinc enriched soil. In addition, measurements obtained from M1 show more variability (Table 3.1; Method - standard errors).

Table 3.1: Concentration group means and standard errors of Zn and Fe for genotypes, methods and soils in the case of the whole grain data.

Genotype	Zn ($\mu\text{g/g}$)	Fe ($\mu\text{g/g}$)		
G1	81.9 \pm 16.7	92.7 \pm 29.6		
G2	73.3 \pm 7.6	60.8 \pm 23.9		
G3	76.9 \pm 0.2	47.7 \pm 12.0		
G4	65.4 \pm 9.8	53.6 \pm 9.4		
G5	63.0 \pm 2.6	45.5 \pm 11.2		
G6	57.4 \pm 8.7	42.7 \pm 13.7		
G7	40.3 \pm 7.9	68.3 \pm 30.1		
G8	80.0 \pm 14.1	80.3 \pm 36.7		
G9	69.6 \pm 9.9	65.3 \pm 33.3		
G10	68.4 \pm 22.3	64.0 \pm 29.8		
$n_G = 2$ concentrations per genotype (G2,...,G10); $n_{G1} = 4$ concentrations for genotype G1.				
Method	Zn ($\mu\text{g/g}$)	Fe ($\mu\text{g/g}$)		
M1	80.5 \pm 22.3	74.3 \pm 16.7		
M2	49.3 \pm 19.7	63.6 \pm 12.7		
$n_M = 11$ concentrations per method.				
Soil	Zn ($\mu\text{g/g}$)	Fe ($\mu\text{g/g}$)		
Normal	62.7 \pm 13.3	60.1 \pm 24.7		
Enriched	76.4 \pm 15.1	70.6 \pm 27.7		
$n_N = 6 * 2$ & $n_E = 5 * 2$ concentrations per field.				
			Genotype coding	
			G1	Zinc-shakti
			G2	Sonalika
			G3	Siete Cerros
			G4	Vorobey
			G5	Baj
			G6	Borlaug 100
			G7	Zincol 2016
			G8	Danphe
			G9	Mayil
			G10	Hgo
			Method coding	
			M1	μ -EDXRF
			M2	triaxial-EDXRF

The presented error bars in Figures 3.4 and 3.5 represent the quadrature sum of the instrumental uncertainty and the standard deviation of all measurements. From Figure 3.4 it is clear that both in the non-biofortified plants as well as in the Zn-rich soil grown plants, the majority of Zn is deposited within the vascular bundle and embryo (see also Figure 3.6). Comparison of overall Zn concentration in the whole grains (Figure 3.5a) showed 10-35% higher values over historical varieties of Siete Cerros T66, Vorobey and Sonalika over the early maturing control Baj, whereas 55 to 90% higher Zn when

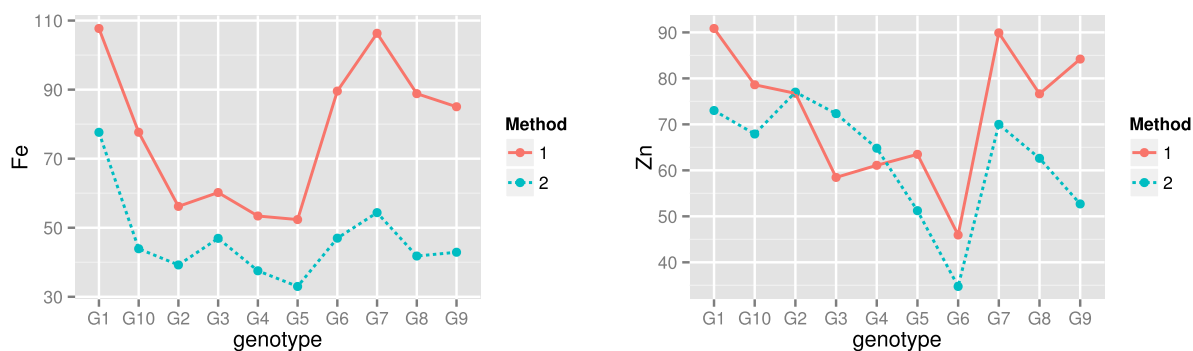


Figure 3.3: Concentrations of iron (Fe) and zinc (Zn) as measured by methods M1 and M2.

compared to recently released high yielding variety Borlaug 100.

About 28% higher Zn in the biofortified Zinc-shakti grown under normal soil Zn levels (sample 1) – the first high Zn variety released in India over the check variety Baj while for Zinc-shakti grown under Zn-enriched soil (sample 8) there was an approximately 60% increase in Zn, followed by 40% higher Zn in Zincol 2016 a high Zn wheat variety released in Pakistan. Similarly, a 81%, 98% and 125% higher Zn of samples 1, 7 and 8, respectively, over the control Borlaug100 was observed. The other 3 biofortified lines (Danphe, Mayil and Hgo) showed 70-82% higher Zn over Borlaug100 and 19-27% increase over the Baj genotype.

The synthetic-hexploid derived drought-tolerant soft wheat variety Vorobey, showed 10 and 56% higher Zn over Baj and Borlaug100, respectively.

The first semi-dwarf green revolution wheat variety Sonalika showed 34% and 90% higher Zn over Baj and Borlaug100, respectively even when grown in a non-Zn-rich environment, outperforming the results of the Zinc-shakti which featured a 27% and 81% increase in Zn, respectively. The biofortification of the Zinc-shakti genotype showed a 25% increase in Zn concentration, within the whole grain, when compared to the same genotype grown in normal conditions without significant loss of crop yield. Unlike other genotypes such as the *Triticum aestivum cv. Roxo* where a 10-fold increase in grain Zn content, from the zeroth non biofortified generation to the second generation (under growth chamber conditions) was achieved [97], the increase in the Zinc-shakti genotype due to biofortification is modest. This can be explained by the fact that for Zn, the bioaccumulation in the grain is limited by transport barriers from the rachis to the vascular bundle, such as the xylem discontinuity in the maternal tissue [102, 103], which reduces the efficiency of soil-applied Zn biofortification, as well as the fact that this genotype is already a result of several biofortified generations, and its metabolic elasticity might be reaching a saturation point. This effect was also seen for *Triticum aestivum cv. Roxo* in reference [97] for higher generations of grains undergoing consecutive Zn biofortification.

The high Zn biofortified wheat lines present significantly higher Zn concentrations

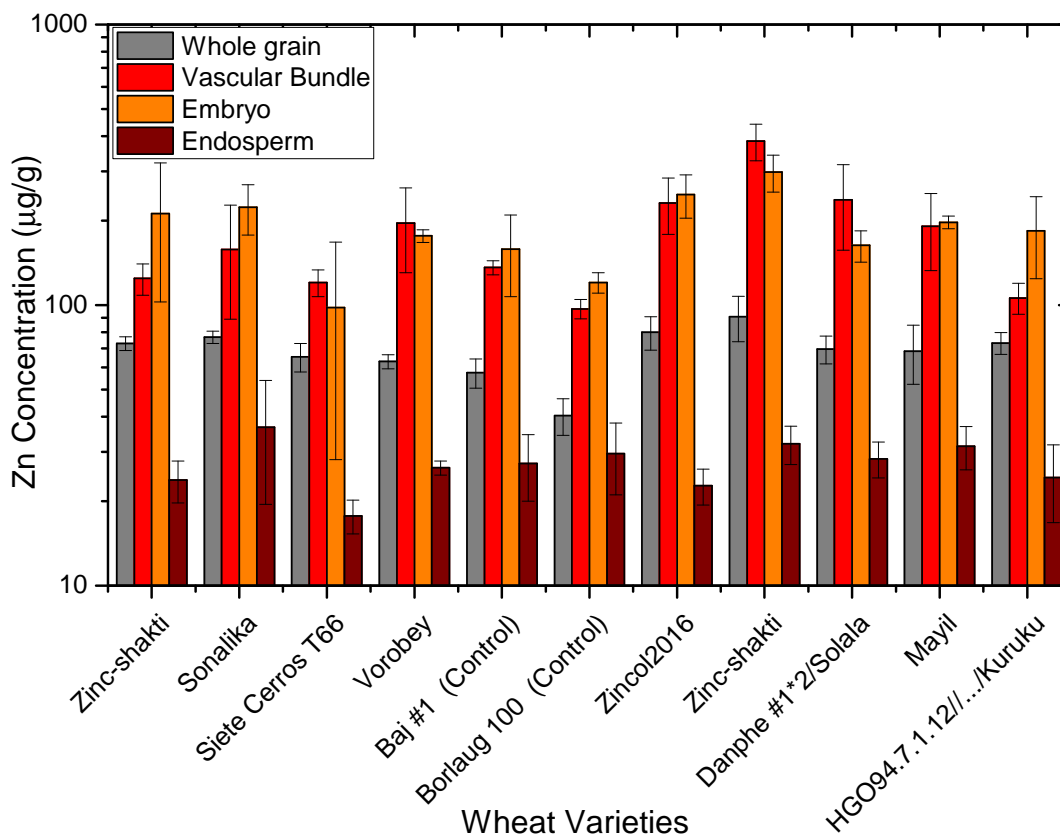


Figure 3.4: Average Zn concentration, in $\mu\text{g/g}$, of all of the studied samples, divided by anatomical structure. The error bars represent the quadrature sum of the instrumental uncertainties with one standard deviation.

over the normal varieties (Baj and Borlaug 100) and the historical varieties also feature higher Zn concentrations even when grown in normal soil with normal fertilization.

3.3.2 Grain structures

As explained in section 3.2.3, three structures within the grain halves were pinpointed by selecting subsets of the pixel spectra from the elemental maps as shown in Figure 3.2.

From Figure 3.5b) one observes a significant increase in Zn deposition within the vascular bundle of the analyzed grains that were subjected to the biofortification procedure when compared to those grown in non-Zn-rich soils. As this organ is the primary transport vehicle of nutrients to the grain, this result is not surprising, however the deposition of Zn within other structures of the grain does not show a very strong correlation with these values (still it is higher in the embryo than in the endosperm). This is indicative that the transport to the grain is very difficult in soil-biofortified plants, nevertheless, the direct connection of the vascular bundle to the embryo, seems to favor Zn uptake when compared to the endosperm for which there is no clear trend. In foliar Zn application,

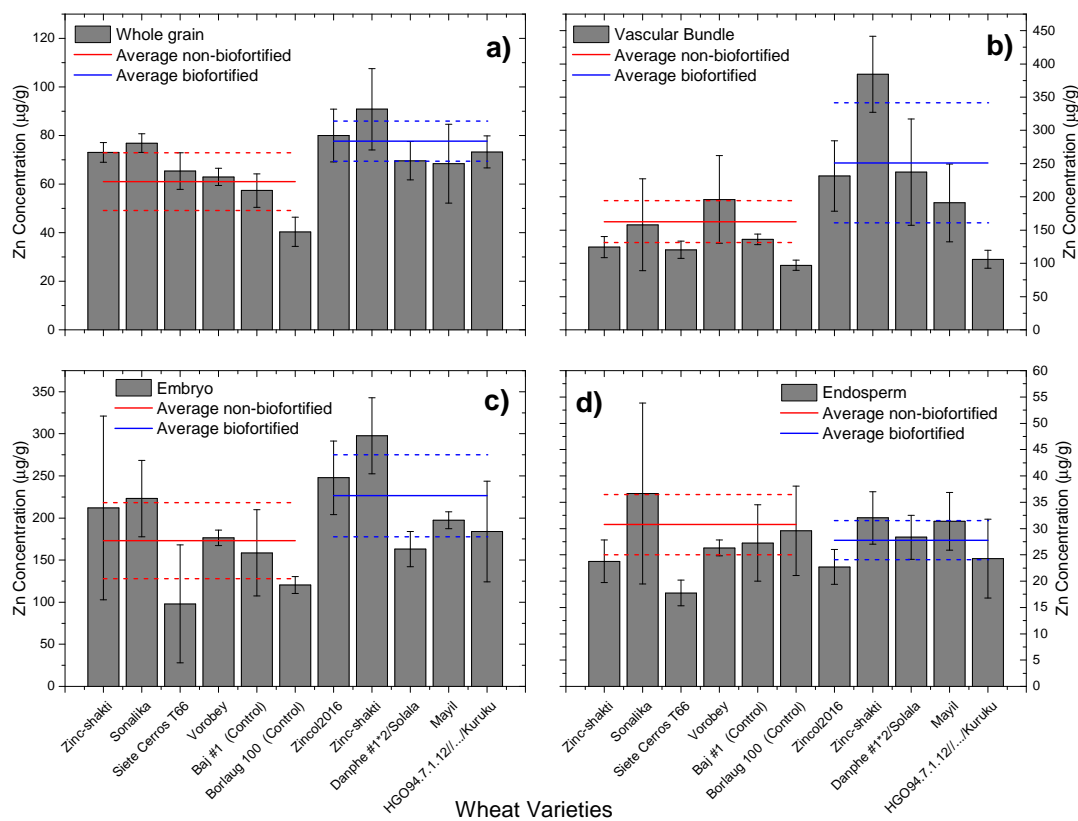


Figure 3.5: Zn concentration, in $\mu\text{g/g}$, of all of the studied samples, divided by anatomical structure. The average values of the samples grown in the Zn-rich soil as well as in normal soil are shown as blue and red solid lines, respectively. The dashed lines represent one standard deviation.

however, specially if applied at early milk/early dough, the metal transport to the endosperm is much higher than soil fertilized biofortification as reported by Ajiboye *et al.* [104] and complemented by our results.

The embryo, which is directly connected to the rachilla, has a preferential uptake of rachis-transported nutrients, similarly to the vascular bundle, which can be directly concluded from the results presented in Figures 3.4 and 3.5 (bottom-left and top-right corners). Similarly to the vascular bundle, the biofortification procedure employed in this work shows a slight average increase of the total Zn concentration in the embryo specially when compared to the control grains Baj and Borlaug100. Curiously, the overall high Zn mass fraction exhibited by the control Zinc-shakti genotype results from a high Zn content embryo, as the other structures (vascular bundle included) do not show very high Zn concentrations, similar to the non-biofortified controls. Nevertheless, the Zn concentration within the embryo, still increases by 40% upon biofortification for this particular genotype.

Regarding the endosperm, which accounts for around 80% of the total biomass of the grain, and corresponds to the grain part which is transformed in the white flour for human

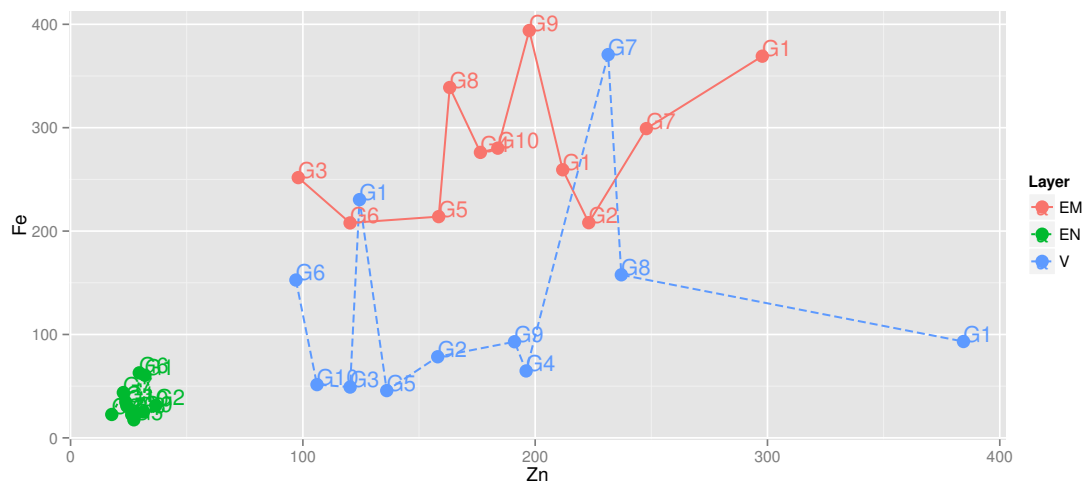


Figure 3.6: Zn and Fe concentrations by kernel anatomic structure in $\mu\text{g/g}$: EM - embryo; EN - endosperm; V - vascular bundle. G1 values are the mean values from both normal and enriched soils.

consumption, the results show that there is no significant change between biofortified and non-biofortified species, independently of the chosen genotype. In fact, for the Zinc-shakti genotype there seems to be a 34% increase in the Zn concentration within the endosperm, but the error bars slightly overlap. Still, as the endosperm accounts for most of the grain’s biomass, even a slight increase in concentration results in a total Zn mass that might be substantial. If the bioavailability of Zn located in the endosperm is high, it can be even better as a way for improving Zn dietary intake problems for high risk populations.

Figure 3.6 shows how Zn and Fe concentrations deposited in each of the three grain structures and Table 3.2 further complements information regarding these concentrations by summarizing the group means and standard deviations of the concentration for genotypes, soils and structures.

3.3.3 Statistical analysis

In this section we study the relationship between Zn and Fe concentrations at the whole grain level as well as at the level of embryo, endosperm and vascular bundle structures. A ranking of all the studied genotypes with regard to Zn and Fe concentrations is also performed. One should note that the statistical results reported below are merely indicative, as the available sample size is small, a fact that was related to both laboratory and beam time limitations and that could not be overcome.

Herein, varieties/genotypes *Zinc-Shakti*, *Sonalika*, *Siete Cerros T66*, *Vorobey*, *Baj*, *Borlaug100*, *Zincol 2016*, *Danphe*, *Mayil* and *Hgo* are coded as G1,...,G10, respectively (see Table 3.1). Note that variety G1 is the only variety grown both in the non-Zn-rich as well as the Zn-rich soil (respectively, *normal* and *enriched* soils).

Table 3.2: Concentration group means and standard errors of Zn and Fe for genotypes, anatomical structures and soils in the case of the structural grain data.

Genotype	Zn ($\mu\text{g/g}$)	Fe ($\mu\text{g/g}$)
G1	179.0 \pm 145.6	174.5 \pm 132.2
G2	139.3 \pm 94.6	106.0 \pm 91.5
G3	78.1 \pm 54.0	107.8 \pm 125.3
G4	133.0 \pm 92.9	121.1 \pm 135.9
G5	107.3 \pm 70.2	92.4 \pm 106.3
G6	82.3 \pm 47.12	141.1 \pm 73.2
G7	167.3 \pm 125.5	237.9 \pm 171.8
G8	142.9 \pm 105.9	173.5 \pm 158.1
G9	140.0 \pm 94.1	170.7 \pm 196.3
G10	104.8 \pm 79.8	120.8 \pm 138.5

$n_G = 3$ concentrations per genotype (G2,...,G10);
 $n_{G1} = 6$ concentrations for genotype G1.

Structure	Zn ($\mu\text{g/g}$)	Fe ($\mu\text{g/g}$)
Embryo	188.9 \pm 56.4	281.7 \pm 63.8
Endosperm	27.3 \pm 5.2	34.1 \pm 15.4
V. bundle	180.2 \pm 83.4	126.1 \pm 99.3

$n_L = 11$ concentrations per anatomical structure.

Soil	Zn ($\mu\text{g/g}$)	Fe ($\mu\text{g/g}$)
Normal	110.1 \pm 69.8	123.9 \pm 97.5
Enriched	158.6 \pm 113.8	175.4 \pm 147.0

$n_N = 6 * 3$ & $n_E = 5 * 3$ concentrations per soil.

Genotype coding	
G1	Zinc-shakti
G2	Sonalika
G3	Siete Cerros
G4	Vorobey
G5	Baj
G6	Borlaug 100
G7	Zincol 2016
G8	Danphe
G9	Mayil
G10	Hgo

3.3.4 Whole grain analysis

Because, in this section, interest lies in studying the linear relationship between Fe and Zn concentrations, we begin by fitting the linear mixed effects model (LMM; equation (3.1)) to the Fe and Zn data, separately, in order to compute the genotypic mean values of Fe and Zn, respectively.

$$\mathbf{y} = \text{Genotype} + (1 \mid \text{Soil}) + (1 \mid \text{Method}) + \boldsymbol{\varepsilon}, \quad \boldsymbol{\varepsilon} \underset{iid}{\sim} N(\mathbf{0}, \sigma^2 \mathbf{I}). \quad (3.1)$$

where \mathbf{y} is the outcome variable in this case elemental concentration, *Genotype* will be the fixed effects variable in this model that represents the contributions of genotype to the measured values, $(1 \mid \text{Soil}) + (1 \mid \text{Method})$ are the two random effects variables that represent the contributions of both soil and method to the measured values, $\boldsymbol{\varepsilon}$ represents the residuals contribution of the remaining non-predicted random effects on the measured values. The residuals follow a normal distribution centered around 0 with σ standard deviation (\mathbf{I} is the identity matrix).

This procedure allows for the removal of the effects, should there be any, of *soil* and *method* from the Fe and Zn concentration variation when computing the genotypic means. Because the classical fit of the LMM may produce biases in the estimation when one or more of its underlying assumptions are violated (e.g., independent, normal and

homoscedastic errors), a robust approach is also considered in this study. In general, robust methods produce similar results to the classical approach when data conforms to model's premises, and allow for more stable results when the data deviate from those. A nice review on these methods can be found in [105].

Table 3.3: Results from the classical and robust fits of model (3.1). σ_s^2 , σ_m^2 and σ_e^2 are the variance associated with soil, method and residuals distributions respectively.

	Type of fit	Estimated Variances ($\mu\text{g/g}$)			Statistical Tests - p-values	
		σ_s^2	σ_m^2	σ_e^2	Shapiro-Wilks test	Levene test
Fe	Classical	96.4	466.1	222.6	0.5652	0.0032
	Robust	0.00	658.9	250.6	–	–
Zn	Classical	109.4	48.0	98.2	0.7386	0.0573
	Robust	159.3	69.4	101.8	–	–

Note: Statistical tests report p-values for the normality and homoscedasticity of the errors tests, respectively, Shapiro-Wilks and Levene's tests.

Results regarding variance components estimates and model validation are displayed in Table 3.3. Both Fe and Zn fitted models pass the normality test of Shapiro-Wilks ($p - \text{value} \gg 0.05$). However, in the case of fit of Fe, there is evidence against the homoscedasticity assumption of the errors, with the Levene's test rejecting the null hypothesis ($p - \text{value} \ll 0.05$). This fact might be enough to justify the differences in results between classical and robust approaches. Here, the robust fit shows that, contrary to what is stated by the classical fit, *soil* has no part at all in explaining the variation in the Fe concentrations (robust $\sigma_s^2 = 0$). Nevertheless, both results agree that *method* is well included in the model as a random effect ($\sigma_m^2 \geq \sigma_e^2$). In the case of the fit of Zn, Levene's null hypothesis is accepted at the 5% significance level by a hair's breadth ($p - \text{value} > 0.05$). In this case, the classical and robust results agree that *soil* plays a major role in the explanation of the Zn concentrations variation ($\sigma_s^2 \geq \sigma_e^2$), an outcome that was expected since soils differ in the sense that one is *normal* and the other one is Zn *enriched*. Approaches also agree that *method* has little part in the explanation of this variation ($\sigma_m^2 \leq \sigma_e^2$).

After the Fe and Zn genotypic means are estimated (fixed effects in model (3.1)), the genotypes are ranked from low to high concentration levels. Results are displayed in Table 3.4. We acknowledge that classical and robust results disagree, in terms of the ranking of the genotypes, only in the case of the Fe concentrations (gray cells). Still, dissent is only seen in the case of genotype G6, which refers to the recently high-yield released control wheat variety *Borlaug 100*, and could be due to the violation of the error homoscedastic premise reported earlier on. Additionally, the range of robust Fe genotypic means is smaller than the classical. In the case of Zn concentrations, there is complete agreement between both classical and robust approaches and the range of Zn genotypic values is also practically the same. Here, in contrast with what happens with Fe concentrations, genotype G6 ranks last, which is an indication of the specific low-Zn content of this particular variety.

Table 3.4: Genotype estimates and ranking after the classical and robust fits of model (3.1). Concentration values are in $\mu\text{g/g}$.

Type of fit	Genotypes*									
	1	2	3	4	5	6	7	8	9	10
Fe	G5	G4	G2	G3	G6	G10	G9	G8	G7	G1
	37.9	40.7	43.0	48.8	63.5	65.5	68.7	70.1	85.1	92.7
	Classical standard errors (se): $\text{se}(G1) \approx 18.3$, $\text{se}(G_i) \approx 20.5$, $i = 2, \dots, 10$.									
Robust	G5	G4	G2	G3	G10	G9	G8	G6	G7	G1
	42.7	45.5	47.7	53.6	60.8	64.0	65.3	68.3	80.3	92.6
	Robust standard errors (se): $\text{se}(G1) \approx 20.4$, $\text{se}(G_i) \approx 21.9$, $i = 2, \dots, 10$.									
Zn	G6	G9	G8	G5	G10	G4	G3	G7	G1	G2
	46.5	62.3	63.5	63.5	67.1	69.1	71.5	73.8	81.9	83.0
	Classical standard errors (se): $\text{se}(G1) \approx 10.3$, $\text{se}(G_i) \approx 12.0$, $i = 2, \dots, 10$.									
Robust	G6	G9	G8	G5	G10	G4	G3	G7	G1	G2
	46.9	61.8	63.0	64.0	66.6	69.6	72.0	73.3	81.8	83.5
	Robust standard errors (se): $\text{se}(G1) \approx 12.1$, $\text{se}(G_i) \approx 13.9$, $i = 2, \dots, 10$.									

* Genotypes G1-G10 sorted in ascending order; gray cells refer to ranking disagreement;

Note: The residuals from the classical fits do not violate the normality assumption.

In the case of Fe, with the exception of genotype G6, which refers to a variety that has never been fortified before, higher levels of concentrations are observed in the genotypes which were assigned to the enriched zinc soil (G7-G10; G1 was assigned to both soils). Notwithstanding, data information is insufficient to conclude that soil has an effect on the levels of Fe concentration. This could be happening due to chance alone or be genotype specific and therefore further study is needed. In particular, the same genotypes should be replicated across the two soils, which was not the case in this study.

To analyze the relationship between Fe and Zn, the Pearson correlation test, Kendall, Spearman [106, 107] and another robust correlation tests [108] were computed. All tests agree in favor of the null hypothesis, i.e., that true correlation is equal to zero. Indeed, three of the methods compute a correlation ≈ 0.11 , which is usually considered as “very weak” correlation.

3.3.5 Grain structures analysis

From both the visual output (Figure 3.6) and the summary statistics (Table 3.2), we acknowledge that Fe and Zn tend to deposit less in the endosperm, which was to be expected [87, 104]. Also, while Fe deposits in higher quantities ($\geq 200 \mu\text{g/g}$) in the embryo, no clear trend is seen for the higher concentrations of Zn ($\geq 200 \mu\text{g/g}$), which deposited both in the embryo and vascular bundle structures. Additionally, it can be seen how much the concentration of Zn increases for genotype G1 from the normal to the Zn enriched soil. Quite curiously, at the vascular bundle structure level, the concentration of Fe for this genotype decreases from the *normal* to the Zn *enriched* soil thus contradicting the observed general trend.

The computation of the Fe and Zn genotypic means via the robust and classical fits of model (3.2) leads to the genotype rankings reported in Table 3.6.

$$\mathbf{y} = \text{Genotype} + (1 | \text{Soil}) + (1 | \text{Structure}) + \boldsymbol{\varepsilon}, \quad \boldsymbol{\varepsilon} \underset{iid}{\sim} N(\mathbf{0}, \sigma^2 \mathbf{I}). \quad (3.2)$$

Results regarding variance components estimates and model validation are displayed in Table 3.5. It is acknowledged that both Fe and Zn fitted models pass the normality test of Shapiro-Wilks and the Levene’s test of the homoscedasticity of the errors. Results between approaches are also similar. In the case of Fe only *structure* has significant effect in the random effects component ($\sigma_{str}^2 \geq \sigma_e^2$). In the case of Zn both *structure* and *soil* have significant effects in the random effects component ($\sigma_s^2, \sigma_{str}^2 \geq \sigma_e^2$) as expected, since both the soil fertilization and the physiology of the grains can significantly influence the Zn uptake.

Table 3.5: Results from the classical and robust fits of model (3.2).

	Type of fit	Estimated Variances ($\mu\text{g/g}$)			Statistical Tests - p-values	
		σ_s^2	σ_m^2	σ_e^2	Shapiro-Wilks test	Levene test
Fe	Classical	0.00	15287	4084	0.1389	0.9072
	Robust	0.00	21833	3089	–	–
Zn	Classical	6253	8071	2147	0.4546	0.6874
	Robust	8490	10571	2147	–	–

Note: Statistical tests report p-values for the normality and homoscedasticity of the errors tests, respectively, Shapiro-Wilks and Levene’s tests.

Table 3.6: Genotype estimates and ranking after the classical and robust fits of model (3.2). Concentration values are in $\mu\text{g/g}$.

Type of fit	Genotypes*										
	1	2	3	4	5	6	7	8	9	10	
Fe	Classical	G5	G2	G3	G10	G4	G6	G9	G8	G1	G7
		92.4	106.0	107.8	120.8	121.1	141.1	170.7	173.5	174.5	237.9
	Classical standard errors (se): $\text{se}(G1) \approx 76.0, \text{se}(Gi) \approx 80.4, i = 2, \dots, 10.$										
Robust	G5	G2	G3	G10	G4	G6	G9	G1	G8	G7	
	92.4	106.0	107.8	120.8	121.1	141.2	164.2	172.4	173.5	194.4	
Robust standard errors (se): $\text{se}(G1) \approx 90.5, \text{se}(Gi) \approx 93.5, i = 2, \dots, 10.$											
Zn	Classical	G10	G9	G8	G7	G3	G6	G5	G1	G4	G2
		51.8	87.0	89.9	114.4	131.7	135.3	160.2	179.0	185.9	192.2
	Classical standard errors (se): $\text{se}(G1) \approx 78.6, \text{se}(Gi) \approx 82.8, i = 2, \dots, 10.$										
Robust	G10	G9	G8	G7	G3	G6	G5	G1	G4	G2	
	51.5	86.7	89.6	114.1	132.0	135.6	160.6	177.0	186.2	192.6	
Robust standard errors (se): $\text{se}(G1) \approx 91.1, \text{se}(Gi) \approx 95.3, i = 2, \dots, 10.$											

* Genotypes G1-G10 sorted in ascending order; gray cells refer to ranking disagreement;

Note: The residuals from the classical fits do not violate the normality assumption.

Table 3.6 shows that the rankings for Zn, again, agree between classical and robust approaches. In the case of Fe, disagreement is only seen in the ranking of genotypes G1

and G8, which interchange. This only occurs because the computed Fe genotypic mean for G1 differs in -2.1 units from the classical to the robust results, which, at this scale can be considered to be negligible.

As to the correlation between Fe and Zn, the Pearson correlation test, Kendall, Spearman [106, 107] and the robust correlation test of [108] agree in favor of the null hypothesis, i.e., that true correlation is, similarly to the whole grain results, equal to zero. However, the three methods now compute a negative correlation of $\simeq -0.30$, which is usually considered as “weak” correlation. Figure 3.7 shows how poorly the classical and robust fits of the linear model (3.3), describe the data, illustrating the lack of correlation.

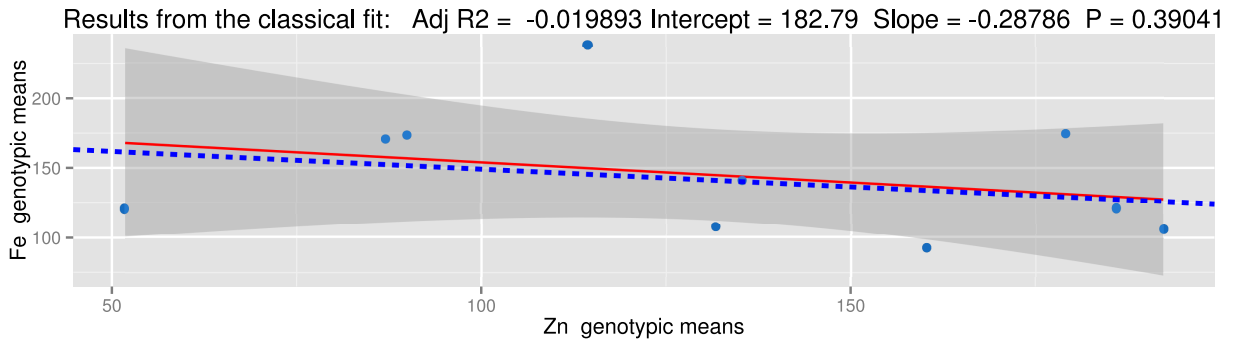


Figure 3.7: Plot of Zn vs Fe concentrations together with fitted classical (red) and robust (dashed blue) regression lines, plus the 95% confidence region (gray) computed from the classical fit.

$$\mathbf{y}_{\text{Fe}} = \mathbf{y}_{\text{Zn}} + \boldsymbol{\varepsilon}, \quad \boldsymbol{\varepsilon} \underset{iid}{\sim} N(\mathbf{0}, \sigma^2 \mathbf{I}). \quad (3.3)$$

We further observe that the ranking of genotypes obtained in Tables 3.2 and 3.6 is not exactly the same. Nevertheless, for Fe, the top 3 genotypes overlap in G1, G7 (robust results) and in the case of Zn, the top 3 genotypes overlap in G1, G2 (both classical and robust results). It should also be underlined that in the case of the structural grain analysis, not all the concentration of Fe and Zn was indeed measured since a part of the grain was discarded (such as the bran and part of the endosperm lying below the exposed bran). Because of this lack of information, to what adds the fact that only one grain per genotype was analyzed with method M1 and the observed higher standard errors, we conclude that the whole grain genotypic ranking results seem more plausible. Although further study is needed in order to fully assess the varieties with better ability to retain Zn and Fe, these results already provide helpful and important information, hinting so far to the existence of varieties that are able to retain high concentrations of Zn and Fe simultaneously, and secondly, suggesting that a compromise between Zn and Fe concentrations needs to be achieved as no significant correlation between those was observed.

As a takeaway from this case study, we can state that, the biofortification procedures applied to the analyzed wheat samples result in around a 30% average increase in overall Zn concentration when compared to other high Zn genotypes, and much higher (35-90%) when compared to the control grains Baj and Borlaug100. It is also shown that this increase in average concentration arises from a big increase in Zn content within the embryo and vascular bundle, with no significant changes, on average, in the endosperm. Nevertheless, for Zinc-shakti, which is a very popular variety in developing countries, we found a 34% increase in concentration within the endosperm, which is a substantial change specially taking into account that the endosperm accounts for almost 80% of the grain's total biomass. The high nutrient contents on the Vascular bundle and embryo, both in the biofortified lines and those which were regularly grown, seem to favor the use of integral wheat flour particularly in countries where low Zn diets are a major public health concern.

The statistical analysis further hints that varieties Zinc-shakti, Sonalika, and Zincol2016 are the top 3 varieties regarding zinc contents with Zinc-shakti, and Zincol2016 also ranking in the top 3 in terms of Fe concentration. Contrary to the classical results, the robust rankings of the genotypes in terms of Fe concentrations, also point to Borlaug100 as a top 3 variety, contrasting with its specific Zn ranking, which comes last.

We conclude that the applied spectroscopic techniques namely triaxial geometry EDXRF and μ -XRF are appropriate for the measurement and mapping of the wheat samples. The methods applied, provided very useful tools to assess the efficiency of the biofortification procedures and have the potential to give feedback to fine tune the procedures even further. This will allow to optimize the nutritional value of the cereal based food, the end product, in such away that dietary benchmarks can be more easily achieved by the consumer.

XRF TECHNIQUE APPLIED TO THE AUTOMOBILE INDUSTRY

4.1 Scope and objectives

The motivation for this project arises from a collaboration between the *Faculdade de Ciências e Tecnologia da Universidade Nova de Lisboa* and *Volkswagen Autoeuropa, lda.*. This work was financed under the PhD scholarship with the reference PDE/BDE/114483/2016, by both *Fundação para Ciência e Tecnologia* and *Volkswagen Autoeuropa, lda.*. This collaboration combines the importance of good air quality control, which is one of the core points of interest of Volkswagen Autoeuropa, lda., with the scientific challenge on the academic side. The main goal is the development of a low-cost working prototype device that is able to access the aerosol composition inside the factory.

The *Volkswagen Autoeuropa, lda.* automobile factory was founded in 1991 as a joint-venture between the Volkswagen AG and Ford Motor Company. Nowadays it is responsible for $\sim 75\%$ of all automobile production in Portugal and represents $\sim 1,8\%$ of the Portuguese GDP[109]. Many of the brand's most known models such as Sharan, Eos, Scirocco have been produced in Autoeuropa, while nowadays the production is focused on the T-Roc model. In 2019, this factory based in Palmela was able to produce 254 600 vehicles averaging ~ 890 cars per day and breaking its own production record. With ~ 5500 workers this factory is the fifth biggest of Volkswagen Group and represents $\sim 6\%$ of all exportation made by Portugal.

As the biggest factory in Portugal and one of the biggest employers in the country, employee safety and well being must be a priority. For this reason, it was identified that the need to better control the air quality inside the factory would be paramount. The company already complies with all the legal requirements, that include verifying the air quality every 2 years. Nevertheless, it is very valuable for a factory to be able to monitor

the aerosol levels inside their facilities on a more real time scope. This need is even greater if we consider that at any given time there are hundreds of workers inside the factory working in the production stations.

Aerosol exposure, as we will discuss in this chapter, can be hazardous to human beings both from short time to long time exposure. Elemental concentrations of suspended matter are key to determine its toxicity to human health and are legislated accordingly. However, legislation is mostly based on short time exposure studies due to their abundance relative to their counterparts. This means that even if some element's dose is legislated with a certain threshold, it is hard to say what happens to an individual that is exposed below this threshold for a full working day, five days a week, through several years. Currently, studies on long time exposure are scarce due to their own premise. The main goal of preventive measures must be to minimize aerosol exposure to well below the legislative thresholds.

Repeated exposure to suspended particles allows for consistent deposition on the human respiratory tract (HRT). The deeper on the HRT these particles can get, the bigger the impact on the health of the individual. This deposition has been associated with chronic inflammatory responses which in turn has been correlated with both cardiovascular and respiratory diseases and conditions. Several autoimmune responses are connected with aerosol inhaling, being allergic reactions the most common one. Since, the HRT is an interface from the atmosphere into the human body, toxic substances that can be suspended onto other particles can cause poisoning (for example heavy metals).

As for the source apportionment of the aerosol, there are several pollutants inside the factory. One of the major contributors, and perhaps the most interesting to study, is soldering and welding fumes that suspend mostly metallic based particles into the factory atmosphere. There are several welding stations across the body shop production line with some being manual, others automated and also mixed stations. These will be at the center of our study given their known impact in the deterioration of the air quality in a factory environment [110][111]. There are also a lot of robots and automated machines inside the factory which may suspend particles of their own due to exhausts or machine wearing. Another source can be identified in painting stations since they aerosolise enormous amounts of particles, however these are isolated from the main assembly line, and hence, not relevant for this analysis. On top of that, workers themselves contribute to the shifting composition of the air, breathing in oxygen and exhaling carbon oxides and water vapor acting as catalysts in new particle formation.

Ventilation is one of the key aspects for air quality maintenance. It is very important that all the aerosol particles are extracted in order to allow for new clean air to be available for breathing. On this front, the factory already possesses a lot of vents capable of extracting air. There are two types of vents: some for general factory air, that are evenly distributed across the buildings, and also vents in more polluting stations (such as welding stations) for more targeted extraction.

Another relevant aspect is that even before the COVID-19 pandemic there were already stations that required some kind of respiratory protection. This might be the best human protection against highly aerosolised environments. This usually comes in the form of filtered masks with stations being classified into three types: no need for mask, needs a strap on filtered mask, needs a higher grade filtered mask with its own air source.

Air quality is one of *Volkswagen Autoeuropa, lda.* focuses and as such this project aims to build a prototype capable of measuring changes to factory air in real time. This device has the following prerequisites:

- self-sustained - has its own power source compatible with the standard power grid
- real time like measurements - it is capable of small acquisitions in time frame of minutes to one hour
- fully automated and independent - it needs to have its own processing units and to be capable of performing several automated tasks
- communications units - it needs to have the capability of measuring and communicating through a platform that's independent of company's infrastructures
- remotely operated - acquisitions and other operations can be launched remotely
- portable - a small enough device that can be transported and moved from station to station
- scalable - must be a blueprint that can be easily reproducible for the purpose of multi device analysis
- low-cost - the price point of the whole instrument must be below 500 €

Our main analysis tool will be based on Energy Dispersive X-Ray Fluorescence (EDXRF) technique[112, 113], which was discussed in section 1.1. As we anticipate that our aerosol samples will have a major contribution from welding, it is expected that a lot of metallic light elements will be found. This technique has great sensitivity to these kind of elements, hence being well suited for this study. Moreover, this is a very versatile technique which allows for cheap and fast quantification of samples with a low level of sample preparation[6]. These characteristics make it very viable to use on devices with specifications as the determined above. This technique allows for both *on-line* and *off-line* measurements without significantly affecting its portability.

For size distribution assessment we have opted to use a mix between binocular micro-camera optical inspection and a scanning electron microscopy (SEM) analysis which will be performed off-line. These two methods will then allow us to get some extra information on the deposited filters particles. Shapes and sizes will then be observed and hence a profile of the deposited aerosol can then be construct.

In the following sections we will give some complementary insight of the object of study of this work - aerosols (4.2). In chapter 5 we will describe design and development of the prototypes built in this project. In this chapter all the engineering decisions and hardware and software parts used will be discussed. In chapter 6 we will present the experimental setups and results achieved with these prototypes as well as their analysis and discussion.

4.2 Aerosols

Aerosol is the term used to refer to the suspension of solid or liquid matter in the air [114] [115]. The history of aerosol observation can be dated back as early as the 1700s, when Dr. Bernardino Ramazzini published "*De Morbis Artificum*" where among other occupational health hazards he reported the effect of dust and chemicals in respiratory organs[116]. Furthermore, throughout centuries there have been many reports of the hazardous effects of what was then called smoke or dust in quotidian life. From forest fires to vulcan eruptions to dust effect in soil deposition, crops ruining or weather changes, numerous observations have been documented.

Even though its negative impacts have thoroughly become common knowledge, aerosol scientific studies are a relatively recent endeavor. The first physicist to really take an interest in studying aerosol properties and behavior was John Aitken whom is widely regarded as the "*father of aerosol science*". The focus on aerosol matter lead to many published papers on the matter essentially between 1880 and 1923[117]. His scientific work was edited by C. G. Knott and published by Cambridge at the University Press in 1923 titled "*Collected Scientific Papers of John Aitken*". In his research, he shows a clear understanding of condensation nuclei creation and development. However, he was most known for his innovative design and construction of the first dust particle counter with which he was able to carry a number of experiments. The first iteration was a bench-top laboratory equipment(Figure 4.1) that suffered many improvements through the years.

Since Aitken many other devices have been developed and the fundamental understanding of aerosol properties has evolved tremendously. However, the scientific community has not always been consistent in what terminology to apply. From dust, to clouds, to particles and aerosols many terms have been applied to refer to air suspended matter. Regardless of the term used, it is accepted that aerosol range in size roughly from 1 nm to 100 μm . As the scale goes as big as the macroscopic range or down to the atomic range, aerosol properties also change as we go from mostly Newtonian physics to molecular and ionic interactions.

Due to the heterogeneous nature of aerosol particles and short lifetimes, there is much we don't completely understand compared to their gaseous state counterparts. Many studies have been focused on the physicochemical characterization, source apportionment and effects on humans and environmental impact [119, 120, 121]. As a matter of fact, climate impact of aerosol particles is one of the main driving forces of this kind of research.

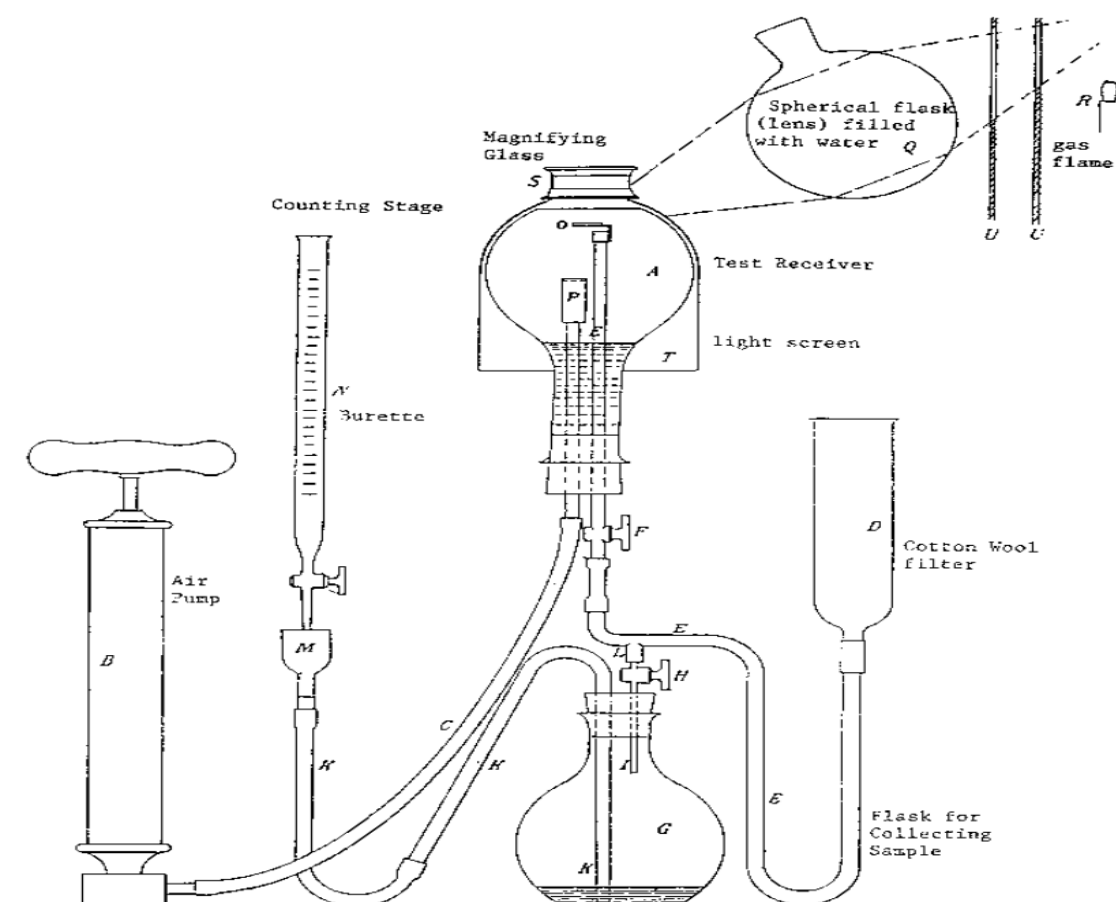


Figure 4.1: John Aitken's first dust particle counter.[118]

The importance of aerosols in cloud formation, precipitation, fog and visibility leads to a need to understand how their physic and chemical structures and compositions influence these processes.

Chemical composition varies immensely from sample site to sample site. This chemical composition is intrinsically connected with the source but also with the interaction with the surrounding atmospheric and meteorological conditions. Sampling particles with very heavy influence of anthropogenic emissions and saturated long lived aerosols leads to much complex compositions than samples retrieved of remote locations. Size distribution is also a very big factor because particles produced with different processes of creation lead to different dimensions.

Aerosols in general are a mixture of inorganic elements, like nitrates and sulfates, and organic elements, either from direct biogenic emissions or from oxidation of organic gaseous species. Carbon is also one of the biggest components of ambient particulate matter, with several molecules resulting from both natural processes and anthropogenic emissions. Inorganic species may include several metallic ions like Na^+ , Al^{3+} , Ca^{2+} , Ni^{2+} , Zn^{2+} , Pb^{2+} that tend to bond chemically with mostly oxidized anions like SO_4^{2-} or NO_3^- . There are also many other radical species contributions to the inorganic part. As

for the organic part, there are hundreds of compounds that differ largely from polarity to aqueous solubility, to source type, to primary or secondary emissions. Overall there are many organic aerosol constituents whose chemical compositions remain unknown despite several studies pursuing that end.

In recent years, various authorities have started publishing several guidelines and laws that establish limits to hazardous substances. Whether the focus is towards species that are found indoors or outdoors, more regulating guidelines are being introduced every year. Relating specifically to workplace environment, the major concern is exposure to cancerous substances, as cancer is the major cause of death for workplace related deaths every year. In Portugal, DGS (Direcção Geral de Saúde) is responsible for establishing lawful limits of exposure to hazardous substances[122, 123, 124] as well as enforcing directives and target limits proposed by WHO (World Health Organization)[125] and approved in diverse European committees. As another example, the ACGIH (American Conference of Government) published the threshold limit values of more than 600 chemicals where approximately 300 are aerosols commonly found in workplaces. Thus aerosol science is vital to not only provide ways to measure substances but also to understand what impact they have on world health.

Even though aerosol related health problems are mostly associated with our respiratory system, skin deposition may also have various negative effects on the human body[126]. Regardless of the route of entry, knowledge of the deposition is mandatory for dose assessment of airborne pollutants. This process is very reliant on the physical characteristics of the actual particles regarding volume and size distribution. Nevertheless, physiology of the individual involved is also a key factor.

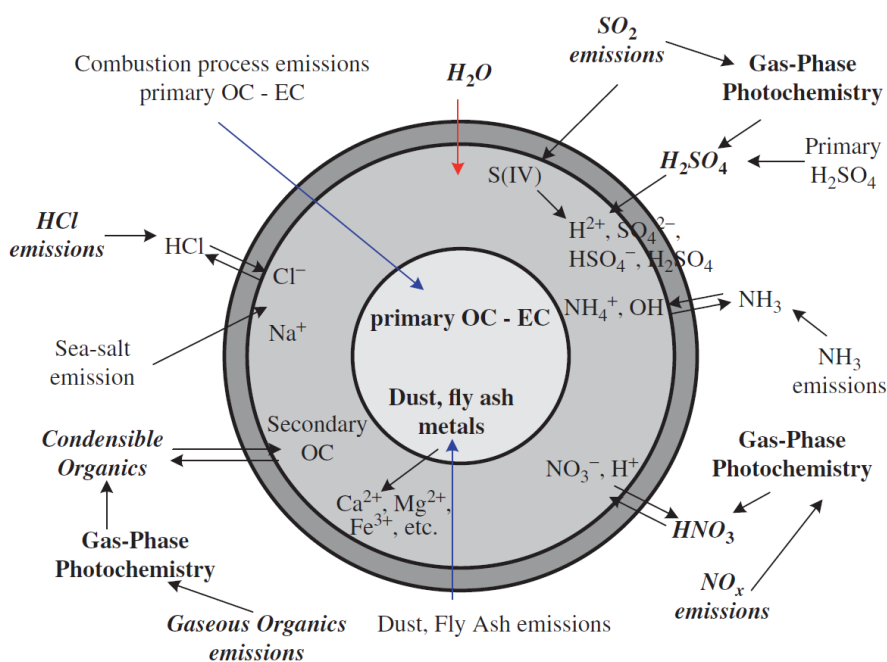


Figure 4.2: Schematic representation of an aerosol chemical interactions.[114]

In aerosol science, the particles are usually subdivided into two groups: primary and secondary. Primary aerosols, as it is suggested by the name, refer to the particles that are directly emitted into the atmosphere, which may occur from combustion, suspensions of soil or sea spray, etc. Secondary aerosols rise from processes of aggregation or nucleation that occur within the atmosphere with other aerosol particles and gas-phase species. Moreover, it is important to reiterate that aerosols might be suspended solid matter or liquid droplets, but can also be mixtures of both matter states. In Figure 4.2 we have a schematic representation of an aerosol and some chemical interactions it might be subject to.

4.2.1 Aerosol properties

Perhaps the most important property of an aerosol is their size distribution. Aerosols can be classified into monodisperse or polydisperse whether the constituting particles have the same or different sizes. Moreover they can be called homogeneous or heterogeneous based on how their particles' chemical composition compares to each other. These particles can be further subdivided into three groups:

- Isometric- If they have approximately the same dimensions in all the three axis like spherical particles.
- Platelets- If they have one dimension significantly smaller than the other two dimensions.
- Fibers- If they have one dimension significantly larger than the other two dimensions.

The most studied and described in the bibliography are certainly the isometric particles due to its simpler nature. However, in recent years, interest towards fibers has been growing due to their particular toxicity to human health [127, 128]. In isometric particles, the diameter is often the chosen parameter to describe the size attribute. Nevertheless, as most particles aren't spherical, settling velocity is normally better suited for size characterization. This is obviously an approximation and implies that we assume that particles with the same settling velocity have the same size. In this approach, we define an equivalent diameter that is known as aerodynamic diameter. Hence, the aerodynamic diameter is the diameter of the unit-density sphere with the same aerodynamic properties of the particle measured. The Stokes diameter is defined in the same way, with the only difference being that it is normalized based on the density of the particle.

The size of an aerosol particle can be determined through various techniques like light-scattering measurements or aerodynamic resistance, electrical mobility and settling velocity measurements. Regardless of the method used, it is always necessary to use an equivalent diameter since direct measurement of individual particles are not useful for

size distribution assessments. The size distribution within an aerosol sample is usually characterized in one of the following ways:

- The 50% cut-off diameter,
- Dosimetric variables related to human exposure,
- Their observed modal distribution.

The 50% cut-off diameter is a parameter that is related with the efficiency of the instrument used for the measurement. In an ideal situation, if we defined a cut-off diameter d , the size distribution would have a sharp vertical line for that value. Bellow that line all the particles would have a diameter smaller than d . Since in real measurements instruments come with an uncertainty, the cut-off curve turns into a hyperbolic tangent like function. This function is centered around the ideal cut-off line which is the point we classify as 50% cut-off diameter - d_{50} . This means that the instrument can filter out particles with smaller diameter than d_{50} with an efficiency of 50%. Obviously, within a real experiment, if we want a bigger efficiency for a specific diameter we just define a cut-off diameter lower than d_{50} .

Dosimetric variables related to human exposure are specific particle sizes that are accepted by the scientific community as good descriptors of impacts on human health. The most used are certainly $PM_{2.5}$ (or fine particles) and PM_{10} . They are actually defined as the group of particles with a diameter smaller than the 50% efficiency cut-off at 2,5 μm and 10 μm , respectively. The subdivisions into these categories are related to how far particles are likely to reach in the respiratory tract with $PM_{2.5}$ depositing further into the pulmonary alveolus. There are also some other classifications as ultrafine, which usually refer to very small clusters with a diameter smaller than 0,1 μm .

When it is described as a multimodal distribution, there is basically a sum of distributions (symmetric or otherwise) centered around a modal value corresponding to each of the modes within the process of development of the observed aerosol. So every particle contained within a certain stage of this process will tend to be distributed along a curve specific to that mode. These stages are usually subdivided into: nucleation mode, Aitken mode, accumulation mode and coarse particle mode. The mathematical distribution associated with size distribution of aerosol, which is perhaps most widely used, is the multilognormal distribution with the expression:

$$\frac{dN}{d(\log(Dp))} = \sum_{i=1}^n \frac{Ni}{\sqrt{2\pi}\log(\sigma_{g,i})} e^{-\frac{(\log(Dp)-\log(\bar{D}_{pg,i}))^2}{2\log^2(\sigma_{g,i})}} \quad (4.1)$$

where N is the number concentration, D_p is the aerosol diameter, n is the number of i modes, with $\bar{D}_{pg,i}$ and $\sigma_{g,i}$ being the mean and standard deviation of the geometric diameter of each mode, respectively. However, some of these curves might become a

little more complex when we take in consideration submodes like the condensation and droplet submodes in which the accumulation mode is usually subdivided into.

In Figure 4.3 we have both the number concentration distribution but also the volume distribution for a typical atmospheric aerosol. Both of these distributions usually appear to be bimodal representing only two of the modes because the other two modes contributions are nearly null. Number concentration distributions typically only have two major peaks for the nucleation and Aitken modes, whereas volume distributions have their big peaks at the accumulation and coarse modes. This is due to the fact that in an typical aerosol there are a lot more ultrafine particles than fine or coarse. Since fine and coarse particles are various units of magnitude larger than their ultrafine counterparts thus making a bigger contribution to the volume distribution.

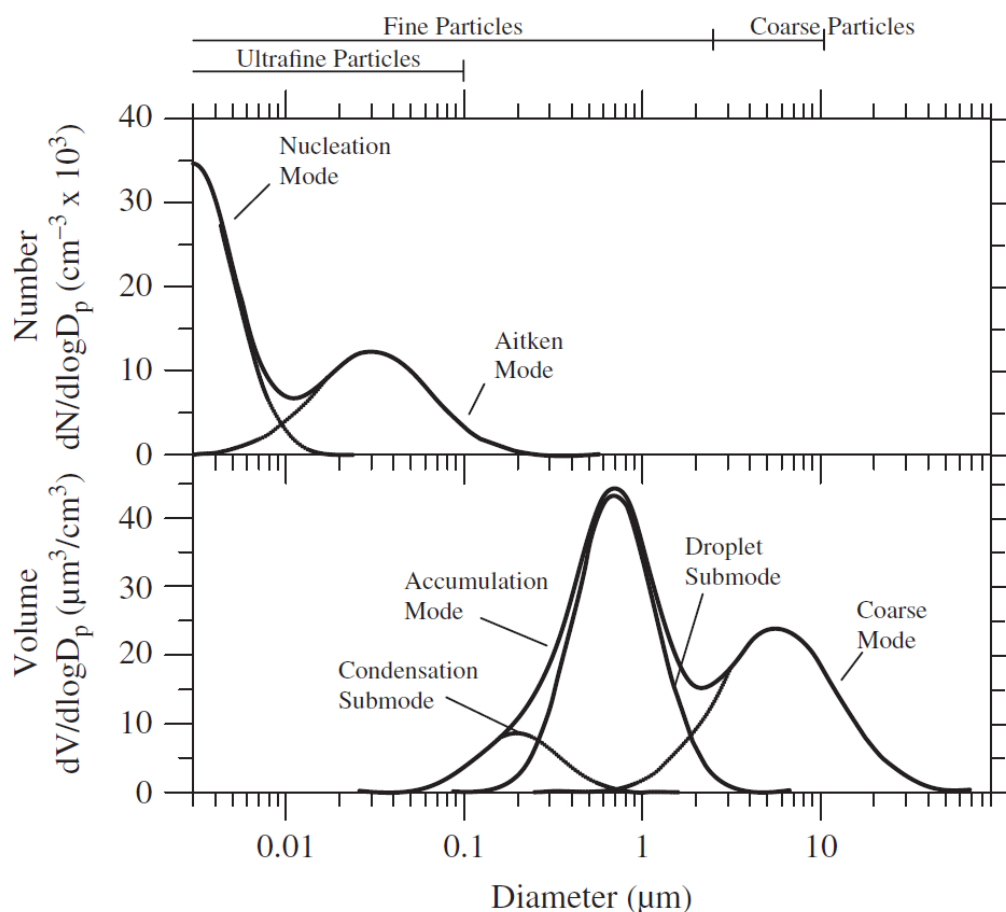


Figure 4.3: Atmospheric aerosol number and volume distributions.[114]

After size and size distribution, the most important aerosol property is chemical composition. This property varies greatly from aerosol to aerosol and it's mostly related to the source - whether it is primary or secondary. Generally speaking the most frequent components are sulfates, nitrates, ammonium, chloride, carbon, water and crustal material. Regarding sources, the most relevant biogenic primary emission is the crustal material

since it is the most common natural aerosol. As for anthropogenic primary emissions the biggest contributor is elemental carbon also known as soot. For secondary particles, the most common are organic clusters, where organic carbon is particularly relevant. Nevertheless, a reasonable amount of inorganic particles (like nitrates, sulfates, ammonium and water) can also be found in most atmospheric aerosols.

The organic part of an aerosol contains a lot of particles that result from secondary processes of oxidation. SOAs (Secondary organic aerosols) constitute a major point of interest of research due to the complex sequence of processes in their genesis[129]. Chemical species like hydrocarbons or carbon oxides like (CO and CO₂) are some of the byproducts of these processes. For this reason, understanding these mechanics is imperative due to their known public health effects[130].

Another possible variant are bioaerosols which are particles of biological nature[131]. In this category are included pollen, fungi, fungal spores, bacteria and viruses, either as a whole or fragmented parts. These fragmentations usually occur as byproducts of desiccation in the atmosphere which leads to these microorganisms to break apart. But even if fragmented, all these bioaerosols can be hazardous to public health. Common correlated symptoms are for example asthma and bronchial hyper-reactivity.

4.2.2 Aerosol health impact

In order to understand aerosol impact on human health we first need to know how the deposition in the human respiratory tract (HRT or human RT) works. The International Commission on Radiological Protection (ICRP) has proposed a model in 1994 [132] that still is one of the most widely used to describe this process. It was developed in an effort to understand specifically the deposition of radioactive particles but has since been adopted as the definitive model of the HRT.

It is important to state that this deposition is intrinsically dependent not only on the size distribution and chemical composition of the aerosol but also on the anatomy and physiology of each individual. Having said that, the mechanisms of deposition are very diverse, being inertial impaction, diffusion and gravitational settling the most important ones. In specific cases there are also some depositions due to electrostatic effects and interception. Electrostatic effects may occur when charged particles from an aerosol alter the electric equilibrium of a surface/wall. It is then possible for other charged particles to electrically bond with that surface. Interception occurs with particles that are "oddly" shaped and is a negligible phenomenon when referring to spherical-like particles. This type of deposition occurs when particles following the air streamlines become too close to the surrounding surfaces and due to their asymmetries, their edges adhere to these surfaces. This mechanism gains great importance when we are talking about fibre-like particles. Meaning that this kind of particles, regardless of their size, have a very high deposition rate due to the interception mechanism and thus warrant separate analysis.

When we want to estimate the dose of particles deposited in the RT we are accounting

for particles deposited through all those processes. This dose rate H (mass deposited in a time interval) can be calculated as:

$$H = n_0 c_A B \left(\alpha \sum_i n_{fine,i} + (1 - \alpha) \sum_i n_{coarse,i} \right) \quad (4.2)$$

with n_0 being the inhalability ratio, c_A the aerosol concentration, B the ventilation rate, α the fine particles mass fraction, $n_{fine,i}$ and $n_{coarse,i}$ being the particle retention in region i of the lung for fine and coarse particles, respectively. The inhalability is defined as the ratio between mass concentration inhaled through the nose or mouth and the total ambient mass concentration.

As we can see from the summations in equation 4.2, the deposition is usually subdivided by anatomical regions i . This is due to the fact that deposition rates for each mode are different, and the size distribution of the aerosol able to reach each region is also different. Therefore, three major deposition fractions (DF) are usually defined: the alveolar region (AL), the tracheobronchial region (TB) and the extrathoracic compartment (ET). The TB region can sometimes be subdivided in upper and lower bronchial as we can see in Figure 4.4. This figure also shows the semiempirical deposition profiles per fraction for uncharged, unit-density spheres orally inhaled at the mean breathing pattern of an adult.

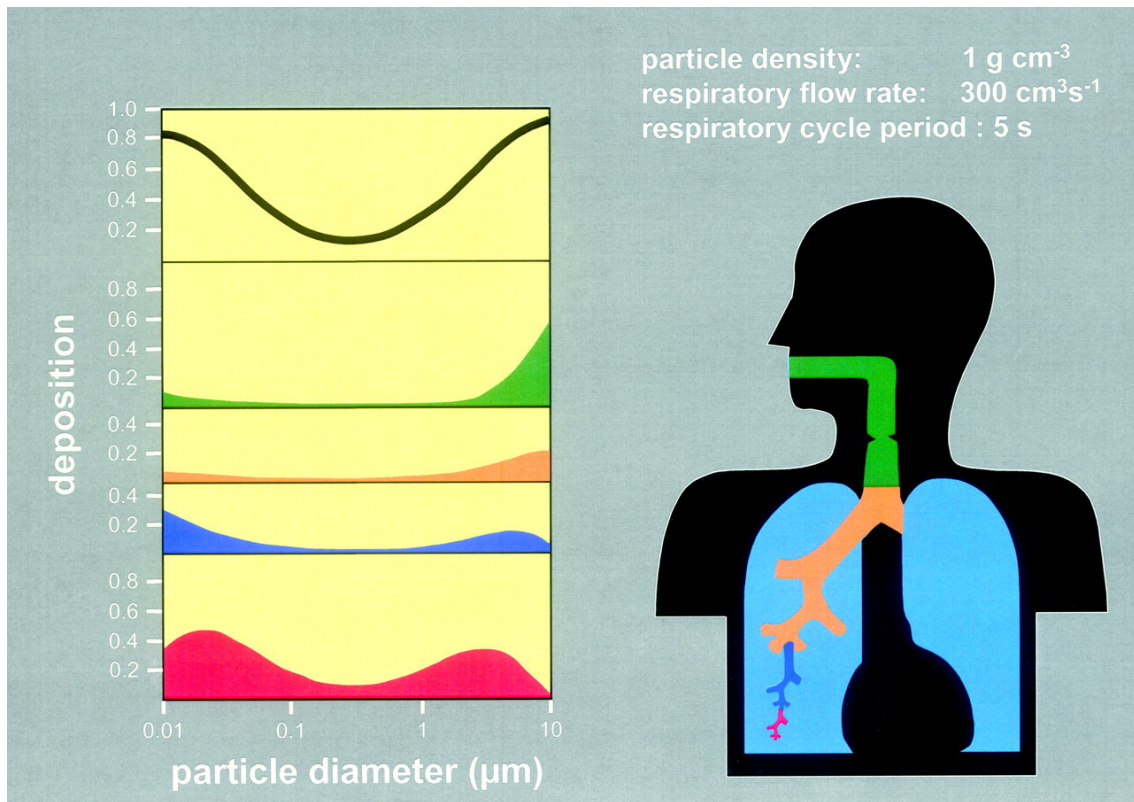


Figure 4.4: Human respiratory tract deposition fractions profiles[133].

As we can see on the first curve (Figure 4.4), we have a typical total deposition profile

with a bimodal form. There is more deposition in the very small particle sizes modes and on the coarse mode, and not a lot in between. The reason for this is the mechanisms through which these depositions on the RT occur. For very small particles the deposition is mainly due to Brownian diffusion, which decreases in importance as the size increases. However, with bigger sizes mechanism like sedimentation and impaction become more important because of the extra inertia of the particles. Therefore, as we get into the coarse mode, particles become less likely to follow the fluid streamlines and start to deposit on nearby surfaces. Hence, there is more deposition for bigger size particles.

Moreover, we can see also that, as expected, the deposition is not uniform across the RT. Keep in mind that this result will vary greatly with different aerosol mixing[134]. Nonetheless, these are typical depositions across the different DFs. We can observe that bigger particles tend to deposit in upper fractions and smaller particles in the lower ones. Aerosolized drugs, for example, use these particle size mechanics to target specific portions of the RT. Some examples of this research topic can be found in [133, 135], where the authors predict that for the ICRP model, if we use $6\mu\text{m}$ unit density particles at an inspiration flow rate of $500\text{ cm}^3/\text{s}$, we can target deposition at the ET with an efficiency of approximately 65%.

With this knowledge, it is now possible to understand the reasoning for the anthropological size classification of aerosols that has been mentioned in 4.2.1. UFPs, $\text{PM}_{2.5}$ and PM_{10} have different deposition efficiencies across the HRT and thus different impact on human health. Legislation itself is also focused on the mass concentration doses of both PMs portions but UFPs are worryingly omitted. This represents an oversimplification of the problem, as even though we might not have a big daily dose from UFPs, their actual number deposition might be higher than PM fractions of the aerosol. The reasoning being that one big $\text{PM}_{2.5}$ deposited equates in mass to hundreds/thousands UFPs. Moreover, as these particles travel further in the RT they deposit more efficiently in AL region and therefore have a bigger probability of entering the bloodstream [136][137]. Nonetheless, health studies on this subject are quite limited and these evidences are very much empirical. It is hard to trace exactly particles from ambient aerosols all the way to the bloodstream and the rest of the human body cells. On top of that, chemical composition of an aerosol will obviously affect not only the deposition efficiency but also the probability of absorption to the bloodstream and its inherent toxicity.

The difficulty in tracing the health problems directly related to aerosols has been a research topic for a long time. Early experiments like the ones from Nolan and Pollak, a Dublin group, relied on condensation nucleus counters (CNC) to basically try to determine how many particles inhaled and how many particles were exhaled. The difference was then assumed to be the number of particles deposited on the HRT, having no way to account for other effects like nucleus coagulation. Furthermore, these experiments were obviously limited by the lack of aerosol size distribution sensibility inherent to the instruments.

Nowadays, with instrumentation continuous evolution, there are a lot of studies like

[138, 139] that have a better grasp of how particles as small as UFPs behave. Research seems to indicate that UFPs have high deposition efficiency in the lungs regardless of their toxicity. Moreover, empirical evidence shows that these particles are very unlikely to be resuspended in such a way that they end up being exhaled, even dozens of hours after exposure. On the other end of the spectrum, coarse particles are more likely to resuspend and being exhaled.

One of the most studied aerosol health impacts is tobacco smoke due to the fact that it is the most common self imposed aerosol. Its hazardous nature is well known and as it was reported by WHO [140] 90% of lung cancer can be avoided by eliminating tobacco use. This is from data retrieved in Europe in the year 2018. This report points out that 27% of all cancer deaths were attributable to tobacco use in 2018. This reality is aggravated in the european region where there is the biggest percentage of smokers *per capita*. Statistics show that there are approximately 209 million smokers, which equates to 29% of the population. Moreover, it has been proven a correlation with several cardiovascular diseases which makes the problem even more serious.

The tobacco worrying numbers also prove how important aerosol studies are because they show how efficiently suspended particles can enter deep into the human body and cause irreparable damage. This is specially true if we consider that there has been proven that nonsmokers are reported to suffer similar health effects when exposed regularly to second hand tobacco smoke. Therefore, we can deduce that an aerosol can have negative health consequences even when they are not forcefully inhaled in high concentrations.

As it has been stated, the mechanisms through which aerosols interact with the human body in order to cause negative effects are not completely understood. More so if we are not talking about the well known case of tobacco. But if we go through the research, it is possible to point out some interesting effects that have been documented. For example, there are several studies that show how common particles with low toxicity such as polystyrene can give rise to proinflammatory responses from the human body due to the fact they have a very large surface area[141]. Also fibre-like aerosol are reported to induce similar responses from the human body due to their elongated shapes. Generally speaking, the bigger the HT's surface area affected by the deposition of external solid particles, the harder it is for the human immune system to cope. Many of these deposited particles are acting as inhibitors of lipoproteic antiinflammatory compounds produced by the human body. This also has been correlated to an increase in systemic oxidation which is proven to cause proatherogenic effects. In other words, the accumulation of particles raises the oxidative stress which leads to an accumulation of nodes in the arteries around the alveolar that constitute a real cardiovascular risk.

What we can conclude from these researches is that even though specific compounds might not be particularly toxic to the human body, they can cause severe diseases in the long run. Their deposition in the HT leads the immune system to treat these particles as threats and produce cytokine proinflammatory compounds that serve as markers of an

inflammation but eventually raise the oxidative level of surrounding cells. As a consequence, this can cause various degrees of damage at cell level and even DNA molecules. To make matters worse, not only are they able to cause inflammatory responses but also studies [142] show that UFPs inhibit anti-inflammatory capacity of the immune system as well. These reoccurring inflammatory responses and high oxidative stress have all been correlated with many cardiopulmonary diseases and even cancer.

Aerosols can have hazardous health effects regardless of which particles are contained in the mix or the affected individual. However, the health impacts can be enhanced if we take look at more toxic particles and more sensible individuals. Aerosols are vehicles to any sort of organic/inorganic/biologic compound into the human cardiovascular system. Therefore, toxic molecules like elemental and organic carbon species lead to very acute negative effects in the human body, either in the short or long term. Suspended and very toxic particles, like heavy metals, can also be delivered into the bloodstream and cause serious damage and even lead to death in certain doses. Another problem are allergenic species that deposit into the HRT and result in allergic reactions, particularly acute for individuals with chronic asthma. Lastly, aerosols can also be the main pathway of biologic organisms like virus into the human body as we are observing in the recent COVID-19 pandemic.

4.2.3 Aerosol measurement techniques

The universe of aerosol instrumentation is quite large given the many properties and measurement procedures involved in this research topic. Hence, depending on what aerosol characteristics we focus on various techniques arise to meet the requirements. Whether we want to study number or mass concentration, size distribution, surface deposition, chemical composition or opacity, we will need either a different instrument or a different analysis. Moreover, these measurements usually need a lot of data treatment and modeling. This is specially true because often we have no means of directly measuring properties as "simple" as size for example. Most of aerosol measurements are actually indirect assessments, in the sense that we are not measuring directly the property of interest. Using the size property as an example, it is usually inferred through the optical, mechanical, aerodynamic or force field mobility properties of aerosol particles and not through a direct measurement.

Aerosol instrumentation is basically subdivided into two major approaches: aerosol sampling instruments and direct-reading instruments. The differences are quite straightforward from their names. The first group of instruments focus on devices capable of gathering particles from the air, whether we impose strict selection rules or not. Particle selection can be of major importance in some sampling environments. Regardless, this approach relies on other devices to do the analysis of the sampled content. Hence, it is needed complementary instrumentation that can do microscopic, gravimetric, optical, spectral or chemical analysis afterwards. Also, results of these techniques are often

regarded as time-averages, and therefore the flow rate and sampling time are two parameters that are important to keep track. These measurements provide several benefits such as using higher resolution instruments afterwards to observe a stationary sample, but can have downsides like particle interaction in the substrate and resuspension (loss of information).

In the other category, both the sampling phase and the analysis phase are blended into one. Nowadays, with the development of modern electronics it is possible for some techniques to deliver an on-the-spot real-time measurement of the property of interest. A fast response with slow delay is primordial to keep track of an ever-changing system like an aerosol in which particles are constantly interacting, changing size distribution and even chemical bonds. However, as it was said before, it is usually necessary for such approach to use indirect assessments of the aerosol property in study. Therefore, it is mandatory to be very meticulous with the calibration of the instrumentation and data may require a lot of post-processing. The obvious consequence to indirect measurements is that the accuracy of your measurements is not only dependent on the resolution of your instrument but also how well the model for calibration correlates with reality.

There are a few instrumental parts that are transversal to many aerosol measuring devices that deserve mentioning. As it is described in this instrumentation sub-chapter [4.2.3](#) many of the measuring techniques rely on similar general approaches, hence the relevance of these generic parts. Generally speaking, in an aerosol instrument there is some sort of inlet stage, a pumping stage, either a collector or a direct reading stage, a flow stage and obviously an electronic stage for control. Furthermore, the inlet stage can be as simple as an open tunnel or it can be a selective sampling inlet. In many applications, there is an extra interest on having very restrictive characteristics on the particles that are being sampled. The most typical restriction is discriminating by size, for example to measure only $PM_{2.5}$ or PM_{10} [[143](#)]. The pumping stage is responsible for forcing the ambient aerosol to go through the sampling inlet into the device. It keeps the sampling aerosol flowing through the device and makes it possible for it to be collected or directly measured on the next stage. This can be accomplished with different approaches but the most common solution is to apply a vacuum pump. The next stage can be either a direct measurement of the sample or a collecting stage, as it has been stated, and will be the defining stage between each type technique. The flow stage is a calibration related stage where, in most instruments, a flow meter is used in order to account for the volume of sampling aerosol and obtain the concentration of the aerosol property of interest.

The first attempt at a general classification of aerosol instrumentation and techniques was done in 1970/71 by Friedlander [[144](#), [145](#)]. Other works have also tried to systematize what the possible aerosol measurements [[146](#)] are, so that these categorizations don't become outdated. To understand these works, we must firstly define some physical properties and quantities in order to be precise about what each technique measures. The approach in these papers usually starts by understanding what chemical specie is in a defined volume at a given time. In order to account for that, we need to consider

probability density functions (*pdfs*). In these overviews they present some, but the most important is the aerosol size-composition time dependent pdf of species with index k , which is defined by $g(t, v, n_1, \dots, n_{k-1})$ for an aerosol with k chemical species and n_i number concentration, where v is the particle volume. This function is defined in such a way that the number of particles dN in a unit volume between v and $v + dv$ and molar composition of each species i between n_i and $n_i + dn_i$ at time t is given by:

$$dN = N_{\infty} g(t, v, n_1, \dots, n_{k-1}) dv dn_1 \dots dn_{k-1} \quad (4.3)$$

where N_{∞} is the total number of particles. The volume of the particle v correlates with the molar composition n_i of each chemical species in the following way:

$$v = \sum_{i=1}^k n_i \bar{v}_i \quad (4.4)$$

where \bar{v}_i is the partial molar volume of species i . Both equations 4.3 and 4.4 serve the purpose of generalizing an approach to what quantities are typically being measured in an aerosol instrument. Even though they can be further generalized and reformulated to account for more aerosol characteristics, not accounted in this form, for example: charge states, morphology or surface composition assessments.

The way to distinguish between different measurements is usually how we integrate over time, size or composition the expression 4.3. Furthermore, some physical properties that are not explicitly included in this expression can also be assessed by the means of a weighting function like $W(v)$ that will be integrated alongside the pdf g . This weighting function will be necessarily different depending on what is intended for being measured. Some straightforward examples include $W(v) = 1$ for condensing nucleus counters (CNCs) and $W(v) = \rho \cdot v$ for mass measurement.

In Table 4.1 there is a summary of how techniques can vary inspired on the works of Friedlander. It is worth keeping in mind that this is only a schematic representation and some figures could not be 100% accurate. Nevertheless, in this table there are also some examples of techniques that fit within the defined categories, even though there may be several more that fit these classifications or slight derivations of them. However, even if instruments are labeled in the same category, it is often very troublesome to compare measurements obtained with two different devices. This is related to something we already mentioned, properties like size are not directly measured but often inferred from other characteristics. This makes cross calibration a very challenging task.

Furthermore, calibration in aerosol measurements can be misleading even if we compare similar instruments. Small differences in size cuts, or different sensitivities to aerosol properties like density or hygroscopicity (interference of water molecules) can lead to divergent results. A complete understanding of the instrument used, regarding what and

Table 4.1: Aerosol measuring instruments classification. *Examples of measuring techniques. Full size on the appendix A.1.

Instrument	Size distribution	Time	Composition	Quantity
Perfect single particle measurement				$N_{\infty} g(t, v, n_1, \dots, n_{k-1}) dv dn_i$
Physical size distribution * Electrical mobility analyzer				$N_{\infty} \cdot \int_{t_1}^{t_2} \int_{v_1}^{v_2} g() dv dn_i dt$
Continuous measurements of integral properties * Condensation nuclei counter * Cloud condensation nuclei * Mass concentration				$N_{\infty} \cdot \int_0^{\infty} \int W(v) g() dv dn_i$
Size resolved mass measurements on a integrated time interval * Cascade impactor				$N_{\infty} \cdot \int_{t_1}^{t_2} \int_{v_1}^{v_2} \rho_p \cdot g() dv dn_i dt$
Time and size integrated measurements of composition * Filter + composition analyser				$N_{\infty} \cdot \int_{t_1}^{t_2} \int_0^{\infty} \int n_j \cdot g() dv dn_i dt$
Time integrated size and composition measurements * Impactor + chemical analyser				$N_{\infty} \cdot \int_{t_1}^{t_2} \int_{v_1}^{v_2} g() n_j dv dn_i dt$

how an aerosol property is measured and the physical and chemical processes that may alter these measurements is essential.

In Table 4.1 we see a schematic representation that starts with a perfect measurement, which is obviously one instrument that outputs all properties with infinite resolution, down to a particle by particle analysis. This is an hypothetical setup, but in real measurements we need to either integrate or average out some the fundamental properties. In the following subsections we will discuss further the instruments within each class, taking in account however that the last two rows in the table correspond to measurements that are combinations of different techniques that will be individually discussed as part of a different category.

4.2.3.1 Size distribution and size resolved measurements

In this section we include the second and fourth categories of measuring instruments from Table A.1. On this matter, we can generally infer a size distribution from:

1. Optical measurements,
2. Electrical mobility measurements,

3. Particle diffusion measurements,
4. Inertia measurements.

Size distribution techniques can also be subdivided into real time measurements and integrated time measurements. The latter requires a sampler step before it can be analyzed by techniques like scanning electron microscopy (SEM)[147] and transmission electron microscopy (TEM)[148]. Both these microscopy techniques rely on projecting a beam of electrons into a sample and then detecting the reflected electrons (SEM) or the transmitted ones (TEM). With the detection of secondary electrons is than possible to constitute a digital image based on the intensity of reflected/transmitted electrons. From these images it is then possible to evaluate solid state structures and particles, allowing for a size description of the sample. Microscopy techniques are commonly used to complement other aerosol measurements due to the fact that they can only analyze integrated time samples.

Optical measurements Real time size distribution measurements can be achieved with optical particle counters (OPCs)[149] which are also widely used. These devices take advantage of scattering of electromagnetic radiation by suspended single particles. Every aerosol particle interacting with the incoming photons can cause them to scatter, and thus changing their direction of propagation by a variable angle. With a photodetector sensor, it is then possible to collect these photons and hence induce electric pulse. The intensity of this pulse will then be used to infer the size of said particle and be binned with other pulses in a size distribution histogram. This pulse intensity to size conversion is obviously variable between instruments because it depends on the light source used, instrument design/geometry and electronics used. Many different devices can be built using this principle where the light source used is usually the defining piece. For example, an incandescent light might be able to infer particle size down to the order of magnitude of $1\mu\text{m}$ while a laser can easily reach a resolution of $0.1\mu\text{m}$.

Electrical mobility measurements Electrical mobility of a charged particle in an electric field can also be correlated with the actual size of that particle. The way this is accomplished is usually by introducing electric fields that separate different size charged particles and therefore allows a size distribution to be obtained. Generally speaking there are three types of instruments that use the electrical mobility separation principles: electrical aerosol analyzers (EAAs), differential mobility analyzers (DMAs) and aerosol particle mass analyzers (APMs).

An EAA uses a mobility classifier to infer particle size. The first step however is forcing the sample to go through an aerosol charger which forces an unipolar charge distribution. Then when these particles go into the mobility classifier they will precipitate according to how high their electrical mobility due to an imposing electric field. So, for every value of electric field imposed, there will be a different electrical mobility cut-off. Thus, by

varying the voltage applied we can have more or less particles precipitating. Using an electrometer it is then possible to plot the signal induced as a function of the electric field. When properly calibrated it is then achievable to obtain a size distribution for the aerosol. The EAA instruments are now somewhat outdated and have been progressively replaced by DMA based instruments [150].

DMA techniques distinguish themselves from EAA by moving on to a differential electrical mobility analyzer rather than an integral one. The DMAs are capable of achieving better resolutions than their integral counterparts. One of the upgrades in the DMA based instruments design is usually being coupled with a bipolar charger. However, in older designs the electrometer is kept from the EAAs which limits the resolution. This stems from the fact that the amplifiers needed to process the electrometer output typically have a bad signal-to-noise ratio. This was solved by introducing a CPC in commercial mobility particle sizers (DMPSs) which are derivative of DMAs. Basically they are constituted by bipolar chargers, a DMA and a CPC. Even though the core parts of the design are different, the principle of operation is similar to EAA instruments where an electric signal is induced in the detector as a function of a varying electric field.

Taking advantage of the scientific breakthroughs regarding scanning electric fields, a new iteration of DMPS have become commercially available: scanning mobility analyzers (SMPS). These implement a scanning electric field and deprecate discrete electric fields which allows for faster on the spot analysis.

All of these differential techniques are widely used and have many applications. With a lot of spin-off designs resulting from the DMA basis, these instruments are very popular within the aerosol scientific community. Being capable of high resolution measurements, typically all the way to ~ 20 nm, and with great size classification, these instruments are very suitable for microscopic aerosols analysis. Furthermore, recently, an effort has been put in order to take this technology all the way to the nanoparticle scale, due to their growing interest.

Besides craving for better size resolutions there have been several applications that require better time resolutions. As an answer to this problem several instruments derivative of DMA technique have been produced in a category called fast mobility particle sizers. These usually take advantage of a design using multiple parallel DMAs that are able to lower the time frame needed for a measurement. Car industries have taken advantage of these kind of devices in the form of engine exhaust particle sizer (EEPS) for example.

The last technique that deserves to be mentioned based on electrical mobility is APM analyzers. These instruments are mass focused rather than size focused. This technology uses two rotating DMA cylinders to impose a centrifugal force on the particles on top of the electrostatic force. With the correct balance between both forces, only particles with a specific charge to mass ratio will go through the APM, and therefore we are able to select particles based on mass. Hence, the mass distribution of the aerosol can be obtained. If an extra DMA is paired with the APM it is then possible to obtain particle density.

Diffusion measurements The third type of size distribution analyzers are techniques based on particle diffusion. In this category, diffusion batteries are the standout application of this principle. The basic idea is that different size particles will have different rates of diffusion through solid surfaces. Hence, in a diffusion battery we have series of capilar-like structures separated by open space where we put particle counters like CPCs. This way, according to their size, particles will reach a different stage in the battery. As we gather the counts at each stage we can bin them into an histogram of the aerosol size distribution.

Inertia measurements The last group of instruments for size distribution, as mentioned above, are techniques based on inertia. In this group, there are two major categories which are particle relaxation size analysers and impactors. The latter is usually implemented alongside optical detectors. Perhaps the most famous instruments in this category are aerodynamic particle sizers (APS). These instruments accelerate the aerosol sample within a nozzle, with the help of a pump. Due to inertia, bigger particles will have lower velocities and smaller particles, and will reach higher velocities. Using optical detection, normally laser based, it is then possible to measure the difference between the initial velocity and the velocity at the nozzle's exit. With this information we can infer the aerodynamic size distribution of our sample. This technique usually works with particles from the sub-micron range to up to dozens of microns.

Some of the most popular aerosol instruments are impactors. There are many configurations and geometries for the impactor instruments. However they all have in common the basic principle of separating particles by their aerodynamic size. Generally speaking, these instruments have a variable number of stages with impact substrates and accelerate the aerosol onto the impaction stages. In a cascade impactor, for example, the acceleration of the aerosol is made by a series of progressively smaller nozzles on both sides of the impaction stages. Each stage will then have a cut-off size and will collect particles above that size threshold. After a user defined sample time, it is then possible to analyze the particles at each stage to determine the amount of particles in each size mode. Adding that information to the flow rate and acquisition time it is then possible to infer the size distribution of the aerosol.

4.2.3.2 Integral properties measurement

This section refers to techniques that fit into the third row category of Table 4.1. As it was the case in the last section, instruments from this category that do not fit into the real time measurements can be paired with techniques like SEM and TEM. The reason for this being that many aerosol techniques end up with deposited substrates that can be later analyzed for different properties. In integral instruments the whole sample is being studied for the determination of specific properties. This properties might be number concentration, mass concentration, optical properties, etc.

Optical number concentration measurements One of the most famous instruments is the condensation nucleus counter (CNC)[151] also known as condensation particle counter (CPC). It is typically operated to measure particles from a few nanometers to the micrometer range. Its operation is based on the passage of the aerosol sample through a supersaturated vapor which promotes condensation onto the passing particles. The process is extended in a way that these clusters grow to a point that is possible to detect using optical apparatus. The older designs were based in the Aitken's particle counter, as described above, which used a magnifying glass to count particles one by one with the human eye. Nowadays, most of these devices include a light scattering source/detector combination to count the particles. With these counts it is then possible to obtain the number concentration of the aerosol.

CPCs can be operated in a single particle counting mode or photometric mode which uses the information of light scattering on multiple particles at the same time to infer number concentration. The first one can usually measure within the range of 10^{-2} cm^{-3} to 10^7 cm^{-3} while the latter can go up to 10^8 cm^{-3} .

Mass concentration measurements Mass concentration is another desired measurement within integral properties of aerosols. In this category the standout techniques are the quartz-crystal microbalance (QCM) and tapered-element oscillating microbalance (TEOM). Both these methods use oscillating surface to infer mass concentration of an aerosol.

In a QCM instrument, particles deposit onto an oscillating quartz crystal surface. This deposition induces a change in the oscillating frequency which can be measured and correlated to the mass deposited. Typically, this deposition is enabled either through inertial impaction or electrostatic precipitation, which is achieved by charging the aerosol particles with the opposite charge of the surface. QCM devices usually can detect changes of $\sim 1 \text{ Hz}$ when vibrating at $\sim 10 \text{ MHz}$, which corresponds to a sensitivity of about 10^9 Hz/g .

In TEOM techniques the crystal is substituted for a tapered element (usually consisting of tube with filter on its extremity). This hollow object is then forcefully oscillated by the means of electronic actuators. This oscillation is optically measured usually by a light emitter and a detector. The mass collected is inferred from the difference in oscillating frequency of the tapered element system. Typical resolution for this device is around g/m^3 range.

Optical properties measurements Optical properties are often of interest as standalone characteristics of an aerosol. Techniques that focus on obtaining the integral properties of a whole aerosol can provide insight and help its characterization. There are several instruments that aim to measure the optical properties of an atmospheric sample, from which light scattering photometers and nephelometers are among the most notorious.

They are used to access properties like atmospheric visibility and visual range that can also be converted into mass concentration under the right circumstances.

Photometers usually provide an output of mass concentration within an atmospheric sample but require very meticulous calibration since what is really being measured is the intensity of light scattering at defined angles from a focused beam light transversing a sample.

Integral nephelometers on the other hand, measure scattering light with a very wide angle array of photoreceptors. Their focus is to measure aerosol light visibility and visual range. However, more recently, they have seen more application in atmospheric mass concentration experiments in urban and rural areas, even with the extensive calibration needed.

4.2.3.3 Chemical composition measurement

Traditionally chemical composition analysis is very much oriented to being a complementary technique for other aerosol instruments, which are deposited onto a substrate. However, new instruments that are able to do real time reading of an aerosol composition have begun to appear more recently. These instruments have particular interest in volatile environments where the elemental and molecular species within an aerosol can change in a matter of minutes/hours.

Several instruments have been developed in the last decades to meet the requirements of atmospheric composition assessment within a time frame of minutes to one hour. All these instruments come with their advantages and drawbacks and usually specialize on measuring specific groups of species. The list of techniques that fits into this section is very broad since so many chemical composition analysis instruments exist. However, the number of instruments capable of measurements of suspended matter in its natural state (or closer to their natural state) narrows considerably the choices.

Some instruments use techniques like particle into liquid samplers (PILS) to do ionic analysis of an aerosol. Others collect particles, process them and apply spectroscopic techniques. Many also try to focus on organic content, more specifically, organic carbon by the means of, for example, thermal pyrolysis. Keep in mind that however these applications are referred as real time measurements, they actually rely on averaging processes across the sampling time used.

Perhaps the most notorious chemical composition analysis instrument for aerosol measurements is the aerosol mass spectrometers (AMS). There are many iterations of these devices from the quadrupole aerosol mass spectrometer (Q-AMS) to the time of flight mass spectrometers (ToF-AMS), with the compact and high resolution versions (C-ToF-AMS and HR-ToF-AMS). Generally speaking, these systems focus on having an energetic process to vaporize and ionize the samples, whether it is through a laser beam or another energetic source. In more advanced devices, both vaporization and ionization byproducts can be separated providing not only an assessment of chemical composition

but also size distribution. Meticulous calibration and quantification are then needed to infer chemical distribution from the mass spectra obtained. Nevertheless, these systems are the closest to real time chemical composition measurements of aerosol samples.

Other spectroscopic techniques have also been widely applied to aerosol science but mostly as post analysis of deposited surfaces. Here X-ray spectroscopy, Raman spectroscopy, ion coupled plasma mass spectroscopy (ICP-MS)[152], amongst others, can have their applications.

4.2.3.4 Filters

Lastly, as a transversal part to many of these measurement types let's take a look at aerosol filters. Filtration is the process of separating particles from an aerosol gaseous system via a porous solid medium. Therefore, measurements performed with filters classify as time integrated and rely on other measuring instruments to resolve the aerosol properties. Air filtration has had many applications not only in air quality assessment studies but also as protection equipment. This has been prominent for several years, in more hazardous workplaces where workers can be subject to the inhalation of harmful suspended particles. Both personal protective filtered equipment like masks and large-scale filtered industrial ventilation systems can be found in this kind of working environments. From clean rooms for nanotechnologies laboratories, to large scale electronics factories, to the pharmaceutical industry, filtered air can be a priority both for good product manufacturing and human protection. Nowadays, air filtration is also widely used in more personal spaces like cars and homes, in order to ensure better air quality and thus contribute to a healthier lifestyle. Filtered masks are today part of the common knowledge and part of everyone's current quotidian lives, as they present the best personal protection against airborne virus.

Air filtration can be subdivided into two types: surface filtration and depth filtration. Surface filtration consists on particle retention on a permeable surface, where overtime the accumulation of particles grows into a cake like structure, which increases the resistance to resuspension. In depth filtration particles are deposited both on the surface and deeper into the filter material as they transverse it. The most common type of depth filters are fiber filters. In these filters a three-dimensional network of filaments constructs a complex and random fibrous grid. As these fibers possess high porosity (typically from 70 to 99 %) they allow the gas to flow all across these structures and particles are captured at different depths by the fibers. Moreover, every particle crossing the filter medium is unlikely to come in contact with more than one fiber due to their diameter being very small relatively to the distance between fibers.

Even though fiber filters are the most used for aerosol sampling application, there are other noteworthy types of particulate filters such as granular filters, fabric filters and membrane filters. The decision between the usage of any of these filters is often intrinsically correlated with application. Granular filters consists on a granular bed substrate

that is able to retain particulate matter and are widely used in the water and sewage industries in order to clean *dirty air*. Fabric filters are made of textile fabrics, which are specifically manufactured for the purpose of aerosol personal protection. These are generally very compact filters that may possess more than one layer of different fabrics for extra protection, even though they are meant to work as surface filters. Another example of surface filters are the membrane filters that consist of perforated material or highly compacted fibrous materials and therefore possess very low porosity.

Fibrous filters are widely used for aerosol sampling and analysis due to their high separation efficiencies of particulate matter combined with a low pressure drop. The ability to use a three dimensional mesh of fibers coupled with the high particle separation provides a low resuspension rate and reduces the probability of particle agglomeration on the filter. This is crucial to minimize the loss of aerosol information. Also, coating and substrate processing can give these filters a very decent temperature resistance, or for example charge the fibers in order to take advantage of electrostatic interactions. Moreover, most fibrous filters have a matrix constitution that is easily removed as background for most of size and composition analysis techniques, not interfering with the measurement of the deposited particles.

PROTOTYPE DESIGN AND DEVELOPMENT

In this work, a series of prototype devices and parts were developed with the final objective of measuring the aerosol composition inside the Autoeuropa, Lda. factory. As it has been stated in chapter 4 this device must follow a list of rules and requirements (see section 4.1) in order to meet the expectations. It was also already presented a list of several techniques and instruments that are used in aerosol science in section 4.2.3. With the mindset that this device must be versatile, low cost, portable instrument we chose to make a solution based on filters deposition [153, 154]. Another low-cost alternative would be the implementation of low-cost optical sensors as done in [155, 156] to provide a particle size distribution analysis. Our general proposal for the design is schematically represented in Figure 5.1.

As it can be observed in Figure 5.1, our core design will be based on a wind tunnel structure, inspired on multiple fluid dynamics experiments which already implement and study this kind of structures. A wind tunnel is an aerodynamic structure capable of guiding a controlled flux of air from one of its ends to the other. *Wind* or air flux can be achieved by creating a differential in a thermodynamic property of the fluid. In most cases, it is done by inducing a pressure differential in order for the air to flow. This can be achieved by the means of a wide array of mechanical devices, all the way from vacuum pumps to simple DC fans.

As the respirable air contains a lot of suspended particles these can be filtered out onto a solid substrate. By keeping the air flowing through the structure we enable deposition, mainly by impaction, onto a substrate surface in the form of an aerosol filter. Once deposited these filters can be used for analysis either in online or offline fashion. This allows for the possibility of studying several of the properties mentioned in 4.2.1 including size distribution and chemical composition.

As our main analysis tool we have chosen EDXRF spectrometry which allows us to

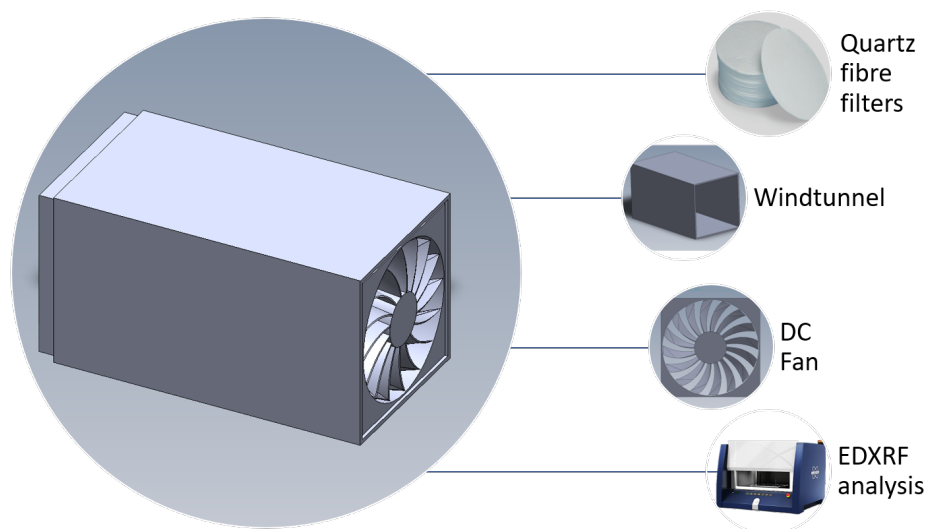


Figure 5.1: Schematic representation of the design approach.

assess the chemical composition of the aerosol. This technique is very versatile and allows us to measure both in real time or integrated time. Meaning that the filters can be either analyzed after sampling in the lab by a benchtop spectrometer or a setup can be developed for an *in loco* analysis. For this purpose, it is only necessary to add to the prototype a small X-ray tube, an X-ray detector and the corresponding acquisition and power electronic components. Then, by opening two windows in the wind tunnel that make a 90° angle between them and the sample it is possible to induce and measure X-ray fluorescence on the deposited aerosol particles.

5.1 Development of the first prototype

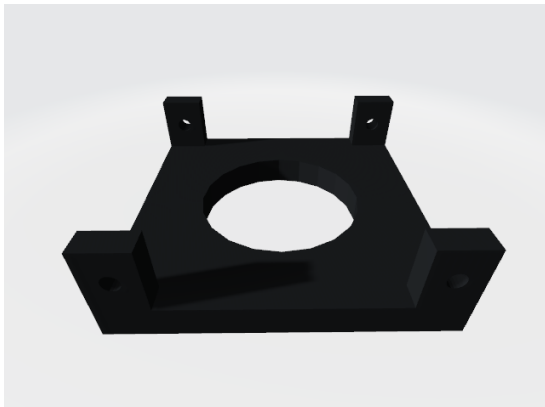
The objective for this stage of the project was to design an instrument that was able to fulfill the basic concepts of the wind tunnel deposition analysis approach. The first decision was the shape, dimensions and materials of the tunnel itself. For this, we had to consider compatibility with other parts that we would later add to the design. We went with a hollow tube with a squared cross-section capable of fitting in a 9.2 cm DC fan with a square frame. We opted by an alloyed steel material for the wind tunnel, due to its availability, price and robustness to both higher temperature and mechanical deformation. This steel tube was then cut to have 18 cm of length in order to let the accelerated air flow through the tube before reaching the filter on the other end.

As it has been stated the DC fan choice was closely related to the shape and size of the wind tunnel. For this part, we looked at several options and ended up choosing 12 V Sunon 9.2 cm DC fan. This fan has a power consumption of 1.68 W and has 3000 rpm.

It is capable of providing 0.86 CFM which corresponds to $1.46 \text{ m}^3/\text{min}$. For its fixation onto the tube we repurposed L shaped metallic plates by drilling $\varnothing 5$ holes. By drilling the same type of holes in the tube was then possible to hold the fan steadily with 8 M5 screws. This design allowed for the DC fan to be easily substituted for another of the same size. This could be valuable if we needed a DC fan with a bigger flux for example. In the end, it was very advantageous as the DC fan sustained damage when the prototype was being transported and ended up needing to be substituted.

As for the filters we went with the circular shaped Pall Tissuquartz™ filters, 2500 QAT-UP. These filters have 9 cm of diameter and were specifically design for air monitoring applications. We ended up choosing these filters over other options not only but specially for their capability to work in high temperature environments. In a typical day of operation it is expected for the air temperature to be raised, since our device will be positioned near welding stations, which heat metals in order to weld them. Not only that but it is also possible for little embers, sparks and small flaming particles to come into contact with the filter and hence it might burn filters with lower resistances to temperature. These filters are also very thin with only 0.4 mm and thus structural resistance might not be overwhelming. Also these filters have a typical air flow rate at 0.7 bar of $73 \text{ Lmin}^{-1}\text{cm}^{-2}$.

The material used in these filters is called quartz fiber and is made from high purity natural quartz crystals. For producing this kind of material it is necessary to heat these crystals with a oxyhydrogen flame in order to soften them up. When they achieve a certain temperature and become sufficiently ductile the quartz rods can then be molded into filaments. These filaments will then create a mesh capable of capturing airborne particles with diameter superior to the mesh dimensions. Many other aerosol experiments have used similar filters [157]. There is also other derivative similar materials that are used for air filtering such as the glass fiber filters we will use on the second prototype. The main difference being that quartz fiber uses only high purity quartz crystals whereas other materials use impure quartz.



(a) CAD drawing of the part to be 3D printed.



(b) CAD drawing of the acrylic part.

Figure 5.2: CAD drawings of the sample holder parts.

If on one end of the wind tunnel we have put a DC fan for air flow, on the other end it was necessary to design a custom sample holder. For this purpose, it was required that these designed parts were able to hold in place the quartz filters while having an opening in the middle that enabled air flow through the filter and thus aerosol deposition. To achieve this result we 3D printed the part constructed on Figure 5.2a and drilled an acrylic board to achieve the part presented in Figure 5.2b. The 3D printed part was to be fixated on the inside of the wind tunnel with M5 screws and bolts. The acrylic part was then positioned on the outside in such a way that the filter would be held in place by being trapped between the two parts. This acrylic part could be removed by unscrewing the M5 screws holding the two parts together and thus it allowed us to manually change filters after an acquisition.

Lastly we included a simple platform where we made the power management of the prototype that is shown in Fig 5.3. This was also an acrylic board that fixated on top of the wind tunnel. It possesses a 3 pin mechanical switch and 2 pin DC jack connector embedded into its frame. By connecting a 12V transformer into DC connector this electric power was then available on the switch. This switch would have its output connector soldered with positive wire of the DC fan. All three grounds would be connected and thus as expected when we turn on the switch the fan would activate.

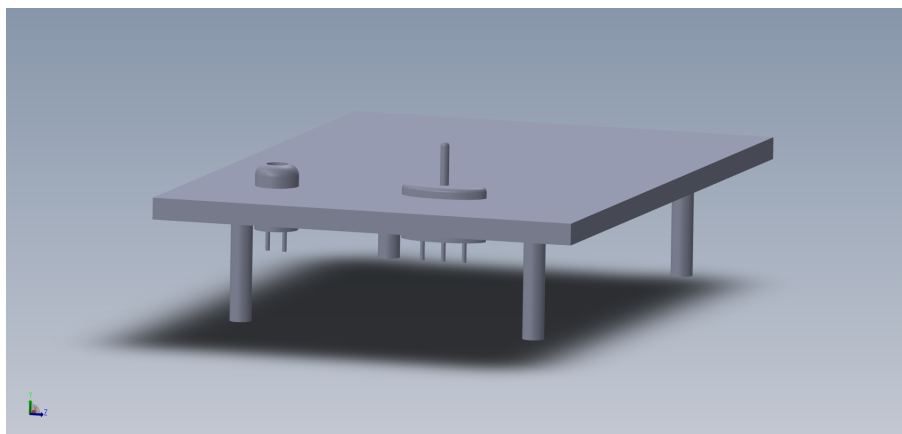


Figure 5.3: Acrylic platform for connections and power management.

The final design is shown in Figure 5.4. In this figure we can see the 4 main views of the design. As it was discussed in this section, part by part, it is straightforward that this is a very inexpensive build. The quartz fiber filters being the most expensive part of this device with a price point under 100 € for a 25 unit package. All the parts were built/assembled in this work. This device met all the requirements of an early prototype being capable of capturing a lot of suspended particles for later analysis on the lab. The results and discussion of these acquisitions will be presented in the next chapter.

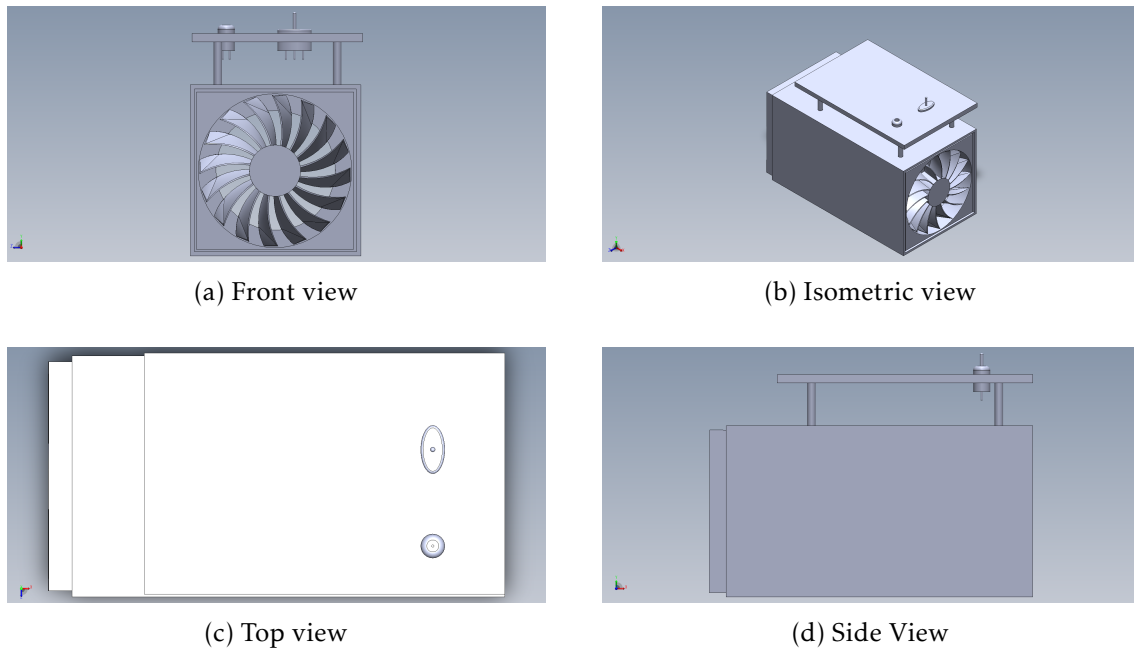


Figure 5.4: Final design of the first prototype from multiple views.

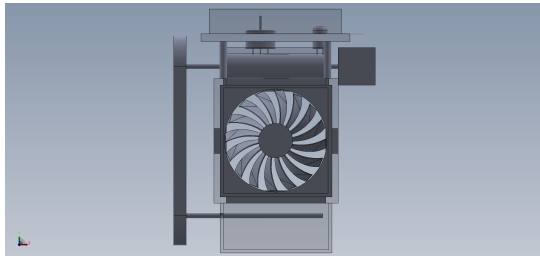
5.2 Development of the second prototype

The first prototype was more of proof of concept for actually showing that with a simple device we were successful in doing integral time aerosol acquisitions. But from its simplicity it suffered for the lack of features such as automation and remote control. This was the focus of the second device developed in this work. The objective is for the device to be able to do air quality measurements as independently and automatically as possible.

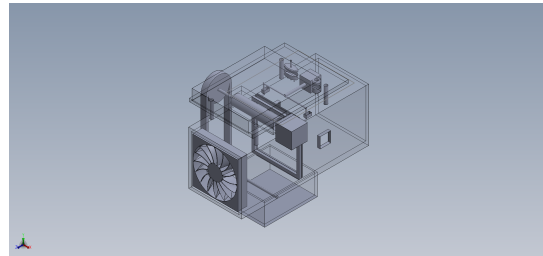
With this mindset the first concept for the second prototype was designed in CAD as shown in Figure 5.5. The increased complexity of this design is very obvious so on top of 4 main views we provide a custom view with labels in order to guide this description. Note also, that due to the increasing complexity some parts were made transparent for ease its comprehension. Therefore, keep in mind that some parts are overlapped in some views.

In this concept, we identified that one of the main changes to the device that needed to be done in order to make the step towards automated operation was to change the filters. Although it would not be completely impossible to perform multiple measurements with disposable circular filters it would elevate to much the complexity of the moving parts inside the prototype. Our solution was to find rolled up filters which would be unrolled every time a new acquisition was going to start. This way there is no break of continuity and we end up with a long tape of multiple acquisitions that can be later analyzed in the lab. Also, this would not hinder the possibility of integrating a spectrometer for real time analysis as the filter substrate is still static in each acquisition.

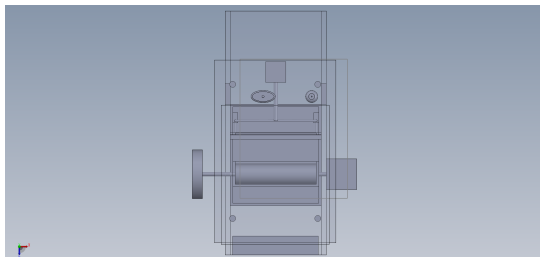
Let ´s now take a look at the label view 5.5e and go through each important part of this concept. 1 and 2 are two motors just represented as two cubic boxes and not the



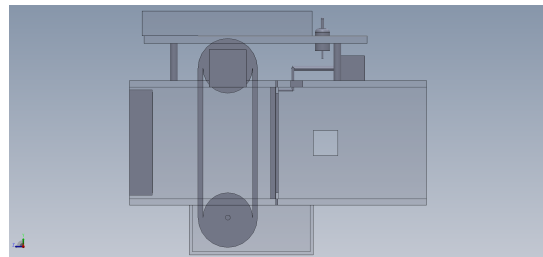
(a) Front view



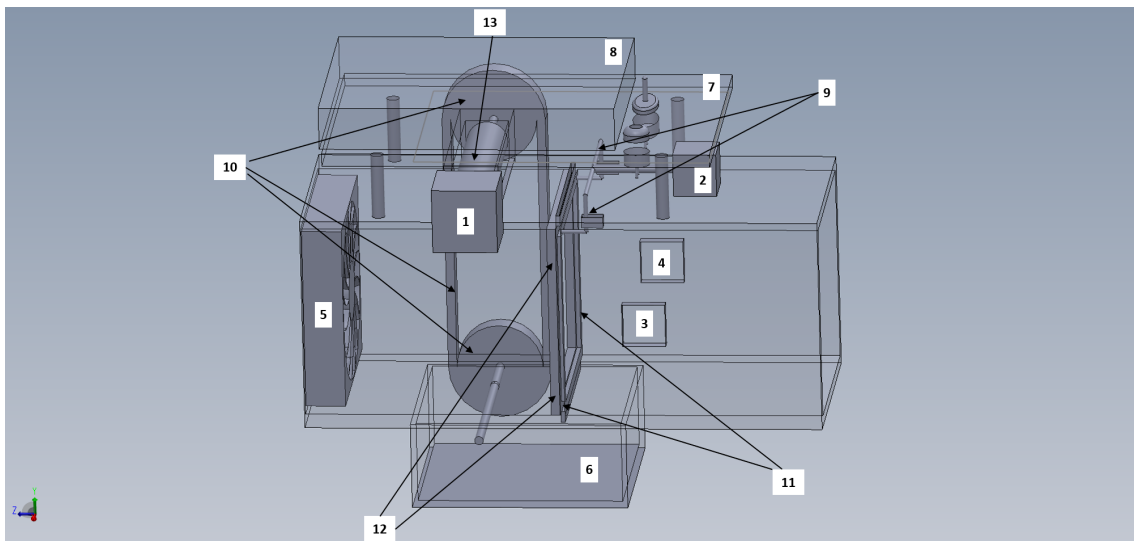
(b) Isometric view



(c) Top view



(d) Side View



(e) View with labels

Figure 5.5: First design of the second prototype from multiple views.

actual shapes. The first actuator **1** was to be the driving force towards unrolling the filters that would be positioned in box with a roller **13**. With the help of the rollers and rubber band represented in **10** and gravity the filter would go through the sample holder into the storing box **6**. The second actuator **2** would act like two state step motor for controlling the sample holder. Basically, with the help of the mechanism **9** when an acquisition started, the moving frame **11** would move next to static frame **12** to hold the filter in place. When the acquisition ended the frame **11** would move away letting the filter lose and allowing it to go into the storing box **6**. **5** and **7** are exactly like in the first prototype de DC fan and the power management and electronics platform respectively. **3** and **4** are open windows on the wind tunnel for the possibility of incorporating an X-ray source and detector on each side of the sample. Lastly, as this is a rather complex prototype an electronics box is marked with **8** for encapsulating all control electronics and processing units.

The design shown in Figure 5.5 is to be consider as a concept only, because when we started looking in what to parts to buy or build for this prototype the design evolved and changed. One of the first things that we explored was how to make custom made controllable sample holder which would hold and release the filters when needed. This is a very important part of device because when we force an air flow within an wind tunnel, this can lead to a very chaotic stream. Thus, it is necessary to hold the filters in place when the DC fan is turned on, in order to prevent damage to the filters and erratic deposition (and possibly resuspension) on the substrate.

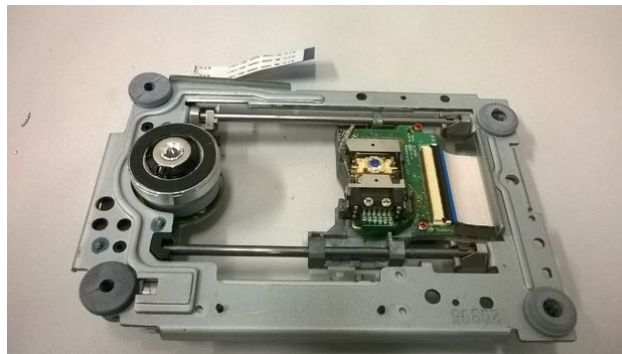


Figure 5.6: DVD optics slide mechanism example.

As we searched for alternatives for this kind of mechanism, we tried to scavenge old electronic parts in the lab. We eventually found something that was able to be adapted to our prototype - a DVD slide mechanism for optically reading the disk. By tearing up a DVD we end up with a generic slide similar to Figure 5.6. The mechanism depicted in this figure is used to move the sliding optic part in the middle very quickly when a DVD is being read. This sliding part includes a laser and photo-detectors which work as an optical micrometer that is able to detect very small changes on a DVD disk track. Moreover, in order to make accurate readings of the spinning DVD, the micrometer needs to have very swift and precise movement. Hence, by using this combination of DC motor

and rails it is possible to control the slide with high precision.

To adapt this kind of mechanism to our endeavors we needed only to remove the optical central part and replace it with an appropriate part. The part used for this purpose was a custom 3D print design shown in Figure 5.7. This part has two holes on each side that fit slides on our DVD mechanism. It also has incorporated the actual sample holder (square with circular hole in the middle) into the same structure. Thus, with a static frame similar to the part presented for the first prototype (5.2b) it is possible to hold the filters steady. The assembling of both parts is shown in Figure 5.8.

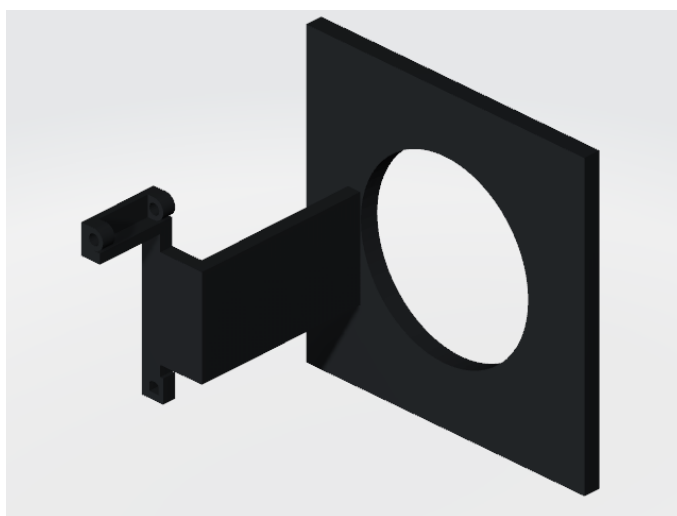


Figure 5.7: CAD drawing of the sliding sample holder part.

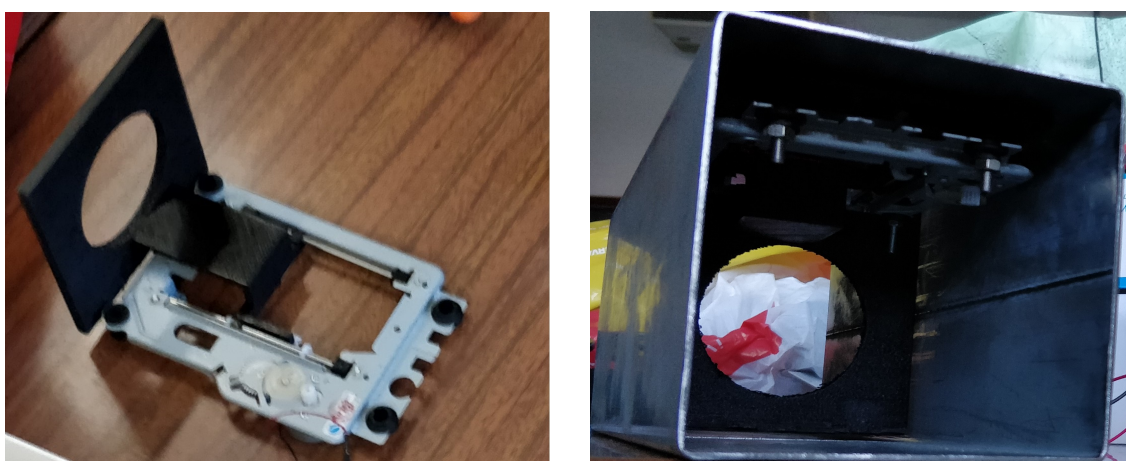


Figure 5.8: Sliding mechanism assemble.

We also had to redesign the filter associated parts. This was mainly due to how big the commercial available rolled up air filters are. We decided to go with Whatman® glass microfiber filters with organic binder, Grade GF 10. These filters have a width of 6 cm but have 42 m of length which even rolled up corresponds to ~ 15 – 18 cm. Therefore, two big cases of around 20 cm of width were needed on top and bottom of the wind tunnel.

These cases were designed in CAD as shown in Figure 5.9 and then were made in acrylic in a specialized manufacturer. These forced us to rearrange certain parts of the design specially the electronics platform that was shifted onto to the side of the wind tunnel. Note also, that we went with glass microfiber filters despite saying in the previous section that quartz fiber is the higher grade for filter materials. This was only due to product availability in the sense that it is harder to find filters in the rolled up format, let alone specifically quartz fiber filters.

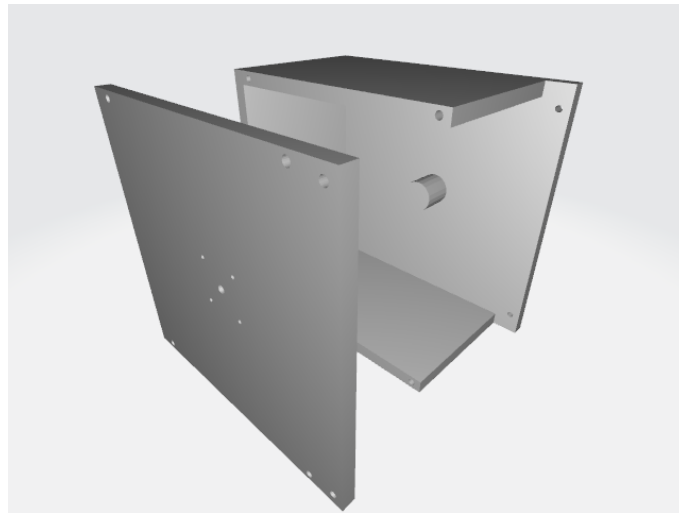


Figure 5.9: CAD drawing of the acrylic boxes to store the filters.

At this point, we also decided to not use the initial concept for the actual mechanism of filter unrolling (5.5e). Instead, we searched for a precise and powerful DC step motor that would fit into the power limitations of the system. The reasoning behind this decision was that if such motor was identified and we found a way to couple it with filter roll, we would be able to push the filters with just the torque of this motor (deprecating any additional mechanisms such as gears or toothed belts). We decided to use the 42BYGHM809 hybrid step motor that works at 2.7 V with a current of 1.7 A. This motor has an holding torque of 48 N.cm which is more than enough for the purpose of unrolling the filters. It also has 4 inputs for control of the stepping done as well as its speed.

After obtaining this motor we then proceeded to design some parts to couple it with the actual filter roll. For that purpose, the parts shown in Figure 5.10 were made in CAD and later 3d printed. The part on the left 5.10a was the first attempt at a coupling mechanism. At this point we still had the concept (5.5) of keeping the roll on the upper side of the wind tunnel unrolling it downwards with both the motor and gravity. So this part would couple with the motor via the hole in the bottom, made to fit tightly with the motor axis.

Eventually, we realized that this mechanism was not as fluid as expected and thus was deprecated. Essentially, the problem was that relying on gravity to guide the filter in a smooth faction through the designated holes in the prototype was not being accomplished

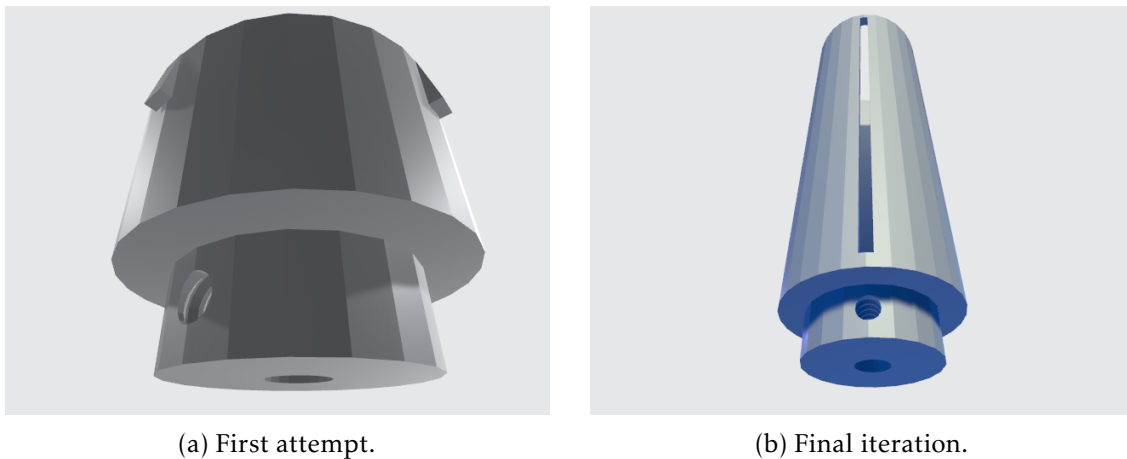


Figure 5.10: CAD drawing of the parts to be 3d printed to couple the motor with the filter roll.

reliably. Hence, we decided to change the approach reversed the filter case to be on the bottom and the case with the motor would be on top of the wind tunnel. With the help of the component illustrated in 5.10b we would couple the axis with the bottom hole of this part. The rest of this part is an hollow cylinder with a narrow entry that we use to grip the extremity of the filter roll. Thus, when properly secured in this part and the motor is activated, it would push the filter upwards and wrap it around this cylinder. The filter case would also have a smooth cylinder on the middle for both support and allowing a smooth rotation. When all of the filter was used or we wanted to analyze some of the acquisitions wrapped around 5.10b, the procedure involves cutting the roll, removing the wrapped filter and fixing the new filter extremity onto the 3d printed coupling part. Overall this filter unrolling mechanism offered much better results and therefore was carried into the final design.

The final design is illustrated in Figure 5.11. The blue hovering part is just a protective case for the electronics that we had on the side of the prototype when we start an on-line sampling process. Moreover, this blue plastic cover and the steel tube have been made transparent to make it possible to see the components inside even though in reality they are obviously opaque. All the parts described are contained in this two pictures, from the DC fan, filter cases, DC motor, electronics, wind tunnel, sample holder mechanism as well as the electronics platform on the side. Those blocks are only representative not actual depiction of the real parts but we have maintained proportions for a easier interpretation. The electronics, connections and power management will be addressed in the following section.

5.3 Electronics

As described above, in the first prototype not much electronics and power management considerations were needed given its simplicity. The circuit can be summarized as shown

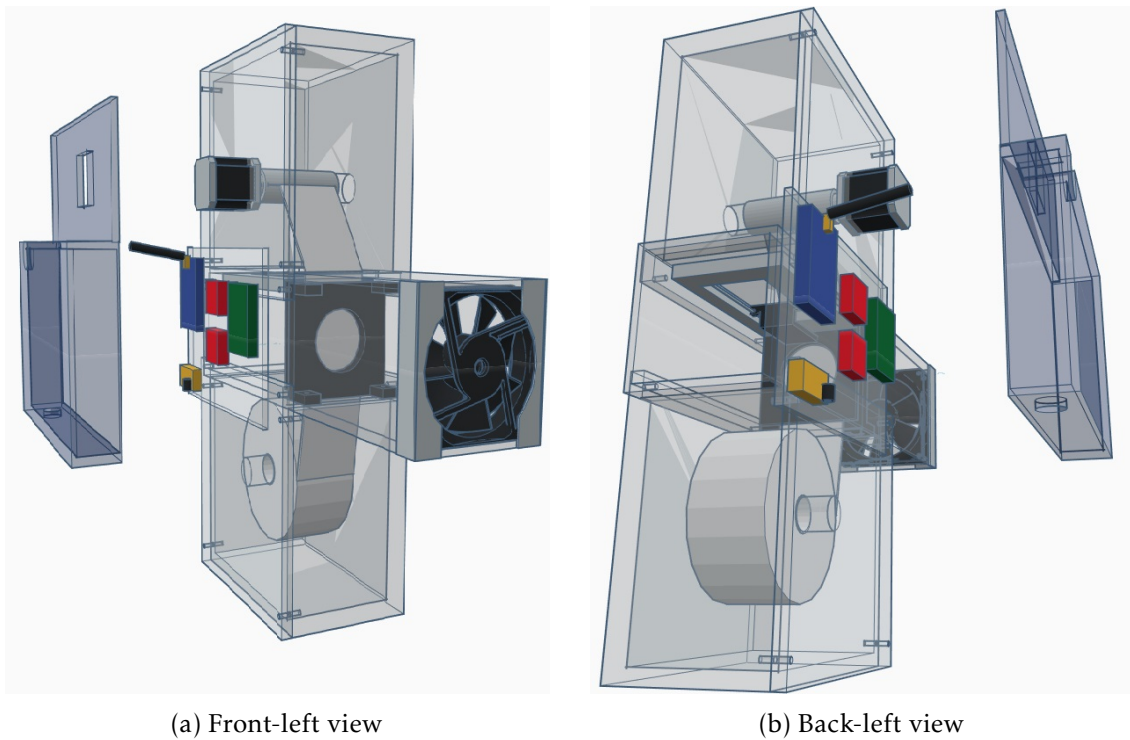


Figure 5.11: Final design of the second prototype from two different views.

in Figure 5.12. The DC supply was provided by a 12 V transformer in interrupted circuit with a manual switch SW1. When toggled to the ON state, the DC current provides the power needed to operate the 12 V DC fan installed. As this was a device with manual acquisitions, there was no needed for programming of any type.

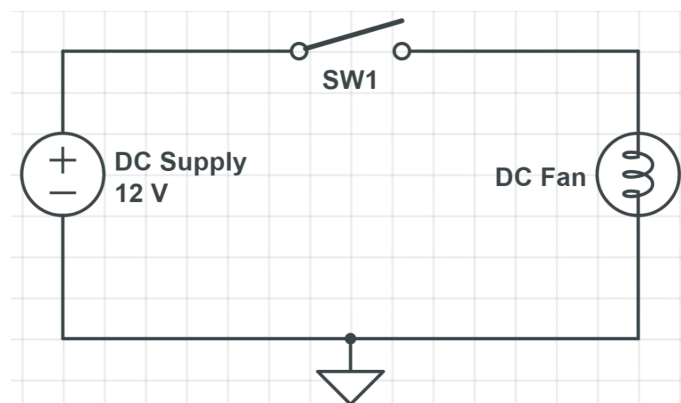


Figure 5.12: Circuit schematic for the first prototype.

In the second prototype some more considerations towards the electronics and programming were needed in order to automate the device. As there were various tasks to be accomplished and coordinated there was a need for central processing units (CPUs) to be in the design. The CPUs used were the ATmega328 included in the widely popular Arduino/Genuino boards. These 8 bits microcontrollers with 16 MHz of clock speed are

cheap and easy to program and work. Furthermore, the actual boards provide a lot of communication, connections and accessibility features. These boards work with a range of supply voltages that is recommended to stay between 7 V to 12 V. They possess 14 digital I/O pins (of which 6 provide PWM output) and 6 analog I/O pins. A USB-A connection is also available for both programming and power supply. Another advantage of using such a popular platform is that there are several of customized enhancement boards that can be connected on top of the main board. For example, in this work we used a commercial GSM/GPRS (Global System for Mobile Communication based on General Packet Radio Service) module in order to get an internet connection in our device. The only drawback that we faced from the Arduino boards was the 2 Mb dynamic memory limit that forced us to optimize the code several times in order to be able to fit all of programmed functions and features. This was the main reason we needed two microcontroller boards, so we could pack all the essential features onto the device.

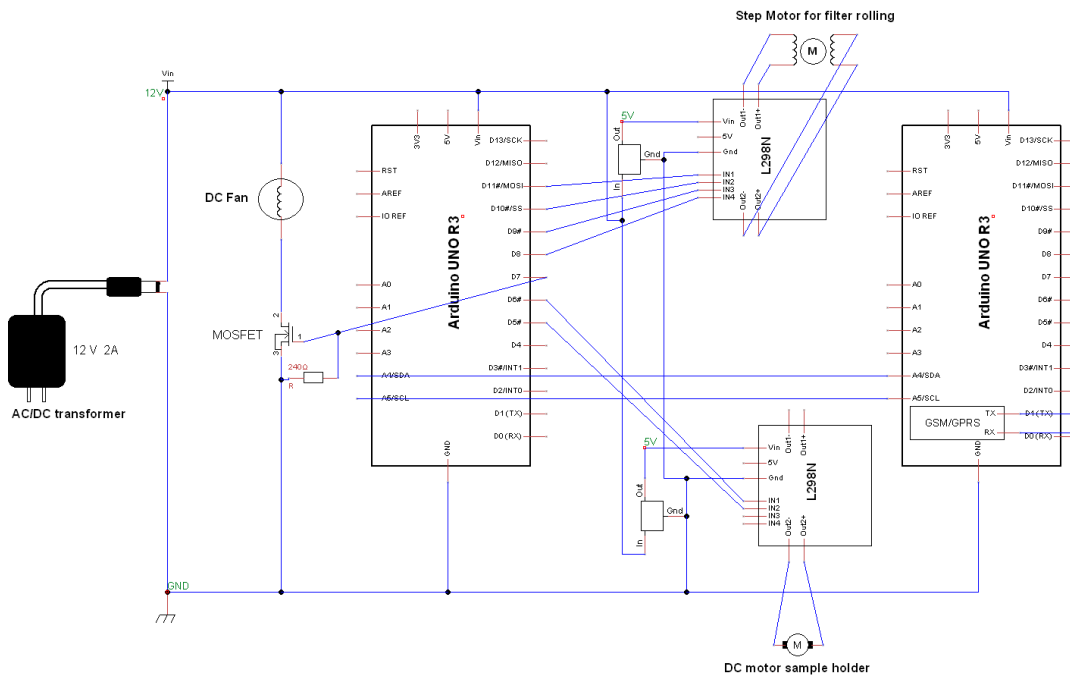


Figure 5.13: Circuit schematic for the second prototype.

The circuit schematic of all the electronic connections for the second prototype is shown in Figure 5.13. Keep in mind that this is circuit representation and thus the physical positions of each component might not be the same as in the figure but the connections and subsequent voltage and current values are. The Arduino on the left of this figure will be addressed as the slave and the one the right as the master. As we can observe the slave will be tasked with controlling all the actuators: the DC Fan, the DC motor of the sample holder and the step motor for filter rolling. The master will be

tasked with the communications aspect having GSM/GPRS shield attached to it. These two Arduinos will also be wired via an I²C (Inter-Integrated Circuit) connection on their analog I/O pins SDA and SCL in order to coordinate parallel and sequential tasks.

Some more components of this design include a MOSFET, 1 resistance of 240 Ω between terminals 1 and 3 of the MOSFET, 2 voltage regulators and 2 motor drivers. We used the MOSFET irf520 which is a n-channel enhancement transistor capable of operating up to 100V or 10A and with a dissipation power of 60W. The voltage regulators were 17805cv which are able to reliably provide a steady 5V output up to a maximum 1.5A current. The motor drivers we chose were the L298N dual full-bridge drivers.

From the Figure (5.13), in an hardware/software point of view, we could define 6 main different systems that allow our device perform as expected:

1. Power source and management;
2. DC fan system;
3. Step motor control;
4. DC motor control;
5. I2C communication;
6. Server communication via GSM/GPRS.

Setting up all these different systems and making them all connect together properly was a very lengthy and complex task which lead to multiple iterations of most of them. For that reason, the full description of the electronics and programming choices is also very technical and lengthy and, as such, it is provided in Appendix B.

PROTOTYPE INSTALLATION AND MEASUREMENTS

In this chapter, we present the instrumentation used for the quantification of the aerosol properties and discuss the results of the analysis of the deposited quartz fiber filters. The sampling steps were performed on the assembly and repair line of the factory. In Figure 6.1 is shown the specific welding station case study. This station is called Framing-2A and serves the purpose of repairing small defects on chassis recently produced via manual welding. On the upper right of the picture we can see our first prototype during one of the sampling times.

In order to better grasp how the complex aerosol mixture inside these manual workstations changes, we have performed various depositions with different sampling times.



Figure 6.1: Installation of the first prototype on a case study welding station (top right).

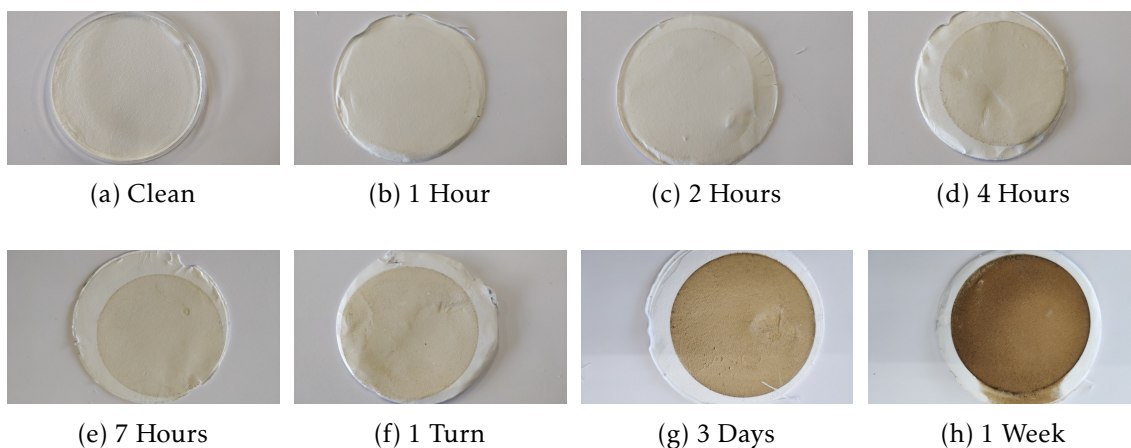


Figure 6.2: Deposited quartz fiber filters.

The smallest sampling time that we were able to achieve and still be able to detect the particle deposited was about 15 min. For the following discussion we have selected a range of filters, that are shown in Figure 6.2, from one hour all the way to one week of deposition time and also included a clean filter for reference. Keep in mind that the length of the sampling procedures shown here is measured from start to finish without taking in account eventual down times in the assembly line. Later in this chapter, for the purpose of analysis, we will use effective sampling times that subtract the known plant wide breaks for meals or just rest. Nevertheless, even these effective description might not be 100% accurate because we have no way of accounting for unscheduled breaks or even small deceleration periods in the assembly line that lead to more down times. These down times can have further impact than just not adding new particles to filter. In fact, there is a possibility for resuspension to become prevalent over deposition on our filters resulting in loss of information and thus more uncertainty in our results. Obviously, down time in a sample with a small deposition time will cause bigger uncertainties on the results because the same down time represents a bigger portion of the whole sampling time.

6.1 Experimental setups

6.1.1 Size distribution analysis

Size distribution analysis was performed using two different methods: optical inspection via a microscope camera and SEM with Energy Dispersive Spectroscopy (EDS) technology. For the purpose of doing the optical inspection of the deposited filters we used the Leica M205C microscope with a lc80 hd camera. This microscope provides a good size resolution, with up to 100x magnification and 12.5:1 zoom and it is able to reach an image size of 0.82×0.61 mm with around $6 \text{ MP} \cdot \text{mm}^{-2}$. Therefore, using this image size, we were able to get images with a pixel size of around $0.4 \times 0.4 \mu\text{m}^2$. With this resolution, we were

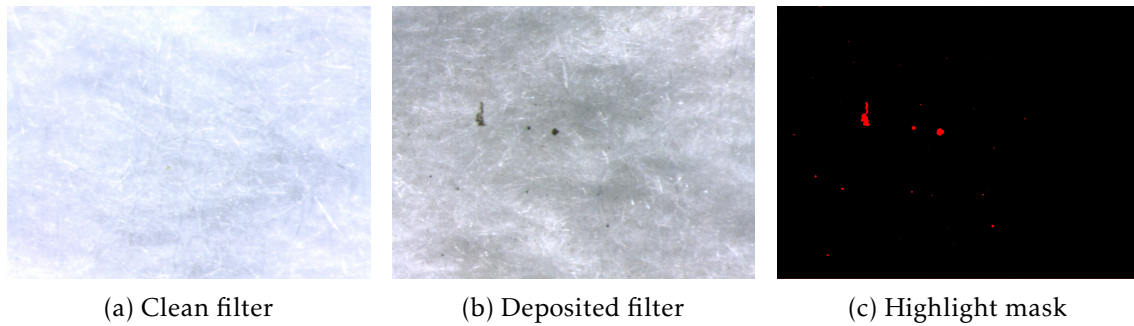


Figure 6.3: Comparison between clean, deposited and the processed particle identification image mask (images size: 0.82x0.61 mm).

able to get some information on the $PM_{2.5}$ fraction and a lot of information on the PM_{10} particles. Moreover, we also were able to observe and measure big particle agglomerates over the $10\ \mu\text{m}$ range using the Leica microscope proprietary software - LAS.

As a complimentary tool, we also developed an image recognition program in Python to detect particles on the obtained images. The full script can be seen in C.3. The motivation to develop this tool was to have some counting and measuring consistency across the >100 images we obtained from the microscope. As we are working with images that are basically highly zoomed pictures of small areas of the deposited filters, our assumptions for what qualifies as a particle are based on how it differentiates from the background mesh. In Figure 6.3, we can see a clean filter, a deposited filter and a processed image mask with the identified particles highlighted. As we expected, the clean filter is a very white mesh while the mesh itself gets darker after deposition due to particles smaller than our detection limit. Nevertheless, there are bigger particles deposited onto the filter within our detection range that we can isolate and measure.

The Python program analysis is based on two kinds of digital filters: a straightforward pixel intensity low-pass filter, and filter for edge detection based on Fourier transforms. The first filter starts by going over all the pixels and calculating the intensity from 0 (black) to 1 (white). It proceeds to fit a Gaussian distribution for these intensities and obtain the mean μ (*mean* in the code) and standard deviation σ (*std* in the code). For the final analysis there are two user input parameters k_1 (*m_t* in the code) and k_2 (*m_t3* in the code) for pixel selection that work as thresholds in the form of $\mu - k_n \sigma$. The lower threshold (k_1) is going to be compared with the result from the Fourier analysis and for this reason lets through a lot of points that will not result in detection. The high threshold (k_2) only accepts those that are various standard deviations away from the mean and represents points that we are certain must be particle constituents. After creating a mask, we then use a clustering method to obtain the amount of clusters and their sizes in pixels. We convert the number of pixels contained in the cluster into the equivalent diameter of the circumference with the same area.

Fourier Transforms are a commonly used tool in image processing for edge detection. For images, 2D Discrete Fourier Transform (DFT) is used to find the frequency domain. A

fast algorithm called Fast Fourier Transform (FFT) is used for calculation of DFT. Hence, by calculating the Fourier Transform for the two directions of the image we are then able to obtain the frequency of intensity change. When scanning the image with the FFT along a direction a high frequency signal usually equates to an edge. While we are in the frequency domain, we are then able to perform some filtering based on the frequency magnitude spectrum. What image processing algorithms usually do is use a shifted FFT small window (the size of this window is a user input - k_3 or *window* in the code) to eliminate low frequencies and obtain only the detected edges. In the end, an Inverse Fourier Transform is applied to the filtered image to reconstruct the image. At this point we apply a user input threshold k_4 (*thresh2* in the code) for selecting only the most important edges. This output is then compared with the image obtained with parameter k_2 to only select edges that correspond to dark pixels, since white filaments from the mesh are also detected. One of our typical outputs can be observed in Figure 6.3c.

To further gather information on size and shape, and make a connection to composition analysis, we also performed a series of measurements with SEM and EDS techniques. For this purpose, we have used a Hitachi TM 3030Plus Tabletop to analyze small samples of our filters. The TM3030Plus has a premium SE detector, which has been incorporated in FE-SEM and VP-SEM, that are well-accepted by users as a high-sensitivity detector. It operates effectively under the low-vacuum environment and allows for quick SE image observation without specimen preparation. This SEM instrument is capable of up to 30000x magnification and works with accelerating voltages of 5 kV to 15 kV. It is also equipped with Energy Dispersive X-ray (EDX) technology that allows for quick composition assessments of the sample's small features. EDX has some similarities with EDXRF in the sense that they rely on similar physical phenomena. However, excitation sources are different and so is its precision. Overall, EDX takes advantage of the beam of electrons from the SEM and gives some insight into the composition of the sample, but for more precise and complete composition quantification EDXRF should be the choice.

6.1.2 Composition analysis

As our main composition analysis tool we have chosen EDXRF spectrometry, which enables the assessment of the elemental concentrations of the deposited aerosol. This technique is very versatile and allows us to measure both in real time or integrated time. Meaning that the filters can be either analyzed after sampling in the lab by a benchtop spectrometer or a setup can be developed for an *in loco* analysis. For the actual results obtained in this work we used the benchtop EDXRF spectrometer M4 Tornado™ Bruker that was previously described in this thesis. However, for the purpose of doing an *in loco* analysis, it is only necessary to add to the prototype a low power X-ray tube, a low-cost solid state X-ray detector and the corresponding acquisition and power electronic components. Then, by opening two windows in the wind tunnel that make a 90° angle between them and the sample it is possible to induce and measure X-ray fluorescence on

the deposited aerosol particles. This however presented some challenges in terms of costs and time. Regardless, the final prototype has already the two holes incorporated for an eventual future implementation.

The combination of commercial X-ray tubes and X-ray detectors are very hard to fit within the budget of 500 €. The reason being that even the smallest and cheapest commercial X-ray instruments will still be well above the budget. Our intended solution was to pair a proportional counter, which is cheaper than the typical X-ray detector, and to develop our own low power X-ray tube using the principle of triboluminescence. This is a very interesting technique which can be applied to generate X-ray photons, as reported by [158, 159, 160], and allows for development of very low-cost X-ray tubes. The principle itself is relatively simple and similar to Van der Graaf generator. Triboluminescence is the phenomenon of creation of photons via mechanical friction between two materials which are far apart in the triboelectric series table. Typically, in a X-ray source using this principle there is band of rubber, which is very negative triboelectrically, that is being forced against against a very positive triboelectrically material like nylon. If this rubber band is rotating at high enough speed inside a vacuum chamber the photons generated can reach the X-ray energy range. Therefore, with the help of a secondary target we can produce a similar output to a classical X-ray source.

For this purpose, we have already tested similar setups in our labs but we never achieved the energy desired for an X-ray source. We have inclusively designed one prototype that we show in Figure 6.4. Nevertheless, we didn't fully pursued this endeavor in

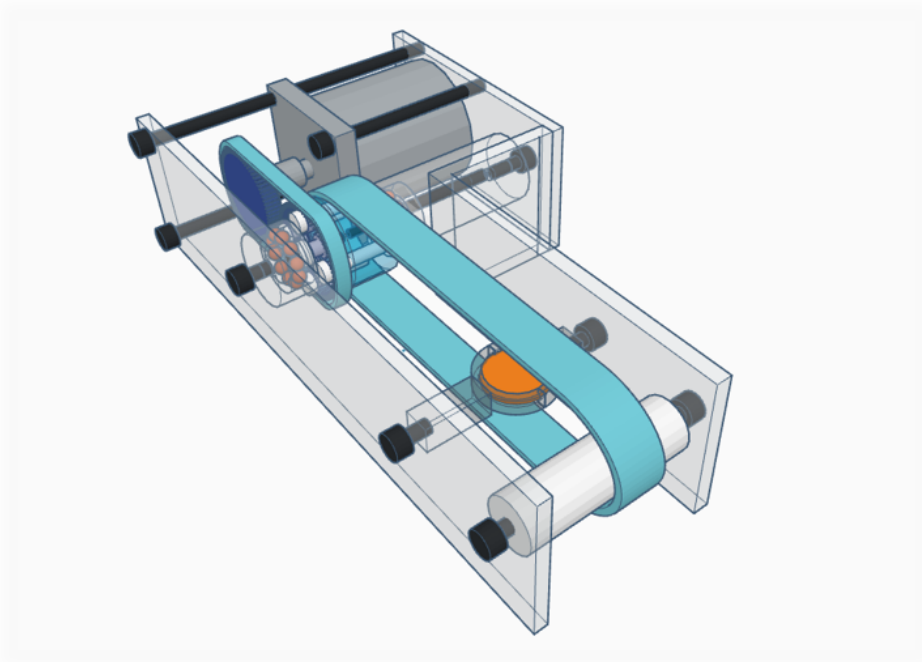


Figure 6.4: Our design of a triboluminescence X-ray source to be encapsulated in an acrylic box in order to conserve the vacuum intended inside.

the end cause it needed more time than the available for the development of this thesis. Moreover, not only the development time would be very long to get it reliably produce the photon beam needed but also it would be a very demanding task to license the whole instrument. X-ray instruments need a special attention when licensing because of their potential to be an hazard to human health, and therefore take a lot of time to ensure that they are safe.

6.2 Results

6.2.1 Size distribution results

Using the Leica microscopic camera we gathered 21 images like Figure 6.3b of each of the 7 filters from Figure 6.2. These images had a size of 0.82x0.61 mm and were arbitrarily chosen from different areas of deposited filters. The objective was to obtain the most accurate representation of the deposited particles size distribution. However, some tendencies are straightforward from the optical inspection as the darker and bigger particles tend to accumulate on the edge of the deposition area. The central areas are usually much more uniform and tend to have smaller particles with a few outliers. In Figure 6.5 we can see a typical image from a central area of the filter and an image from the border.

Applying the Python algorithm described above we were able to process all the 147 images to obtain a size distribution of the particles in the filter. A visual representation of the size distribution obtained can be seen in Figure 6.6. This distribution was obtained by using 1 μm bins and using the corresponding normalized number of particles per mm^2 . This is done by dividing the particle concentrations by $d\log(D_p) = \log(D_{pu}) - \log(D_{pl})$ where D_{pu} and D_{pl} are the upper and lower limits of the corresponding bin.

As it has been evidenced in Figure 6.5, there is a lot of variability across the deposited filters. Even in areas close to each other the number and sizes of particles deposited can

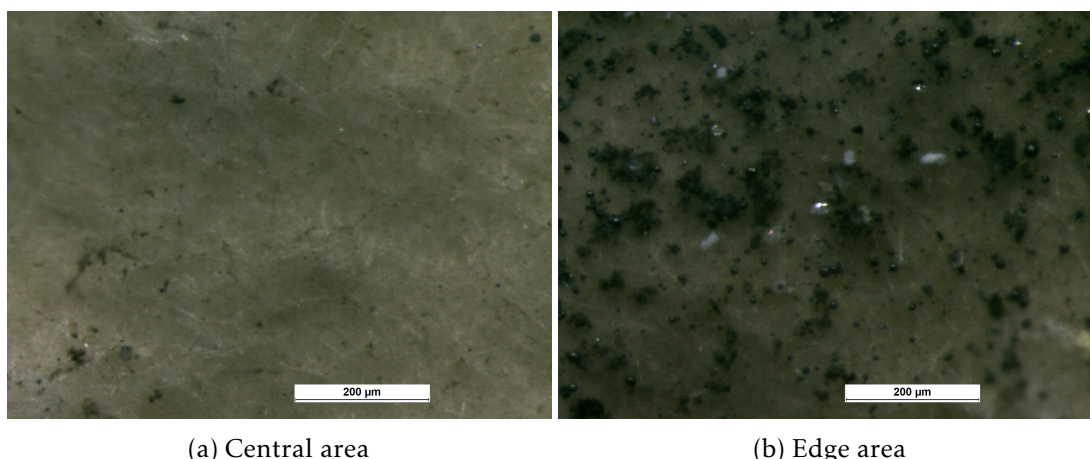


Figure 6.5: Microscopic images obtained of the filter in Figure 6.2g.

Table 6.1: Particles per mm^2 binned by size for each of the deposited filters shown in Figure 6.2. Values averaged across 21 images per filter.

Bins (μm)	Particles per mm^2						
	1h	2h	4h	7h	1t	3d	1w
PM_{2.5}	77.81	94.99	219.63	244.47	472.31	2098.52	4710.63
PM₁₀	89.23	111.52	259.39	286.39	544.93	2273.97	5174.07
Coarse ($>10 \mu\text{m}$)	2.83	4.06	7.37	5.38	11.24	28.23	57.13

vary drastically. Hence, the values observed in Figure 6.6 are obtained from averages of the number of particles across every image obtained of that specific filter. This introduces some uncertainty in the sense that the area selection might have a big impact on the results of these averages even when it was randomized. However, we believe that our sample size is enough to get a good sense of how particles of different sizes vary across our filters.

These results are also interesting to visualize in a graphic form. In Figure 6.6, we plot the number of particles in each filter by bin diameter from Table 6.1. It is interesting to observe that using logarithmic axes, the curves plotted resemble the theoretical predictions from chapter 1. Moreover, these curves seem to approximate the bimodal logarithmic distributions like we have shown in 4.3.

Taking a look now at the values obtained it is obvious that there is a clear tendency to have bigger quantities of smaller particles and smaller quantities of bigger particles. Moreover, it is clear that there is a correlation of the number of particles in each bin and deposition time. Nevertheless, the bins on the bottom and top are affected by bigger uncertainties albeit for completely different reasons. The smaller bins are the most affected by the uncertainty of the method of particle detection itself as in many cases the small particles can have an area as low as 1 pixel. Furthermore, small particles might not differentiate enough from the background in this optical inspection technique. The biggest bins on the other hand are the most affected by the lack of statistics, as there are few particles fitting this bin is improbable to get an accurate representation of the whole filter even with 21 images, which represent around 0,3% of the total deposited area. Nevertheless, most of aerosol analysis focus on smaller particles and therefore we chose to display the bins up to $30 \mu\text{m}$.

From other studies such as [136] we see that size distributions can vary significantly both from the welding technique and from the used heated materials and binders. Therefore, from the curves in Figure 6.6 we can hypothesize that our soldering fumes assumes the typical multimodal logarithmic distribution seen in most of the cited aerosol papers, with at least one maximum for the observed mode being present below our limit of detection. There is also a small rise on all of our data for the bin of $4 \mu\text{m}$ that might be interpreted as small local maximum, but is probably not enough to identify a new size mode. Moreover, these curves seem to approximate the modal logarithmic distributions

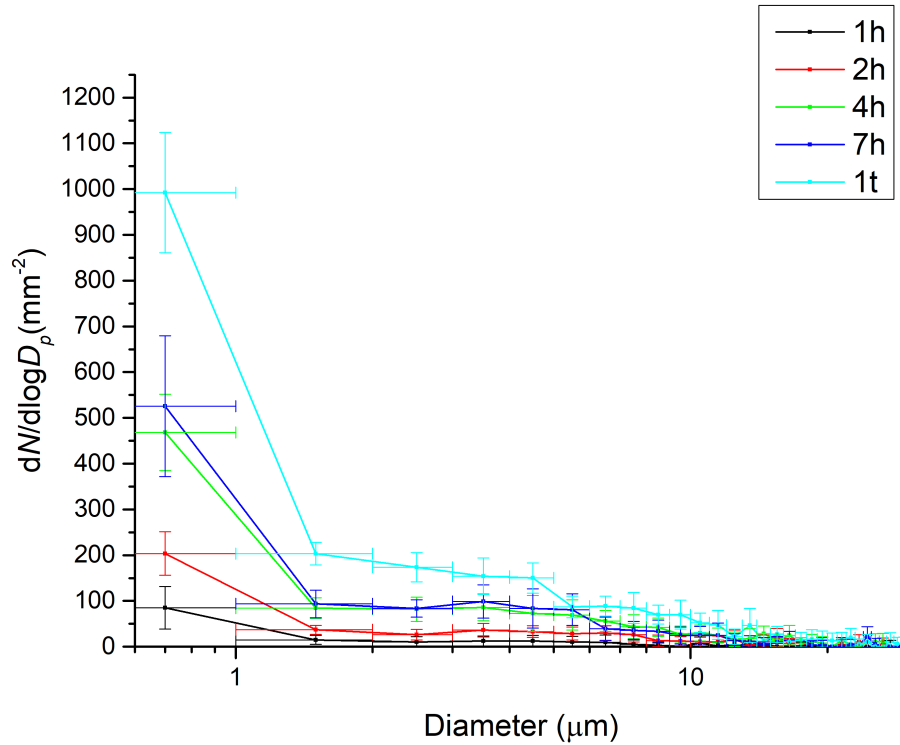


Figure 6.6: Particle concentration per mm^2 normalized by the logarithm of the corresponding bin particle diameter. X error bars are estimated by bin size and Y error bars are estimated using the standard deviation of our datasets.

predicted in chapter 1 like we have shown in 4.3.

Reiterating the data from our set of images we were also able to assess some common particle fractions. Note however that obtained values are using actual diameter of the aerosol particles deposited and not the typical aerodynamic diameter used in other studies and thus might not be directly comparable. The results are shown in Table 6.1. As expected, these fractions are also proportional with deposition time. The only common category that we are not able to quantify is ultra fine particle fractions (UFPs) given the fact that they are below the instrument's level of detection. We can also extrapolate the averages of the total number of particles for each of these categories deposited in our filters with a total area of 3600 mm^2 . For $\text{PM}_{2.5}$ the total number of particles ranges from around 2.8×10^5 in the 1 hour deposition to 1.7×10^7 in a 1 week deposition. In the case of PM_{10} , the total number of particles ranges from around 3.2×10^5 in the 1 hour deposition to 1.9×10^7 in a 1 week deposition. Lastly, coarse particles are roughly estimated to range from around 1.0×10^4 in the 1 hour deposition to 2.1×10^5 in a 1 week deposition.

At this point, we had a good sensitivity to the deposited particles size distribution, so we proceeded to go on a closer inspection what these particles look like and what they are made of. For this purpose, we analyzed small sample of one of our filters in the SEM with EDX described in the methods section. A large diversity of particles were found in terms

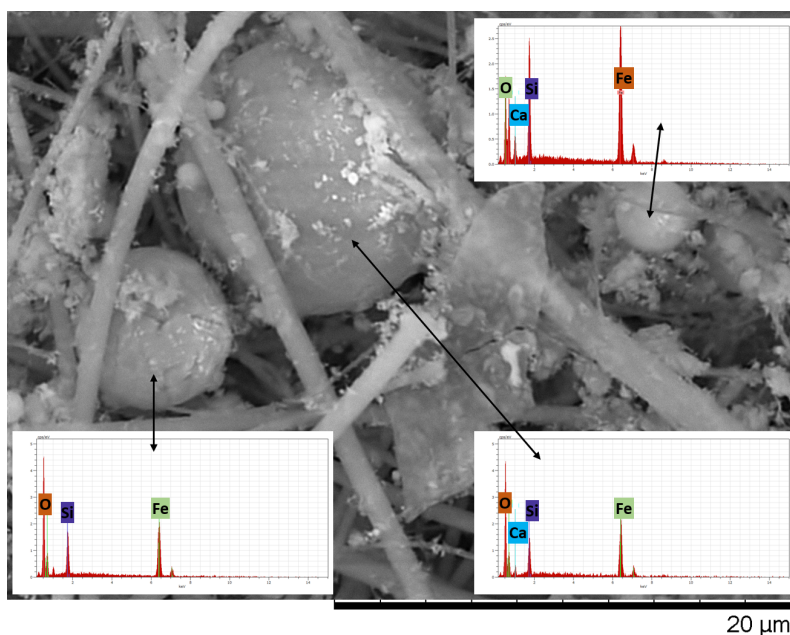


Figure 6.7: SEM image with overlapping spectra obtained with EDX for the highlighted small area.

of composition, size and shapes. Let's start with the most common particles found - iron particles, shown in Figure 6.7. As it is evidenced by the EDX spectrum overlapped on this figure the spherical-like structures that EDM detects are iron particles. The fiber-like structures are the filter mesh made of SiO_2 and thus the presence of both elements on the spectrum. Some residual amounts of calcium can also be found on these structures.

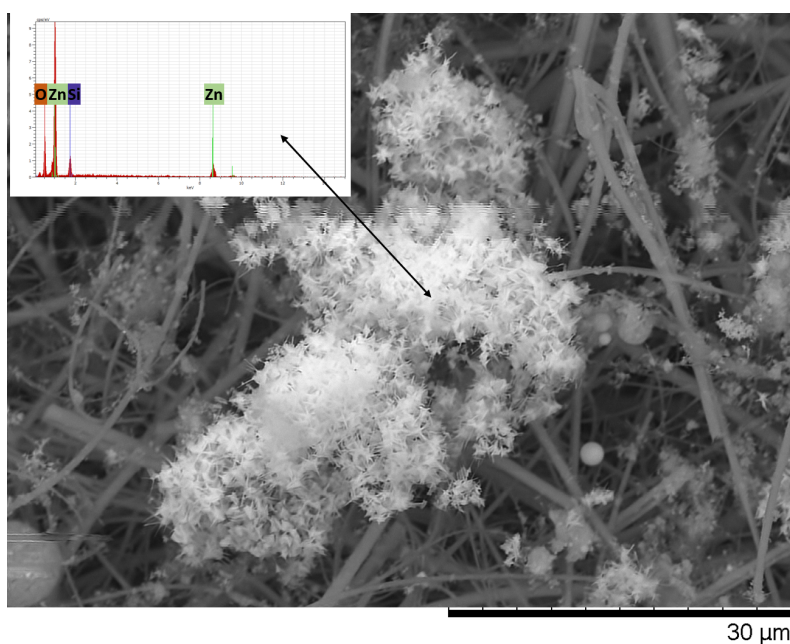
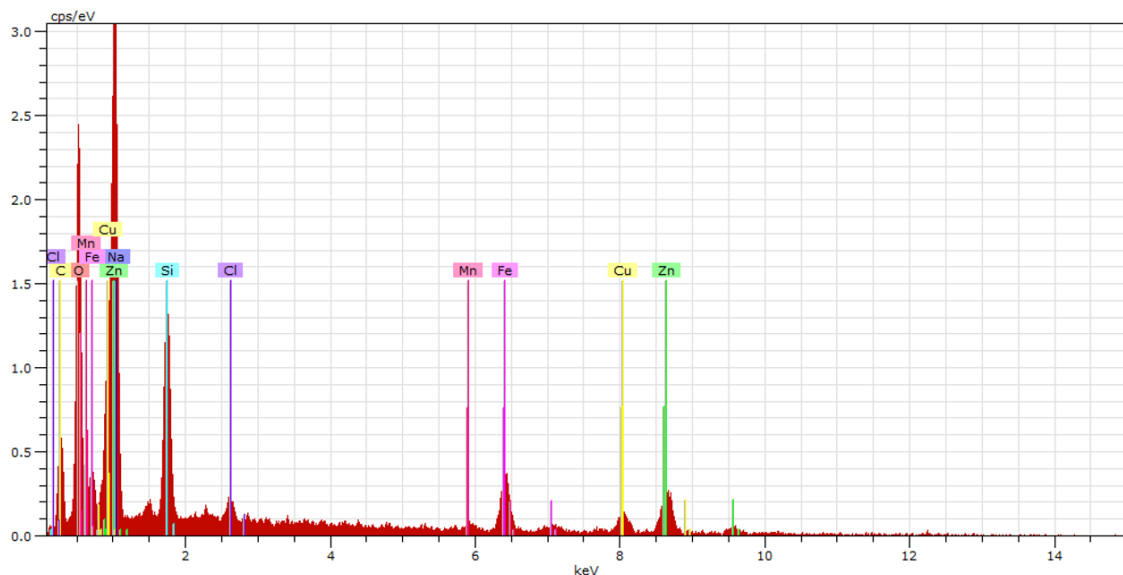


Figure 6.8: SEM image with overlapping spectra obtained with EDX for the highlighted small area.

Another common type of particle is shown in Figure 6.8, is pure zinc particle as evidenced by the spectrum. This one is a rarer occurrence of a very big agglomerate with a fractal like structure. Zinc is more commonly found all across the filters in the shape of very small fractals on top of other particles or around the filters' filaments.



(a) SEM image



(b) EDX spectrum of the highlighted area

Figure 6.9: SEM image and EDX spectrum of a complex particle.

These two types of particles (Figures 6.7 and 6.8) make up a big cross section of our deposited particles. They assume the *purest* forms of the corresponding elements however several other more complex particles can be found via SEM. These are often

oddly shaped particles composed of an array of different elements both inorganic and organic. One example of such particle can be found in Figure 6.9. As the spectrum shows they are composed of iron and zinc, but also have non negligible amounts of carbon, sodium, copper, manganese and chlorine. The carbon indicates some kind of organic matter, while copper and manganese are probably metal impurities of soldering fumes mostly constituted by iron and zinc. Sodium is most likely from the soldering binder used in the workstation, as sodium silicate is widely used for that specific purpose[161].

Overall, we found a high variability in shapes and forms in this analysis. These three examples cover most types of particles found, as well as all the elements found. All other particles were either a reiteration of these forms or blend between them of the most various sizes and shapes. Nevertheless, one thing to note is that one of the difficulties imposed by the SEM technique is measuring poorly attached very light particles. This stems from the fact that the electron beam projected by the SEM needle is enough to bombard the particle and propel them off the substrate. This means that we weren't able to measure every interesting feature of deposited filters because light particles would sometimes disappear from the image as soon as the electron beam approached the sample. We were able to identify that many of the particles that fit this description were the more *pure* forms of copper and manganese.

6.2.2 Composition results

As it was stated above, we have performed a series of EDXRF measurements of our deposited quartz fiber filters. For this purpose, every single filter was analyzed and quantified in the M4 Tornado™. The measurements were performed in vacuum and were performed around the half hour time frame. One example of EDXRF spectra obtained over the course of these measurements is shown in Figure 6.10.

As we can observe from the deposited filter spectrum (black) there are very prominent peaks for some elements. These elements are similar to what was found in the SEM analysis of individual featured particles. Note, however, that in a EDXRF spectrometer we are able to map a larger area of the filters and hence we can obtain a more global view of all elements presents in our sample. Nevertheless, as it is common with XRF analysis we always have a background due, mainly, to Bremsstrahlung radiation that impacts the limits of detection of the spectrometer, meaning that some lower concentration elements might not be detected.

As we pointed out before, the filters used are made of SiO₂ and hence there will be high quantities of both these elements. Moreover, there are also big peaks for the L_α and L_β of rhodium that are due to the X-ray source inside our spectrometer and hence are not taken in account upon elemental quantification. From these spectra comparison we determine that the trace elements of these depositions are iron, zinc, manganese and copper. There are some other identifiable elements transversal to most our spectra such as calcium, potassium, and sodium. Calcium and potassium are very much present in the

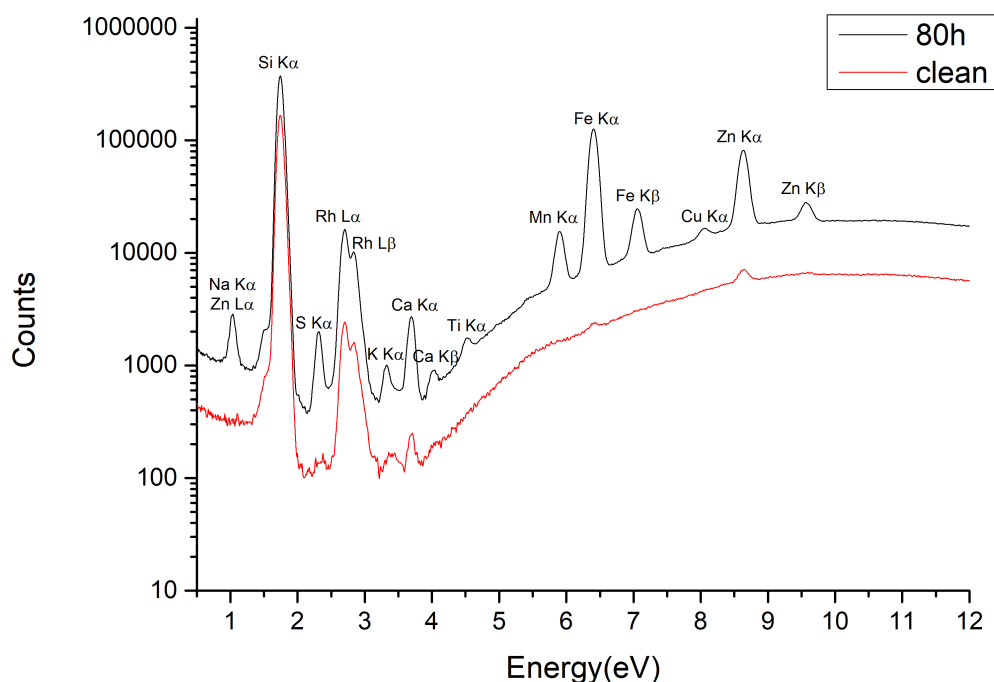


Figure 6.10: Typical EDXRF spectrum obtained by mapping our deposited quartz fiber filters. The two filters shown are the same as figures 6.2a and 6.2h.

clean filter spectra and could be elements used in the filter mesh treatment. Sodium as we have stated above is most likely a solder binder. Residual quantities of lead, chlorine, sulfur and titanium can be also found in some spectra, however they are barely above our detection limit and do not follow any trend with deposition time.

Overall, the trace elements of our samples have a pretty linear behavior with deposition time. Meaning, the longer a filter was subject to aerosol deposition the bigger the concentrations of trace elements, as we can see in Figure 6.11. For the analysis in this figure, we quantified, using standardized maps, the concentrations of each of the elements that we wanted to study. Moreover, we defined for each filter two areas for quantification: the total deposited circular sample area and central zone with about half the diameter. The reasoning behind this split was due to fact that the edges of the deposition area are by far more heavily deposited than the central area. Therefore, it might be interesting to assess the difference between these two areas. Also keep in mind that these are concentrations values, which are in $\mu\text{g/g}$ and therefore is not impossible for the central part to equate a bigger a concentration than the total area deposited (as it happens on the 6h filter for Copper).

Note, however, that in Figure 6.11 we decided to use only points with up to 8h (1 work shift) of deposition. The reasoning behind this conscious decision was that we are calibrating an instrument to work as close to real time as possible. Moreover, we saw

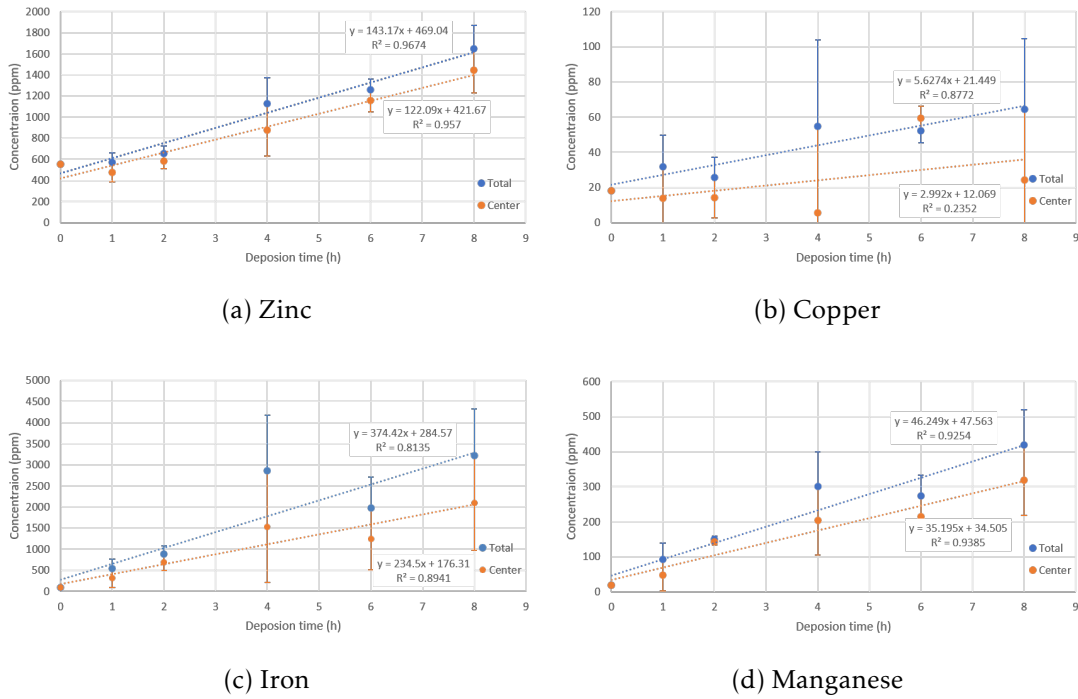


Figure 6.11: Concentrations comparison across all the filters of the most prevalent trace elements of the EDXRF analysis: Fe, Zn, Mn and Cu. All these plots show both the results for the total deposited particles and the central area of deposition. Error bars are estimated from the difference between the concentrations in the two different areas. This is representative of the particle deposition variability that is the biggest source of uncertainty in this type of measurements.

some tendency for the points above 1 day of deposition to be below the linear trends. We attribute this to some particle saturation on the filters but also to resuspension. The fact is that this assembly line worked, when we were measuring, two 8h turns a day and *rested* one 8h turn a day. Meaning, that the continuous *clean* air flux would enable resuspension of deposited material back into the air, thus, leading to a loss of information.

Nonetheless, the increase in concentration is unequivocal linear for most of the elements/areas defined and has no distinguishable saturation effect for the points shown in Figure 1.5. This is evidenced by $R^2 > 0.8$ for every element with zinc and manganese being over $R^2 > 0.9$. Copper measurements in central area do not exhibit any linearity with time and seem to indicate that most copper particles are localized on the edges of deposition. There is also an outlier for the 4h filter that exhibits above average concentrations. Visually this outlier is easier to detect in the iron plot. This is due to the fact that the prototype is installed in a repair line of the factory, which means that only chassis with defects will go through this assembly line. Meaning that there might be an hourly variability of cars going through this factory line that might lead to deviations from the projected trend. We can also see this outlier in a smaller magnitude in the manganese and copper plots but not so much in the zinc one. This might lead us to believe, knowing that the solder material is based on an iron/zinc metallic league, that the manganese and

copper present on our samples are iron impurities.

The linearity of these elements also makes us consider adding, in the future, a small X-ray source and low-cost proportional counter detector to this prototype, since we don't need to have a big photon energy resolution and can easily estimate all the elements concentrations from the fluorescence photon number. This would allow for quick composition assessment directly on the factory line.

Regarding the area concentration difference we obtain that the average relative difference is 15.0%, 42.4%, 35.4% and 22.6% for zinc, copper, iron and manganese, respectively. From this results we can see that zinc has a lower probability of being forced into the edge area compared to iron. This is probably due to the particles shapes that we saw in the last section. As we have seen, zinc is usually in fractal like particles and iron is in spherical like particles. This means that adhesion to the filter mesh is more likely from the zinc fractal like particles, which have multiple points of connection to the fibers. On the other hand, spherical particles are more aerodynamic and more likely to be carried into the edge of deposition by the constant flow. Moreover, from the SEM inspection we were also able to observe that zinc is usually present in bigger agglomerates, while iron spherical particles were present across a wider range of diameters. Obviously, particles with more inertia are more unlikely to be moved and thus, once again, iron particles will be more likely to go to the edges than zinc particles. Copper and manganese roughly follow the same trend as iron and therefore support the theory that their presence on our samples is due to iron impurities.

Table 6.2: Mass comparison between the XRF analysis and microcamera observations. The last column corresponds to the ammount of particles needed with $0,4 \mu\text{m}$ of diameter to account for the missing mass.

Time (h)	Mass XRF (μg)	Mass microcamera (μg)	Number of particles ($d=0.4 \mu\text{m}$)
80	15547	3607	6.28×10^{10}
48	7528	3053	2.36×10^{10}
8	2348	1074	6.70×10^9
6	1562	1394	8.81×10^8
4	1510	888	3.27×10^9
2	848	529	1.68×10^9
1	513	277	1.24×10^9

With these results we can extrapolate how much mass of the trace elements we accumulate in each one of the filters. As the above concentrations are in ppms, which equate into $\mu\text{g/g}$ in terms of mass and knowing that our filters have an effective mass of 3.23 g we can calculate each element's total mass. The sum of the resulting masses can then be compared to the deposited mass from the number of particles accounted in the micro camera observation as shown in Table 6.2. The estimation of mass for those observations can be achieved if we assume that the particles are spherical and have a density derived from the ratio of trace elements in the EDXRF analysis - 7.56 g/cm^3 . Thus, reprocessing

those images to sum the masses of every single particle in an image and averaging the results across images from the same set we obtain the values displayed in Table 6.2.

If we compare the masses obtained by the two different methods we observe that on average the microcamera analysis does only account for a small fraction of the total mass detected via XRF. This was to be expected for several reasons. First, there is a lot of variability between each image and filter areas which introduces a lot of uncertainty on the counting process. Second, a method based on optic observation of particle against a background will always underestimate the number of particles due to tone variability. Finally, we are not able assess particles under $0.4 \mu\text{m}$ of diameter which constitute the biggest number fraction of any aerosol.

We can then do a purely hypothetical calculation of the number of particles needed to fill the missing mass assuming a diameter of $0.4 \mu\text{m}$ (last column table 6.2). In reality, we will have as big of a diversity in diameters below $0.4 \mu\text{m}$ as we have above $0.4 \mu\text{m}$ and thus these numbers of particles will be underestimated. As a counterpoint, the uncertainty in the number of bigger particles might be enough to balance this underestimation, as any coarse particle has a major impact on deposited mass, unlike ultrafine particles. Therefore, these values serve only as an indication of the amount of particles that might be unaccounted for.

CONCLUSIONS

In this work, we have provided a practical review of the XRF technique by studying its applicability to very diverse industries with samples of biomedical interest. We have provided three different case studies where the only common denominator is the use of XRF. These endeavors prove the versatility and potential for this technique to be used across many scientific subjects. Even though the studies are all of biomedical interest, due to their inherent impact on human health, samples were also very heterogeneous not only in chemical composition but also in physical state. The robustness of this technique is further accentuated by this fact and the ability to do a multi-elemental analysis of samples allows for great composition assessment results. When coupled with different complimentary techniques it provides a very in-depth study with a very complete sample characterization.

The first case study that we present in this thesis is the study of pharmaceutical pills for trace elements and contaminants alike. The pharmaceutical industry as we have mentioned in this text represents one of the big applications of the XRF technique due to being a relatively cheap method that provides results compliant with some of the most used standards like the European Pharmacopeia. In this work, we have used this technique with triaxial geometry for fast and accurate multi-elemental analysis of five different popular iron supplements in Brazil. The analytical method for quantification using standard samples was also reviewed in-depth and cross-calibrated using ICP-AES. The aim of this study was to observe how the labeled values of the nutrients compare to actual measured elemental concentration on the pills. The EDXRF quantification shows that the iron content in these pills is found to be compliant with the advertised percentage on each brand's box. However, we have found non-negligible concentrations of contaminants, namely manganese and nickel. Our analysis detects nickel content up to 14.4% of the PDE for Noripurum and manganese content up to 7.2% of the PDE(permitted daily exposure) for

Anemifer. The less contaminated drug analyzed was Sulferbel with 5.0% of the PDE of nickel and 4.3% of the PDE of manganese. While manganese can be either a beneficial nutrient or a toxic substance depending on the dose and thus this value can be acceptable, nickel on the other hand as no nutritional value and it is only regarded as toxic to the human body and thus this value urges for better quality control.

On the second case study we have focused on the agronomy/food industry. For this study, we have used a set of eleven biofortified and non-biofortified wheat varieties developed at the International Maize and Wheat Improvement Center (CIMMYT), Mexico. We have used both a benchtop micro-XRF spectrometer as well as a custom built triaxial EDXRF spectrometer to provide insight into element concentration, localization and biofortification efficiency. We have also provided a full statistical analysis of the results across the multiple genotypes, biological structures and types of biofortification. The biofortification procedures applied to the analyzed wheat samples result in around a 30% average increase in overall Zn concentration when compared to other high Zn genotypes, and much higher (35-90%) when compared to the control grains. This increase in zinc content is also traced specifically within the grain to the embryo and vascular bundle whereas the endosperm doesn't show major changes. There is however an outlier for Zinc-shakti where there is a 34% increase of Zn in the endosperm which is substantial. This represents a good prospect for this genotype since it is a very popular cereal among some developing countries. Moreover, the importance of increasing zinc specifically in the endosperm can not be overstated since it constitutes almost 80% of the biomass of wheat grain. Even if we already assume integral wheat flour, it is that much important to have increased zinc content in the endosperm for the zinc availability in the final product to be maximized.

In the third and biggest case study the objective was to analyze the atmospheric aerosol inside the biggest factory in Portugal - Volkswagen Autoeuropa, Lda. For this purpose, we have developed and constructed two prototypes for the deposition of the suspended particles onto quartz-fiber filters. As it is expected in an I&D project, a lot of sketches, 3D drawings, technical drawings, as well as electronics, mechanical and programming ideas were produced. While the most important for the final designs are presented in this text there were many concepts and endeavors that were explored and abandoned. However, the three variables that were the most impacting on the development time were: keeping the total price of the instrument down, the acquisition of parts/materials and delivery waiting timings and the limited access to the plant and its infrastructures. Nevertheless, as it been mentioned before, two working devices were produced to properly deposit the aerosol onto fiber filters and allowed us to quantify various aerosol properties.

As for the analysis of our samples we made use of mostly three different techniques: EDXRF, micro-camera binocular inspection and SEM with EDX. EDXRF is a very popular composition assessment tool that allows for a very sensitive, fast and non-destructible analysis of samples. With an EDXRF spectrometer we were then able to map large and small areas alike of our deposited filters. This allowed us to determine that our core trace

elements across our samples were the four metallic elements: iron, zinc, manganese and copper. Some other elements were also present in our analysis such as chlorine, calcium and potassium that we attribute to sources other than the work performed on this specific workstation. Silicon and oxygen are also very present in the spectra because they are the matrix of quartz-fiber filters. Moreover, we observed in this analysis that the filter deposition was not homogeneous. Instead our observations show that due to the specific air flow inside the wind tunnel higher concentrations of elements can be found near the edges of deposition. We estimate that the average concentration difference between the center area and the edge of deposition to be around 27%.

Another interesting feature that we observe on our filters is a high linearity between the elemental concentrations in the filters and deposition time. This means that our concept of using a proportional counter with a custom made triboluminescent X-ray source to do the XRF analysis would work well. The reason being that with high linearity we don't have to have great energy resolution and instead we can calibrate our system to assess each elements concentration via a ratio of the total counts number. Sadly due to the reasons explained on chapter 6 we were not able to implement on-line XRF analysis.

The micro-camera binocular inspection allowed us to make a size distribution analysis of our samples. For this we obtained over 100 highly zoomed pictures of our samples and processed them via an image recognition script developed by us. This allowed for an analysis based on equivalent diameter size bins. We were able to extrapolate, for example, that our filters had a total amount of PM_{2.5} that ranged from around $2,8 \times 10^5$ in 1 hour deposition to $1,7 \times 10^7$ in a 1 week deposition, with a detection limit of around $0,4 \mu\text{m}$. The amount of particles on each size bin also follows a proportional relationship with deposition time.

The electron microscopy analysis with SEM/EDS allowed us to merge our composition analysis with the size distribution analysis. With the SEM technique we obtained various contrast images of very small windows of our deposited filters. The EDS capabilities of this instrument gave us a quick composition analysis of interesting features in our filters. Therefore, we were also able to assess the shapes of various structures within our samples. As expected the filter itself provided a very intricate and chaotic background of filaments in these images. Our most common trace element, iron, was distributed all across the samples in the shape of sphere like particles of vary diverse sizes. We were also able to detect zinc particles that exhibit very fractal like structures. The remaining elements appear in much more complex agglomerates of particles with no characteristic shape.

BIBLIOGRAPHY

- [1] K. D. D. Cunha, J. A. M. Pereira, and C. V. B. Leite. “PIXE and PDMS Methods Applied to Aerosols Analysis.” In: *Aerosol Science and Technology* 6826.32:5 (2010), pp. 453–464. DOI: [10.1080/027868200303579](https://doi.org/10.1080/027868200303579).
- [2] P. Cardoso, P. Amaro, J. P. Santos, J. T. de Assis, and M. L. Carvalho. “Determination of Nickel and Manganese Contaminants in Pharmaceutical Iron Supplements Using Energy Dispersive X-ray Fluorescence.” In: *Applied Spectroscopy* 71.3 (2017). PMID: 27694429, pp. 432–437. DOI: [10.1177/0003702816670912](https://doi.org/10.1177/0003702816670912). URL: <https://doi.org/10.1177/0003702816670912>.
- [3] D Guimarães, A. A. Dias, M Carvalho, M. L. Carvalho, J. P. Santos, F. R. Henriques, F Curate, and S Pessanha. “Quantitative determinations and imaging in different structures of buried human bones from the XVIII-XIXth centuries by energy dispersive X-ray fluorescence – Postmortem evaluation.” In: *Talanta* 155 (2016), pp. 107–115. ISSN: 0039-9140. DOI: <https://doi.org/10.1016/j.talanta.2016.04.028>. URL: <https://www.sciencedirect.com/science/article/pii/S0039914016302673>.
- [4] M. Guerra, M. Manso, S. Pessanha, S. Longelin, and M. L. Carvalho. “Theoretical and experimental study on the angular dependence of scattering processes in X-ray fluorescence systems.” In: *X-Ray Spectrometry* 42.5 (2013), pp. 402–407. DOI: [10.1002/xrs.2491](https://doi.org/10.1002/xrs.2491). eprint: <https://onlinelibrary.wiley.com/doi/pdf/10.1002/xrs.2491>. URL: <https://onlinelibrary.wiley.com/doi/abs/10.1002/xrs.2491>.
- [5] P. Cardoso, T. C. Mateus, G Velu, R. Singh, J Santos, M. Carvalho, V. M. Lourenço, F. Lidon, F. Reboredo, and M. Guerra. “Localization and distribution of Zn and Fe in grains of biofortified bread wheat lines through micro- and triaxial-X-ray fluorescence spectrometry.” In: *Spectrochimica Acta Part B: Atomic Spectroscopy* 141 (2018). DOI: [10.1016/j.sab.2018.01.006](https://doi.org/10.1016/j.sab.2018.01.006).
- [6] I. Queralt, E. Marguá, and R Van Grieken. “Sample Preparation for X-Ray Fluorescence Analysis.” In: 2016, pp. 1–25. ISBN: ISBN: 9780470027318. DOI: [10.1002/9780470027318.a6806m.pub3](https://doi.org/10.1002/9780470027318.a6806m.pub3).

- [7] A. Gojska and E. Mišta. “Analysis of the Elemental Composition of the Artefacts from the Kosewo Archaeological Site.” In: *Acta Physica Polonica A* 130 (2016), pp. 1415–1419. DOI: [10.12693/APhysPolA.130.1415](https://doi.org/10.12693/APhysPolA.130.1415).
- [8] L. Martins. “X-ray fluorescence analysis using a standardless method.” Doctoral dissertation. Universidade Nova de Lisboa - Faculdade de Ciências e Tecnologia, 2019.
- [9] R. E. V. Grieken and A. A. Markowicz. *Handbook of X-Ray Spectrometry Second Edition , Revised and Expanded edited by*. Second Edi. Marcel Dekker, Inc., 2002. ISBN: 0824706005.
- [10] D. E. Porter. “High intensity excitation sources for X-ray energy spectroscopy.” In: *X-Ray Spectrometry* 2.2 (1973), pp. 85–89. DOI: [10.1002/xrs.1300020208](https://doi.org/10.1002/xrs.1300020208). URL: <https://onlinelibrary.wiley.com/doi/abs/10.1002/xrs.1300020208>.
- [11] Diana Guimarães. “Measurement of lead concentration in biological tissues by atomic spectroscopy techniques.” Doctoral dissertation. Universidade Nova de Lisboa - Faculdade de Ciências e Tecnologia, 2011.
- [12] O Klein and Y Nishina. “Über die Streuung von Strahlung durch freie Elektronen nach der neuen relativistischen Quantendynamik von Dirac.” In: *Zeitschrift für Physik* 52.11 (1929), pp. 853–868. ISSN: 0044-3328. DOI: [10.1007/BF01366453](https://doi.org/10.1007/BF01366453). URL: <https://doi.org/10.1007/BF01366453>.
- [13] C. G. Barkla. “Polarisation in Secondary Röntgen Radiation Author.” In: *Proceedings of the Royal Society of London . Series A* 77.516 (1906), pp. 247–255.
- [14] E Gillam and H. T. Heai. “Some problems in the analysis of steels by X-ray fluorescence.” In: *British Journal of Applied Physics* 3.11 (1952), pp. 353–358. ISSN: 0508-3443. DOI: [10.1088/0508-3443/3/11/304](https://doi.org/10.1088/0508-3443/3/11/304). URL: <http://dx.doi.org/10.1088/0508-3443/3/11/304>.
- [15] H. J. Beattie and R. M. Brissey. “Calibration Method for X-Ray Fluorescence Spectrometry.” In: *Analytical Chemistry* 26.6 (1954), pp. 980–983. ISSN: 0003-2700. DOI: [10.1021/ac60090a009](https://doi.org/10.1021/ac60090a009). URL: <https://doi.org/10.1021/ac60090a009>.
- [16] J. Sherman. “The theoretical derivation of fluorescent X-ray intensities from mixtures.” In: *Spectrochimica Acta* 7 (1955), pp. 283–306. ISSN: 0371-1951. DOI: [https://doi.org/10.1016/0371-1951\(55\)80041-0](https://doi.org/10.1016/0371-1951(55)80041-0). URL: <https://www.sciencedirect.com/science/article/pii/0371195155800410>.
- [17] R. M. Rousseau. “Fundamental algorithm between concentration and intensity in XRF analysis 1—theory.” In: *X-Ray Spectrometry* 13.3 (1984), pp. 115–120. ISSN: 0049-8246. DOI: <https://doi.org/10.1002/xrs.1300130306>. URL: <https://doi.org/10.1002/xrs.1300130306>.

- [18] R. M. Rousseau. “Fundamental algorithm between concentration and intensity in XRF analysis 2—practical application.” In: *X-Ray Spectrometry* 13.3 (1984), pp. 121–125. ISSN: 0049-8246. DOI: <https://doi.org/10.1002/xrs.1300130307>. URL: <https://doi.org/10.1002/xrs.1300130307>.
- [19] R. M. Rousseau and M. Bouchard. “Fundamental algorithm between concentration and intensity in XRF analysis. 3—Experimental verification.” In: *X-Ray Spectrometry* 15.3 (1986), pp. 207–215. ISSN: 0049-8246. DOI: <https://doi.org/10.1002/xrs.1300150311>. URL: <https://doi.org/10.1002/xrs.1300150311>.
- [20] G. E. Falchini, A. Malezan, M. E. Poletti, E. Soria, M. Pasqualini, and R. D. Perez. “Analysis of phosphorous content in cancer tissue by synchrotron micro-XRF.” In: *Radiation Physics and Chemistry* 179 (2021), p. 109157. ISSN: 0969-806X. DOI: <https://doi.org/10.1016/j.radphyschem.2020.109157>. URL: <https://www.sciencedirect.com/science/article/pii/S0969806X20301183>.
- [21] U. Majewska, D. Banaś, J. Braziewicz, S. Gózdź, A. Kubala-Kukuś, and M. Kucharzewski. “Trace element concentration distributions in breast, lung and colon tissues.” eng. In: *Physics in medicine and biology* 52.13 (2007), pp. 3895–3911. ISSN: 0031-9155 (Print). DOI: [10.1088/0031-9155/52/13/016](https://doi.org/10.1088/0031-9155/52/13/016).
- [22] M. Piacenti da Silva, O. L. A. D. Zucchi, A. Ribeiro-Silva, and M. E. Poletti. “Discriminant analysis of trace elements in normal, benign and malignant breast tissues measured by total reflection X-ray fluorescence.” In: *Spectrochimica Acta Part B: Atomic Spectroscopy* 64.6 (2009), pp. 587–592. ISSN: 0584-8547. DOI: <https://doi.org/10.1016/j.sab.2009.05.026>. URL: <https://www.sciencedirect.com/science/article/pii/S058485470900130X>.
- [23] Y. Kolmogorov, V. Kovaleva, and A. Gonchar. “Analysis of trace elements in scalp hair of healthy people, hyperplasia and breast cancer patients with XRF method.” In: *Nuclear Instruments and Methods in Physics Research Section A: Accelerators, Spectrometers, Detectors and Associated Equipment* 448 (2000), pp. 457–460. DOI: [10.1016/S0168-9002\(00\)00236-9](https://doi.org/10.1016/S0168-9002(00)00236-9).
- [24] A. Maziar, D. Shahbazi-Gahrouei, M. B. Tavakoli, and V. Changizi. “Non Invasive XRF Analysis of Human Hair for Health State Determination of Breast Tissue.” eng. In: *Iranian journal of cancer prevention* 8.6 (2015), e3983–e3983. ISSN: 2008-2398. DOI: [10.17795/ijcp-3983](https://doi.org/10.17795/ijcp-3983). URL: <https://pubmed.ncbi.nlm.nih.gov/26855721https://www.ncbi.nlm.nih.gov/pmc/articles/PMC4736071/>.
- [25] D. Pearson, S. Chakraborty, B. M. Duda, B. Li, S. Deb, E. Brevik, and D. Ray. “Water Analysis via Portable X-ray Fluorescence Spectrometry.” In: *Journal of Hydrology* 544 (2017), pp. 172–179. DOI: [10.1016/j.jhydrol.2016.11.018](https://doi.org/10.1016/j.jhydrol.2016.11.018).

- [26] X. Hou, H. L. Peters, Z. Yang, K. A. Wagner, J. D. Batchelor, M. M. Daniel, and B. T. Jones. "Determination of trace metals in drinking water using solid-phase extraction disks and X-ray fluorescence spectrometry." eng. In: *Applied spectroscopy* 57.3 (2003), pp. 338–342. ISSN: 0003-7028 (Print). DOI: [10.1366/000370203321558263](https://doi.org/10.1366/000370203321558263).
- [27] J.-J. S. Huang, S.-C. Lin, L. Löwemark, S. Y. H. Liou, Q. Chang, T.-K. Chang, K.-Y. Wei, and I. W. Croudace. "Rapid assessment of heavy metal pollution using ion-exchange resin sachets and micro-XRF core-scanning." In: *Scientific Reports* 9.1 (2019), p. 6601. ISSN: 2045-2322. DOI: [10.1038/s41598-019-43015-x](https://doi.org/10.1038/s41598-019-43015-x). URL: <https://doi.org/10.1038/s41598-019-43015-x>.
- [28] Y. Fiamegos, S. Papoci, C. Dumitrascu, M. Ghidotti, T. Zdiniakova, F. Ulberth, and M. B. de la Calle Guntiñas. "Are the elemental fingerprints of organic and conventional food different? ED-XRF as screening technique." In: *Journal of Food Composition and Analysis* 99 (2021), p. 103854. ISSN: 0889-1575. DOI: <https://doi.org/10.1016/j.jfca.2021.103854>. URL: <https://www.sciencedirect.com/science/article/pii/S0889157521000545>.
- [29] K Kodom, K Preko, and D Boamah. "X-ray Fluorescence (XRF) Analysis of Soil Heavy Metal Pollution from an Industrial Area in Kumasi, Ghana." In: *Soil and Sediment Contamination: An International Journal* 21.8 (2012), pp. 1006–1021. ISSN: 1532-0383. DOI: [10.1080/15320383.2012.712073](https://doi.org/10.1080/15320383.2012.712073). URL: <https://doi.org/10.1080/15320383.2012.712073>.
- [30] J. Q. McComb, C. Rogers, F. X. Han, and P. B. Tchounwou. "Rapid screening of heavy metals and trace elements in environmental samples using portable X-ray fluorescence spectrometer, A comparative study." eng. In: *Water, air, and soil pollution* 225.12 (2014), p. 2169. ISSN: 0049-6979. DOI: [10.1007/s11270-014-2169-5](https://doi.org/10.1007/s11270-014-2169-5). URL: <https://pubmed.ncbi.nlm.nih.gov/25861136https://www.ncbi.nlm.nih.gov/pmc/articles/PMC4386753/>.
- [31] A. Ene, A. Bosneaga Sion, and L. Georgescu. "Determination of heavy metals in soils using XRF technique." In: *Romanian Journal of Physics* 55 (2010), pp. 815–820.
- [32] H. L. Byers, L. J. McHenry, and T. J. Grundl. "XRF techniques to quantify heavy metals in vegetables at low detection limits." In: *Food Chemistry: X* 1 (2019), p. 100001. ISSN: 2590-1575. DOI: <https://doi.org/10.1016/j.fochx.2018.100001>. URL: <https://www.sciencedirect.com/science/article/pii/S2590157518300014>.
- [33] S. Zhou, Z. Yuan, Q. Cheng, Z. Zhang, and J. Yang. "Rapid in situ determination of heavy metal concentrations in polluted water via portable XRF: Using Cu and Pb as example." In: *Environmental Pollution* 243 (2018), pp. 1325–1333. ISSN: 0269-7491. DOI: <https://doi.org/10.1016/j.envpol.2018.09>.

087. URL: <https://www.sciencedirect.com/science/article/pii/S0269749118327398>.
- [34] B. Sauer, Y. Xiao, M. Zoontjes, and C. Kroll. "Application of X-ray fluorescence spectrometry for screening pharmaceutical products for Elemental Impurities according to ICH guideline Q3D." In: *Journal of Pharmaceutical and Biomedical Analysis* 179 (2020), p. 113005. ISSN: 0731-7085. DOI: <https://doi.org/10.1016/j.jpba.2019.113005>. URL: <https://www.sciencedirect.com/science/article/pii/S0731708519319338>.
- [35] D. J. Kalnicky and R Singhvi. "Field portable XRF analysis of environmental samples." In: *Journal of Hazardous Materials* 83.1-2 (2001), pp. 93–122. DOI: [10.1016/S0304-3894\(00\)00330-7](https://doi.org/10.1016/S0304-3894(00)00330-7). URL: <https://www.scopus.com/inward/record.uri?eid=2-s2.0-0035821440&doi=10.1016%2FS0304-3894%2800%2900330-7&partnerID=40&md5=91bd8897537969ba7e4b87b28debe073>.
- [36] F. Fujiwara, R. Jiménez, J. Marrero, D. Gómez, and P. Smichowski. "Antimony as a traffic-related element in size-fractionated road dust samples collected in Buenos Aires." In: *Microchemical Journal* 97.1 (2011), pp. 62–67. ISSN: 0026-265X. DOI: [10.1016/j.microc.2010.05.006](https://doi.org/10.1016/j.microc.2010.05.006). URL: <http://dx.doi.org/10.1016/j.microc.2010.05.006>.
- [37] G. C. Lough, J. J. Schauer, J.-S. Park, M. M. Shafer, J. T. Deminter, and J. P. Weinstein. "Emissions of metals associated with motor vehicle roadways." In: *Environmental Science and Technology* 39.3 (2005), pp. 826–836. DOI: [10.1021/es048715f](https://doi.org/10.1021/es048715f). URL: <https://www.scopus.com/inward/record.uri?eid=2-s2.0-13544260515&doi=10.1021%2Fes048715f&partnerID=40&md5=4f69d810c8cffffd08e98c5f3f2dcf918>.
- [38] K Castro, N Proietti, E Princi, S Pessanha, M. L. Carvalho, S Vicini, D Capitani, and J. M. Madariaga. "Analysis of a coloured Dutch map from the eighteenth century: The need for a multi-analytical spectroscopic approach using portable instrumentation." In: *Analytica Chimica Acta* 623.2 (2008), pp. 187–194. ISSN: 0003-2670. DOI: <https://doi.org/10.1016/j.aca.2008.06.019>. URL: <https://www.sciencedirect.com/science/article/pii/S0003267008011367>.
- [39] A. Anitha, A. Brasoveanu, M. Duarte, S. Hughes, I. Daubechies, J. Dik, K. Janssens, and M. Alfeld. "Restoration of X-ray fluorescence images of hidden paintings." In: *Signal Processing* 93.3 (2013), pp. 592–604. ISSN: 0165-1684. DOI: <https://doi.org/10.1016/j.sigpro.2012.09.027>. URL: <https://www.sciencedirect.com/science/article/pii/S0165168412003659>.

- [40] K. Langstraat, A. Knijnenberg, G. Edelman, L. van de Merwe, A. van Loon, J. Dik, and A. van Asten. "Large area imaging of forensic evidence with MA-XRF." In: *Scientific Reports* 7.1 (2017), p. 15056. ISSN: 2045-2322. DOI: [10.1038/s41598-017-15468-5](https://doi.org/10.1038/s41598-017-15468-5). URL: <https://doi.org/10.1038/s41598-017-15468-5>.
- [41] M. Arredondo and M. T. Núñez. "Iron and copper metabolism." In: *Molecular Aspects of Medicine* 26.4-5 SPEC. ISS. (2005), pp. 313–327. ISSN: 00982997. DOI: [10.1016/j.mam.2005.07.010](https://doi.org/10.1016/j.mam.2005.07.010).
- [42] J. L. Beard, J. A. Wiesinger, and J. R. Connor. "Pre- and Postweaning Iron Deficiency Alters Myelination in Sprague-Dawley Rats." In: *Developmental Neuroscience* 25.5 (2003), pp. 308–315. ISSN: 0378-5866. URL: <http://www.karger.com/DOI/10.1159/000073507>.
- [43] K. N. Agarwal. "Iron and the brain: neurotransmitter receptors and magnetic resonance spectroscopy." In: *British Journal of Nutrition* 85.Suppl 2 (2007), S147–S150. ISSN: 0007-1145. DOI: [10.1049/BJN2000307](https://doi.org/10.1049/BJN2000307). URL: http://journals.cambridge.org/abstract/{_}S0007114501001040.
- [44] World Health Organization. "the Global Prevalence of Anaemia in 2011." In: *WHO Report* (2011), p. 48. ISSN: 1368-9800. DOI: [10.1017/S1368980008002401](https://doi.org/10.1017/S1368980008002401). URL: http://apps.who.int/iris/bitstream/10665/177094/1/9789241564960{_\}eng.pdf?ua=1.
- [45] J. D. Haas and T. Brownlie. "Iron deficiency and reduced work capacity: a critical review of the research to determine a causal relationship." In: *The Journal of nutrition* 131.2S-2 (2001), 676S–688S; discussion 688S–690S. ISSN: 0022-3166.
- [46] Y. Balarajan, U. Ramakrishnan, E. Özaltın, A. H. Shankar, and S. V. Subramanian. "Anaemia in low-income and middle-income countries." In: *The Lancet* 378.9809 (2016), pp. 2123–2135. ISSN: 0140-6736. DOI: [10.1016/S0140-6736\(16\)62304-5](https://doi.org/10.1016/S0140-6736(16)62304-5). URL: [http://dx.doi.org/10.1016/S0140-6736\(16\)62304-5](http://dx.doi.org/10.1016/S0140-6736(16)62304-5).
- [47] N. Kozuki, A. C. Lee, and J. Katz. "Moderate to Severe , but Not Mild , Maternal Anemia Is Associated with Increased Risk of Small for gestational Age outcomes." In: *The Journal of Nutrition* 142 (2012), pp. 358–362. DOI: [10.3945/jn.111.149237](https://doi.org/10.3945/jn.111.149237). There.
- [48] J. E. Toblli, G. Cao, L. Olivieri, and M. Angerosa. "Comparative Study of Gastrointestinal Tract and Liver Toxicity of Ferrous Sulfate, Iron Amino Chelate and Iron Polymaltose Complex in Normal Rats." In: *Pharmacology* 82.2 (2008), pp. 127–137. ISSN: 0031-7012. URL: <http://www.karger.com/DOI/10.1159/000142728>.
- [49] A. N. d. V. Sanitária. *ANVISA webpage*. URL: <http://portal.anvisa.gov.br/wps/portal/anvisa/home>.

- [50] K. A. Fliszar, D. Walker, and L. Allain. "Profiling of Metal Ions Leached from Pharmaceutical Packaging Materials." In: *PDA Journal of Pharmaceutical Science and Technology* 60.6 (2006), pp. 337–342. URL: <http://journal.pda.org/content/60/6/337.abstract>.
- [51] World Health Organization. "Trace elements in human nutrition and health World Health Organization." In: *Who* (1996).
- [52] J. L. Aschner and M. Aschner. "Nutritional aspects of manganese homeostasis." In: *Molecular Aspects of Medicine* 26.4-5 SPEC. ISS. (2005), pp. 353–362. ISSN: 00982997. DOI: [10.1016/j.mam.2005.07.003](https://doi.org/10.1016/j.mam.2005.07.003).
- [53] L. Duedahl-Olesen. *Persistent Organic Pollutants and Toxic Metals in Foods*. 2013, pp. 308–333. ISBN: 9780857092458. DOI: [10.1533/9780857098917.2.308](https://doi.org/10.1533/9780857098917.2.308). URL: <http://www.sciencedirect.com/science/article/pii/B9780857092458500131>.
- [54] E. Comissionl. "Recommendation from the Scientific Committee on Occupational Exposure Limits for manganese and inorganic manganese compounds." In: June (2011), pp. 1–23.
- [55] Y. Chervona, A. Arita, and M. Costa. "Carcinogenic Metals and the Epigenome: Understanding the effect of Nickel, Arsenic, and Chromium." In: *Metallomics : integrated biometal science* 4.7 (2012), pp. 619–627. ISSN: 1756-5901. DOI: [10.1039/c2mt20033c](https://doi.org/10.1039/c2mt20033c). URL: <http://www.ncbi.nlm.nih.gov/pmc/articles/PMC3687545/>.
- [56] T. Magalhães, M. L. Carvalho, A. Von Bohlen, and M. Becker. "Study on trace elements behaviour in cancerous and healthy tissues of colon, breast and stomach: Total reflection X-ray fluorescence applications." In: *Spectrochimica Acta - Part B Atomic Spectroscopy* 65.6 (2010), pp. 493–498. ISSN: 05848547. DOI: [10.1016/j.sab.2010.04.001](https://doi.org/10.1016/j.sab.2010.04.001). URL: <http://dx.doi.org/10.1016/j.sab.2010.04.001>.
- [57] H. Romanowicz-Makowska, E. Forma, M. Bryś, W. Małgorzata Krajewska, and B. Smolarz. "Concentration of cadmium, nickel and aluminium in female breast cancer." In: *Polish Journal of Pathology* 62.4 (2011), pp. 257–261. ISSN: 12339687.
- [58] EFSA. "Scientific Opinion on the risks to public health related to the presence of nickel in food and drinking water." In: *EFSA Journal* 13.2 (2015), p. 4002. ISSN: 1831-4732. DOI: [10.2903/j.efsa.2015.4002](https://doi.org/10.2903/j.efsa.2015.4002). URL: <http://www.efsa.europa.eu/en/efsajournal/pub/4002>.
- [59] The United States Pharmacopeial Convention. "⟨ 231 ⟩ HEAVY METALS." In: *Revision Bulletin* (2015), pp. 1–2.
- [60] The United States Pharmacopeial Convention. "⟨232⟩ -Elemental impurities- Limits." In: *Revision Bulletin* (2013), pp. 1–3.

- [61] The United States Pharmacopeial Convention. “⟨233⟩ Elemental Impurities — Procedures.” In: *Revision Bulletin c* (2013), pp. 232–234.
- [62] T. Wang, J. Wu, R. Hartman, X. Jia, and R. S. Egan. “A multi-element ICP-MS survey method as an alternative to the heavy metals limit test for pharmaceutical materials.” In: *Journal of Pharmaceutical and Biomedical Analysis* 23.5 (2000), pp. 867–890. ISSN: 07317085. DOI: [10.1016/S0731-7085\(00\)00361-7](https://doi.org/10.1016/S0731-7085(00)00361-7).
- [63] G. M. Scelfo and A. R. Flegal. “Lead in calcium supplements.” eng. In: *Environmental health perspectives* 108.4 (2000), pp. 309–313. ISSN: 0091-6765. DOI: [10.1289/ehp.00108309](https://doi.org/10.1289/ehp.00108309). URL: <https://pubmed.ncbi.nlm.nih.gov/10753088><https://www.ncbi.nlm.nih.gov/pmc/articles/PMC1638001/>.
- [64] J. F. Kauffman, B. J. Westenberger, J. D. Robertson, J. Guthrie, A. Jacobs, and S. K. Cummins. “Lead in pharmaceutical products and dietary supplements.” eng. In: *Regulatory toxicology and pharmacology : RTP* 48.2 (2007), pp. 128–134. ISSN: 0273-2300 (Print). DOI: [10.1016/j.yrtph.2007.03.001](https://doi.org/10.1016/j.yrtph.2007.03.001).
- [65] Q. Tu, T. Wang, and V. Antonucci. “High-efficiency sample preparation with dimethylformamide for multi-element determination in pharmaceutical materials by ICP-AES.” In: *Journal of Pharmaceutical and Biomedical Analysis* 52.2 (2010), pp. 311–315. ISSN: 07317085. DOI: [10.1016/j.jpba.2010.01.008](https://doi.org/10.1016/j.jpba.2010.01.008). URL: <http://dx.doi.org/10.1016/j.jpba.2010.01.008>.
- [66] J. Sims, A. Smith, D. Patel, R. Batchelor, and J. Carreira. “Automated sample preparation for icp analysis of active pharmaceutical ingredients and intermediates.” In: *Journal of Laboratory Automation* 16.5 (2011), pp. 377–380. ISSN: 22110682. DOI: [10.1016/j.jala.2010.10.006](https://doi.org/10.1016/j.jala.2010.10.006). URL: <http://dx.doi.org/10.1016/j.jala.2010.10.006>.
- [67] E Margui, C Fontas, A Buendia, M Hidalgo, and I Queralt. “Determination of metal residues in active pharmaceutical ingredients according to European current legislation by using X-ray fluorescence spectrometry.” In: *Journal of Analytical Atomic Spectrometry* 24.9 (2009), pp. 1253–1257. ISSN: 0267-9477. DOI: [10.1039/B904064A](https://doi.org/10.1039/B904064A). URL: <http://dx.doi.org/10.1039/B904064A>.
- [68] P. T. Palmer, R. Jacobs, P. E. Baker, K. Ferguson, and S. Webber. “Use of field-portable XRF analyzers for rapid screening of toxic elements in FDA-regulated products.” eng. In: *Journal of agricultural and food chemistry* 57.7 (2009), pp. 2605–2613. ISSN: 1520-5118 (Electronic). DOI: [10.1021/jf803285h](https://doi.org/10.1021/jf803285h).
- [69] S. Arzhantsev, X. Li, and J. F. Kauffman. “Rapid Limit Tests for Metal Impurities in Pharmaceutical Materials by X-ray Fluorescence Spectroscopy Using Wavelet Transform Filtering.” In: *Analytical Chemistry* 83.3 (2011), pp. 1061–1068. ISSN: 0003-2700. DOI: [10.1021/ac1028598](https://doi.org/10.1021/ac1028598). URL: <https://doi.org/10.1021/ac1028598>.

- [70] S Al-Omari, A. A. Mubarak, M Al-Noaimi, F Afaneh, A Aqili, I Hamarneh, and N Mustapha. "Multielemental analysis of pharmaceuticals derived from plant seeds by energy dispersive X-ray fluorescence spectrometry." In: *Instrumentation Science & Technology* 44.1 (2016), pp. 98–113. ISSN: 1073-9149. DOI: [10.1080/10739149.2015.1057845](https://doi.org/10.1080/10739149.2015.1057845). URL: <https://doi.org/10.1080/10739149.2015.1057845>.
- [71] E. Marguí, K. Van Meel, R. Van Grieken, A. Buendía, C. Fontàs, M. Hidalgo, and I. Queralt. "Method for the determination of Pd-catalyst residues in active pharmaceutical ingredients by means of high-energy polarized-beam energy dispersive X-ray fluorescence." In: *Analytical Chemistry* 81.4 (2009), pp. 1404–1410. ISSN: 00032700. DOI: [10.1021/ac8021373](https://doi.org/10.1021/ac8021373).
- [72] P. Geisser. "Safety and Efficacy of Iron (III) -hydroxide Polymaltose Complex." In: 57.Iii (2007), pp. 439–452. ISSN: 0004-4172. DOI: [10.1055/s-0031-1296693](https://doi.org/10.1055/s-0031-1296693).
- [73] S. Pessanha, A. Guilherme, and M. L. Carvalho. "Comparison of matrix effects on portable and stationary XRF spectrometers for cultural heritage samples." In: *Applied Physics A: Materials Science and Processing* 97.2 (2009), pp. 497–505. ISSN: 09478396. DOI: [10.1007/s00339-009-5251-x](https://doi.org/10.1007/s00339-009-5251-x).
- [74] A Rindby. "Software for energy-dispersive X-ray fluorescence." In: *X-Ray Spectrometry* 18.3 (1989), pp. 113–118. ISSN: 1097-4539. DOI: [10.1002/xrs.1300180308](https://doi.org/10.1002/xrs.1300180308). URL: <http://dx.doi.org/10.1002/xrs.1300180308>.
- [75] M. L. Carvalho, J. Ferreira G., P. Amorim, M. I. M. Marques, and M. T. Ramos. "Study of heavy metals and other elements in macrophyte algae using energy-dispersive x-ray fluorescence." In: *Environmental Toxicology and Chemistry* 16.4 (1997), pp. 807–812. ISSN: 1552-8618. DOI: [10.1002/etc.5620160427](https://doi.org/10.1002/etc.5620160427). URL: <http://dx.doi.org/10.1002/etc.5620160427>.
- [76] EMEA European Medicines Agency. "Guideline on the Specification Limits for Residues of Metal Catalysts or Metal Reagents." In: *Regulation document* February (2008), pp. 1–34. DOI: [CPMP / SWP / QWP / 4446 / 00corr..](https://doi.org/10.25964/CPMP/SWP/QWP/4446/00corr..) arXiv: [SWP / QWP / 4446 / 00corr](https://arxiv.org/abs/SWP/QWP/4446/00corr). [CPMP].
- [77] M. Guerra, C. Ferreira, M. L. Carvalho, J. P. Santos, and S. Pessanha. "Distribution of toxic elements in teeth treated with amalgam using μ -energy dispersive X-ray fluorescence." In: *Spectrochimica Acta Part B: Atomic Spectroscopy* 122 (2016), p. 114.
- [78] M. Guerra, S. Longelin, S. Pessanha, M. Manso, and M. L. Carvalho. "Development of a combined portable x-ray fluorescence and Raman spectrometer for in situ analysis." In: *Review of Scientific Instruments* 85.6 (2014).

- [79] B. Kyriacou, K. L. Moore, D. Paterson, M. D. de Jonge, D. L. Howard, J. Stangoulis, M. Tester, E. Lombi, and A. A. T. Johnson. "Localization of iron in rice grain using synchrotron X-ray fluorescence microscopy and high resolution secondary ion mass spectrometry." In: *Journal of Cereal Science* 59.2 (2014), p. 173.
- [80] L. Lu, S. Tian, H. Liao, J. Zhang, X. Yang, J. M. Labavitch, and W. Chen. "Analysis of Metal Element Distributions in Rice (*Oryza sativa* L.) Seeds and Relocation during Germination Based on X-Ray Fluorescence Imaging of Zn, Fe, K, Ca, and Mn." In: *PLoS ONE* 8.2 (2013), e57360.
- [81] K. L. Moore, M. Schröder, E. Lombi, F.-J. Zhao, S. P. McGrath, M. J. Hawkesford, P. R. Shewry, and C. R. M. Grovenor. "NanoSIMS analysis of arsenic and selenium in cereal grain." In: *New Phytologist* 185.2 (2010), p. 434.
- [82] R. C. Power, D. C. Salazar-García, R. M. Wittig, and A. G. Henry. "Assessing use and suitability of scanning electron microscopy in the analysis of micro remains in dental calculus." In: *Journal of Archaeological Science* 49 (2014), p. 160.
- [83] E. Lombi, E. Smith, T. H. Hansen, D. Paterson, M. D. de Jonge, D. L. Howard, D. P. Persson, S. Husted, C. Ryan, and J. K. Schjoerring. "Megapixel imaging of (micro)nutrients in mature barley grains." In: *Journal of Experimental Botany* 62.1 (2011), p. 273.
- [84] K. R. Trijatmiko, C. Dueñas, N. Tsakirpaloglou, L. Torrizo, F. M. Arines, C. Adeva, J. Balindong, N. Oliva, M. V. Sapasap, J. Borrero, J. Rey, P. Francisco, A. Nelson, H. Nakanishi, E. Lombi, E. Tako, R. P. Glahn, J. Stangoulis, P. Chadha-Mohanty, A. A. T. Johnson, J. Tohme, G. Barry, and I. H. Slamet-Loedin. "Biofortified indica rice attains iron and zinc nutrition dietary targets in the field." In: *Scientific Reports* 6 (2016), p. 19792.
- [85] H. Gallardo, I. Queralt, J. Tapias, M. Guerra, M. L. Carvalho, and E. Marguí. "Possibilities of low-power X-ray fluorescence spectrometry methods for rapid multielemental analysis and imaging of vegetal foodstuffs." In: *Journal of Food Composition and Analysis* 50 (2016), p. 1.
- [86] I. Cakmak, M. Kalayci, Y. Kaya, A. A. Torun, N. Aydin, Y. Wang, Z. Arisoy, H. Erdem, A. Yazici, O. Gokmen, L. Ozturk, and W. J. Horst. "Biofortification and Localization of Zinc in Wheat Grain." In: *Journal of Agricultural and Food Chemistry* 58.16 (2010), p. 9092.
- [87] I. Ramos, I. M. Pataco, M. P. Mourinho, F. Lidon, F. Reboredo, M. F. Pessoa, M. L. Carvalho, J. P. Santos, and M. Guerra. "Elemental mapping of biofortified wheat grains using micro X-ray fluorescence." In: *Spectrochimica Acta Part B: Atomic Spectroscopy* 120 (2016), p. 30.
- [88] T. Iwai, M. Takahashi, K. Oda, Y. Terada, and K. T. Yoshida. "Dynamic changes in the distribution of minerals in relation to phytic acid accumulation during rice seed development." In: *Plant Physiol* 160.4 (2012), p. 2007.

- [89] S. H. Choi, J. S. Kim, J. Y. Lee, J. S. Jeon, J. W. Kim, R. E. Russo, J. Gonzalez, J. H. Yoo, K. S. Kim, J. S. Yang, and K. S. Park. "Analysis of arsenic in rice grains using ICP-MS and fs LA-ICP-MS." In: *Journal of Analytical Atomic Spectrometry* 29.7 (2014), p. 1233.
- [90] B. Meng, X. Feng, G. Qiu, C. W. N. Anderson, J. Wang, and L. Zhao. "Localization and Speciation of Mercury in Brown Rice with Implications for Pan-Asian Public Health." In: *Environmental Science & Technology* 48.14 (2014), p. 7974.
- [91] M. Aslam, P. Ellis, S. Berry, Y. Latunde-Dada, and P Sharp. "Enhancing mineral bioavailability from cereals: Current strategies and future perspectives." In: *Nutrition Bulletin* 43 (2018), pp. 184–188. DOI: [10.1111/nbu.12324](https://doi.org/10.1111/nbu.12324).
- [92] WHO. *The world health report. Reducing risks, promoting healthy life*. Tech. rep. World Health Organization, 2002.
- [93] N. Roohani, R. Hurrell, R. Kelishadi, and R. Schulin. "Zinc and its importance for human health: An integrative review." In: *Journal of Research in Medical Sciences : The Official Journal of Isfahan University of Medical Sciences* 18.2 (2013), p. 144.
- [94] R. S. Gibson. "Zinc: the missing link in combating micronutrient malnutrition in developing countries." In: *Proc Nutr Soc* 65.1 (2006), p. 51.
- [95] M. W. Blair. "Mineral Biofortification Strategies for Food Staples: The Example of Common Bean." In: *Journal of Agricultural and Food Chemistry* 61.35 (2013), p. 8287.
- [96] G. Velu, I. Ortiz-Monasterio, I. Cakmak, Y. Hao, and R. P. Singh. "Biofortification strategies to increase grain zinc and iron concentrations in wheat." In: *Journal of Cereal Science* 59.3 (2014), p. 365.
- [97] F. C. Lidon, A. S. Almeida, A. R. Costa, A. S. Bagulho, P. Scotti-Campos, J. N. Smedo, B. Maçãs, J. Coutinho, N. Pinheiro, C. Gomes, A. E. Leitão, I. P. Pais, M. M. Silva, F. H. Reboredo, M. F. Pessoa, and J. C. Ramalho. "Sequential zinc and iron biofortification of bread-wheat grains: from controlled to uncontrolled environments." In: *Crop and Pasture Science* 66 (2015), p. 1097.
- [98] I. M. Pataco, F. C. Lidon, I. Ramos, K. Oliveira, M. Guerra, M. F. Pessoa, M. L. Carvalho, J. C. Ramalho, A. E. Leitão, J. P. Santos, P. S. Campos, M. M. Silva, I. P. Pais, and F. H. Reboredo. "Biofortification of durum wheat (*Triticum turgidum* L. ssp. durum (Desf.) Husnot) grains with nutrients." In: *Journal of Plant Interactions* 12.1 (2017), p. 39.
- [99] D. Shah, H. S. Sachdev, T. Gera, L. M. De-Regil, and J. P. Pena-Rosas. "Fortification of staple foods with zinc for improving zinc status and other health outcomes in the general population." In: *Cochrane Database Syst Rev* 6 (2016), p. Cd010697.

- [100] Y.-Q. Zhang, Y. Deng, R.-Y. Chen, Z.-L. Cui, X.-P. Chen, R. Yost, F.-S. Zhang, and C.-Q. Zou. "The reduction in zinc concentration of wheat grain upon increased phosphorus-fertilization and its mitigation by foliar zinc application." In: *Plant and Soil* 361.1 (2012), p. 143.
- [101] D. F. Calderini and I. Ortiz-Monasterio. "Grain Position Affects Grain Macronutrient and Micronutrient Concentrations in Wheat." In: *Crop Science* 43.1 (2003), p. 141.
- [102] T. P. O'Brien, M. E. Sammut, J. W. Lee, and M. G. Smart. "The Vascular System of the Wheat Spikelet." In: *Functional Plant Biology* 12.5 (1985), p. 487.
- [103] S. Y. Zee and T. P. O'Brien. "A Special Type of Tracheary Element Associated with "Xylem Discontinuity" in the Floral Axis of Wheat." In: *Australian Journal of Biological Sciences* 23.4 (1970), p. 783.
- [104] B. Ajiboye, I. Cakmak, D. Paterson, M. de Jonge, D. Howard, S. Stacey, A. Torun, N. Aydin, and M. McLaughlin. "X-ray fluorescence microscopy of zinc localization in wheat grains biofortified through foliar zinc applications at different growth stages under field conditions." In: *Plant and Soil* 392.1-2 (2015), p. 357.
- [105] R. A. Maronna, R. D. Martin, and V. J. Yohai. "Robust statistics, theory and methods." In: *Robust Statistics*. John Wiley & Sons, Ltd, 2006, pp. i–xx.
- [106] M. Hollander and D. A. Wolfe. *Nonparametric statistical methods*. New York: John Wiley & Sons, 1973.
- [107] D. J. Best and D. E. Roberts. "Algorithm AS 89: The Upper Tail Probabilities of Spearman's Rho." In: *Journal of the Royal Statistical Society. Series C (Applied Statistics)* 24.3 (1975), p. 377.
- [108] U. Bodenhofer and F. Klawonn. "Robust rank correlation coefficients on the basis of fuzzy." In: *Mathware & Soft Computing* 15.1 (2008), p. 5.
- [109] Volkswagen Autoeuropa, Lda. *Media*. URL: <https://www.volkswagenautoeuropa.pt/media/>. (accessed: 19.01.2019).
- [110] A. T. Zimmer and P. Biswas. "Characterization of the aerosols resulting from arc welding processes." In: *Journal of Aerosol Science* 32.8 (2001), pp. 993–1008. ISSN: 0021-8502. DOI: [https://doi.org/10.1016/S0021-8502\(01\)00035-0](https://doi.org/10.1016/S0021-8502(01)00035-0). URL: <https://www.sciencedirect.com/science/article/pii/S0021850201000350>.
- [111] J. Wang, T. Hoang, E. L. Floyd, and J. L. Regens. "Characterization of Particulate Fume and Oxides Emission from Stainless Steel Plasma Cutting." In: *Annals of Work Exposures and Health* 61.3 (2017), pp. 311–320. ISSN: 2398-7308. DOI: [10.1093/annweh/wxw031](https://doi.org/10.1093/annweh/wxw031). URL: <https://doi.org/10.1093/annweh/wxw031>.

- [112] A. Viksna, E. S. Lindgren, P. Standzenieks, and J. Jacobsson. “EDXRF and TXRF analysis of elemental size distributions and environmental mobility of airborne particles in the city of Riga , Latvia.” In: *X-Ray Spectrometry* 33.August (2004), pp. 414–420. DOI: [10.1002/xrs.742](https://doi.org/10.1002/xrs.742).
- [113] D. Guimarães, M. L. Carvalho, V. Geraldés, I. Rocha, L. C. Alves, and J. P. Santos. “Lead in liver and kidney of exposed rats: Aging accumulation study.” In: *Journal of Trace Elements in Medicine and Biology* 26.4 (2012), pp. 285–290. ISSN: 0946-672X. DOI: <https://doi.org/10.1016/j.jtemb.2012.02.006>. URL: <https://www.sciencedirect.com/science/article/pii/S0946672X12000090>.
- [114] I. Colbeck and M. Lazaridis. *Aerosol Science: Technology and Applications*. 2014. ISBN: 978-1-119-97792-6. DOI: [10.1002/9781118682555.ch1](https://doi.org/10.1002/9781118682555.ch1).
- [115] D. M. Hyder and J. Jonsson. “Aerosols sampling and sample treatment methods: a review and state of the art.” In: *Air Pollution and Pollutants*. 2014, pp. 295–316. ISBN: 978-1-941249-02-4.
- [116] T. Bianchi, M. Belingheri, A. Nespoli, G. D. Vito, and M. A. Riva. “Occupational Risks in Midwifery : From Bernardino Ramazzini to Modern Times.” In: *Safety and Health at Work* 10.2 (2019), pp. 245–247. ISSN: 2093-7911. DOI: [10.1016/j.shaw.2018.11.002](https://doi.org/10.1016/j.shaw.2018.11.002). URL: <https://doi.org/10.1016/j.shaw.2018.11.002><https://www.ncbi.nlm.nih.gov/pmc/articles/PMC6598806/pdf/main.pdf>.
- [117] J Podzimek. “John Aitken ’ s Contribution to Atmospheric and Aerosol Sciences — One Hundred Years of Condensation Nuclei Counting.” In: *American Meteorological Society* 70.12 (1989), pp. 1538–1545.
- [118] P. H. McMurry. “The History of Condensation Nucleus Counters.” In: *Aerosol Science and Technology* 33.4 (2000), pp. 297–322. DOI: [10.1080/02786820050121512](https://doi.org/10.1080/02786820050121512). URL: <https://doi.org/10.1080/02786820050121512>.
- [119] C. A. Pope III and D. W. Dockery. “Health Effects of Fine Particulate Air Pollution: Lines that Connect.” In: *Journal of the Air & Waste Management Association* 56.6 (2006), pp. 709–742. DOI: [10.1080/10473289.2006.10464485](https://doi.org/10.1080/10473289.2006.10464485). URL: <https://doi.org/10.1080/10473289.2006.10464485>.
- [120] M Kanakidou, J. H. Seinfeld, S. N. Pandis, I Barnes, F. J. Dentener, M. C. Facchini, and R. V. Dingenen. “Physics Organic aerosol and global climate modelling : a review.” In: *Atmos. Chem. Phys.* 5 (2005), pp. 1053–1123.
- [121] M Hallquist, J. C. Wenger, U Baltensperger, Y Rudich, D Simpson, M Claeys, and J Dommen. “Physics The formation , properties and impact of secondary organic aerosol : current and emerging issues.” In: *Atmos. Chem. Phys.* 9 (2009), pp. 5155–5236.

- [122] *Diário da República, 2.ª série — N.º151 — 6 de Agosto de 2008*. 2007.
- [123] *Diário da República, 1.ª série — N.º 186 — 23*. 2010.
- [124] Direção-Geral de Saúde. *GUIA TÉCNICO N.º2 - VIGILÂNCIA DA SAÚDE DOS TRABALHADORES EXPOSTOS A AGENTES QUÍMICOS CANCERÍGENOS, MUTAGÉNICOS OU TÓXICOS PARA A REPRODUÇÃO*. Tech. rep. 2017.
- [125] World Health Organization. “WHO Air quality guidelines for particulate matter, ozone, nitrogen dioxide and sulfur dioxide.” In: (2005).
- [126] K. G. Andersson, J Roed, M. A. Byrne, and H Hession. “Deposition of contaminant aerosol on human skin.” In: *Journal of Environmental Radioactivity* 85.2 (2006), pp. 182–195. ISSN: 0265-931X. DOI: <https://doi.org/10.1016/j.jenvrad.2004.04.016>. URL: <https://www.sciencedirect.com/science/article/pii/S0265931X05002158>.
- [127] Y. S. Cheng and W.-C. Su. “Thoracic fraction of inhaled fiber aerosol.” eng. In: *Journal of occupational and environmental hygiene* 10.4 (2013), pp. 194–202. ISSN: 1545-9632 (Electronic). DOI: [10.1080/15459624.2012.762608](https://doi.org/10.1080/15459624.2012.762608).
- [128] M. Riediker, D. Zink, W. Kreyling, G. Oberdörster, A. Elder, U. Graham, I. Lynch, A. Duschl, G. Ichihara, S. Ichihara, T. Kobayashi, N. Hisanaga, M. Umezawa, T.-J. Cheng, R. Handy, M. Gulumian, S. Tinkle, and F. Cassee. “Particle toxicology and health - where are we?” In: *Particle and Fibre Toxicology* 16.1 (2019), p. 19. ISSN: 1743-8977. DOI: [10.1186/s12989-019-0302-8](https://doi.org/10.1186/s12989-019-0302-8). URL: <https://doi.org/10.1186/s12989-019-0302-8>.
- [129] J. H. Kroll and J. H. Seinfeld. “Chemistry of secondary organic aerosol: Formation and evolution of low-volatility organics in the atmosphere.” In: *Atmospheric Environment* 42.16 (2008), pp. 3593–3624. ISSN: 1352-2310. DOI: <https://doi.org/10.1016/j.atmosenv.2008.01.003>. URL: <http://www.sciencedirect.com/science/article/pii/S1352231008000253>.
- [130] J. Mauderly and J. Chow. “Health Effects of Organic Aerosols.” In: *Inhalation toxicology* 20 (2008), pp. 257–288. DOI: [10.1080/08958370701866008](https://doi.org/10.1080/08958370701866008).
- [131] J Douwes, P Thorne, N Pearce, and D Heedrik. “Bioaerosol Health Effects and Exposure Assessment: Progress and Prospects.” In: *The Annals of Occupational Hygiene* 47.3 (2003), pp. 187–200. ISSN: 0003-4878. DOI: [10.1093/annhyg/meg032](https://doi.org/10.1093/annhyg/meg032). URL: <https://doi.org/10.1093/annhyg/meg032>.
- [132] ICRP. *Human Respiratory Tract Model fro Radiological Protection*. Vol. 24. 1-3. Pergamon, 1994.

- [133] J. Heyder. “Deposition of Inhaled Particles in the Human Respiratory Tract and Consequences for Regional Targeting in Respiratory Drug Delivery.” In: *Proceedings of the American Thoracic Society* 1.4 (2004), pp. 315–320. DOI: [10.1513/pats.200409-046TA](https://doi.org/10.1513/pats.200409-046TA). URL: <https://www.atsjournals.org/doi/abs/10.1513/pats.200409-046TA>.
- [134] J. Ching and M. Kajino. “Aerosol mixing state matters for particles deposition in human respiratory system.” In: *Scientific Reports* 8.1 (2018), p. 8864. ISSN: 2045-2322. DOI: [10.1038/s41598-018-27156-z](https://doi.org/10.1038/s41598-018-27156-z). URL: <https://doi.org/10.1038/s41598-018-27156-z>.
- [135] V. Martins, M. Cruz Minguillón, T. Moreno, X. Querol, E. de Miguel, M. Capdevila, S. Centelles, and M. Lazaridis. “Deposition of aerosol particles from a subway microenvironment in the human respiratory tract.” In: *Journal of Aerosol Science* 90 (2015), pp. 103–113. ISSN: 0021-8502. DOI: <https://doi.org/10.1016/j.jaerosci.2015.08.008>. URL: <https://www.sciencedirect.com/science/article/pii/S0021850215001342>.
- [136] M. Lehnert, B. Pesch, A. Lotz, J. Pelzer, B. Kendzia, K. Gawrych, E. Heinze, R. Van Gelder, E. Punkenburg, T. Weiss, M. Mattenklott, J.-U. Hahn, C. Möhlmann, M. Berges, A. Hartwig, T. Brüning, and W. S. Group. “Exposure to inhalable, respirable, and ultrafine particles in welding fume.” eng. In: *The Annals of occupational hygiene* 56.5 (2012), pp. 557–567. ISSN: 1475-3162. DOI: [10.1093/annhyg/mes025](https://doi.org/10.1093/annhyg/mes025). URL: <https://pubmed.ncbi.nlm.nih.gov/22539559https://www.ncbi.nlm.nih.gov/pmc/articles/PMC3387834/>.
- [137] W.-C. Su, Y. Chen, M. Bezerra, and J. Wang. “Respiratory deposition of ultrafine welding fume particles.” In: *Journal of Occupational and Environmental Hygiene* 16.10 (2019), pp. 694–706. ISSN: 1545-9624. DOI: [10.1080/15459624.2019.1652306](https://doi.org/10.1080/15459624.2019.1652306). URL: <https://doi.org/10.1080/15459624.2019.1652306>.
- [138] A. Ibalduerra, H. Wichmann, and W. Kreyling. “Epidemiological Evidence on Health Effects of Ultrafine Particles.” In: *Journal of Aerosol Medicine* 15.2 (2002), pp. 189–201.
- [139] D. Q. Rich, W. Zareba, W. Beckett, P. K. Hopke, D. Oakes, and M. W. Frampton. “Are Ambient Ultrafine , Accumulation Mode , and Fine Particles Associated with Adverse Cardiac Responses in Patients Undergoing Cardiac Rehabilitation ?” In: *June 2014* (2012). DOI: [10.1289/ehp.1104262](https://doi.org/10.1289/ehp.1104262).
- [140] World Health Organization. *EUROPEAN TOBACCO USE - Trends Report 2019*. Tech. rep. World Health Organization Europe, 2019.
- [141] D. M. Brown, M. R. Wilson, W. Macnee, V. Stone, K. Donaldson, and K. T. Appl. “Size-dependent proinflammatory effects of ultrafine polystyrene particles: a role for surface area and oxidative stress in the enhanced activity of ultrafines.” In:

- Toxicol Appl Pharmacol* 199 (2001), pp. 191–199. DOI: [10.1006/taap.2001.9240](https://doi.org/10.1006/taap.2001.9240).
- [142] J. A. Araujo, B. Barajas, M. Kleinman, X. Wang, B. J. Bennett, K. W. Gong, M. Navab, J. Harkema, C. Sioutas, A. J. Lulis, and A. E. Nel. “Ambient Particulate Pollutants in the Ultrafine Range Promote Early Atherosclerosis and Systemic Oxidative Stress.” In: *Circulation Research* 102.5 (2008), pp. 589–596. DOI: [10.1161/CIRCRESAHA.107.164970](https://doi.org/10.1161/CIRCRESAHA.107.164970).
- [143] P. Orellano, J. Reynoso, N. Quaranta, A. Bardach, and A. Ciapponi. “Short-term exposure to particulate matter (PM10 and PM2.5), nitrogen dioxide (NO2), and ozone (O3) and all-cause and cause-specific mortality: Systematic review and meta-analysis.” In: *Environment International* 142 (2020), p. 105876. ISSN: 0160-4120. DOI: <https://doi.org/10.1016/j.envint.2020.105876>. URL: <https://www.sciencedirect.com/science/article/pii/S0160412020318316>.
- [144] S. K. Friedlander. “THE CHARACTERIZATION OF AEROSOLS DISTRIBUTED WITH RESPECT TO SIZE AND CHEMICAL COMPOSITION*.” In: 1 (1970), pp. 295–307.
- [145] S. K. Friedlander. “THE CHARACTERIZATION OF AEROSOLS DISTRIBUTED WITH RESPECT TO SIZE AND CHEMICAL COMPOSITION II. CLASSIFICATION AND DESIGN OF AEROSOL MEASURING DEVICES*.” In: 2 (1971), pp. 331–340.
- [146] P. H. McMurry. “A review of atmospheric aerosol measurements.” In: *Atmospheric Environment* 34 (2000).
- [147] A. Broström, K. I. Kling, K. S. Hougaard, and K. Mølhave. “Complex Aerosol Characterization by Scanning Electron Microscopy Coupled with Energy Dispersive X-ray Spectroscopy.” In: *Scientific Reports* 10.1 (2020), p. 9150. ISSN: 2045-2322. DOI: [10.1038/s41598-020-65383-5](https://doi.org/10.1038/s41598-020-65383-5). URL: <https://doi.org/10.1038/s41598-020-65383-5>.
- [148] J. Ching, K. Adachi, Y. Zaizen, Y. Igarashi, and M. Kajino. “Aerosol mixing state revealed by transmission electron microscopy pertaining to cloud formation and human airway deposition.” In: *npj Climate and Atmospheric Science* 2.1 (2019), p. 22. ISSN: 2397-3722. DOI: [10.1038/s41612-019-0081-9](https://doi.org/10.1038/s41612-019-0081-9). URL: <https://doi.org/10.1038/s41612-019-0081-9>.
- [149] N. Sang-Nourpour and J. S. Olfert. “Calibration of optical particle counters with an aerodynamic aerosol classifier.” In: *Journal of Aerosol Science* 138 (2019), p. 105452. ISSN: 0021-8502. DOI: <https://doi.org/10.1016/j.jaerosci.2019.105452>. URL: <https://www.sciencedirect.com/science/article/pii/S0021850219305567>.

- [150] N. Tippayawong. “An overview of differential mobility analyzers for size classification of nanometer-sized aerosol particles.” In: *Songklanakarín J. Sci. Technol* 30 (2).March (2008), pp. 243–256.
- [151] M. R. Stolzenburg and P. H. McMurry. “An Ultrafine Aerosol Condensation Nucleus Counter.” In: *Aerosol Science and Technology* 14.1 (1991), pp. 48–65. ISSN: 0278-6826. DOI: [10.1080/02786829108959470](https://doi.org/10.1080/02786829108959470). URL: <https://doi.org/10.1080/02786829108959470>.
- [152] A. I. Barros, F. C. Pinheiro, C. D. B. Amaral, R. Lorençatto, and J. A. Nóbrega. “Aerosol dilution as a simple strategy for analysis of complex samples by ICP-MS.” In: *Talanta* 178 (2018), pp. 805–810. ISSN: 0039-9140. DOI: <https://doi.org/10.1016/j.talanta.2017.10.024>. URL: <https://www.sciencedirect.com/science/article/pii/S0039914017310639>.
- [153] J. C. Hains, L. A. Chen, B. F. Taubman, B. G. Doddridge, and R. R. Dickerson. “A side-by-side comparison of filter-based PM_{2.5} measurements at a suburban site : A closure study.” In: *Atmospheric Environment* 41 (2007), pp. 6167–6184. DOI: [10.1016/j.atmosenv.2007.04.008](https://doi.org/10.1016/j.atmosenv.2007.04.008).
- [154] S Akbarnezhad, A Amini, A Soltani Goharrizi, T Rainey, and L Morawska. “Capacity of quartz fibers with high filtration efficiency for capturing soot aerosol particles.” In: *International Journal of Environmental Science and Technology* 15.5 (2018), pp. 1039–1048. ISSN: 1735-2630. DOI: [10.1007/s13762-017-1457-1](https://doi.org/10.1007/s13762-017-1457-1). URL: <https://doi.org/10.1007/s13762-017-1457-1>.
- [155] D Holstius, A. Pillarissetti, K Smith, and E Seto. “Field calibrations of a low-cost aerosol sensor at a regulatory monitoring site in California.” In: *Atmospheric Measurement Techniques* 7 (2014). DOI: [10.5194/amt-7-1121-2014](https://doi.org/10.5194/amt-7-1121-2014).
- [156] S. Sousan, K. Koehler, G. Thomas, J. H. Park, M. Hillman, A. Halterman, and T. M. Peters. “Inter-comparison of low-cost sensors for measuring the mass concentration of occupational aerosols.” In: *Aerosol Science and Technology* 50.5 (2016), pp. 462–473. ISSN: 0278-6826. DOI: [10.1080/02786826.2016.1162901](https://doi.org/10.1080/02786826.2016.1162901). URL: <https://doi.org/10.1080/02786826.2016.1162901>.
- [157] L. A. Chen, J. C. Chow, J. G. Watson, H. Moosm, and W. P. Arnott. “Modeling reflectance and transmittance of quartz-fiber fillter samples containing elemental carbon particles : Implications for thermal / optical analysis.” In: *Journal of Aerosol Science* 35 (2004), pp. 765–780. DOI: [10.1016/j.jaerosci.2003.12.005](https://doi.org/10.1016/j.jaerosci.2003.12.005).
- [158] C. G. Camara, J. V. Escobar, J. R. Hird, and S. J. Putterman. “Correlation between nanosecond X-ray flashes and stick – slip friction in peeling tape.” In: *Nature* 455.October (2008). DOI: [10.1038/nature07378](https://doi.org/10.1038/nature07378).
- [159] J. R. Hird, C. G. Camara, S. J. Putterman, J. R. Hird, C. G. Camara, and S. J. Putterman. “A triboelectric x-ray source A triboelectric x-ray source.” In: *Applied Physics Letters* 133501.98 (2011), pp. 1–4. DOI: [10.1063/1.3570688](https://doi.org/10.1063/1.3570688).



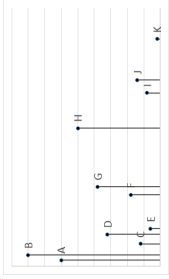

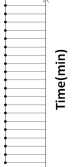

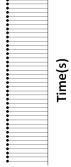
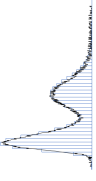

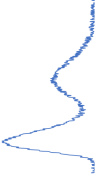
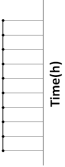
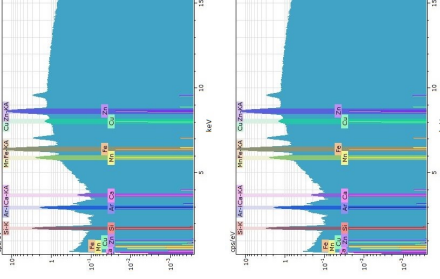
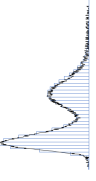

- [160] D Krämer, B Lühmann, and R Frahm. “New developments for the investigation of hard X-rays emitted by peeling adhesive tapes New developments for the investigation of hard X-rays emitted.” In: *Review of Scientific Instruments* 055104.84 (2013). DOI: [10.1063/1.4803155](https://doi.org/10.1063/1.4803155).
- [161] V. B. Rajeswari, S. S. Paramashivan, S. Mohan, S. K. Albert, and R. M. “Effect of substituting fine rutile of the flux with nano TiO₂ on the improvement of mass transfer efficiency and the reduction of welding fumes in the stainless steel SMAW electrode.” In: *High Temperature Materials and Processes* 39.1 (2020), pp. 117–123. DOI: [doi:10.1515/htmp-2020-0030](https://doi.org/10.1515/htmp-2020-0030). URL: <https://doi.org/10.1515/htmp-2020-0030>.
- [162] Tinsine Electronics. *GSM/GPRS Shield Datasheet*. URL: <https://www.tinyosshop.com/datasheet/GSM%20Shield%20Datasheet.pdf>.
- [163] SIMCOM. *TCP/IP Application Note*. URL: https://simcom.ee/documents/SIM900/SIM900_TCPIP_Application%20Note_V1.02.pdf.

A P P E N D I X



APPENDIX 1

Table A.1: Aerosol measuring instruments classification. *Examples of measuring techniques.

Instrument	Size distribution	Time	Composition	Quantity
Perfect single particle measurement				$N_{\infty} g(t, v, n_1, \dots, n_{k-1}) dv dn_i$
Physical size distribution * Electrical mobility analyzer				$N_{\infty} \cdot \int_{v_1}^{v_2} \int_{n_1}^{n_2} g(v) dv dn_i dt$
Continuous measurements of integral properties * Condensation nuclei counter * Cloud condensation nuclei * Mass concentration				$N_{\infty} \cdot \int_0^{\infty} W(v) g(v) dv dn_i$
Size resolved mass measurements on a integrated time interval * Cascade impactor				$N_{\infty} \cdot \int_{v_1}^{v_2} \int_{n_1}^{n_2} \rho_p \cdot g(v) dv dn_i dt$
Time and size integrated measurements of composition * Filter + composition analyser				$N_{\infty} \cdot \int_{v_1}^{v_2} \int_0^{\infty} n_j \cdot g(v) dv dn_i dt$
Time integrated size and composition measurements * Impactor + chemical analyser				$N_{\infty} \cdot \int_{v_1}^{v_2} \int_{n_1}^{n_2} g(v) n_j dv dn_i dt$



APPENDIX 2

This appendix provides an in-depth analysis of the electronic and programming side of the development of the second prototype, going through the list of systems mentioned in Section 5.3. The full version of the samples of code discussed will be provided in Appendix C.

B.1 Power source and management

The components are powered with a standard AC/DC transformer with 12 V and 2 A. The 12 V were chosen based on the component that required more voltage which was the 12 V 9 mm DC fan. Also this voltage is within the range needed to power up the Arduinos like we mentioned above. Therefore, these 12 V can be used directly to power both the Arduinos and the DC fan. In order to obtain the 5 V needed for the two motors we need to step down this voltage which is simpler than the other way around. The 2 A was actually an increment over a previous AC/DC transformer with 1A that we tried and was not able to provide the power needed without overheating. With this one, on the other hand we managed to get a stable operation over the course of days/months.

Overheating is actually one of the power management concerns through all of this design since operation does not rely on a steady current drain. Instead the measuring process done by this device relies on several triggers that activate/deactivate components and consequently small bursts of electric current happen in the corresponding components. Therefore, we went through numerous hardware and software optimizations steps in order to get the available components to comply with expected performance. While there are some parts that don't need power management at all like the GSM/GPRS shield, the transistor and the voltage regulators actually needed some tinkering in order to not overheat. The voltage regulator before the step motor, for example, only activates for less

than five seconds in each measurement, which is enough, but if it wasn't it would burn.

B.2 DC fan

The DC fan was really the only system in our first prototype, which in that case was directly wired to the power source via a manual mechanical switch. In this case, as the DC fan operation is part of a larger system, we needed to make some small tweaks in order for this to be compatible with the automation/remote control mindset. There were plenty of solutions that we could have used but in the end we went with a digital switch based on n-Channel Enhancement mode MOSFET (Metal Oxide Semiconductor Field Effect Transistor).

The MOSFET is a type of field effect transistor with an insulated gate from the channel where the voltage at the gate terminal determines the conductivity. Simply put, this kind of electronic component is constituted by 3 terminals: the gate, the source and the drain. It uses the field effect on a doped semiconductor at its core to enable or disable electric charges to flow from the source to the drain. This works as digital switch where the voltage at the gate controls the regime of conduction of the transistor.

In our setup, as we can see in Figure 5.13, we connect the MOSFET gate directly to the gate to control it with a digital output of 0 or 1 which equates to 0 V and 5 V respectively. The source is grounded and the drain is connected to the negative terminal of the DC Fan. Its positive terminal is connected to the 12 V line of the supply. Therefore, when we send a digital 0 to the MOSFET gate the DC Fan is on a open circuit and thus no current flows. On the other hand, when we send a digital 1 the DC fan activates because 12 V are applied to its terminals.

In terms of code in the Arduino framework this is a very easy task to accomplish with the following lines (from C.1.2) being used in the slave program¹:

```
1 int IN3 = 7;
2
3 pinMode(IN3, OUTPUT);
4 digitalWrite(IN3, LOW);
5
6 void dcfan(String com){
7   if (com == "on"){
8     digitalWrite(IN3, HIGH);
9   }
10  else if (com == "off"){
11    digitalWrite(IN3, LOW);
12  }
13 }
```

¹Note that every snippet of code might not be exactly as it was implemented and is usually stripped down to its core fundamentals for easier understanding of each section. For full versions refer to C.

where a void function `dcfan()` is defined to accept an input from the I²C communication *com* and do a digital write accordingly to the pin *IN3* (digital I/O pin 7) that is connected to the MOSFET and define the output as *HIGH* or *LOW*.

B.3 Step motor control

As it has been stated before we have chosen to use in this work the 42BYGHM809 stepper motor. Even though it is labeled at working voltage of 2.7 V we were able to operate it at 5 V provided from the voltage regulators as this is only requested to use once for a 1/2 seconds maximum in each measurement that has time frame of minutes or hours. This overvoltage operation leads to more current being pulled which causes heating of both the voltage regulators and the motor driver dissipators. Nevertheless, we managed in our final iteration of the circuitry, the reliable operation of this step motor without any overheating. By adding these two extra electronic layers consisting of voltage regulator and motor driver we are also adding extra protection from these current spikes to our motor.

The voltage regulator is a passive electronic component and thus doesn't perform any kind of digital control. We only need to properly connect this component to the 12 V voltage line and the ground and it produces a 5 V output. However, the operation of the motor driver needs digital control by the slave Arduino. The code used for this control of the driver and consequently the step motor is (from [C.1.2](#)):

```
1 #include <Stepper.h>
2 int IN4 = 8;
3 int IN5 = 9;
4 int IN6 = 10;
5 int IN7 = 11;
6
7 const int stepsPerRevolution = 400; // 400 steps=1 revolution
8
9 // initialize the stepper library on pins 8 through 11:
10 Stepper myStepper(stepsPerRevolution, 8, 9, 10, 11);
11
12 pinMode(IN4, OUTPUT);
13 pinMode(IN5, OUTPUT);
14 pinMode(IN6, OUTPUT);
15 pinMode(IN7, OUTPUT);
16
17 myStepper.setSpeed(60);
18
19 void stepper() {
20   myStepper.step(stepsPerRevolution);
21   delay(500);
22   digitalWrite(IN4, LOW);
23   digitalWrite(IN5, LOW);
24   digitalWrite(IN6, LOW);
```

```
25 | digitalWrite(IN7, LOW);  
26 | delay(500);  
27 | }
```

where we define void function `stepper()` to perform one full rotation of the step motor. This implementation takes advantage of the stepper motor library that is included with the Arduino software that we import as *Stepper.h*. With this library we can create an object of the type *Stepper* with the information on the number of steps per revolution (*stepsPerRevolution*), which varies from step motor to step motor, as well as the information of the pins that will be used for this control (digital I/O pins 8,9,10,11). Then by performing one of the supported operations for this type of object - `.step()` - we can activate the motor driver to produce a stepping operation with the number of steps needed. The library itself is programmed to send a sequence of *LOW* and *HIGH* on all 4 wires that will via the motor driver, activate/deactivate the coils of the step motor to make the precise motion needed for the application at hand. In our device we perform 400 steps in order to achieve one full rotation every time this function is called at the start of a measurement. This operation takes about 500 ms and then we proceed to set all pins to *LOW* to prevent any reminiscent unwanted current to circulate in the motor coils.

B.4 DC motor control

The DC motor from the recycled DVD tray is much more straightforward. It is a standard 5 V DC motor which means that if you set a voltage difference between its terminals of a value on the range [-5 V, 5 V] you will activate motion on the motor. The bigger the absolute value of voltage difference is the higher the speed at which it performs. Applying a positive voltage difference makes the motor turn one way and applying a negative voltage difference makes it turn the other way.

Having this motor connected to a motor driver serves two purposes: electric safety from current peaks and allows us to control when and how long the motor is activated. To achieve this we used the following code (from [C.1.2](#)):

```
1 | int IN1 = 5;  
2 | int IN2 = 6;  
3 |  
4 | pinMode(IN1, OUTPUT);  
5 | pinMode(IN2, OUTPUT);  
6 |  
7 | void open() {  
8 |     digitalWrite(IN1, LOW);  
9 |     digitalWrite(IN2, HIGH);  
10 |    delay(200);  
11 |  
12 |    digitalWrite(IN1, HIGH);  
13 |    digitalWrite(IN2, HIGH);  
14 |    delay(500);
```

```

15  digitalWrite(IN1, LOW);
16  digitalWrite(IN2, LOW);
17  delay(500);
18  }
19
20  void close(){
21    digitalWrite(IN1, HIGH);
22    digitalWrite(IN2, LOW);
23    delay(200);
24
25    digitalWrite(IN1, HIGH);
26    digitalWrite(IN2, HIGH);
27    delay(500);
28    digitalWrite(IN1, LOW);
29    digitalWrite(IN2, LOW);
30    delay(500);
31  }

```

where we define two void functions `open()` and `close()`. Basically, we set the pins that connect to the motor driver (digital I/O 5 and 6) to opposing logic voltage levels. This way we are able to make the opening and closing motion with the sliding tray. As we are using a supply of 5 V from the voltage regulator which is the maximum for this motor, we get full speed in both positive directions and thus these operations are concluded in 200 ms. Afterwards, we redefine our output pins firstly as both *HIGH* then both *LOW*. This is the standard procedure to safely stop the motion of this kind of motor.

B.5 I²C communication

As it was stated above, in this device development in order to subdivide tasks and stay within memory limits we have adopted a two Arduino system with a master and a slave. The slave is in charge of actuators and its functionalities have been showcased in the snippets of code in the last subsections. The master has the task to coordinate the operation of the slave and communicate with an external server. The communication between the two Arduinos is via the I²C protocol and hence the reason we call one of the Arduinos master and the other slave. This is a very popular, synchronous, serial communication protocol that was developed in 1982 by the company *Philips*. In a very brief description, we can say that the connection between two devices is established via 2 bidirectional lines SDA (serial data line) and SDK (serial clock line). Through these two lines the protocol dictates that the master initiates communication with the slave via its physical address and sends not only the packets of data via SDA but also the clock timings via SDK. The slave usually cannot start the communication but can respond if programmed accordingly.

As expected, this section will include the code related to both the master and the slave programming. Starting with the master we have (from [C.1.1](#)):

```

1  #include <Wire.h>

```

```
2
3 Wire.begin();
4
5 sample_time=atol(resp)*1000*60;
6 Wire.beginTransmission(9); // transmit to device #9
7 Wire.write("m"); // sends
8 Wire.endTransmission(); // stop transmitting
9 delay(200);
10 Wire.beginTransmission(9); // transmit to device #9
11 Wire.write(resp); // sends
12 Wire.endTransmission(); // stop transmitting
13 delay(sample_time);
```

where most of this code is inside the main loop of the master program. I²C is very straightforward to implement communication protocol with the Arduino software, as once again, it comes with the library to implement it, imported as *Wire.h*. Basically, communication is open via the `begin()` operation and then transmission can be started via the `beginTransmission()` operation to the slave address. In this case we send the order to start measuring with an *m* character and then transmit the desired duration of the sampling process via the variable *resp*. Finally, the master waits idle for the duration of sampling time.

On the slave side we have the following code (from C.1.2):

```
1 #include <Wire.h>
2
3 String data= "";
4 bool op= 0;
5
6 Wire.begin(9); // Start the I2C Bus as Slave on address 9
7 Wire.onReceive(receiveEvent); // Attach a function to trigger on receive
8
9 void receiveEvent(int bytes) {
10     data="";
11     while( Wire.available()){
12         data+= (char)Wire.read();
13     }
14     Serial.println(data);
15 }
16
17 void loop() {
18     if (data=="m") {
19         while(data=="m"){
20             delay(500);
21         }
22         if(data!="m") {
23             sample_time=data.toInt()*1000*60;
24             open();
25             op=1;
26             stepper();
```



```
27     close();
28     op=0;
29     dcfan("on");
30     delay(sample_time);
31     dcfan("off");
32     data="";
33 }
34 }
35 }
```

where we initiate the I²C wire ports as slave in address 9 and make it wait for data. Then we proceed to attach a function to the trigger associated with the data reception event. In this function, we basically transcribe the serialized char packets sent and reconstruct the original string message. Meanwhile, we have the main slave loop running. In this snippet we show the most important part of our loop function that is the detection of the information to measure and according procedure. In our actual deployed code we have several more functions to operate individual actuators and show status of operation through LEDs, among other features, but those end up serving more of debug tools. In this loop, we wait for the message to measure, that is the char *m* as we have seen in the master code. When this happens, the slave knows it needs to make a measurement however it waits for information on sampling time. When this information arrives, the slave starts the procedure and invokes many of the functions already shown in other snippets of code. Nevertheless, the procedure is: open sample holder, activate stepper to unroll filters, close sample holder, turn on the DC fan, wait sampling time, turn off the DC fan and go back to waiting for a measurement.

B.6 Server communication via GSM/GPRS

GSM communication and server setup was the hardest part of the development of this device. There were plenty of difficulties in the task of connecting this device to a server that we could control. The major one stems from the fact that it is being done by GSM/GPRS instead of the much more straightforward Ethernet cable connection or even the Wifi wireless connection that would still be much easier to implement. The drawbacks of GSM/GPRS are numerous from the lack of support, to the difficulty to operate within a plant facility that acts like a Faraday cage due to its metallic construction and makes GSM cell reception unreliable at best. Nevertheless, given the fact that corporate secrecy might be compromised by giving this device access to the plant internal network we had to pursue this solution.

The correct deployment of both a client and server took several iterations and eventually spread across a few months. Not only it was needed to build a server from scratch, but also a client program for the Arduino with GSM shield that was stable enough to guarantee continuous communication. As we were exploring for the first time both of these endeavors, many setbacks occurred from limited memory to harder to figure out

instability issues. In the end, however, we managed to get both parts fully operational without any known bugs and will proceed to present the final outcome.

GSM communication

Let's start with the client program that we run on the Arduino master with the GSM/GPRS shield. The one we used for this work was the TinySine SIM 900 Arduino shield[162]. This shield comes with several features being the most important the SIM card holder, the GSM antenna and the SIM 900 modem[163]. Inserting an SD SIM card on the card holder and installing the shield on top of the Arduino provides the opportunity to connect this device to the internet. Communication between the Arduino and the SIM 900 modem is achieved via software serial by the for digital I/O pins 0 and 1 that are the RX (receiver) and TX (transaction) lines respectively. These are the same lines used by the Arduino USB bootloader.

For this purpose, every step of the process must be programmed at a very low level, since there are very few libraries we can use that actually work as intended for our setup. The type of instructions that a SIM card accepts to connect it's network are in the form of GSM AT commands which is the abbreviation for ATtention commands. Another reason for this designation is that every command starts with *AT*. This a widely used technology for many types of the older dial-up internet modems all the way to modern mobile phones GSM modems. However, even though there are some similarities across all modems AT commands, most of them are modem specific. These set of commands can be used not only for establishing an internet connection but can also be used to send SMS and start phone calls. In this work we obviously didn't use any of those types of communication.

Having stated the complexity of establishing all the communications needed for this work, the actual number of lines of code is not that extensive. The complexity in this case comes from choosing the exact right commands, at the exact timing and order, so that the communication doesn't stop, fail or bug out. The initialization of the modem as well as the attachment to the GSM network looks like this in our Arduino code (this is a condensed representation as we will not go into detail of every module used, full version is C.1.1):

```
1 #include "SIM900.h"
2 #include <SoftwareSerial.h>
3 #include "inetGSM.h"
4
5 static char at1[3]="at";
6 static char at2[9]="at+cpin?";
7 static char at3[13]="at+cpin=3220";
8 static char at4[8]="at+csq";
9 static char at5[9]="at+creg?";
10 static char at6[10]="at+cgatt?";
11 static char at7[55]="at+cstt=\"net2.vodafone.pt\", \"vodafone\", \"vodafone\"";
12 static char at8[9]="at+ciicr";
```

```

13 static char at9[9]="at+cifsr";
14
15 void setup(){
16   if (gsm.begin(9600))
17     Serial.println(F("\nstatus=READY"));
18   else Serial.println(F("\nstatus=IDLE"));
19   gsmcommand(at1,true);
20   gsmcommand(at2,true);
21   gsmcommand(at3,true);
22   gsmcommand(at4,false);
23   gsmcommand(at5,false);
24   gsmcommand(at6,false);
25   gsmcommand(at7,false);
26   gsmcommand(at8,false);
27   gsmcommand(at9,false);
28   gsm.WhileSimpleRead();
29 }

```

where we import some libraries that give us some access to some functions like `gsm.begin()`. Basically, in this part of the setup we want to follow a recipe to get our device logged in into the GSM network. We need to: unlock the sim via PIN, then ask for registration in the network, then provide our carrier APN (access point name) information, in this case we have SIM from Vodafone, then establish the GPRS connection and get a local IP for our device. Note, that some commands are actual instructions and other act like queries of the status of the connection. Regardless, we have found that all of them were actually needed for proper setup. Note that we didn't use *AT* strings directly onto the `gsm` commands. This was done for the purpose of memory optimization, where we define the strings as static variables in order to save some dynamic memory.

After being registered into the network we can then start the processes that will give us access to the internet. Very briefly, we can say that the steps needed for this are to first establish a TCP/IP connection with the server IP address and then we need to do HTTP interactions in the forms of *HTTP get* and *HTTP post*. Other solutions could have also been possible if the Arduino IP address was public and not local IP inside the Vodafone network. This would allow us to program a server on the Arduino that would wait for requests. As that is not possible in this case our Arduino must request periodically information on the measurement status from a remote server. Our code for the communication with the server and slave looked like this, with some functions being omitted for easier reading (from C.1.1):

```

1 #include "SIM900.h"
2 #include <SoftwareSerial.h>
3 #include "inetGSM.h"
4
5 InetGSM inet;
6 char msg[200];
7 char resp[16];

```

```
8
9 static char server[15]="193.136.125.67";
10 static char path1[12]="/acq/temp1/";
11 static char path2[13]="/acqt/temp1/";
12
13 void loop() {
14   httpget(path1);
15   Serial.println(F("resp"));
16   Serial.println(resp[0]);
17   if(resp[0]=='N'){
18     delay(1000);
19     Serial.println(F("No"));
20     delay(200);
21   }
22   else if(resp[0]=='G'){
23     delay(1000);
24     httpget(path2);
25     sample_time=atol(resp)*1000*60;
26     Serial.print(F("Sample_time:_"));
27     Serial.println(sample_time);
28     delay(4000);
29     Wire.beginTransaction(9); // transmit to device #9
30     Wire.write("m"); // sends
31     Wire.endTransmission(); // stop transmitting
32     delay(200);
33     Wire.beginTransaction(9); // transmit to device #9
34     Wire.write(resp); // sends
35     Wire.endTransmission(); // stop transmitting
36     httppost();
37     delay(sample_time);
38     httppostt();
39   }
40   else{
41     delay(1000);
42     delay(200);
43   }
44   delay(60000);
45 }
```

where we define the main loop for our Arduino master code. Note that in this snippet of the code there are different `httpget()` and `httppost()` but not any function for the TCP/IP connection start. The reason for this is that the TCP/IP is open and close for every `httpget()` or `httppost()` inside their corresponding functions (that are omitted). Nevertheless, we provide to the Arduino both the IP address of the public server `193.136.125.67` and the paths for the measurement information `/acq/temp1/` and `/acqt/temp1/`.

The Arduino starts by doing an `httpget(path1)` to get the information from the server if it is supposed to start a measurement or not. The possible responses are *Go* or *No*. If not, it basically waits for a little over 1 minute to try again. This was done for the purpose of

not overloading both Arduino and the network with constant requests as well as to save some mobile data. The downside is that we can wait up to 1 minute for the measurement procedure to start which is completely acceptable for our purposes. If the response from the server is affirmative then it needs to do an `httpget(path2)` to obtain the measuring time. Once this TCP/IP connection closes with response obtained the information is sent via I²C to the slave as we discussed above. When the measurement starts the Arduino sends an `httppost()` changing the server side measurement status to *Started*. In the end of the sampling time it sends another `httppost()` changing the server side measurement status to *Finished*.

Server setup

Let's now make an overview of how we set up the server. When looking into this part of the project, we opted to build this server to be a public IP address because, as we explained above, the Arduino couldn't be addressed specifically inside its network. This meant that all kind of connections must be done the other way around, with the Arduino making requests and the server idle waiting for them. We achieved this by contacting the IT department having them register our DNS - <http://protautoeuropa.pub.df.fct.unl.pt/>, to a virtual machine (VM) with public IP 193.136.125.67. Inside this VM we were then able to build our public server. In this section we will now proceed to explain how we built this server, what functions are implemented and what is the meaning of the information present in the front page (whose clickable url is shown above).

We decided to develop the server and website with the Django framework. Django is a high-level Python Web framework that encourages rapid development and clean, pragmatic design. This is a very well documented and popular framework that is relatively easy to get into. Adding that to the versatile capabilities of python programming with thousands of libraries for the most diverse applications, this seemed like the best approach.

Django starts with an empty project where you have file that is called *manage.py* which acts like your main program and when run compiles the rest of the files. You don't usually tinker with this file, instead there are other files that will build the functionalities and appearance of your server, such as: *settings.py* (C.2.6), *urls.py* (C.2.4C.2.5), *models.py* (C.2.2), *views.py* (C.2.1) and *admin.py* C.2.3. These are the files that you will need build upon in order to program your server.

In C.2.6 we define the global settings for our server. Properties like the server directory, language, timezone, allowed hosts, type of database used, etc. can be defined here. From all these perhaps the most relevant to refer is that our server was built using database type known *sqlite3*. This is important because different databases have different requirements and different ways to query the information stored in them. Server databases run in background and are updated with each new interaction with the server. In order to change any type of variable or restructure an existing one you need to migrate the database. This

allows for constant track of the server operation that is persistent even when the server is not running or even if the machine is turned off.

There exist actually two files called *urls.py* (C.2.4C.2.5) in two different directories of your server project. Simply put, these files have the task to reference what is shown using what path in the server website. As it might be straightforward to assume you have to program every view of your website to do something specific. *urls.py* files summarize all the possible views and defines their paths.

The core of our server will be defined in *models.py* and *views.py*. In C.2.2 we define the classes of the objects available in the database as well as their properties and operations. In this file we define two models classes *SensorType* and *SensorData*. The *SensorType* class is defined with the following code:

```
1 from django.db import models
2 from django.core.validators import validate_comma_separated_integer_list
3
4 class SensorType(models.Model):
5     name = models.CharField(max_length=100)
6     code = models.SlugField(max_length=50)
7     description = models.TextField(blank=True)
8     min_value = models.FloatField()
9     max_value = models.FloatField()\
10     units = models.CharField(max_length=100)
11     a_type = [('0', 'Single'), ('1', 'Multiple'),]
12     acq_type = models.CharField(max_length=2, choices=a_type, default=0,)
13     acq_time = models.IntegerField(default=0)
14     acq_times = models.CharField(max_length=10000,validators=[
15         ↪ validate_comma_separated_integer_list], blank=True, null=True,default='
16         ↪ ')
17     acq = [('0', 'Idle'),('1', 'Waiting_for_aquisition'),('2', 'Acquiring'),('3',
18         ↪ 'Acquisition_complete'), ]
19     acquiring = models.CharField(max_length=2, choices=acq, default=0,)
20     val_type = [('0', 'Single_Value'), ('1', 'List'),]
21     data_type = models.CharField(max_length=2, choices=val_type, default=0, )
22     log= models.FileField(upload_to='',default='log.txt')
23     rlog= models.FileField(upload_to='',default='requestlog.txt')
24
25     def ch_acq(self,val):
26         self.acquiring=val
27
28     def load_acqs(self):
29         values = [int(x) for x in self.acq_times.split(',') if x]
30         return values
31
32     def acq_update(self):
33         try:
34             values=self.load_acqs()
35         except (AttributeError):
36             values=[]
```

```

34     try:
35         del values[0]
36         self.acq_times=str(values).strip('[]')
37     except (IndexError):
38         pass
39     (...)

```

where we define the properties and operations for objects of this class. This class has the purpose of generating different types of sensors that the Arduino can then refer by their code when delivering data or asking if an acquisition of that sensor is required. This will allow us to create different kinds of inputs for telemetry purposes that the Arduino can then send.

With this in mind, every *SensorType* object has a full name that shows on the website (*name*), a *code* which is an abbreviated name to refer to this sensor and brief description field for administrative reasons (*description*). It also has a defined minimum and maximum value (*min_value* and *max_value*) and units field (*units*). Then we define the acquisition type (*acq_type*) has a single measurement or multiple sequential measurements. If the first is chosen it has a property *acq_time* which is the number of minutes to acquire. If multiple measurements is chosen then we use the property *acq_times* for listing all the different sampling times in the sequential set of measurements. Then we define a measurement status property *acquiring* which indicates if this sensor is: idle, waiting for and acquisition, acquiring or finished. The output type of this sensor is defined in the property *data_type* has a single value or an array. Finally, regarding properties there are two *.txt* log files which save information on the measurement activity with timestamps (*log*) and acquisitions requests with timestamps (*rlog*).

This class also includes three main defined operations: *ch_acq*, *load_acqs* and *acq_update*. With *ch_acq* we can internally change the property *acquiring* to the status parsed. *load_acqs* is an internal operation that returns the measuring times programmed in the current acquisition set. Finally, *acq_update* updates the queue of measurements in the set removing already finished acquisitions.

The second class defined in these models files is the *SensorData* which uses the following code:

```

1  from django.db import models
2  from django.utils.dateparse import parse_datetime
3
4  class SensorData(models.Model):
5      time = models.DateTimeField(auto_now_add=True)
6      type = models.ForeignKey(SensorType, related_name='data', on_delete=models.
7          ↪ CASCADE)
8      value = models.FloatField(default=0)
9      val_list=models.CharField(max_length=10000,default=list)
10     (...)

```

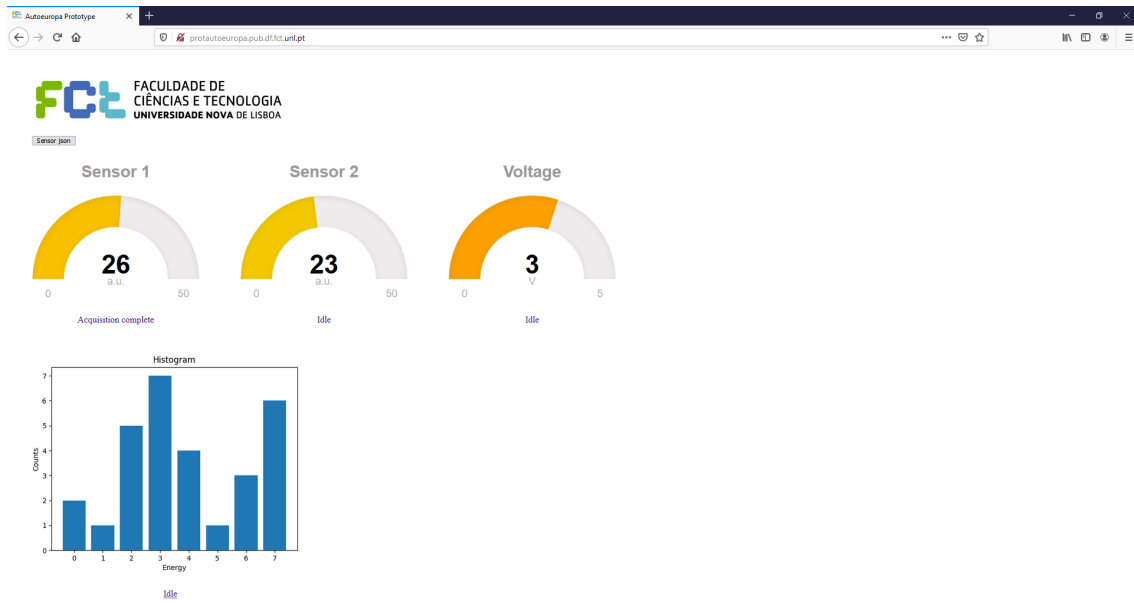


Figure B.1: Server homepage developed for this thesis.

where we define the properties of these classes of objects. This is a simpler object whose purpose is solely to carry the data from the sensor. Hence, this object will have an attribute *time* which is the timestamp and a type of data which will be associated with corresponding *SensorType* object's type of output. Accordingly, this *SensorData* object will either use the property *value* or the property *val_list*.

Let's now take a look at the views file (C.2.1). The purpose of this file is define how data will be presented in the website as well as define what actions can be performed. This is a bigger file so let's take a look at what the main functions are: *home*, *acquire*, *acquire_time*, *plot*, *sensor* and *history*. We won't go into much detail on the last two as the *sensor* action is associated with json output page for mostly debug purposes and the *history* action tracks the values of sensor with time. One important note is that we programmed everything in this server to be as future proof as possible. What this means is that, even though we didn't have an installed spectrometer in our prototype, we have programmed the server in such a way that is prepared to accept such data and track it with functions like *history*. This was even tested by sending randomly generated data with the Arduino.

Every one of these functions is associated with an url of our website. Some of these actions also work through custom made html templates (C.2.7, C.2.8) and javascript files that we won't discuss in this main text as they weren't developed by us. The references for the three javascripts used are: [Raphaël 2.1.0 - JavaScript Vector Library](#), [JustGage](#) and [jQuery v1.10.2](#).

The *home* function defines what the [homepage](#) of our website looks like with the code:

```

1 from django.shortcuts import render
2 from .models import SensorType, SensorData
3

```



```

4 def home(request):
5     return render(request, 'home/index.html', {'sensors': SensorType.objects.
        ↪ filter(data_type='0'), 'sensor_graphs': SensorType.objects.filter(
        ↪ data_type='1'),})

```

where we process a request to access the [homepage](#) and fetch the needed sensor objects from the database. The output is shown in Figure B.1. Where we present the logo of our University as button to this homepage followed by a json button that activates the output from the *sensor* action. After that, we show the capabilities of information display of this server by providing several graphs and values. The presented data as it has been said above consists of dummy values sent by the Arduino and is a proof of concept. The meter displays are js scripts that fill up when the page is loaded and the histogram is processed with python's *matplotlib* in the function *plot* from the views file. Using this library within this function we are able to process a standard python plot and convert it as an image HTTP response. The graph generated is stored as an image separately in the [url](#) that can be accessed by clicking on histogram in the homepage. Clicking on the meter displays will give you access to the recent recorded values for that sensor. Bellow each one of the sensor types we can see their acquisition status.

Perhaps the most important function defined server side is the *acquire* function. In this we define how the server processes client interactions for measurement purposes. This function uses the following code:

```

1 from django.shortcuts import render
2 from django.http import HttpResponse, HttpResponseForbidden
3 from .models import SensorType, SensorData
4 from datetime import datetime, timedelta
5
6 def acquire(request, code):
7     if request.method == 'GET':
8         try:
9             now = datetime.now()
10            rlog=open("requestlog.txt", "a+")
11            rlog.write(now.strftime("%m/%d/%Y,_%H:%M:%S"))
12            rlog.write("___")
13            rlog.write("GET")
14            rlog.write("\n")
15            rlog.close()
16            sensor = SensorType.objects.get(code=code)
17            sensor.rlog.name='requestlog.txt'
18            sensor.save()
19            if(sensor.acquiring=='1'):
20                return HttpResponse('Go')
21            else:
22                return HttpResponse('No')
23        except SensorType.DoesNotExist:
24            return HttpResponseForbidden
25

```

```

26     if request.method == 'POST':
27         try:
28             sensor = SensorType.objects.get(code=code)
29             value=request.POST['St']
30             if(value=='S' and request.META['HTTP_USER_AGENT']=='Arduino/1.0'):
31                 sensor.ch_acq('2')
32                 sensor.acq_update()
33                 sensor.save()
34                 now = datetime.now()
35                 log=open("log.txt", "a+")
36                 log.write(now.strftime("%m/%d/%Y,_%H:%M:%S"))
37                 log.write("___")
38                 log.write(sensor.get_acquiring_display())
39                 log.write("\n")
40                 log.close()
41                 sensor.log.name='log.txt'
42                 sensor.save()
43                 return HttpResponse(sensor.code + ":" + sensor.acquiring)
44             if(value=='F' and request.META['HTTP_USER_AGENT']=='Arduino/1.0'):
45                 if(sensor.acq_type=='1' and sensor.acq_times!=''):
46                     sensor.ch_acq('1')
47                     sensor.save()
48                 else:
49                     sensor.ch_acq('3')
50                     sensor.save()
51                     now = datetime.now()
52                     log=open("log.txt", "a+")
53                     log.write(now.strftime("%m/%d/%Y,_%H:%M:%S"))
54                     log.write("___")
55                     log.write(sensor.get_acquiring_display())
56                     log.write("\n")
57                     log.close()
58                 return HttpResponse(sensor.code + ":" + sensor.acquiring)
59
60         except SensorType.DoesNotExist:
61             return HttpResponseForbidden
62
63     return HttpResponse()

```

where we process the incoming *HTTP get* and *HTTP post* requests sent to each sensor. For this reason each generated sensor will have its own acquisition interface url such as [this](#). If an *HTTP get* request is sent to this address, the server starts by logging this request with a timestamp in *requestlog.txt*. Then it proceeds to check the internal server status for that sensor and sends an *HTTPResponse* accordingly. This means that if that sensor is marked with *Waiting for acquisition* server side the response is *Go* and otherwise the response is *No*.

If the server receives an *HTTP post* request it must check both its headers and the body. Most importantly on the header front other than the most standard header tags the client

must identify itself as *Arduino/1.0*. Regarding the body of the request the value that the server is expecting to be posted must be in the form *'St=x'* where *x* will either be *'S'* or *'F'*. The *'St'* here stands for status, while *'S'* means starting and *'F'* finished. When the server receives a *post* with the value *St=S* it knows that the Arduino started the measurement and thus changes in the database of the server the status for that sensor to *Acquiring*. Meanwhile, this measurement start is also logged into a *log.txt* with a timestamp. When the server receives a *post* with the value *St=F* it knows that the Arduino finished the measurement and thus changes in the database of the server the status for that sensor to *Finished*. This also logged into the same log file with a timestamp so we have an accurate history of measurements and their corresponding duration. If any of the header or body message restrictions is not complied by the client the server returns an error response.

Another complementary measurement function is also defined in the views file - *acquire_time*. As we have seen in the Arduino code, after receiving an authorization to start an acquisition it also must request the desired duration. The server handles this requests with:

```

1 from django.shortcuts import render
2 from django.http import HttpResponse, HttpResponseForbidden
3 from .models import SensorType, SensorData
4
5 def acquire_time(request, code):
6     if request.method == 'GET':
7         try:
8             sensor = SensorType.objects.get (code=code)
9             if (sensor.acq_type=='0' or sensor.acq_times==''):
10                return HttpResponse (sensor.acq_time)
11            if (sensor.acq_type=='1'):
12                acq_times=sensor.load_acqs ()
13                return HttpResponse (acq_times [0])
14
15        except SensorType.DoesNotExist:
16            return HttpResponseForbidden
17
18    if request.method == 'POST':
19        return HttpResponse ()
20
21    return HttpResponse ()

```

where we establish a request interface with the server such as [this](#). In this case the server is only waiting for *HTTP get* requests. When these requests happen the server provides that sensor specific next in queue, acquisition time to the client in the form of integer number. Every request that do not follows these rules will result in an error.

Finally, let's talk about the administration part of this server. In *admin.py* you define what this admin page looks like, what functionalities it has available and what info is accessible. Every server in the Django framework is featured with admin page by default. In this admin section of the server we must provide an user and password that is created



Figure B.2: Server admin page screenshots.

on the machine running the server by giving a superuser command. In Figure B.2 we provide some screenshots of this page.

We have configured this admin page to the purposes of this project in C.2.3. In Figure B.3 we provide more screenshots of this admin page that provide insight on how the superuser can alter in this server. As we have reiterated throughout this server description we have two main types of objects *SensorType* and *SensorData* and thus in our admin page we can deal with these separately. In Figure B.3b we see the overview for the most recent *SensorData* entries for each sensor. In this page we can: open each set to export the data, select multiple sets and delete them from the database and generate new entries. In Figure B.3a we see the overview for all the possible available *SensorType*. In this page we can: remove or add sensors to the list, clear all sensor data associated, see the logs, quickly give the order to acquire for multiple selections, quickly remove the order to acquire for multiple selections. In Figure B.3c we see for *Sensor 1* what we can edit of this object. Here we can manually set for this sensor the acquisition status and acquisitions duration as well as other minor properties.

B.6. SERVER COMMUNICATION VIA GSM/GPRS

The screenshot shows the Django administration interface for 'Sensor Types'. The header includes 'Django administration' and 'WELCOME, CARDOSO. VIEW SITE / CHANGE PASSWORD / LOG OUT'. The breadcrumb trail is 'Home > Home > Sensor Types'. The main heading is 'Select Sensor Type to change' with an 'ADD SENSOR TYPE +' button. Below this is an 'Action:' dropdown menu and a 'Go' button, with '0 of 4 selected' indicated. A list of sensor types is shown, each with a checkbox: 'SENSOR TYPE', 'Histogram', 'Sensor 1', 'Sensor 2', and 'Voltage'. At the bottom, it says '4 Sensor Types'.

(a) Sensor Type overview in the admin page

The screenshot shows the Django administration interface for 'Sensor Data'. The header includes 'Django administration' and 'WELCOME, CARDOSO. VIEW SITE / CHANGE PASSWORD / LOG OUT'. The breadcrumb trail is 'Home > Home > Sensor Data'. The main heading is 'Select Sensor Data to change' with an 'ADD SENSOR DATA +' button. Below this is an 'Action:' dropdown menu and a 'Go' button, with '0 of 12 selected' indicated. A list of sensor data entries is shown, each with a checkbox and details like date, time, sensor type, and value. A 'FILTER' sidebar is visible on the right, with 'By type' options: 'All', 'Histogram', 'Sensor 1', 'Sensor 2', and 'Voltage'.

(b) Sensor Data overview in the admin page

The screenshot shows the Django administration interface for editing 'Sensor 1'. The header includes 'Django administration' and 'WELCOME, CARDOSO. VIEW SITE / CHANGE PASSWORD / LOG OUT'. The breadcrumb trail is 'Home > Home > Sensor Types > Sensor 1'. The main heading is 'Change Sensor Type' with a 'HISTORY' button. The form contains several fields: 'Name' (Sensor 1), 'Code' (temp1), 'Min value' (0.0), 'Max value' (50.0), 'Acq time' (1), 'Acq times' (empty), 'Units' (a.u.), and 'Description' (empty text area). Below the form are 'Log' and 'Rlog' sections, each with 'Currently: log.txt' and 'Change: Explorer...' buttons. At the bottom, there are 'Acquiring' (Acquisition complete), 'Data type' (Single Value), and 'Acq type' (Single) dropdown menus. At the very bottom, there are 'Delete', 'Save and add another', 'Save and continue editing', and 'SAVE' buttons.

(c) Sensor 1 edit options

Figure B.3: Screenshots of the administration features.



APPENDIX 2

In this appendix we will present all the code developed for this work.

C.1 Arduino Code

C.1.1 Arduino Master

```
1 #include "SIM900.h"
2 #include <SoftwareSerial.h>
3 #include "inetGSM.h"
4
5 #include <Wire.h>
6
7 char msg[200];
8 char resp[16];
9 int numdata;
10
11 int i=0;
12 bool ok;
13 char c[32];
14 char cc[32];
15
16 int s;
17 int count=0;
18 int count2=0;
19
20 char end_c[2];
21
22 static char server[15]="193.136.125.67";
23 static char path1[12]="/acq/templ/";
24 static char path2[13]="/acqt/templ/";
25
26 static char at1[3]="at";
27 static char at2[9]="at+cpin?";
28 static char at3[13]="at+cpin=3220";
29 static char at4[8]="at+csq";
30 static char at5[9]="at+creg?";
31 static char at6[10]="at+cgatt?";
32 static char at7[55]="at+csstt=\"net2.vodafone.pt\", \"vodafone\", \"vodafone\"";
33 static char at8[9]="at+ciicr";
```

APPENDIX C. APPENDIX 2

```
34 static char at9[9]="at+cifsr";
35
36 int char_diff=0;
37
38 long int sample_time=0;
39
40
41 void setup()
42 {
43     Wire.begin();
44     end_c[0]=0x1a;
45     end_c[1]='\0';
46
47     //Serial connection.
48     Serial.begin(9600);
49     Serial.println(F("GSM_Shield_testing."));
50
51     //Start configuration of shield with baudrate.
52     //For http uses is raccomanded to use 4800 or slower.
53     if (gsm.begin(9600))
54         Serial.println(F("\nstatus=READY"));
55     else Serial.println(F("\nstatus=IDLE"));
56
57     gsmcommand(at1,true);
58     gsmcommand(at2,true);
59
60     gsmcommand(at3,true);
61     gsmcommand(at4,false);
62     gsmcommand(at5,false);
63 // gsmcommand("at+cipmux=1",false);
64 // gsmcommand("at+cipmode=0",false);
65     gsmcommand(at6,false);
66 // gsmcommand("at+cstt=\"internet\"",false);
67     gsmcommand(at7,false);
68
69     gsmcommand(at8,false);
70     gsmcommand(at9,false);
71     gsm.WhileSimpleRead();
72
73     httpget(path2);
74 }
75
76 char httpget(char* path){
77     memset(msg,0,200);
78     Serial.println(server);
79     Serial.println(path);
80     numdata=inet.httpGET(server, 80,path,msg, 200);
81
82     Serial.println(F("\nNumber_of_data_received:"));
83     Serial.println(numdata);
84     Serial.println(F("\nData_received:"));
85     Serial.println(msg);
86     gsm.WhileSimpleRead();
87     inet.disconnectTCP();
88
89     if(numdata<180){
90         if(count2==3){
91             Serial.println(F("Reset"));
92             count2=0;
93             setup();
94             httpget(path);
95             return;
96         }
97         else{
98             count2++;
99             httpget(path);
100             return;
101         }
102     }
```



```

103 | memset (resp,0,16);
104 | char_diff=numdata-182;
105 | for (int i = 0; i < char_diff; i++){
106 |     resp[i]=msg[numdata-char_diff+i];
107 | }
108 | Serial.println (resp);
109 | return (resp);
110 | }
111 |
112 | char httpgett (char* path){
113 |     memset (msg,0,200);
114 |
115 |     numdata=inet.httpGET(server, 80,path,msg, 200);
116 |
117 |     Serial.println (F("\nNumber_of_data_received:"));
118 |     Serial.println (numdata);
119 |     Serial.println (F("\nData_received:"));
120 |     Serial.println (msg);
121 |     gsm.WhileSimpleRead ();
122 |     inet.disconnectTCP ();
123 |
124 |     if (numdata<180) {
125 |         if (count2==3) {
126 |             Serial.println (F("Reset"));
127 |             count2=0;
128 |             setup ();
129 |             httpgett (path);
130 |             return;
131 |         }
132 |         else{
133 |             count2++;
134 |             httpgett (path);
135 |             return;
136 |         }
137 |     }
138 |     resp[0]=msg[numdata-2];
139 |     resp[1]=msg[numdata-1];
140 |     Serial.println (resp);
141 |     return (resp);
142 | }
143 |
144 | char httppost () {
145 |     memset (msg,0,200);
146 |     numdata=inet.httpPOST(server, 80, path1, "St=S",msg, 200);
147 |     Serial.println (F("\nNumber_of_data_received:"));
148 |     Serial.println (numdata);
149 |     Serial.println (F("\nData_received:"));
150 |     Serial.println (msg[-2]);
151 |     delay (1000);
152 |     gsm.WhileSimpleRead ();
153 |     inet.disconnectTCP ();
154 |     return (msg);
155 | }
156 |
157 | char httppostt () {
158 |     memset (msg,0,200);
159 |     numdata=inet.httpPOST(server, 80, path1, "St=F",msg, 200);
160 |     Serial.println (F("\nNumber_of_data_received:"));
161 |     Serial.println (numdata);
162 |     Serial.println (F("\nData_received:"));
163 |     Serial.println (msg[-2]);
164 |     delay (1000);
165 |     gsm.WhileSimpleRead ();
166 |     inet.disconnectTCP ();
167 |     return (msg);
168 | }
169 |
170 | void loop () {
171 |     httpget (path1);

```

APPENDIX C. APPENDIX 2

```

172 //httpget();
173 Serial.println(F("resp"));
174 Serial.println(resp[0]);
175 if(resp[0]=='N'){
176     delay(1000);
177     Serial.println(F("No"));
178     Wire.beginTransmission(9); // transmit to device #9
179     Wire.write("l1"); // sends
180     Wire.endTransmission(); // stop transmitting
181     delay(200);
182 }
183
184 else if(resp[0]=='G'){
185     delay(1000);
186     httpget(path2);
187     sample_time=atol(resp)*1000*60;
188     Serial.print(F("Sample_time:_"));
189     Serial.println(sample_time);
190
191     Wire.beginTransmission(9); // transmit to device #9
192     Wire.write("l2"); // sends
193     Wire.endTransmission(); // stop transmitting
194     delay(200);
195     delay(4000);
196     Wire.beginTransmission(9); // transmit to device #9
197     Wire.write("m"); // sends
198     Wire.endTransmission(); // stop transmitting
199     delay(200);
200     Wire.beginTransmission(9); // transmit to device #9
201     Wire.write(resp); // sends
202     Wire.endTransmission(); // stop transmitting
203     httppost();
204     delay(sample_time);
205     httppostt();
206 }
207 else{
208     delay(1000);
209     Wire.beginTransmission(9); // transmit to device #9
210     Wire.write("l3"); // sends
211     Wire.endTransmission(); // stop transmitting
212     delay(200);
213 }
214 delay(60000);
215 }
216
217
218 void serialswread()
219 {
220     gsm.SimpleRead();
221 }
222
223 int checkok(char* cc)
224 {
225     s=0;
226     for (int i = 0; i < 32; i++){
227         if(cc[i+1]=='K' && cc[i]=='O'){
228             s=1;
229             break;
230         }
231         if(cc[i+4]=='R' && cc[i+3]=='O' && cc[i+2]=='R' && cc[i+1]=='R' && cc[i]=='E'){
232             s=2;
233             break;
234         }
235     }
236     memset(cc,0,32);
237     return s;
238 }
239
240 void gsmcommand(char* str,bool override_error)

```

```

241 {
242   Serial.println(str);
243   gsm.SimpleWriteln(str);
244   s=0;
245   gsm.read(c,32);
246   Serial.println(c);
247   s=checkok(c);
248
249   if(s==2 && !override_error && count<4){
250     delay(500);
251     count=count+1;
252     Serial.println(count);
253     gsmcommand(str,override_error);
254   }
255   else if(count==4){
256     count=0;
257     setup();
258   }
259   memset(c,0,32);
260 }

```

C.1.2 Arduino Slave

```

1  #include <Wire.h>
2  #include <Stepper.h>
3
4  unsigned long sample_time=0;
5  int IN1 = 5;
6  int IN2 = 6;
7  int IN3 = 7;
8  int IN4 = 8;
9  int IN5 = 9;
10 int IN6 = 10;
11 int IN7 = 11;
12
13 const int stepsPerRevolution = 400; // 400 steps=1 rotation
14
15 // initialize the stepper library on pins 8 through 11:
16 Stepper myStepper(stepsPerRevolution, 8, 9, 10, 11);
17
18 int LED = 13;
19 String data= "";
20 int i=0;
21
22 bool open= 0;
23
24 void setup() {
25   // Define the LED pin as Output
26   pinMode(LED, OUTPUT);
27   digitalWrite(LED, LOW);
28
29   // Start the I2C Bus as Slave on address 9
30   Wire.begin(9);
31   // Attach a function to trigger when something is received.
32   Wire.onReceive(receiveEvent);
33
34   Serial.begin(9600);
35
36   myStepper.setSpeed(60);
37   pinMode(IN1, OUTPUT);
38   pinMode(IN2, OUTPUT);
39   pinMode(IN3, OUTPUT);
40   pinMode(IN4, OUTPUT);
41   pinMode(IN5, OUTPUT);
42   pinMode(IN6, OUTPUT);
43   pinMode(IN7, OUTPUT);

```

```
44 | digitalWrite(IN3, LOW);
45 |
46 | }
47 |
48 | void open() {
49 |     digitalWrite(IN1, LOW);
50 |     digitalWrite(IN2, HIGH);
51 |     delay(200);
52 |
53 |     digitalWrite(IN1, HIGH);
54 |     digitalWrite(IN2, HIGH);
55 |     delay(500);
56 |     digitalWrite(IN1, LOW);
57 |     digitalWrite(IN2, LOW);
58 |     delay(500);
59 | }
60 |
61 | void close() {
62 |     digitalWrite(IN1, HIGH);
63 |     digitalWrite(IN2, LOW);
64 |     delay(200);
65 |
66 |     digitalWrite(IN1, HIGH);
67 |     digitalWrite(IN2, HIGH);
68 |     delay(500);
69 |     digitalWrite(IN1, LOW);
70 |     digitalWrite(IN2, LOW);
71 |     delay(500);
72 | }
73 |
74 | void dcfan(String com) {
75 |     if (com == "on") {
76 |         digitalWrite(IN3, HIGH);
77 |     }
78 |     else if (com == "off") {
79 |         digitalWrite(IN3, LOW);
80 |     }
81 | }
82 |
83 | void stepper() {
84 |     Serial.println("rolling");
85 |     myStepper.step(stepsPerRevolution);
86 |     delay(500);
87 |     digitalWrite(IN4, LOW);
88 |     digitalWrite(IN5, LOW);
89 |     digitalWrite(IN6, LOW);
90 |     digitalWrite(IN7, LOW);
91 |     delay(500);
92 | }
93 |
94 | void receiveEvent(int bytes) {
95 |
96 |     data="";
97 |     while( Wire.available() ){
98 |         data+= (char)Wire.read();
99 |     }
100 |     Serial.println(data);
101 | }
102 |
103 | void loop() {
104 |
105 |
106 |     if (data == "open" && open == 0) {
107 |         abrir();
108 |         aberto=1;
109 |         Serial.println("Open");
110 |         data="";
111 |     }
112 | }
```

```
113 if (data == "close" && open == 1) {
114     fechar();
115     aberto=0;
116     Serial.println("Closed");
117     data="";
118 }
119
120 if (data == "step") {
121     Serial.println("Unroll");
122     myStepper.step(-stepsPerRevolution);
123     stepper();
124     data="";
125 }
126
127 if (data == "dcfan") {
128     Serial.println("On");
129     dcfan("on");
130     delay(1000);
131     ventoinha("off");
132     data="";
133 }
134 if (data == "led0") {
135     Serial.println("ON");
136     digitalWrite(LED, HIGH);
137     delay(3000);
138     digitalWrite(LED, LOW);
139     delay(500);
140     data="";
141 }
142 if (data == "l1") {
143     Serial.println("NO");
144     digitalWrite(LED, HIGH);
145     delay(500);
146     digitalWrite(LED, LOW);
147     delay(500);
148     digitalWrite(LED, HIGH);
149     data="";
150 }
151 if (data == "l2") {
152     Serial.println("GO");
153     digitalWrite(LED, HIGH);
154     delay(500);
155     digitalWrite(LED, LOW);
156     delay(500);
157     digitalWrite(LED, HIGH);
158     delay(500);
159     digitalWrite(LED, LOW);
160     delay(500);
161     digitalWrite(LED, HIGH);
162     data="";
163 }
164 if (data == "l3") {
165     Serial.println("No_Connection");
166     digitalWrite(LED, HIGH);
167     delay(500);
168     digitalWrite(LED, LOW);
169     delay(500);
170     digitalWrite(LED, HIGH);
171     delay(500);
172     digitalWrite(LED, LOW);
173     delay(500);
174     digitalWrite(LED, HIGH);
175     delay(500);
176     digitalWrite(LED, LOW);
177     delay(500);
178     digitalWrite(LED, HIGH);
179     data="";
180 }
181
```

```

182 | if (data=="m") {
183 |   Serial.println(data);
184 |   while(data=="m"){
185 |     delay(500);
186 |   }
187 |   Serial.println(data);
188 |   if(data!="m"){
189 |     sample_time=data.toInt()*1000*60;
190 |     Serial.println(sample_time);
191 |     open();
192 |     open=1;
193 |
194 |     stepper();
195 |
196 |     close();
197 |     open=0;
198 |
199 |     Serial.println("ON");
200 |     ventoinha("on");
201 |     delay(sample_time);
202 |     ventoinha("off");
203 |     data="";
204 |   }
205 | }
206 | }

```

C.2 Server Code

C.2.1 Views

```

1 | import json
2 | from django.shortcuts import render
3 | from django.http import HttpResponse, HttpResponseForbidden
4 | from .models import SensorType, SensorData
5 | from django.views.decorators.csrf import csrf_exempt
6 | from django.views import generic
7 | from datetime import datetime, timedelta
8 | from django.utils.timezone import get_current_timezone
9 | import matplotlib.pyplot as plt
10 | import numpy as np
11 | from django.conf import settings
12 | from matplotlib.backends.backend_agg import FigureCanvasAgg
13 | import io
14 |
15 |
16 | def plot(request,code):
17 |     # Data for plotting
18 |     sensor = SensorType.objects.get(code=code)
19 |     data = SensorData.objects.filter(type=sensor)
20 |     val=data[0].val_list.split(',')
21 |     l=len(val)
22 |     e = np.arange(0, l, 1)
23 |     c = [float(i) for i in val]
24 |
25 |     fig, ax = plt.subplots()

```

```

26     ax.bar(e, c)
27     plt.xticks(e,e)
28     ax.set(xlabel='Energy', ylabel='Counts',
29           title=sensor.name)
30     buf = io.BytesIO()
31     plt.savefig(buf, format='png')
32     canvas = FigureCanvasAgg(fig)
33     canvas.print_png(buf)
34
35     plt.close(fig)
36     response = HttpResponse(buf.getvalue(),content_type = 'image/png')
37     return response
38
39 def home(request):
40     return render(request, 'home/index.html', {'sensors': SensorType.objects.
41         ↪ filter(data_type='0'),'sensor_graphs': SensorType.objects.filter(
42         ↪ data_type='1'),})
43
44 @csrf_exempt
45 def acquire(request, code):
46     if request.method == 'GET':
47         try:
48             now = datetime.now()
49             rlog=open("requestlog.txt","a+")
50             rlog.write(now.strftime("%m/%d/%Y,_%H:%M:%S"))
51             rlog.write("____")
52             rlog.write("GET")
53             rlog.write("\n")
54             rlog.close()
55             sensor = SensorType.objects.get(code=code)
56             sensor.rlog.name='requestlog.txt'
57             sensor.save()
58             if(sensor.acquiring=='1'):
59                 return HttpResponse('Go')
60             else:
61                 return HttpResponse('No')
62         except SensorType.DoesNotExist:
63             return HttpResponseForbidden
64
65 if request.method == 'POST':
66     try:
67         sensor = SensorType.objects.get(code=code)
68         value=request.POST['St']
69         if(value=='S' and request.META['HTTP_USER_AGENT']=='Arduino/1.0'):
70             sensor.ch_acq('2')
71             sensor.acq_update()
72             sensor.save()
73             now = datetime.now()
74             log=open("log.txt","a+")
75             log.write(now.strftime("%m/%d/%Y,_%H:%M:%S"))

```

```

74         log.write("_ _ _")
75         log.write(sensor.get_acquiring_display())
76         log.write("\n")
77         log.close()
78         sensor.log.name='log.txt'
79         sensor.save()
80         return HttpResponse(sensor.code + ":" + sensor.acquiring)
81     if(value=='F' and request.META['HTTP_USER_AGENT']=='Arduino/1.0'):
82         if(sensor.acq_type=='1' and sensor.acq_times!=''):
83             sensor.ch_acq('1')
84             sensor.save()
85         else:
86             sensor.ch_acq('3')
87             sensor.save()
88             now = datetime.now()
89             log=open("log.txt","a+")
90             log.write(now.strftime("%m/%d/%Y,_%H:%M:%S"))
91             log.write("_ _ _")
92             log.write(sensor.get_acquiring_display())
93             log.write("\n")
94             log.close()
95             return HttpResponse(sensor.code + ":" + sensor.acquiring)
96
97     except SensorType.DoesNotExist:
98         return HttpResponseForbidden
99
100    return HttpResponse()
101 def acquire_time(request, code):
102     if request.method == 'GET':
103         try:
104             sensor = SensorType.objects.get(code=code)
105             if(sensor.acq_type=='0' or sensor.acq_times==''):
106                 return HttpResponse(sensor.acq_time)
107             if(sensor.acq_type=='1'):
108                 acq_times=sensor.load_acqs()
109                 return HttpResponse(acq_times[0])
110
111         except SensorType.DoesNotExist:
112             return HttpResponseForbidden
113
114     if request.method == 'POST':
115         return HttpResponse()
116
117     return HttpResponse()
118
119
120 @csrf_exempt
121 def sensor(request):
122     if request.method == 'GET':
123         response_data = {}

```



```

124
125     # Get the latest sensor data for each sensor type
126     for sensor in SensorType.objects.all():
127         sensor_data = sensor.data.first()
128         if sensor_data and sensor.data_type=='0':
129             response_data[sensor.code] = sensor_data.value
130         elif sensor_data and sensor.data_type=='1':
131             response_data[sensor.code] = sensor_data.val_list
132
133     # Send the result as JSON
134     return HttpResponse(json.dumps(response_data), content_type="application/
        ↪ json")
135
136 if request.method == 'POST':
137     # Check if the sensor code exists and store the value in the database
138     for sensor, value in request.POST.items():
139         try:
140             sensor_type = SensorType.objects.get(code=sensor)
141             sensor_data = SensorData()
142             sensor_data.type = sensor_type
143             if(sensor_type.data_type=='0'):
144                 sensor_data.value = float(value)
145             elif(sensor_type.data_type=='1'):
146                 sensor_data.val_list = value
147             sensor_data.save()
148             sensor_type.ch_acq('3')
149             sensor_type.save()
150         except (SensorType.DoesNotExist, ValueError):
151             pass
152
153     return HttpResponse()
154
155 return HttpResponseForbidden
156
157 def history(request, code, year, month, day):
158     if request.method == 'GET':
159         try:
160             sensor = SensorType.objects.get(code=code)
161             settings.TIME_ZONE
162             start_time = datetime(int(year), int(month), int(day), tzinfo=
        ↪ get_current_timezone())
163             end_time = start_time + timedelta(days=1)
164
165             # Get data for the given sensor code
166             all_sensor_data = sensor.data.filter(time__range=(start_time,
        ↪ end_time)).all()
167             sensor_data = []
168             if all_sensor_data:
169                 for i in range(0, len(all_sensor_data) - 1):

```

```

170         if all_sensor_data[i].time.minute != all_sensor_data[i + 1].
171             ↪ time.minute:
172             sensor_data += [all_sensor_data[i]]
173         return render(request, 'home/history.html', {
174             'date': start_time,
175             'previous_date': start_time - timedelta(days=1),
176             'next_date': end_time,
177             'sensor': sensor,
178             'sensor_data': reversed(sensor_data),
179         })
180     except SensorType.DoesNotExist:
181         return HttpResponseForbidden
182
183     return HttpResponseForbidden

```

C.2.2 Models

```

1 from django.db import models
2 from django.utils.dateparse import parse_datetime
3 from django.core.validators import validate_comma_separated_integer_list
4
5 class SensorType(models.Model):
6     name = models.CharField(max_length=100)
7     code = models.SlugField(max_length=50)
8     min_value = models.FloatField()
9     max_value = models.FloatField()
10    acq_time = models.IntegerField(default=0)
11    acq_times = models.CharField(max_length=10000, validators=[
12        ↪ validate_comma_separated_integer_list], blank=True, null=True, default
13        ↪='')
14    units = models.CharField(max_length=100)
15    description = models.TextField(blank=True)
16    log= models.FileField(upload_to='', default='log.txt')
17    rlog= models.FileField(upload_to='', default='requestlog.txt')
18    acq = [
19        ('0', 'Idle'),
20        ('1', 'Waiting_for_aquisition'),
21        ('2', 'Acquiring'),
22        ('3', 'Acquisition_complete'),
23    ]
24    acquiring = models.CharField(
25        max_length=2,
26        choices=acq,
27        default=0,
28    )
29    val_type = [
30        ('0', 'Single_Value'),
31        ('1', 'List'),
32    ]

```

```

31     data_type = models.CharField(
32         max_length=2,
33         choices=val_type,
34         default=0,
35     )
36     a_type = [
37         ('0', 'Single'),
38         ('1', 'Multiple'),
39     ]
40     acq_type = models.CharField(
41         max_length=2,
42         choices=a_type,
43         default=0,
44     )
45
46     def ch_acq(self, val):
47         self.acquiring=val
48
49     def load_acqs(self):
50         values = [int(x) for x in self.acq_times.split(',') if x]
51         return values
52
53
54     def acq_update(self):
55         try:
56             values=self.load_acqs()
57         except (AttributeError):
58             values=[]
59         try:
60             del values[0]
61             self.acq_times=str(values).strip('[]')
62         except (IndexError):
63             pass
64
65     class Meta:
66         verbose_name = 'Sensor_Type'
67         verbose_name_plural = 'Sensor_Types'
68         ordering = ['name']
69
70     def __str__(self):
71         return self.name
72
73
74 class SensorData(models.Model):
75     time = models.DateTimeField(auto_now_add=True)
76     type = models.ForeignKey(SensorType, related_name='data', on_delete=models.
77         ↪ CASCADE)
78     value = models.FloatField(default=0)
79     val_list=models.CharField(max_length=10000,default=list)

```

```

80     class Meta:
81         verbose_name = 'Sensor_Data'
82         verbose_name_plural = 'Sensor_Data'
83         ordering = ['-time']
84
85     def __str__(self):
86         if self.type.data_type=='0':
87             return '%s_-%s_-%.5f%s' % (self.time.strftime("%d/%m/%Y-%H:%M:%S"),
88                 ↪ self.type, self.value, self.type.units)
89         if self.type.data_type=='1':
90             return '%s_-%s_-%s' % (self.time.strftime("%d/%m/%Y-%H:%M:%S"),
91                 ↪ self.type, self.val_list)

```

C.2.3 Admin

```

1  from django.contrib import admin
2  from .models import SensorType, SensorData
3  from django.urls import reverse
4  from django.http import HttpResponse, HttpResponseForbidden
5
6  def acquire(model_admin, request, queryset):
7      queryset.update(acquiring='1')
8  acquire.short_description = "Acquire"
9
10 def stop(model_admin, request, queryset):
11     queryset.update(acquiring='0')
12 stop.short_description = "Stop"
13
14
15 def clear_sensor_data(model_admin, request, queryset):
16     for sensor_type in queryset:
17         SensorData.objects.filter(type=sensor_type).delete()
18 clear_sensor_data.short_description = "Clear_sensor_data"
19
20 def log(model_admin, request, queryset):
21     q=queryset.get()
22     l=q.log.file.open(mode=None)
23     r=l.read()
24     return HttpResponse(r, content_type="text/plain")
25 log.short_description = "See_log.txt"
26
27 def rlog(model_admin, request, queryset):
28     q=queryset.get()
29     l=q.rlog.file.open(mode=None)
30     r=l.read()
31     return HttpResponse(r, content_type="text/plain")
32 rlog.short_description = "See_rlog.txt"
33
34 class SensorTypeAdmin(admin.ModelAdmin):

```

```

35     actions = [clear_sensor_data, acquire, stop, log, rlog]
36
37     class SensorDataAdmin(admin.ModelAdmin):
38         list_filter=('type',)
39
40     admin.site.register(SensorType, SensorTypeAdmin)
41     admin.site.register(SensorData, SensorDataAdmin)

```

C.2.4 App Urls

```

1     from django.urls import path, re_path
2     from . import views
3
4     urlpatterns = [
5         path('', views.home, name='index'),
6         re_path('acq/(?P<code>[a-zA-Z0-9-_]+)', views.acquire, name='acquire'),
7         re_path('acqt/(?P<code>[a-zA-Z0-9-_]+)', views.acquire_time, name='
           ↳ acquire_time'),
8         re_path('graphs/(?P<code>[a-zA-Z0-9-_]+)', views.plot, name='plot'),
9         path('sensor/', views.sensor, name='sensor'),
10        re_path('history/(?P<code>[a-zA-Z0-9-_]+)/(?P<year>\d{4})/(?P<month>\d{2})
           ↳ /(?P<day>\d{2})/', views.history, name='history'),
11    ]

```

C.2.5 Site Urls

```

1     from django.contrib import admin
2     from django.urls import include, path
3     from django.conf.urls.static import static
4     from django.conf import settings
5
6     urlpatterns = [
7         path('', include('home.urls')),
8         path('admin/', admin.site.urls),
9     ] + static(settings.STATIC_URL, document_root=settings.STATIC_ROOT)

```

C.2.6 Settings

```

1     import os
2
3     BASE_DIR = os.path.dirname(os.path.dirname(os.path.abspath(__file__)))
4
5     SECRET_KEY = ''
6
7     DEBUG = True
8
9     ALLOWED_HOSTS = ['127.0.0.1', '192.168.1.69']

```

APPENDIX C. APPENDIX 2

```
10 |
11 | # Application definition
12 |
13 | INSTALLED_APPS = [
14 |     'home.apps.HomeConfig',
15 |     'django.contrib.admin',
16 |     'django.contrib.auth',
17 |     'django.contrib.contenttypes',
18 |     'django.contrib.sessions',
19 |     'django.contrib.messages',
20 |     'django.contrib.staticfiles',
21 | ]
22 |
23 | MIDDLEWARE = [
24 |     'django.middleware.security.SecurityMiddleware',
25 |     'django.contrib.sessions.middleware.SessionMiddleware',
26 |     'django.middleware.common.CommonMiddleware',
27 |     'django.middleware.csrf.CsrfViewMiddleware',
28 |     'django.contrib.auth.middleware.AuthenticationMiddleware',
29 |     'django.contrib.messages.middleware.MessageMiddleware',
30 |     'django.middleware.clickjacking.XFrameOptionsMiddleware',
31 | ]
32 |
33 | ROOT_URLCONF = 'mysite.urls'
34 |
35 | TEMPLATES = [
36 |     {
37 |         'BACKEND': 'django.template.backends.django.DjangoTemplates',
38 |         'DIRS': [os.path.join(BASE_DIR, 'templates')],
39 |         'APP_DIRS': True,
40 |         'OPTIONS': {
41 |             'context_processors': [
42 |                 'django.template.context_processors.debug',
43 |                 'django.template.context_processors.request',
44 |                 'django.contrib.auth.context_processors.auth',
45 |                 'django.contrib.messages.context_processors.messages',
46 |             ],
47 |         },
48 |     },
49 | ]
50 |
51 | WSGI_APPLICATION = 'mysite.wsgi.application'
52 |
53 |
54 | DATABASES = {
55 |     'default': {
56 |         'ENGINE': 'django.db.backends.sqlite3',
57 |         'NAME': os.path.join(BASE_DIR, 'db.sqlite3'),
58 |     }
59 | }
```

```

60
61 AUTH_PASSWORD_VALIDATORS = [
62     {
63         'NAME': 'django.contrib.auth.password_validation.
           ↳ UserAttributeSimilarityValidator',
64     },
65     {
66         'NAME': 'django.contrib.auth.password_validation.MinimumLengthValidator',
           ↳
67     },
68     {
69         'NAME': 'django.contrib.auth.password_validation.CommonPasswordValidator'
           ↳ ,
70     },
71     {
72         'NAME': 'django.contrib.auth.password_validation.
           ↳ NumericPasswordValidator',
73     },
74 ]
75
76
77 LANGUAGE_CODE = 'en-us'
78
79 TIME_ZONE = 'Europe/Lisbon'
80
81 USE_I18N = True
82
83 USE_L10N = True
84
85 USE_TZ = True
86
87
88 MEDIA_ROOT = BASE_DIR
89
90 MEDIA_URL = ''
91
92 STATIC_ROOT = os.path.join(BASE_DIR, 'static')
93
94 STATIC_URL = '/static/'

```

C.2.7 History html

```

1 {% load static %}
2 <!DOCTYPE html>
3 <html>
4 <head>
5     <link rel="apple-touch-icon" sizes="57x57" href="{% static "/ico/apple-icon-57
           ↳ x57.png" %}>

```

```
6 <link rel="apple-touch-icon" sizes="60x60" href={% static "/ico/apple-icon-60
  ↳ x60.png" %}>
7 <link rel="apple-touch-icon" sizes="72x72" href={% static "/ico/apple-icon-72
  ↳ x72.png" %}>
8 <link rel="apple-touch-icon" sizes="76x76" href={% static "/ico/apple-icon-76
  ↳ x76.png" %}>
9 <link rel="apple-touch-icon" sizes="114x114" href={% static "/ico/apple-icon
  ↳ -114x114.png" %}>
10 <link rel="apple-touch-icon" sizes="120x120" href={% static "/ico/apple-icon
  ↳ -120x120.png" %}>
11 <link rel="apple-touch-icon" sizes="144x144" href={% static "/ico/apple-icon
  ↳ -144x144.png" %}>
12 <link rel="apple-touch-icon" sizes="152x152" href={% static "/ico/apple-icon
  ↳ -152x152.png" %}>
13 <link rel="apple-touch-icon" sizes="180x180" href={% static "/ico/apple-icon
  ↳ -180x180.png" %}>
14 <link rel="icon" type="image/png" sizes="192x192" href={% static "/ico/
  ↳ android-icon-192x192.png" %}>
15 <link rel="icon" type="image/png" sizes="32x32" href={% static "/ico/favicon
  ↳ -32x32.png" %}>
16 <link rel="icon" type="image/png" sizes="96x96" href={% static "/ico/favicon
  ↳ -96x96.png" %}>
17 <link rel="icon" type="image/png" sizes="16x16" href={% static "/ico/favicon
  ↳ -16x16.png" %}>
18 <link rel="manifest" href={% static "/ico/manifest.json" %}>
19 <meta name="msapplication-TileColor" content="#ffffff">
20 <meta name="msapplication-TileImage" content={% static "/ico/ms-icon-144x144.
  ↳ png" %}>
21 <meta name="theme-color" content="#ffffff">
22
23 <script type="text/javascript" src="https://www.google.com/jsapi"></script>
24 <script type="text/javascript">
25     google.load("visualization", "1", {packages:["corechart"]});
26     google.setOnLoadCallback(drawChart);
27     function drawChart() {
28         var data = new google.visualization.DataTable();
29         data.addColumn('datetime', 'Hora');
30         data.addColumn('number', '');
31         {% for data in sensor_data %}
32             data.addRow([new Date("{{_data.time|date:"c"_"}}"), {{ data.value
  ↳ }}]);
33         {% endfor %}
34
35         var options = {
36             title: '{{ sensor.name }} ({{ sensor.units }}) - {{ date|date:"d/m/Y"
  ↳ }}',
37             legend: { position: 'none' }
38         };
39
```



```

40     var chart = new google.visualization.LineChart(document.getElementById('
      ↪ chart_div'));
41     chart.draw(data, options);
42 }
43 </script>
44 <title>Monitoramento de Processo - Histórico - {{ sensor.name }} - {{ date|
      ↪ date:"d/m/Y" }}</title>
45 </head>
46 <body>
47 <div id="logo" style="padding:_20px_0_0_40px">
48   <a href="{% _url_ 'index' _%}">
49 </div>
50 <div id="chart_div" style="width:_900px;_height:_500px;"></div>
51 <div style="width:_900px;_text-align:_center;">
52   <<
53   <a href="{% _url_ 'history' _code=sensor.code_year=previous_date.year|
      ↪ stringformat:"04i" _month=previous_date.month|stringformat:"02i" _day=
      ↪ previous_date.day|stringformat:"02i" _%}">Dia anterior</a>
54   |
55   <a href="{% _url_ 'history' _code=sensor.code_year=next_date.year|stringformat:
      ↪ "04i" _month=next_date.month|stringformat:"02i" _day=next_date.day|
      ↪ stringformat:"02i" _%}">Próximo dia</a>
56   >>
57 <!-- </div>
58 <div style="width:_900px;_text-align:_center;">
59   <a href="{% _url_ 'index' _%}">Tela principal</a>
60 </div> -->
61 </body>
62 </html>

```

C.2.8 Home html

```

1  {% load static %}
2  <!DOCTYPE html>
3  <html>
4  <head>
5    <link rel="apple-touch-icon" sizes="57x57" href="{% static "/ico/apple-icon-57
      ↪ x57.png" %}">
6    <link rel="apple-touch-icon" sizes="60x60" href="{% static "/ico/apple-icon-60
      ↪ x60.png" %}">
7    <link rel="apple-touch-icon" sizes="72x72" href="{% static "/ico/apple-icon-72
      ↪ x72.png" %}">
8    <link rel="apple-touch-icon" sizes="76x76" href="{% static "/ico/apple-icon-76
      ↪ x76.png" %}">
9    <link rel="apple-touch-icon" sizes="114x114" href="{% static "/ico/apple-icon
      ↪ -114x114.png" %}">
10   <link rel="apple-touch-icon" sizes="120x120" href="{% static "/ico/apple-icon
      ↪ -120x120.png" %}">

```

```

11 <link rel="apple-touch-icon" sizes="144x144" href={% static "/ico/apple-icon
    ↳ -144x144.png" %}>
12 <link rel="apple-touch-icon" sizes="152x152" href={% static "/ico/apple-icon
    ↳ -152x152.png" %}>
13 <link rel="apple-touch-icon" sizes="180x180" href={% static "/ico/apple-icon
    ↳ -180x180.png" %}>
14 <link rel="icon" type="image/png" sizes="192x192" href={% static "/ico/
    ↳ android-icon-192x192.png" %}>
15 <link rel="icon" type="image/png" sizes="32x32" href={% static "/ico/favicon
    ↳ -32x32.png" %}>
16 <link rel="icon" type="image/png" sizes="96x96" href={% static "/ico/favicon
    ↳ -96x96.png" %}>
17 <link rel="icon" type="image/png" sizes="16x16" href={% static "/ico/favicon
    ↳ -16x16.png" %}>
18 <link rel="manifest" href={% static "/ico/manifest.json" %}>
19 <meta name="msapplication-TileColor" content="#ffffff">
20 <meta name="msapplication-TileImage" content={% static "/ico/ms-icon-144x144.
    ↳ png" %}>
21 <meta name="theme-color" content="#ffffff">
22
23 <script src={% static "/js/jquery.js" %}></script>
24 <script src={% static "/js/raphael.js" %}></script>
25 <script src={% static "/js/justgage.js" %}></script>
26 <script type="text/javascript">
27     {% for sensor in sensors %}
28         var {{ sensor.code }}Gauge;
29     {% endfor %}
30
31     $(function() {
32         {% for sensor in sensors %}
33             {{ sensor.code }}Gauge = new JustGage({
34                 id: "{{_sensor.code_}}-gauge",
35                 value: 0,
36                 min: {{ sensor.min_value }},
37                 max: {{ sensor.max_value }},
38                 title: "{{_sensor.name_}}",
39                 label: "{{_sensor.units_}}",
40                 refreshAnimationTime: 1000,
41                 refreshAnimationType: "linear"
42             });
43         {% endfor %}
44
45         update();
46     });
47
48     function update() {
49         $.getJSON("sensor", function (data) {
50             {% for sensor in sensors %}
51                 if (data["{{_sensor.code_}}"] != undefined) {
52                     {{ sensor.code }}Gauge.refresh(data["{{_sensor.code_}}"]);

```

```

53         }
54         {% endfor %}
55     });
56     setTimeout("update()", 1000);
57 }
58
59 </script>
60 <title>Autoeuropa Prototype</title>
61 <style>
62     body {
63         transform: scale(0.84);
64         transform-origin: 0 0;
65         overflow:hidden;
66     }
67
68 </style>
69 </head>
70 <body>
71 <div id="logo" style="padding:_20px_0_0_40px">
72     <a href="{%_url_'index'_}">
74 </div>
75 <form>
76     <button formaction="{%_url_'sensor'_}">Sensor json</button>
77 </form>
78 </div>
79 {% for sensor in sensors %}
80 <a href="/history/{{_sensor.code_}}/{%_now_'Y/m/d'_}">
81 <div id="{{_sensor.code_}}-gauge" style="float:_left;_width:_420px;_height:_
82     ↪ 336px;"> <div style="vertical-align:middle;_width:_420px;_height:_100px;
83     ↪ _text-align:center;_font-size:Large;">{{ sensor.get_acquiring_display
84     ↪ }} </div> </div>
85 </a>
86 {% endfor %}
87 <p style="position:_relative;_width:_1px;_height:_336px;">
88
89 <div
90 {% for sensor in sensor_graphs %}
91 <div style="float:left">
92 <a href="/graphs/{{_sensor.code_}}">
93
94  <div style="vertical-align:middle;_width:_640px;_height:_30px;
96     ↪ _text-align:center;_font-size:Large;">{{ sensor.get_acquiring_display
97     ↪ }} </div>

```

```
96 </a>
97 </div>
98 {% endfor %}
99 </div>
100 </body>
101 </html>
```

C.3 Image processing script

```
1 from numpy import array
2 import os
3 import math
4 import numpy as np
5 import matplotlib.pyplot as plt
6 import cv2
7 import scipy.ndimage.measurements as mnts
8 try:
9     from PIL import Image
10 except ImportError:
11     import Image
12 import xlswriter
13
14
15 img_prfx='Filtro_1s_'
16 ran=[*range(10,31,1)]
17 img_sfx='.jpg'
18 images = [img_prfx + str(r) + img_sfx for r in ran]
19
20 m_t=1.4 # 1 para 3d, 1.5 para 1t
21 m_t3=2.9 # 1.8/2 para 3d, 3/3.8 para 1t
22 thres2=0.08#0.15 para 1t, 0.08/0.1? para 3d
23 window=12#12
24
25 def fourier_anal(im,thres,w):
26     img = cv2.imread(im,0)
27     f = np.fft.fft2(img)
28     fshift = np.fft.fftshift(f)
29     magnitude_spectrum = 20*np.log(np.abs(fshift))
30
31     rows, cols = img.shape
32     crow,ccol = int(rows/2) , int(cols/2)
33     fshift[crow-w:crow+w, ccol-w:ccol+w] = 0
34     f_ishift = np.fft.ifftshift(fshift)
35     img_back = np.fft.ifft2(f_ishift)
36     img_back = np.abs(img_back)
37
38     img_backb=img_back/255
39     img_backb[img_backb > thres] = 1
```

```

40     img_backb[img_backb < thres] = 0
41
42     return (img_backb)
43
44
45 def img_anal(im):
46     plt.close('all')
47     img = Image.open(im)
48     xim = array(img);
49     s=np.shape(xim);
50
51     xx=np.zeros((s[0],s[1]))
52
53     for i in range(0, s[0]-1):
54         for j in range(0, s[1]-1):
55             xx[i][j] = 0.299 *xim[i, j, 0] + 0.587 *xim[i, j, 1] + 0.114 *xim[i, j, 2]
56
57     mean=np.mean(xx/255)
58     std=np.std(xx/255)
59
60     thres=mean-(m_t*std)
61     if (mean-(m_t3*std)>0):
62         thres3=mean-(m_t3*std)
63     else:
64         thres3=0.01
65
66     xim=xx/255;
67     xim2=xx/255;
68     s=np.shape(xim);
69
70     xim[xim > thres] = 1
71     xim[xim < thres] = 0
72
73     xim_inv=np.logical_not(xim).astype(float)
74
75     xim2[xim2 > thres3] = 1
76     xim2[xim2 < thres3] = 0
77
78     xim2_inv=np.logical_not(xim2).astype(float)
79
80     img_backb=fourier_anal(im,thres2>window)
81
82     fft_comp=img_backb*xim_inv+xim2_inv
83     fft_comp[fft_comp > 1]=1
84
85     fft_comp3d = np.zeros([1536, 2048, 3], dtype=np.uint8)
86     fft_comp3d[:, :, 0]=fft_comp*255
87
88     mask_img = Image.fromarray(fft_comp3d)
89     mask_img.save(im[0:-4]+"_mask.jpeg")

```

```

90
91     fft_comp=fft_comp[0:1534,0:2046]
92     labeled, clusters = mnts.label(fft_comp)
93
94     sizes = mnts.sum(fft_comp, labeled, index=range(clusters + 1))
95
96     sizes = sizes.astype(int)
97     diam = 2*np.sqrt(sizes*0.16/math.pi)#0.4 um/pixel obter raio baseado na
98         ↪ area dos pixeis
99
100     labeledBySize = diam[labeled]
101
102     fig, ax = plt.subplots()
103     n,bins,patches=ax.hist(diam, bins = [0,1,2,3,5,10,15,20,30,50,100])
104     ax.set_xticks([0,1,2,3,5,10,15,20,30,50,100])
105     ax.set_xticklabels([0,1,2,3,5,10,15,20,30,50,100])
106     ax.set_xlabel('Bins(micrometers)')
107     ax.set_ylabel('Counts')
108     ax.set_title('Histogram_representation_of_' + im[0:-4])
109     fig.set_size_inches(18.5, 10.5)
110     fig.savefig(im[0:-4]+'_hist.png',dpi=100)
111     plt.close()
112
113     background = Image.open(im)
114     overlay = Image.open(im[0:-4]+"_mask.jpeg")
115
116     new_img = Image.blend(background, overlay, 0.5)
117     new_img.save(im[0:-4]+"_with_mask.jpeg")
118
119     m=max(diam)
120
121     return(labeledBySize,diam,clusters,fft_comp,n,bins,mean,std)
122
123 file_path=os.getcwd()+'\\Output_'+img_prfx[-3:-1]+'.xlsx'
124 workbook = xlsxwriter.Workbook(file_path)
125 worksheet = workbook.get_worksheet_by_name(img_prfx[:-1])
126 if worksheet is None:
127     worksheet = workbook.add_worksheet(img_prfx[:-1])
128 worksheet.write(0, 0, 'Area_exposta')
129 worksheet.write(1, 0, 60*60)
130 worksheet.write(0, 1, 'Area_lupa')
131 worksheet.write(1, 1, 0.615*0.82)
132 worksheet.write(0, 2, 'm_t')
133 worksheet.write(1, 2, m_t)
134 worksheet.write(0, 3, 'm_t3')
135 worksheet.write(1, 3, m_t3)
136 worksheet.write(0, 4, 'thres2')
137 worksheet.write(1, 4, thres2)
138 worksheet.write(0, 5, 'window')
139 worksheet.write(1, 5, window)
140 worksheet.write(0, 6, 'mean_intensity')

```

```
139 worksheet.write(0, 7, 'standard_deviation')
140 worksheet.write(2, 0, 'Bin(microns)')
141
142 mean_m=0
143 std_m=0
144 for nu in ran:
145
146     im=images[nu-10];
147     labeledBySize,diam,clusters,fft_comp,n,bins,mean,std=img_anal(im)
148
149     mean_m=mean_m+mean
150     std_m=std_m+std
151
152     worksheet.write(3+len(bins),int(im[-6:-4])-9,im[-6:-4])
153     worksheet.write_column(4+len(bins),int(im[-6:-4])-9,diam)
154
155     worksheet.write_column(3,0,bins[1:])
156     worksheet.write_column(3,int(im[-6:-4])-9,n)
157     print(im)
158
159 worksheet.write(1, 6, mean_m/len(ran))
160 worksheet.write(1, 7, std_m/len(ran))
161
162 worksheet.write(2, len(ran)+1, 'Average')
163 worksheet.write_formula(3,len(ran)+1,'=AVERAGE(B4:V4)')
164 worksheet.write(2, len(ran)+2, 'Particles/mm2')
165 worksheet.write_formula(3,len(ran)+2,'=W4/$B$2')
166 worksheet.write(2, len(ran)+3, 'Total_filter_particles')
167 worksheet.write_formula(3,len(ran)+3,'=X4*$A$2')
168
169 workbook.close()
```